Understanding in vivo degradation of mesoporous silica therapeutic vectors through in situ ellipsometry

Elisa Bindini

THÈSE DE DOCTORAT
DE SORBONNE UNIVERSITÉ

École doctorale : Physique et Chimie des Matériaux

réalisée

au Laboratoire de Chimie de la Matière Condensée de Paris

présentée par

Elisa BINDINI

Sujet de la thèse :

Understanding *in vivo* degradation of mesoporous silica therapeutic vectors through in situ ellipsometry.

soutenue le 6 juillet 2018

devant le jury composé de :

Pr.	Mika LINDEN	Rapporteur
Dr.	Jacques LENG	Rapporteur
Pr.	Jean-Marc FRIGERIO	Examinateur
Dr.	Marco FAUSTINI	Membre invité
Pr.	Clément SANCHEZ	Membre invité
Dr.	Andrea CATTONI	Co-encadrant
Dr.	Cédric BOISSIÈRE	Directeur de thèse

The research conducted in this Ph.D. thesis was performed between the Laboratoire de Chimie de la Matière Condensée de Paris and the Centre for Nanoscience and Nanotechnology C2N. The work was financially supported by the Région île de France and the Collège de France.

Contents

Acknowledgments

There are many people I would like to thank for being a part of this great adventure.

First of all, my supervisor Cédric Boissière for giving me a free hand to explore the world of mesoporous materials and much more. For listening, encouraging, teaching me to raise always new questions and to look old problems from a new angle, pushing me to raise always new possibilities and take new challenges.

My co-supervisor Andrea Cattoni for essential help and support. For inspirational discussions and being always available also if he had three deadlines the day after.

I would like to thank my thesis committee: Mika Linden, Jacques Leng and Jean-Marc Frigerio for accepting to evaluate and discuss my work.

L'équipe procedés: Marco, Guillaume, Igor, Quentin, Benjamin, Zeinab, Chirine.. because we struggled a lot, but together was easier. For all the great chats, all your input and ideas, coffee breaks and funny moments which made these three years special. Honorable mention to Olivier who was the best flat-mate I could ever have and the best friend, too.

All you guys in the lab who welcome me in the best way, making Paris my second home and who during the years shared with me all the joy and all the pain of research. Thank you also for the many discussions, parties, pétanques and saint-hilaire evenings, for making life lighter. With a special thought to Anael, Anne, Natacha, Francisco, César, Jessie, Guillame G., Johanna, Guillaume M. and Elham.

The Marcoussis crew: Juan, Niccolò, Carlos, Marijana, Kostantinos for all your help and support and for making my time in the Marcoussis desert a great time. Thank you also for the many great parties and endless discussions. Juan I will never thank you enough for all your help while I was struggling with microfluidics.

Omar Azzaroni and all the people of the soft-matter laboratory in Argentina: Lorena, Juan, Matias, Waldemar, Gonzalo, Juan, Facundo, Doris, Antonieta, Esteban, Agustin (the two of them) for the infinite discussions at lunch, for being great scientists and amazing people. I spent one of the best moment of my life with you guys.

The great family: Angi, Sofi, J, Simo, Lore. Friends who are always there for you even if we are scattered all over he world (and God bless WhatsApp). You are my strength. Thank you Poggio for the XPS accelerated course and all the moral support, the beers and the fun. Thank you Marco, everything started because of you.

My family for your love and support. For listening and encouraging me, even when you don't understand what i'm talking about.

Finally, Fred for always being on my side supporting me in life, even when i'm really *chiante*. For love and patience.

Merci beaucoup.

Introduction

Nanoparticles-based controlled drug-delivery systems are one of the most promising tool for human health care. In the last decades, many platforms based on nanoparticles have been developed for diagnosis and therapy of major diseases, especially cancer. Porous materials able to load and release drugs in a controlled manner have been widely investigated as biocompatible vectors. Ideally, a targeted drug delivery vector should be able to target specific areas in the body and release its cargo at controlled rate when it is needed, avoiding secondary effects due to overdose and maximizing the therapeutic efficiency. Porous particles with gate-keeping mechanisms responding to stimuli such as pH, redox potential, light-triggering, temperature, etc. have been developed but many porous carriers still rely on diffusion to release the encapsulated drugs.

Among these platforms, silica NPs provide many advantages, such as highly controllable size and shape, high drug payload, low toxicity, and excellent biocompatibility. They dissolve in physiological conditions and their degradation products, namely orthosilicic acid, can be easily excreted through kidneys. Mesoporous silica NPs have a porous structure with pores diameters from 2 to 50 nm and can bond active biomolecules and drugs by physical adsorption or covalent binding.

However, a detailed understanding of the behavior of mesoporous silica nanoparticles in biological environments is needed to push the technology towards a clinical standard.

In particular, dissolution of mesoporous silica NPs, influences their biodurability, their potential toxicity and their drug release kinetics and should be investigated deeply to predict nanoparticles fate *in vivo*. Attention should be paid to carefully identify the parameters that affect the dissolution of particles such as surface area, size, and surrounding media. Indeed, these studies should be designed to mimic the relevant *in vivo* environment.

In this thesis we propose a study of mesoporous silica degradation in biological relevant conditions realized through *in situ* ellipsometry on model thin films, in complex media containing proteins and in dynamic flow.

Ellipsometry provides the thickness and the optical constants of the analyzed thin film and

can follow their evolution during dissolution process. The structure of mesoporous silica nanocarriers is reproduced on thin films which, because of their plane interface can be studied by ellipsometry. Nevertheless, ellipsometry can't be performed in opaque liquids so we use two different setups for transparent buffer-solutions and for real biological fluids such as serum and blood. In the latter case we employ a setup for total internal reflection ellipsometry (TIRE), able to work in opaque fluids.

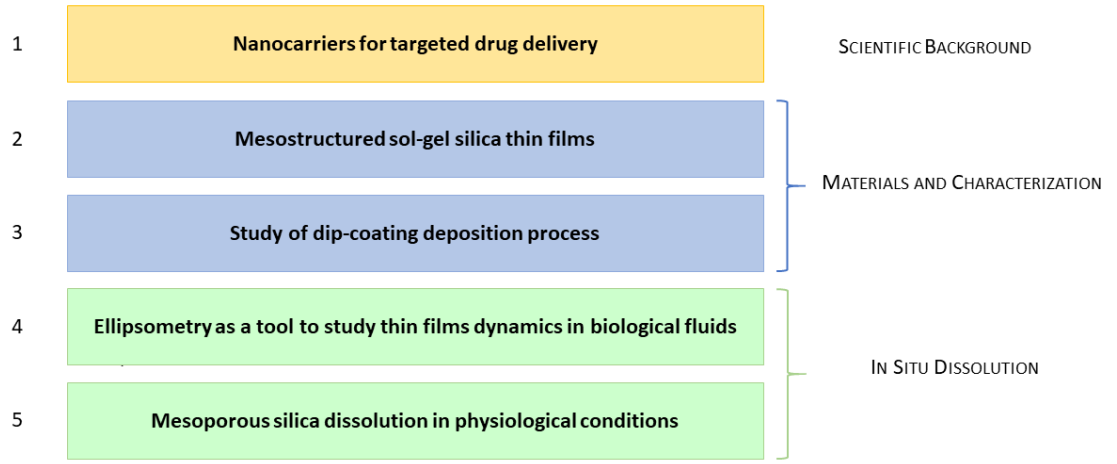

The thesis is organized in five chapters as illustrated in the figure above.

Chapter 1 aims to present the state-of-the-art regarding drug delivery systems based on nanoparticles, discussing biocompatibility and toxicity, targeting mechanisms and *in vivo* degradation. Particular attention is brought on mesoporous silica nanoparticles and their biomedical applications, which are the focus of this work. **Chapter 2** reviews sol-gel chemistry and nanostructuration methods, along with all the techniques involved in the preparation and characterization of mesoporous silica thin films and extensively employed in this thesis. A detailed study on dip-coating deposition technique was carried out since the good control of the layer thickness is fundamental for degradation experiments reproducibility, and it is reported in **Chapter 3**.

Chapter 4 describes the ellipsometry technique and the total internal reflection mode (TIRE) employed for analysis in biological fluids. We discuss the design and optimization of TIRE setup, which we propose to couple with a microfluidic channel to perform dissolution experiments in flow conditions. Results are presented and discussed in **Chapter 5** in which dissolution rate of silica at 37 °C are reported for several physiological fluids. First, a general model for mesoporous silica dissolution is proposed and parameters affecting

dissolution such as surface area and porous structure are discussed. Finally, the influence of protein adsorption and liquid flow rate on mesoporous silica dissolution kinetics are highlighted.

Chapter I

Nanocarriers for targeted drug delivery

I.1 Nanotechnology for health care

Probably one of the biggest innovations brought by nanotechnology is its application to medical science: Nanomedicine, which has radically changed the way we approach medicine. In the lecture "There's plenty of room at the bottom" given by Richard Feynman in 1959 at Caltech [1], which is usually referred to as the origin of nanotechnology, there were the first revolutionary ideas of nanomedicine. In his speech Feynman considered the possibility that patients may in the future *swallow the surgeon*, and talked about designing and manipulating very small robots to be introduced into the human body for repairing altered cellular processes or for healing injuries. Feynman pointed out that the biological systems and the cellular mechanisms work on very tiny scale and he said: *"Consider the possibility that we too can make things very small, which does what we want, when we want - and that we can manufacture an object that maneuvers at that level"*. At that time all of this was just imagination, but with the technical advances of the 1970s and the 1980s nanotechnology moved the first steps. A very important technical progress was the invention of the scanning tunneling microscope which allowed, for the first time, the visualization of individual atoms. Latterly, significant technical advances as atomic force microscopy, atomic layer deposition and nanocrystal synthesis made nanotechnology evolve quickly and the first nanomaterials appeared, along with their applications.

The understanding of molecular and supramolecular world developed with nanotechnology allowed to unravel the complexity of biointeractions, and the possibility to create devices for imaging and manipulation of biological structures became real. A major-

ity of biological processes occur at the nanoscale: DNA, proteins, antibodies, lipids and self-assembled structures made of these building blocks are nanosized materials. Understanding the relation between the structures and the properties of these nanomaterials is mandatory if we want to be able to successfully fight against diseases and injuries, given that biology uses nanostructures to manage cellular processes.

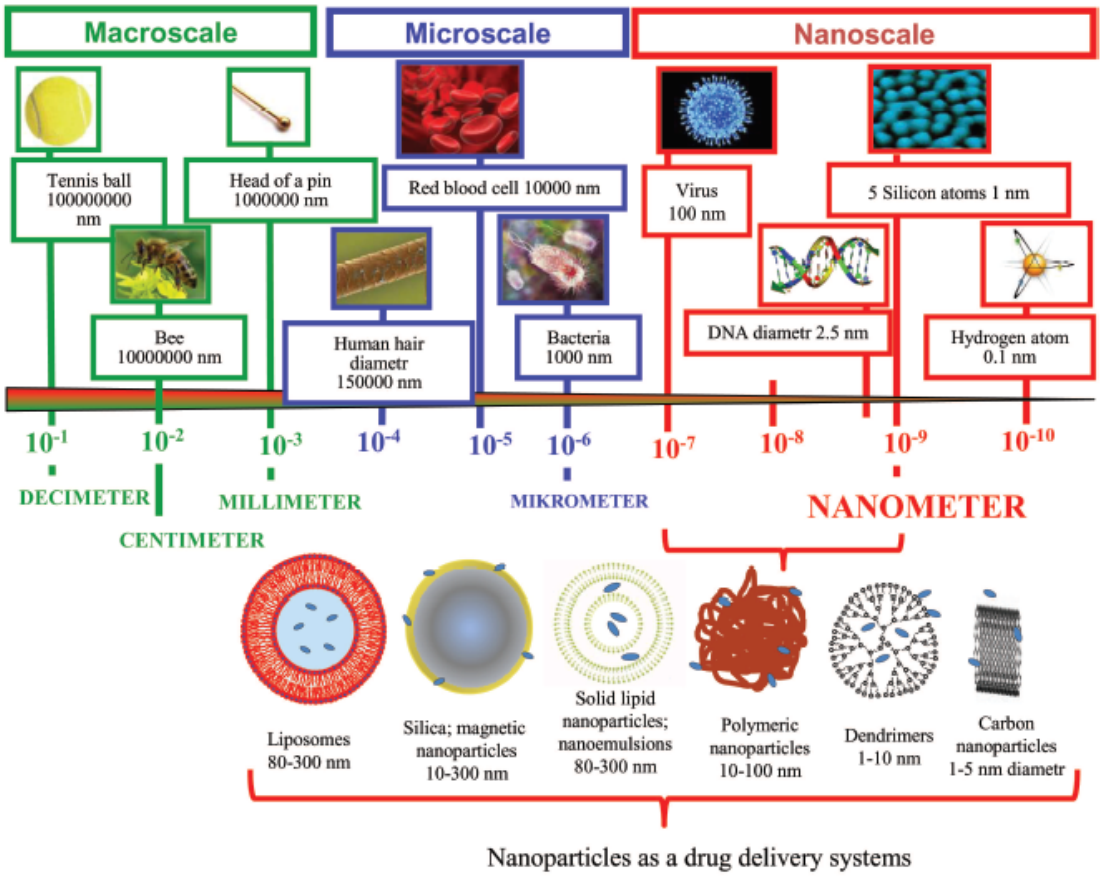

Figure I.1 – Nanoparticle drug delivery systems and the related scales.

Nowadays we produce many artificial nanostructures able to interact with complex, self-assembled biological nanosystems, allowing the manipulation of biological processes.
Nanofibers and nanopatterned substrates are used to produce biomimetic scaffolds [2, 3] where cells spread and proliferate to form bone tissue [4], muscle [5] or epithelial tissue [6].
Solutions of nanoparticles have been used as tissue glues or as hemostatic materials to stop internal bleeding [7–9].
Many diseases, including cancer, are associated with alteration in cellular metabolic path-

ways which produce specific signals, for example circulating biomarkers. Detecting these signals is crucial for rapid and early diagnosis which, until now, has been limited by the lack of biosensors capable of probing the concerned zone. Nanomaterials can interact with biological signals through their chemical, optical or magnetic properties, becoming a powerful tool for *in vivo* diagnostics. Several types of nanoparticles are being used for imaging and labeling, because they can be detected with different techniques exploiting their peculiar properties such as fluorescence, optical absorption, magnetic force or Raman scattering. A commonly used imaging technology rely on magnetic resonance (MRI) and allows to monitor magnetic nanomaterials in living tissues. These nanoparticles are generally made up of a magnetic core, often in iron oxides Fe_3O_4 or γ-Fe_2O_3 or metals, and an hydrophilic surface coating [10–14]. Fluorescent nanoparticles are also extensively used for cells imaging. They can consist in polymeric [15,16] or silica particles [17,18], labeled with fluorophores, or surface-stabilized quantum-dots [19–22]. Moreover, nanoparticles are noninvasive and avoid tissue disruption and consequent complications.
The key feature of nanoparticles for imaging and diagnostics is that their properties depend on their size and size can be easily tuned during synthesis. Furthermore the surface of nanomaterials can be engineered to control immunoreaction, biodistribution and cellular uptake or to make them interact with specific biomarkers, for example conjugating a precise antibody on the surface to target the antigen.

I.2 Nanomedicine and Drug Delivery

Nanoparticles are powerful therapeutic and diagnostic tools, in particular they can be used as drug delivery carriers, improving the effectiveness of healing treatments. In fact, conventional drugs are administered systemically and distributed to the whole body: lacking specific targeting, they are largely degraded and excreted before reaching the diseased tissue. The inability to establish which organs are concerned by the drugs effects is one of the main limitations of medicine. In cancer treatment, for example, the therapeutic agent needs to be delivered to individual tumor cells in sufficient quantity to be effective but without harming healthy cells. This is indeed the biggest challenge of anticancer therapies: delivering drugs to the pathological areas and confine them there, which allows exploiting their therapeutic effect while limiting detrimental side effects due to overdose. Reducing the uncontrolled dispersal of drugs all over the body, targeted delivery keeps drug concentration in the therapeutic window, maximizing its efficacy, with no need to inject high doses of therapeutics which bring adverse reactions.

The key characteristic of nanovectors is their versatility. They are multicomponent systems which can be designed to accumulate preferentially in some parts of the body. They can include biosensors which target some specific cells and integrate stimuli responsive drug release mechanisms to deliver the drug only under specific environmental conditions. If the particles need to be used as diagnostic tools they have to show peculiar magnetic or optical properties, while if they are supposed to be drug carriers they have to be able to host their cargo, either by covalent bonding or, in the case of porous particles, by absorption in the pores.

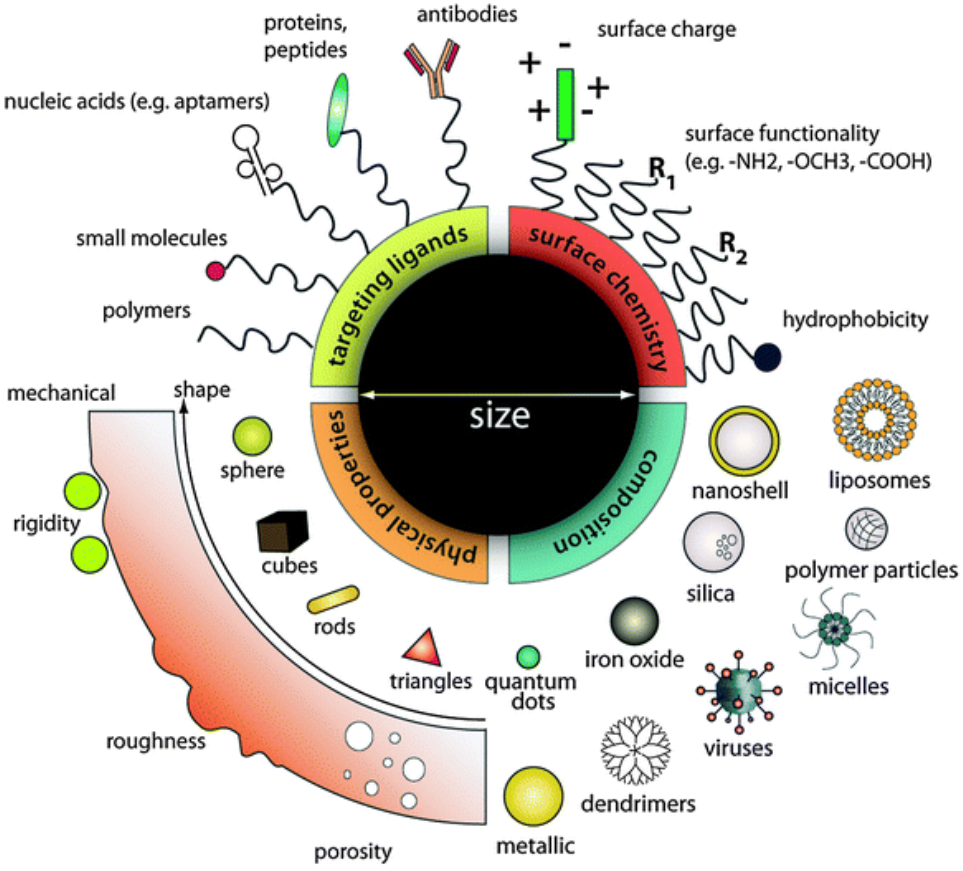

Figure I.2 – The design of nanoparticles for biomedical applications involves numerous aspects: composition, size and shape can be tuned to control physical properties and biodistribution; the surface chemistry can make NPs stealth, to avoid accelerated clearance by the immune system (with PEGylation for example) and can modify the particle surface charge to improve stability and cell uptake; the functionalization with specific ligands allows targeted delivery and drugs can enhance their stability and solve solubility problems through bonding/encapsulation in NPs. Image reported from [23]

Over the past few decades, many nanoparticle platforms have been exploited as drug delivery vehicles, belonging to a wide range of materials such as polymers [24, 25], metals

[26] and ceramics [27].

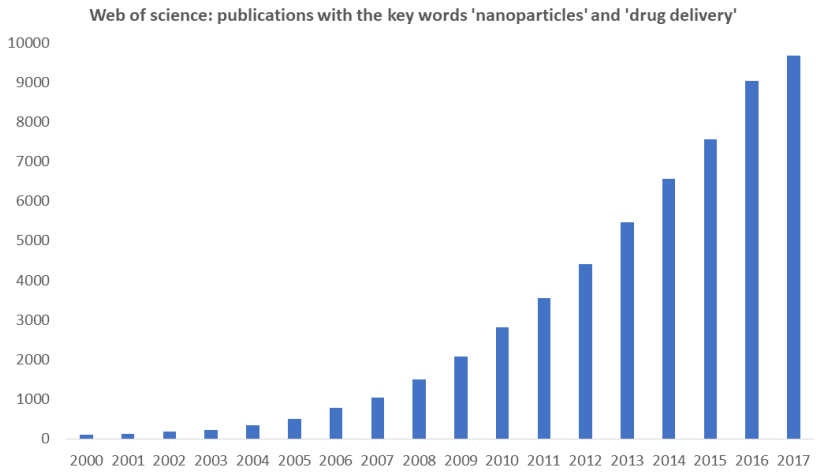

Figure I.3 – Growth of the number of publication with keywords 'drug delivery' and 'nanoparticle'. Data from Web of Science.

The number of publications concerning nanoparticles employed as therapeutic vectors is spreading (figure I.3), and, to date, 50 nanopharmaceuticals have been approved by US FDA (Food and Drug Administration) and are available for use in clinical practice, while even more are being tested in clinical trials [28]. Most of them are previously existing drugs encapsulated in nanoparticles and, in the majority of cases, they rely on passive targeting through EPR effect, which involves nonspecific accumulation in diseased tissue (see section I.4.1). Nanoparticles used in approved nanodrug formulations or under evaluation in clinical trials currently include liposomes, polymers, micelles, nanocrystals, metals/metal oxides and other inorganic materials, proteins and dendrimers (figure I.4).

A huge part of nanopharmaceutical approved or in clinical trials is made by anticancer and antimicrobial nanodrugs. However, there are also formulations being developed for autoimmune conditions, psychiatric disorders, anesthesia, arthritis, metabolic disorders, ophthalmic conditions, and others (see table I.1).

Most of the formulations approved haven't demonstrated improved efficacy or targeting compared to the free drug, but they have shown reduced toxicity. In the case of cancer therapy, which is still the main field of application for nanodrugs, the chemotherapeutic agents are often insoluble in water and they require toxic solubilizing excipients, as in the case of paclitaxel. The dose of such chemotherapeutics has to be limited to avoid systemic toxicity, necessarily reducing their efficacy. Encapsulation in nanoparticles offers

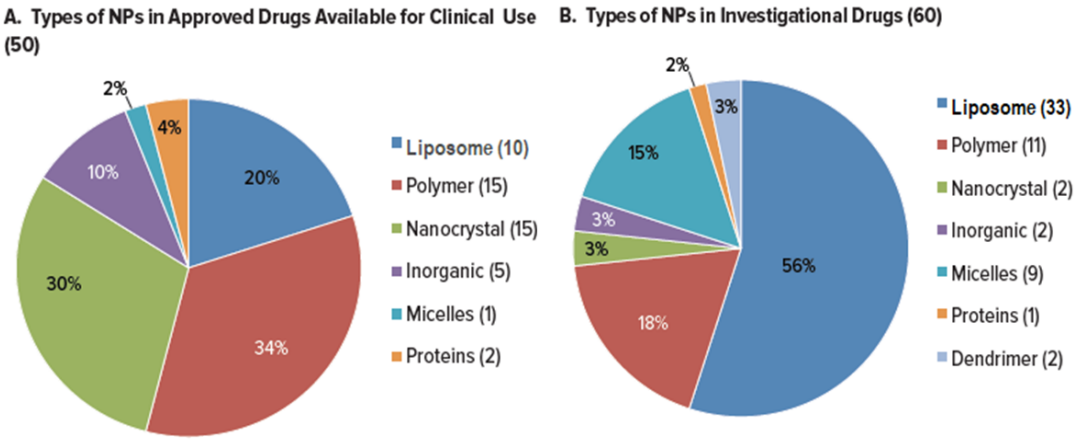

Figure I.4 – Types of nanoparticles in A. approved nanodrugs and B. nanoformulations currently in clinical trials. Adapted from [29]

a viable solution to administrate higher doses of hydrophobic drugs without employing toxic agents, thus many chemotherapies have been approved as nanoformulation and more are in clinical development. Abraxane (nab-paclitaxel, Celgene) is a formulation of paclitaxel conjugated to albumin nanoparticles and was approved by the FDA in 2005 for metastatic breast cancer. It has now been indicated as treatment also for other cancers. It is more tolerable than conventional paclitaxel, because of the absence of toxic solvents and can be administered to patients at a considerably higher dose, increasing its efficacy.

The first approved nanodrug was Doxil (doxorubicin hydrochloride, Janssen) in 1995, to treat Kaposi's sarcoma. It showed reduced cardiotoxicity compared to the free drug and nowadays it is employed also to treat breast and ovarian cancer [29].

Anyway, the number of nanodrugs which survives clinical development is still small, because often they are unable to demonstrate a significant improvement in efficacy and because improved toxicity could be achieved employing other drugs with simpler production processes. For example, liposomal formulations of cisplatin (L-NDDP, SPI-77, lipoplatin, and Li-PlaCis) proved to be less toxic than free cisplatin but brought no benefit in terms of efficacy. Since other less nephrotoxic platinum alternatives (such as carboplatin) already exist, there was no further development of liposomal cisplatin [30].

In fact, research on nanotherapeuticals is flourishing but the transition from academia to production lines is still very poor. There are multiple obstacles and challenges in bringing drug delivery nanocarriers to the market, which can be resumed in three main groups: safety and toxicity issues, production and cost issues and regulation problems.

Safety and toxicity issues

To avoid unpredictable side effects, characterization of nanomaterials in biological environments is mandatory. There is a huge amount of data concerning polymers, liposomes and micelles (which is the reason of their dominance in nanodrugs available for use in clinical practice), but the problem with nanoparticles is that for every new formulation (change of size, charge, shape, surface coating) new tests are necessary. Moreover, NPs can interact with many different organs and living tissues, triggering potentially harmful responses. Thus, the analysis of the interactions between nanoparticles and biological systems is a very long process, which needs many tests for every modification of the material employed. This procedure can't be avoided and results in a huge amount of time and money to bring the product on the market.

Regulation issues

One of the greater problems is the lack of standard protocols to characterize nanodrugs and their toxicity, which causes a spreading of informations difficult to compare. Standards for characterization have yet not been defined but major efforts have been made. The US Nanotechnology Characterization Laboratory (NCL), in collaboration with FDA has published guidelines on nanomaterials characterization that include some standards to evaluate their toxicity [31].
Nanotherapeutic products are currently regulated within a conventional regulatory framework but they need additional expert evaluations about their safety and efficacy, because of their structural complexity.
From the regulatory perspective, the main challenges concern the applicability of current methods and tools to assess characterization and biodistribution of emerging nanotherapeutics, particularly related to their and impact on the living systems. A huge work needs to be done to obtain classifications of converging technologies and to define critical product characteristics predictive of product performance in vivo (e.g. size , shape, surface chemistry and porosity). Therefore, both the EMA (European Medicines Agency) and the FDA constantly update their guidelines to evaluate nanomaterials, in the attempt to shape a safe and efficient regulatory framework for nanotherapeutics.

Production and cost issues

One of the factors that limits the commercialization of nanodrugs is that the production costs of nanoparticles for biomedical use are very high. In fact, their synthesis is often

challenging and made of multiple steps to fulfill all the requirements needed. They have to be stable enough to be processed further and to be stocked in large quantities and their synthesis must avoid toxic reagents which traces can be harmful in their final application. They have to be biodegradable and biocompatible, and they need to be masked from the immune system through a surface coating (usually made of hydrophilic polymers, or lipids). Then, if they are used for diagnostics they need special optical, magnetic or thermic properties, which often depends on size. Thus, the NPs size distribution during the production process must be very narrow. If they serve as drug carriers they need to charge an high quantity of load and possibly a mechanism to release it in a controlled way or in special conditions.

Moreover, NPs production process needs industrial infrastructures which include a nanocharacterization laboratory (for physical, chemical, and biological characterization of nanomaterials intended for medical use), a pilot line to scale up laboratory preparation of nanomaterials, according to industrial and regulatory standards, and a coordination with clinical organizations to perform pre-clinical tests. Compared with conventional formulations, the control of nanomaterials often presents greater scientific and technical challenges, to achieve reproducibility from batch to batch with respect to particle size distribution, charge, and porosity and to have the product stable enough to be stocked and to remove undesired nanostructures. This implies very high fabrication costs which needs to be justified by an important benefit over conventional formulations to have the product commercialized.

In fact, the nanodrugs currently available are all very simple formulations, often made of polymers, micelles or liposomes, which avoid further steps of surface coating to mask them from the immune system, and they rely on passive targeting through EPR effect, not bringing any ligand to target specific cells. This avoid delicate functionalization steps and expensive reagent such as anti-bodies. More the architecture of the nanoparticle is complex and more is production is expensive and complicated. This means that to be produced and sold it has to be very efficient in his task. To date, NPs based on active targeting (specific binding of a ligand on the NP surface to a receptor on the cells surface) haven't shown an important gain in therapeutic effects compared to conventional drugs, but the latest trends in approval and clinical trials of nanodrugs saw an increasing percentage of active targeted nanoparticles [29]. One example is is SGT-53 (SynerGene Therapeutics), which contains an antitransferrin antibody fragment that binds with a transferring glycoprotein receptor on cancer cells and it is being studied for the treatment of solid tumors and metastatic pancreatic cancer [32].

I.2.1 Multifunctional NPs

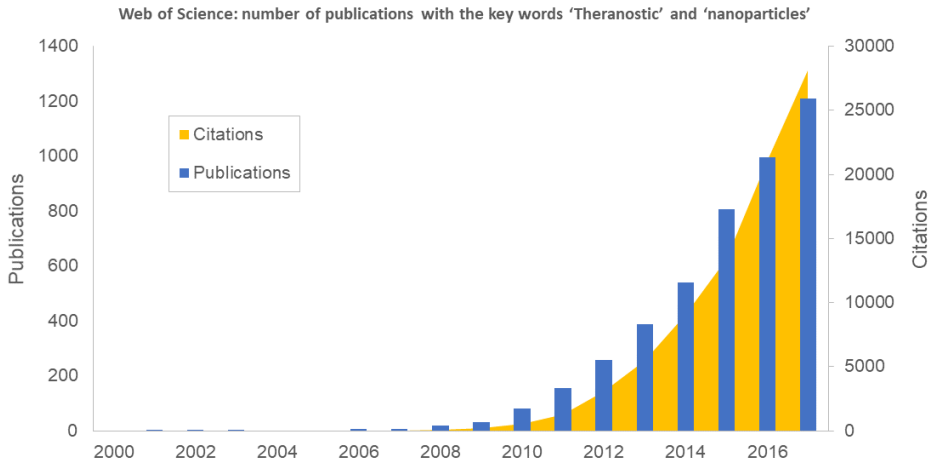

Figure I.5 – The growth in the number of publications (vertical axis scale on the right) and number of citations per year (vertical axis scale on the left), concerning theranostic platforms which combine diagnostic and therapeutic properties in a single nanoparticle-based system. Data from Web of Science.

In the last years another important research trend is the development of multi-functional nanoparticles which can integrate multiple functions such as diagnosis, imaging, targeted delivery and controlled release in one individual platform. Such efforts to combine diagnostic and therapeutic capabilities into a single agent are commonly defined with the term "theranostics" and represent a very active research field which counts currently around 1000 publications per year (figure I.5).

An overview on multi-functional nanoparticles is given in figure I.6 and extensively discussed in a review by Bao et al. [33] recently. Such theranostic platforms include very often inorganic functional components such as metals, metal oxides or semiconductors. They have peculiar optical, magnetic and plasmonic properties which can be easily tuned controlling their size and shape.

Gold nanoparticles, for example, are good contrast agent for optical imaging but they can also be used for photo-thermal therapy, so one can visualize exactly where nanoparticles are accumulated and treat the area thermally [34,35]. Gold nanoparticles owe they peculiar optical properties to localized surface plasmon resonance, which absorbs light at specific frequency. The light absorbed is mainly emitted by gold nanoparticles as scattered light, which makes them suitable tools for optical imaging, while the remaining energy is converted into heat. For *in vivo* application, the absorption frequency should be within

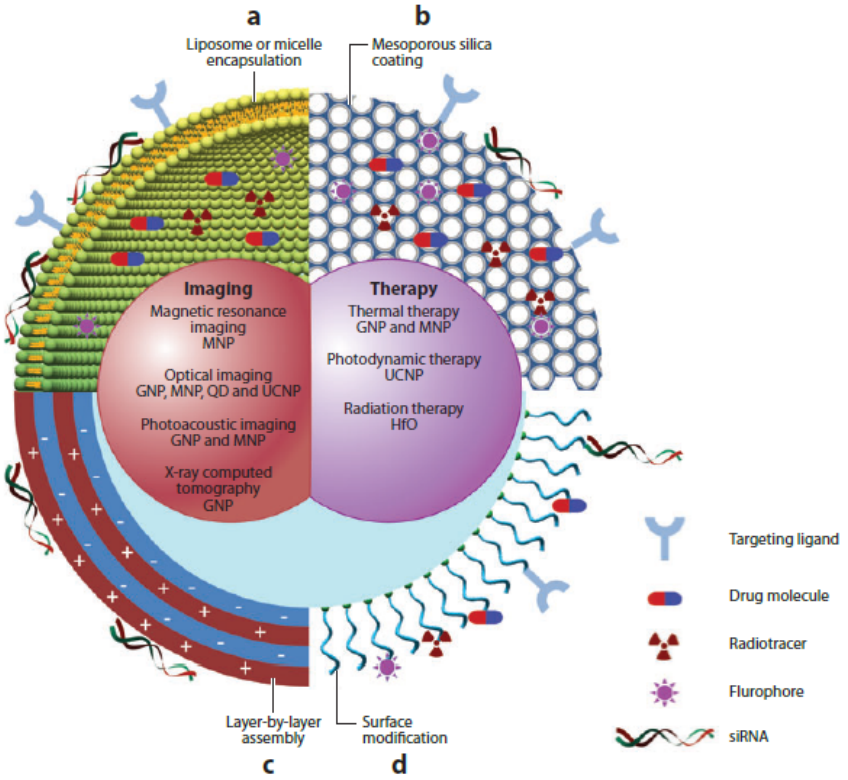

Figure I.6 – Schematic representation of multifunctional nanoparticles for drug delivery and diagnostics. They can be designed as a combination of an inorganic nanocrystal and a coating layer which can include (a) mycelles or liposomes, (b) mesoporous silica, (c) layer-by-layer assembly and (d) surface grafted moieties. Reproduced from [33]

the optical transparent window of human tissues (between 650 and 1300 nm) so light can penetrate deep into the tissue without being rapidly attenuated. Luckily the absorption spectra of gold nanoparticles is tunable with their size and shape [36] and can be shifted from the visible to the near infrared region, allowing the use of gold nanostructures for *in vivo* imaging and photo-termal therapy [37]. These nanoparticles can also be loaded with drugs and provide the combined effects of chemotherapy and thermal therapy in one singular platform. To date, the FDA has not yet approved any gold-based nanodrugs, but they are under evaluation as delivery vehicles for the extremely toxic antitumor agent TNFα. In the clinical trials they demonstrated reduced toxicity but they were rapidly cleared by the reticuloendothelial system, to date a new nanoformulation of gold NPs conjugated with PEG is being developed to deliver TNFα (Aurimune, from CytImmune) and has been found to decrease clearance rate and improve accumulation in tumors through

EPR effect.

Not every type of nanoparticle is naturally multi-functional, as gold nanoparticles are, but often they are composites in which each part brings a different functionality. For example, it is common to find core-shell structures in which an inorganic core is encapsulated into a mesoporous silica shell or into a lipid bilayer or a biopolymer coating. In this case the inorganic core is used for imaging, due to his physical properties, while the coating layer allows including drug molecules, fluorescent tracers and targeting ligands. Moreover the nanoparticles surface can be engineered to provide biocompatibility and stability.

Iron oxide NPs have been studied in numerous clinical trials as contrast enhancement reagents for magnetic resonance imaging (MRI). However, FDA-approved iron oxide nanoparticles are employed as iron replacement therapies for the treatment of anemia associated with chronic kidney disease (CKD). Some of them are reported in table I.1. These formulations are made by an iron oxide core, coated with hydrophilic polymers (e.g., dextran, sucrose), and provide a slow dissolution of the iron, allowing administration of large doses without exceeding free iron levels in the blood.

Superparamagnetic iron oxide nanoparticles (SPIONs), particularly iron oxide and magnetite have been used as non-targeted contrast agents for MRI. Some SPION drug formulations have received FDA approval, such as Feraheme (ferumoxytol, AMAG Pharmaceuticals), even if it is currently indicated mainly as an iron substitute therapy for anemia condition associated with CKD. However, this nanoformulation is also being studied as an imaging agent in numerous clinical trials [32]. SPIONs can be also used for hyperthermia treatments, thanks to the energy that they release when excited in a magnetic field and several SPIONS are currently being investigated as hyperthermia agents against tumors, showing promising clinical results. For example, Nanotherm (MagForce AG) is a formulation of SPIONs coated with aminosilanes for local hyperthermia treatment of glioblastoma tumors. It is injected directly into the tumor, and heated through the application of an alternating magnetic field. The tumor microenvironment reaches in this way a temperature of 40-45 ° C and cell death is provoked. Nanotherm is currently awaiting FDA approval.

Among silica-based systems, Cornell Dots (C Dots) are fluorescent core-shell silica nanoparticles that are being developed at Cornell University as a diagnostic and therapeutic tool for cancer treatment. They have a silica core labeled with a near-infrared organic dye surrounded by a pure silica shell, which is coated with polyethylene glycol (PEG). Compared to free dye equivalents in solution, the C Dots are 20 to 30 times brighter and they showed improved photo-stability. They were originally designed as diagnostic tools

to map tumors, however they showed ability to induce cancer cell death *in vitro* when cancer cells are in a state of nutrient deprivation, while high concentrations were well-tolerated under normal conditions. When administrated to mice, tumors also reduced. They are undergoing human clinical trial since 2010. [38] The same research group at Cornell University is developing mesoporous C dots to host drugs, and C-dots conjugated with antibodies to target specific cancer cells [39, 40].

Organic nanoparticles have been widely explored as well, constituted by polymers, proteins, dendrimers or lipids, especially liposomic systems.

Liposomes are lipid vesicles with a large aqueous center in which they can host hydrophilic compounds, while hydrophobic molecules can be embedded in the lipid bilayer; they carry drugs across biological barriers overcoming cellular uptake and improving biodistribution, being suitable vectors for many kinds of drugs [41, 42]. FDA approved many formulations where drugs are encapsulated in liposomes and they showed improved stability and bioavailability (see table I.1).

Polymeric nanoparticles are also widely investigated as nanocarriers because of their good stability *in vitro* and *in vivo* and the possibility to easily graft multiples molecules and ligands on their surface, making them very versatile. Moreover, they're usually made up of biodegradable polymers such as poly(lactic acid) (PLA), poly(glycolic acid), poly(ε-caprolactone) and their copolymers, avoiding problems of toxicity; poly(ethylene glycol) (PEG), poly(ethylene oxide) PEO, and poly(propylene oxide) (PPO) are also used to synthesize nanoparticles which have great biocompatibility [43–45]. Polycyanoacrylate nanoparticles have proved themselves effective for brain delivery [46, 47].

Table I.1 – List of nanodrugs approved by US FDA and available for clinical practice [29]

Trade name (Manufacturer)	**Generic name**	**Indications**	Benefit of NP*
Liposome NPs			
Curosurf (Chiesi USA)	Poractant alfa	Respiratory distress syndrome	Increased delivery with smaller volume, decreased toxicity
Doxil (Janssen)	Doxorubicin HCl liposome injection	Karposi's sarcoma, ovarian cancer, multiple myeloma	Increased delivery to disease site, decreased systemic toxicity
Abelcet (Sigma-Tau)	Liposomal amphotericin B lipid complex	Fungal infections	Decreased toxicity
Depodur (Pacira Pharmaceuticals)	Liposomal morphine sulphate	Postoperative analgesia	Extended release
Marquibo (Spectral Pharmaceuticals)	Liposomal vincristine	ALL	Increased delivery to tumor site, decreased systemic toxicity
Onivyde (Ipsen Biopharmaceuticals)	Liposomal irinotecan	Pancreatic cancer	Increased delivery to tumor site, decreased systemic toxicity
Visudyne(Bausch and Lomb)	Liposomial verteporfin	Ocular histoplasmosis, myopia	Increased delivery to site of diseased vessels, photosensitive release
Vyxeos(Jazz Pharmaceuticals)	Liposomal daunorubicin and cytarabine	AML	Increased efficacy through synergistic delivery of co-encapsulated agents

Trade name (Manufacturer)	**Generic name**	**Indications**	Benefit of NP*
Polymer NPs			
Adagen (Leadiant Biosciences)	Pegademase bovine	SCID	Longer circulation time, decreased immunogenicity
Adynovate (Shire)	Antiemophilic factor, pegylated	Hemophilia	Greater protein stability, longer half-life
Cimzia (UCB)	Certolizumab pegol	Crohn's disease, rheumatoid arthritis, psoriatic arthritis	Longer circulation time, greater stability *in vivo*
Copaxone (Teva)	Glatimer acetate	Multiple sclerosis	Controlled clearance
Eligard (Tolmar)	Leuprolide acetate and polymer	Prostate cancer	Longer circulation time, controlled payload delivery
Mircera (Vifor)	Methoxy polyethylene glycol-epoetin beta	Anemia	Greater aptamer stability
Pegasys (Genentech)	Pegylated IFN alpha-2a	Hepatitis B, Hepatitis C	Greater protein stability
Plegridy (Biogen)	Pegylated IFN beta 1-a	Multiple sclerosis	Greater protein stability
Renvela; Renagel (Genzyme)	Sevelamer carbonate; Sevelamer HCl	CKD	Longer circulation time and therapeutic delivery
Zilretta (Flexion Therapeutics)	Triamcinolone acetonide	Osteoarthritis knee pain	extended release

Trade name (Manufacturer)	**Generic name**	**Indications**	Benefit of NP*
Micelle NPs			
Estrasorb (Novavax)	Micellar estradiol	Vasomotor symptoms in menopause	Controlled delivery
Nanocrystal NPs			
Avinza (Pfizer)	Morphine sulfate	Psychostimulant	Greater drug loading and bioavailability
EquivaBone (Zimmer Biomet)	Hydroxyapatite	Bone substitute	Mimics bone structure
Emend (Merck)	Aprepitant	Antiemetic	Greater absorption and bioavailability
Invega Sustenna (Janssen)	Paliperidone palmitate	Schizophrenia, schizoaffective disorder	Slow release of low-solubility drug
NanOss (RTI Surgical)	Hydroxyapatite	Bone substitute	Mimics bone structure
Rapamune (Wyeth Pharmaceuticals)	Sirolimus	Immunosuppressant	Greater bioavailability
Ritalin NA (Novartis)	Methylphenidate HCl	Psychostimulant	Greater drug loading and bioavailability
Tricor (AbbVie)	Fenofibrate	Hyperlipidemia	Greater bioavailability, simpler administration
Zanaflex (Acorda)	Tizanidine HCl	Muscle relaxant	Greater drug loading and availability

Trade name (Manufacturer)	**Generic name**	**Indications**	Benefit of NP*
Inorganic NPs			
Dexferrum (American Regent)	Iron dextran	Iron deficiency in CKD	Increased dose
Feraheme (AMAG Pharmaceuticals)	Ferumoxytol	Iron deficiency in CKD	Prolonged, steady release with less frequent dosing
Ferrlecit (Sanofi-Aventis)	Sodium ferric gluconate complex in sucrose injection	Iron deficiency in CKD	Increased dose
Protein NPs			
Abraxane (Celgene)	Albumin-bound paclitaxel	Breast cancer, pancreatic cancer	Greater solubility, increased delivery to tumor, decreased toxicity
Ontak (Eisai)	Denileukin diftitox	Cutaneous T-cell lymphoma	Targeted T-cell specificity, lysosomal escape

* Compared with conventional formulations

ALL = acute lymphoblastic leukemia; AML = acute myeloid leukemia; CKD = chronic kidney disease;

HCl = hydrochloride; IFN = interferon; SCID = severe combined immunodeficiency disease.

I.3 Biocompatibility and Immunoreaction

For using nanoparticles as nanomedicine tools they need to be stable *in vivo* and to have good biocompatibility. A surface coating of polymers or lipids is usually an effective way to avoid particles aggregation and fast dissolution, providing them stability in biological media [14,48–51]. Hydrophilic polymer such as poly(ethylene glicol) (PEG) can constitute a protective shell for nanoparticles and lower the non-specific adsorption of proteins, hindering the organism immunoreaction and thus insuring longer circulation times.

I.3.1 Accelerated Blood Clearance

In order for a drug delivery device to achieve its goals, it must remain in the bloodstream long enough to reach its therapeutic target, but nanoparticles undergo immune recognition due to their relatively large size: they have the same dimensions as viruses, against which our immune system developed a very effective defense. The phenomenon of accelerated blood clearance (ABC) is responsible of fast elimination of nanoparticles from bloodstream and it is due to a rapid uptake of NPs by macrophages of the reticuloendothelial system (RES). The macrophages of the RES remove nanoparticles from the circulation through phagocytosis, but they can identify them only through specific proteins, called opsonines, bonded or adsorbed onto the particle surface. The opsonines are blood proteins which start to bind very quickly to every particle injected in the bloodstream, in a process called opsonization, which triggers recognition by the phagocytes and following elimination. Once internalized by the macrophage, the nanoparticles are rapidly cleared through the liver within few hours. Thus, masking the nanoparticles to avoid opsonization is critical to enhance nanocarriers blood circulation times.

I.3.2 Making *stealth* nanoparticles

The simplest strategy to overcome this problem is to play on the size of NPs. In fact, particles bigger than 200 nm are removed very efficiently by the RES, and colloids smaller than 6 nm are quickly cleared through the kidneys. So, in order to be retained as long as possible, the size of nanocarriers can range from 6 to 200 nm, with an optimum between 50 and 100 nm, which is also the size range to exploit the EPR effect to reach diseased tissues, as described in section I.4.1. The anisotropy of the nanoparticles is another parameter playing a role in the kinetics of cellular uptake process. It has been observed that a little anisotropy can promote the cellular uptake while a strong anisotropy can facilitate renal clearance [52].

The mentioned properties are important to extend circulation times of NPs but they are not sufficient to retain the carriers in the bloodstream long enough to reach their target cells. Some surface engineering needs to be performed to hide the nanoparticles from the immune system.
One widely used method to slow down opsonization is covering the nanoparticles with molecules which reduce the hydrophobic and electrostatic interactions between opsonines and the particle surface. These coatings are usually made up of long hydrophilic polymer chains, the most employed being PEG (poly ethylene glycol) and PEG-containing copolymers, which demonstrated their effectiveness in minimizing blood protein adsorption and extend the circulation time of nanoparticles [53–55]. The results are promising but still a huge amount of nanoparticles accumulates in the liver and doesn't target the tumor. An interesting strategy to improve the targeting is to cover the nanoparticles with PEG and then add cationic polymers containing amine moieties: the particle remains hydrophile but gains a positive surface charge which favors its interaction with cellular membranes and its subsequent uptake, as described in section I.4.1. However the synthesis needs to be properly tuned to avoid a too high charge density which would destroy the cellular membranes and reduce the circulation times of nanoparticles. This type of coating has been tested *in vivo* by Meng et al., showing a significant improvement in targeting tumors in comparison with a simple PEG coating [56].

I.4 Targeting strategies

The innovation about nanocarriers is the possibility of reaching injured tissue, such as cancer cells, avoiding healthy tissues and the ability of releasing cytotoxic molecules only where they are needed. This allows the formulation of drugs that couldn't be employed in conventional chemotherapy because either highly toxic or insoluble in water, for example. The goal of medical research on drug delivery devices is to make them passively or actively target tumors or diseased tissues. The two approaches are detailed in the following sections.

I.4.1 Passive targeting

In order to improve the preferential accumulation of nanoparticles in tumors, one strategy is to take advantage of the existing differences between pathological and healthy tissues. Tumors show leaky blood vessels, presenting many large fenestrations (from 100 nm to several hundreds of nm) due to fast and defective angiogenesis (the formation of new blood

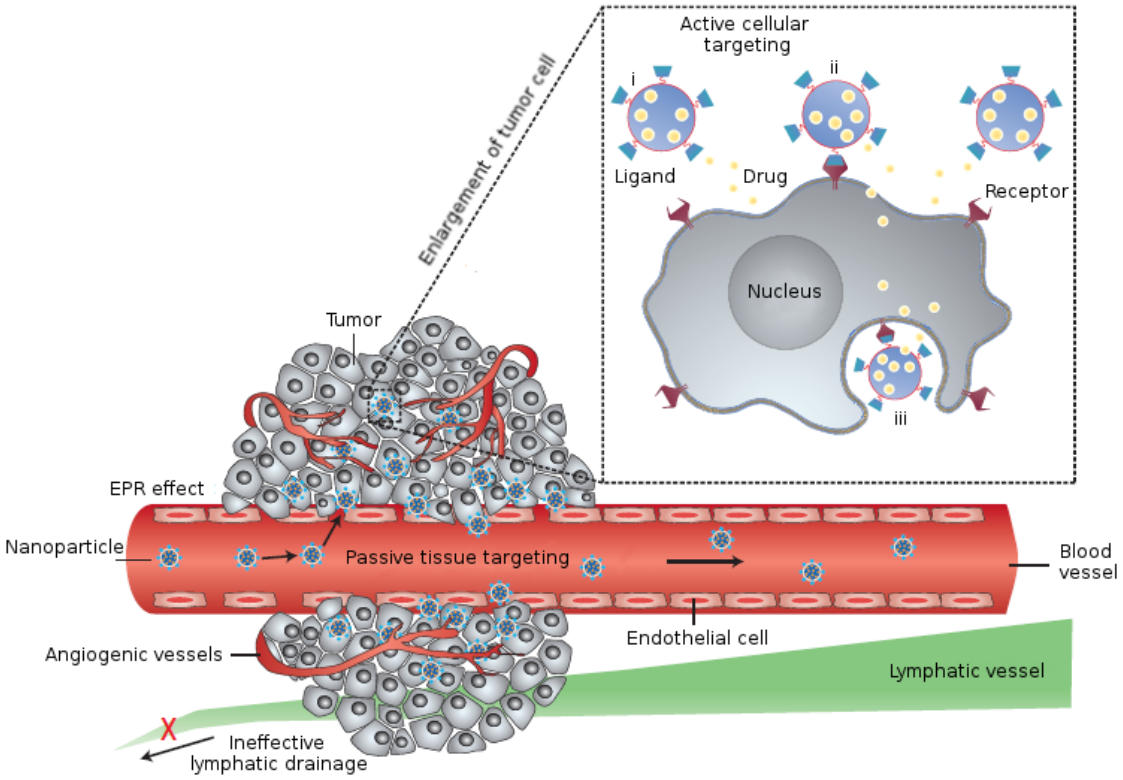

Figure I.7 – Nanoparticles can reach tumors through Enhanced Permeation and Retention effect (EPR), exploiting the leakiness of angiogenic blood vessels, in an approach called passive targeting. Besides, nanocarriers can identify their target cells through ligand-receptor interactions, through an active targeting approach. Image reproduced from [57]

vessels from existing ones) typical of pathological processes. The leakiness of tumor vasculatures is due to the rapid proliferation of endothelial cells and the lack of pericytes; this condition enhances vessels permeability allowing nanoparticles and large macromolecules to pass into tumors. Moreover, nanoparticles are retained in the cancer because of tumors inefficient lymphatic drainage, while in normal tissues macromolecules are cleared by the lymphatic system through the constant drainage of the extracellular fluid. The interstitial fluid is thus renewed very often and the solutes and colloids contained in it are recycled to the circulation. In tumors, this important lymphatic function is defective and the extracellular fluid is retained, along with the nanoparticles and macromolecules within it. Molecules smaller than 6 nm are able to diffuse back to the blood circulation but bigger objects accumulate. This phenomenon is referred to as enhanced permeation and retention effect (EPR) and it is the main responsible of passive accumulation of nanoparticles in tumors.

The EPR effect greatly depends on the physicochemical properties of nanocarriers, such as size, shape, charge and surface chemistry. In the first place, a high blood concentration of nanoparticles is important to ensure extravasation into tumors and prevents the efflux back to the blood stream. Consequently, it is mandatory to extend circulation times of nanoparticles, hiding them from the immune system through *stealth* coatings which decrease their interaction with opsonins and consequently delay their uptake by macrophages (see section I.3.2).

The size of the nanovectors is a crucial parameter to have an efficient accumulation in tumors through EPR effect: the average fenestration in tumor blood vessels being around 100 nm, nanoparticles bigger than this cut-off usually are not able to penetrate in tumors. Among nanoparticles which are smaller than 100 nm, the larger ones diffuse in the tumors more slowly than smaller ones but if their size is below 6 nm they undergo rapid renal clearance, being not suitable for drug delivery application. The rapid elimination through the kidneys of small-size imaging probes have been demonstrated, showing poor accumulation in the main organs and a clearance of more than 50% of the injected dose within 24h. Many contrast agents used for MRI or CT imaging or the near-infrared dyes used for optical imaging have dimensions in this range (< 6 nm) and are rapidly cleared via the kidneys [58, 59]. Thus the optimal size of nanoparticles for tumor targeting through EPR effect is between 6 and 100 nm. Furthermore, not all the tumors have the same permeability and knowing the specific tumor biology is important to design an effective nanocarrier. For example, if the tumor is hyper-permeable, NP of 30, 50, 70 or 100 nm show similar distributions, however only particles smaller than 70 nm can efficiently penetrate and accumulate in poorly permeable tumors [60]. It is important to remind that not only cancer is concerned by EPR effect, in fact there are other pathologies which show similar characteristic to tumor vasculature, such as cardiovascular conditions.

Thus, size is for sure a very important parameter, but the nanoparticles shape may also play a role: spherical objects will not interact with the surrounding environment the same way as rod-shaped or disc-shaped particles. In fact, it has been observed that nanorods tumor distribution kinetics differs from biodistribution of their spherical counterparts: nanorods with an aspect ratio of 10 show similar blood circulation profiles compared to spherical nanoparticles with equivalent hydrodynamic radius, however they extravasate in tumors 4 times faster. Moreover, they diffuse deeper in the cancer [61], even if they could penetrate cells less efficiently, as discussed in section I.5.3. In many biological processes the shape and the deformability of nanosized objects are crucial to ensure the proper working of the whole system, therefore these parameters need to be considered

when designing a drug delivery device, in order to maximize its effectiveness.
Surface charge have a significant impact on all the nanoparticles biointeractions, particularly on protein adsorption and cellular uptake of nanocarriers. Indeed, several studies seem to confirm that positively charged nanoparticles are internalized much faster than neutral or negatively charged ones [56,62] despite their shorter blood circulation times [63]. Such an effect could be related to the negatively charged character of cell membranes, which favors adhesion and up-take of positive nanoparticles.
The discovery of EPR effect paved the way for future cancer therapy, however we still need to understand the importance of many parameters to be able to entirely exploit it. For example, EPR shows a big variability between patients and its effectiveness greatly depends on tumor biology and microenvironment. Besides, EPR effect increases the accumulation of drug nanocarriers in tumors but not necessarily improves their ability to penetrate inside cells. In order to enhance the affinity of drug delivery vehicles for their targeted cells, the surface of NPs is modified with targeting ligands in the so-called active targeting approach, presented in the next section.

I.4.2 Active targeting

Although passive targeting serves as basis for nanocarriers drug delivery, it still suffers lack of control. For this reason, many efforts have been made to design nanocarriers which can selectively bind to target cells. In order to achieve this goal, nanoparticles are functionalized with molecules called ligands, which bind to specific receptors onto the cell surface: through ligand-receptor interactions nanovectors find their target cells and bind to them. Once bound, nanoparticles are quickly internalized by cells and release their cargo. Commonly employed ligands include macromolecules such as antibodies, nucleic acids, proteins, sugars, peptides and small molecules such as vitamins. Their target molecules, often also called receptors, can be proteins, lipids or sugars located on the surface of cells. Actively-targeted NPs have increased affinity for their target cells but they need to be in their proximity to interact with them, so this type of NPs still relies on EPR effect to reach the tumors and need to be designed to have long blood circulation times. Active targeting doesn't change much the biodistribution of nanomaterials but increases the NPs uptake, enhancing therapeutic efficacy.
In order to be effective, this strategy needs to target receptors or antigens which are over-expressed on the surface of target cells in comparison with normal cells. For example, folate receptor (FR) is a membrane receptor over-expressed on the surface of many cancer cells including lung, brain, breast and ovarian cancer cells, while it shows limited expres-

sion on healthy cells, on which it is poorly accessible from the bloodstream. The ligand used to target FR is Folic acid (FA, also called vitamin B9 or folate), a nutrient required for cell proliferation and involved in the biosynthesis of nucleotides. Cancer cells proliferate very fast and they need nutrients to maintain their fast-growing metabolism, thus they overexpress receptors for nutrition as FR and Transferrin receptor (TfR). Folic acid and transferrin (a protein which delivers iron to cells) have been bound to nanocarriers outer surface improving intracellular delivery *in vivo* [64, 65].

Ligands are often linked to the surface of NPs through covalent bonds which can be performed directly on the surface (Gold NPs reaction with thiols) or on functional groups specifically added to improve the reactivity of the material (e.g. OH and NH_2 on inorganic NPs). The density of ligands on the surface of nanoparticles greatly affects their affinity for targets and thus, their uptake rate. Multiple ligands can show cooperative effects: once a ligand binds to its substrate, the subsequent binding of the adjacent ligands are thermodynamically favored. Moreover, the multiple interactions of NPs with the cell force a local concentration of the receptors which triggers the wrapping of the cellular membrane, beginning nanoparticles internalization (see section I.5.3). Nevertheless, high density of ligands not always improves the cellular uptake, in fact the surface decoration with ligands changes the properties of NPs: surface charge and hydrophobicity are modified, and hydrodynamic size is also different. This alteration modifies the biodistribution and circulation times, in some cases improving the macrophage clearing. Therefore, the ligand density has to be properly tuned to optimize the efficacy of actively-targeted nanocarriers and its influence on the nanoparticles *in vivo* interactions has always to be considered.

An interesting approach to this issue is given by Ashley et al. [14] encapsulating a porous silica nanoparticle in a lipid bilayer through liposome fusion, creating a so-called photocell (figure I.8). In this configuration, the outer surface is dynamic and, when one ligand identifies its target and binds to it, the other ligands can migrate on the lipid bilayer to maximize the exposure to cell receptors. With this method, the advantage of multiple cooperative binding is retained employing a small density of ligands, avoiding the complications linked to the presence of many ligands on the surface. The protocells charged with Doxorubicine (a widely employed anti cancer drug) proved themself very effective, they target tumors much better than liposomes-Doxorubicine systems and they are less toxic to healthy cells.
Many antibodies have been studied as targeting ligands but they face some important limitations which narrow their application *in vivo*. First of all, they are large macro-

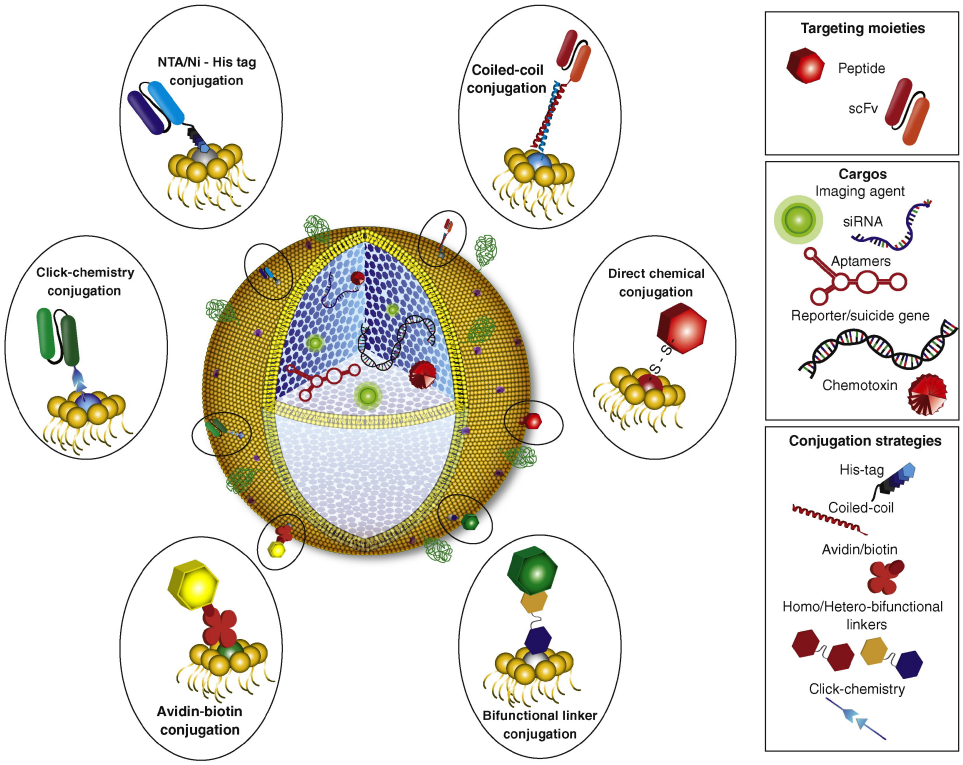

Figure I.8 – Representative design of a functionalized protocell, constitued by a mesoporous silica core (blue in figure) and a lipid bilayer outer shell. Tumor-targeting ligands (peptides or proteins, such as recombinant human scFvs) can be conjugated to functional groups on the surface of the protocell lipid bilayer. The mesoporous core can host a wide variety of cargos such as chemotoxins, genes, siRNA, aptamers or imaging agents. Polyethylene glycol can be conjugated on the surface (green coil) to enhance circulation times. Image reproduced from [66]

molecules of about 150 kDa and their size complicates conjugation, especially on small nanoparticles, besides they increase the hydrodynamic radius of the NPs remarkably. Moreover, their physiological role is to recognize antigens and signaling them to immune cells or macrophages to be cleared from the bloodstream, so they compromise circulation times of NPs. Other proteins, such as transferrin (Tf) [67], have been used as targeting ligands because of their three-dimensional shape, which provides them high affinity with specific substrates but, as antibodies, they also enhance the size of NPs because of their bulky nature. Moreover, their tertiary structure being modified, they can lose the affinity for their target after conjugation. Smaller molecules as peptides have also been studied as targeting ligands. In this case they doesn't impact much on the nanoparticles size and they have simpler three-dimensional interactions. The most used are peptides containing the sequence RGD (arginine-glycine-aspartic acid) which bind to integrine receptors

overexpressed on angiogenic endothelial cells. Another family of ligands is represented by short, single-stranded oligonucleotides (DNA or RNA) but, if their specificity is high, their stability in biological environment is easily threaten by nucleases. On the contrary, small molecules such as folic acid have good stability and small size and they overcome many of the limitations previously described. Nevertheless, small molecules ligands are limited in number, because the screening process to identify new efficient affinity ligands for interested substrates are long and difficult. The most used ligands of small size are folic acid to target folate receptor (FR), triphenylphosphonium (TPP) to target mithocondria and several carbohydrates to target lectins (cellular membrane proteins). To conclude, actively-targeted nanoparticles are under evaluation and some formulation are already in clinical development, they still face many restraints but they could open the path for a more efficient therapy of many diseases, allowing optimization of drug delivery and limitation of side effects.

I.5 *In vivo* degradation and toxicity

Nanomaterials have unique characteristics due to their size and in the last decades they have been employed in a wide range of applications such as electronics, coatings, batteries, optics, composites, cosmetics, paints, medicine etc. The human and environmental exposure to nanomaterials have reached a level which makes mandatory to assess its possible hazard to human health. When employed in medicine, nanomaterials are designed to follow specific routes, mainly they are injected in the blood circulation. Anyway, nanoparticles produced on an industrial scale for applications other than medicine can also reach the human body, via the airways, through ingestion or passing through the skin. Because of their high surface-to-volume ratio, materials at the nano scale are very reactive and interact with living systems and this makes it necessary to understand not only the nanomaterial dynamics but also the surrounding environment, because nanoparticles properties are modified when introduced in a biological system. Nanotoxicology studies became necessary, given the exponential growth of nanotechnology, to prevent a harmful, unregulated use of nanomaterials. Evaluation of the *in vivo* hazard of nanomaterials is still at an early stage but key factors involved in nano-bio interactions have been identified in the last years, along with the main mechanisms of toxicity including protein misfolding, production of reactive oxygen species and cellular membrane damage. A quick overview is given in the following sections about nanoparticles pathway within the body and how the biological environment reacts to NPs presence.

I.5.1 The nano-bio interface

When a nanomaterial comes in contact with biological components, a complex dynamic interface is formed: the interactions with biomolecules modify the forces which usually control nanoparticles in colloidal suspension, for their part, nanomaterials interfere in biomolecules reactions and functions, causing a great impact. The interface between nanomaterials and biological systems is influenced by many parameters including physicochemical characteristics of the nanoparticles and properties of the suspending media, besides membrane and biomolecules interactions. What makes the characterization of this interface so difficult is that many parameters are involved and it's not simple to separate their contributions; considering that the nanoparticle properties such as size, shape , surface charge, porosity, surface roughness, crystallization and surface hydrophobicity are all important characteristic to determine interaction at the bio-interface. Moreover chemical composition and surface functionalization have of course a huge impact. The liquid media is equally important to shape the interface: its ionic strength, pH and the presence of biological macromolecules (e.g. proteins) control the NPs aggregation and dissolution, furthermore ions and macromolecules can adsorb onto the surface of the nanoparticles, changing their hydrodynamic radius and surface charge, promoting or hindering agglomeration and modifying the forces acting on particle-medium interface (electrostatic repulsive forces and attractive Van der Waals forces).
Modeling the nano-bio interface presents one more difficulty: the system is not at steady-state. It evolves continuously, due to the presence of cells which actively interact with the NPs through binding, uptake, production of proteins and ions transfers. The internalization of NPs trough ligand-receptor identification and membrane wrapping further complicates the interactions involved and expose NPs to a different environment inside the cell.
When it comes to the interface between biological systems and nanomaterials all of this must be considered to make this field evolve and to perform a safe use of nanomaterials. A nanoparticle entering a biological medium is not the same object that in synthesis solvent. Its surface is modified and the forces through which it interacts with the medium and the other particles completely depend on this new state.

I.5.2 Protein corona

Physiological fluids, such as blood and interstitial fluid, contain a complex mixture of proteins, so when nanoparticles enter a physiological environment they are rapidly coated by proteins which adsorb on their surface, forming what is known as "protein corona".

The corona modifies the size, surface chemistry and aggregation state of the nanomaterials dramatically, shaping them as they will be "seen" by cells and biological interfaces. It is formed of an inner layer of strongly bound proteins, called hard corona, and an outer layer of weakly adsorbed protein in fast exchange with the environment, known as soft corona. It is this new hybrid object (nanoparticle + protein corona) which determines transport kinetics and interactions of nanomaterials in a biological environment.

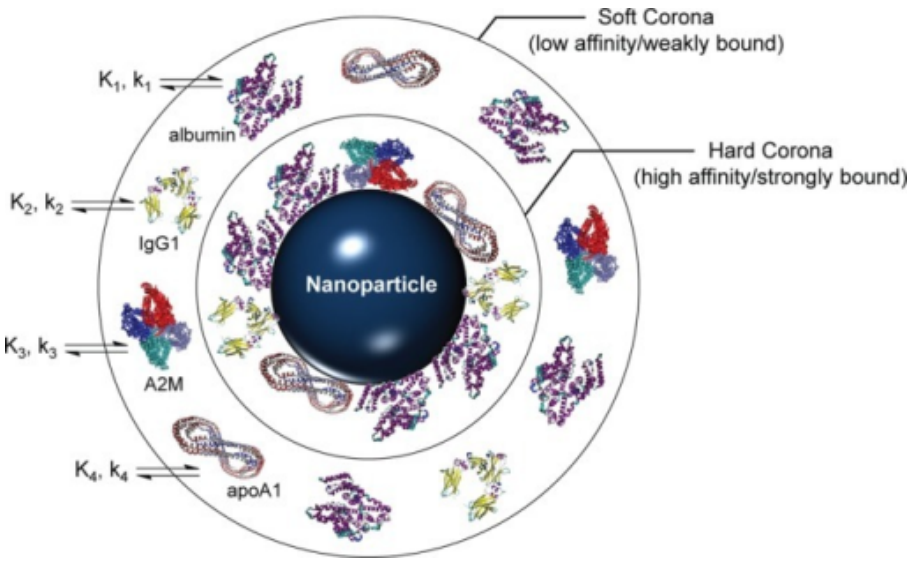

Figure I.9 – Schema of protein corona formation on a nanoparticle surface. The corona formation is a kinetic (k) and thermodynamic (K) process which depends on the surface characteristic of the nanoparticles, such as functionalization and charge. It exist an inner layer of strongly bound proteins and an outer layer of adsorbed proteins which exchange rapidly with the environment. Serum proteins commonly observed in NP coronas are shown: serum albumin, immunoglobulin G1 (IgG1), alpha-2 macroglobulin (A2M), and apolipoprotein A-1 (apoA1). Reproduced from [68].

Physicochemical properties of the nanoparticles, such as surface functionalization, charge and size influence the composition and evolution of the protein corona which, in turn, controls particle's bioactivity, determining their interaction with cells, targeting activity and circulation times [69, 70]. Size in particular defines the curvature of the surface which is responsible for the adsorbed protein amount and composition, smaller particles generally showing higher protein adsorption, due to their bigger curvature, which decrease steric hindrance between adsorbed macromolecules [69,71]. Surface charge is also relevant for the adsorption of biomolecules, but it will never avoid completely the formation of protein corona, as demonstrated by Qiu et al. using nanoparticles differently charged: the positive ones adsorbed a greater amount of protein in comparison to negative ones

but a corona is formed around all the systems investigated [72].

Protein corona is a dynamic interface which exchanges over time with the surrounding environment; in a first time, higher-abundance protein with fast kinetics are adsorbed preferentially on the NP's surface, to be displaced later by lower-abundance proteins with higher affinity. Understanding the evolution of protein corona *in vivo* is critical to obtain effective and non toxic nanocarriers. Corona composition also depends on the biological fluid investigated; in blood, human serum albumine (HSA) and fibrinogen are the main components, no matter particle size or material, because they are the most abundant blood proteins. Anyway, they seem to be in great part on the soft corona, in fact when washed and centrifuged, NPs show a very different corona, where the amount of HSA is drastically reduced and there is an enrichment of apolipoprotein A-I and antithrombine-III, both low abundance proteins, as reported by Kokkinopoulou et al. [73] and an high amount of immunoglobulins. Binding to immunoglobulins leads to particle opsonization and phagocytosis.

Anyway, when particles are internalized by cells they are exposed to a different environment in comparison with bloodstream, and their corona can undergo modification. There are several studies, well discussed in the review of Feliu et al. [74], and the majority of them showed that even passing though different biological environments, the protein corona keeps a stable fingerprint of the first fluid encountered. It has been demonstrated that protein corona can hinder the aggregation of nanoparticles, stabilizing them in biological media [70,75] and it can influence dissolution rates of nanocarriers and drug release kinetics, as reported by Shahabi et al. in the case of mesoporous silica particles [70], where drug release rate has been found lower in presence of protein corona, probably due to a diffusion barrier formed by the protein layer, which act as a sort of protective shell. The presence of protein corona has to be considered when designing a targeted nanocarrier, the layer of biomolecules could indeed shield the ligands bound on the surface, limiting the access to them, moreover proteins could compete with the interaction between ligands and receptors [76,77].

On the other hand, particles have reverse effects on biomolecules which can be harmful, and it's important to understand this type of interactions to design safe nanoparticle drug delivery systems. In fact, binding to nanoparticles can affect the structure and function of proteins, they can unfold and be denaturated by the contact with the particle's surface, losing their function such as enzymatic activity, with catastrophic effects on cellular methabolism, and they can also undergo fibrillation due to the contact with nanomaterials [78,79]. The modification of protein structure is one of the main mechanism

of toxicity associated with nanoparticles *in vivo*.
The so-called "biological identity" of nanoparticles controls all the particle's interactions *in vivo* and strongly depends from many parameters, that's why, to be relevant, characterization of nanomaterials should be done within the investigated biological medium and not in cell culture medium or buffers, which usually have a much lower protein ratio, producing a significantly different protein corona and, consequently, different bio-interactions. In fact, despite many studies, it is still very difficult to predict the behavior of nanoparticles *in vivo* starting from their intrinsic properties, because when NPs enter physiological environments their physicochemical properties critically change and the system's complexity doesn't allow easy representative modeling.

I.5.3 Cell uptake

For particle uptake to occur, the free energy at the interface must be lowered enough to overcome the resisting forces which inhibit the internalization. These forces include the stretching of cellular membrane, the diffusion of receptors until the binding site and the hydrophobic exclusion of polar moieties. Particle adhesion depends on specific (ligand-mediated) and nonspecific binding interactions with the cellular membrane, which can, subsequently, wrap around the particle in a process called receptor-mediated endocytosis and start the particle uptake, as illustrated in figure I.10. In order to start the process of internalization, a critical number of ligand-receptor interaction must be achieved, and receptors need to migrate through the membrane towards the binding site, in a process that has its own diffusion rate constant, with an optimal value to achieve wrapping. Then, the energy released from these cooperative interactions must be enough to overcome the folding and stretching of the membrane around the particle.
The nanoparticle properties such as surface charge, hydrophobicity and size influence the nonspecific interactions with the membrane, and it has always to be considered that these characteristics change once particles enter in a biological environment, as highlighted in section I.5.2. Surface coatings can optimize nonspecific interaction to favor particles uptake, for example adding positive charges to be attracted by the negative charged domains on the cell membrane, anyway this strategy has to be properly tuned because positive charged particles are identified and eliminated faster by the macrophages. The role of surface charge is mainly linked to the corona formation before internalization, in fact it controls the amount of protein which adsorb more on less strongly on the nanoparticle surface. When cells interact with NPs the latest are already covered with proteins and their surface change has been modified, in some cases inversed. So, if positive charges

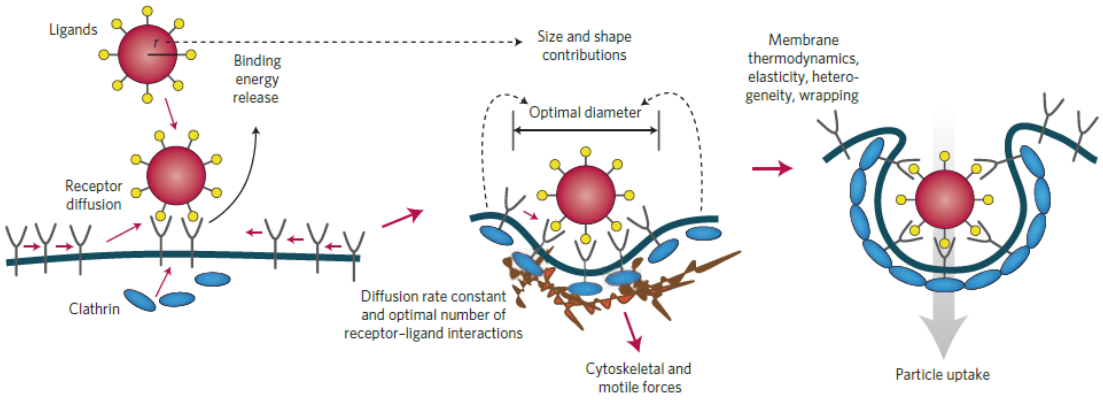

Figure I.10 – For particle uptake to occur, specific and nonspecific interactions must decrease the free energy at the contact site to overcome resistive forces such as ligands diffusion and membrane stretching. Clathrins are protein components that mediate energy-dependent uptake of particles and are activated when the first receptors bind to ligands. Nanoparticles are represented as red spheres with attached ligands (yellow dots). These ligands bind to membrane receptors (Y-shaped), triggering the membrane wrapping and the particle uptake. Reproduced from [80]

remain accessible, they will favor interaction with the cellular membrane which often exposes negative charged functions, otherwise the NPs are probably internalized preferentially because of their higher amount of protein on the surface. In fact, as highlighted by Qiu et al., positively charged particles have a wider protein corona and they show higher uptake ratio even if their surface charge after adsorption is inversed [72].

Size affects the cellular uptake greatly, and it exists an optimal size of nanoparticles to have efficient wrapping, which depends on ligand density (receptor-mediated uptake) and surface characteristics (non-receptor-mediated uptake). Generally speaking, bigger particles require huge receptors movements to reach a sufficient number of interactions, so the receptors diffusion kinetics can be very slow, at the same time, for little NPs it is more difficult to reach a critical number of interactions to trigger membrane wrapping, and sometimes they agglomerate to form bigger objects before being internalized. This have been investigated on Gold NPs, which show an optimum size around 50 nm, while smaller (14 nm) and bigger (74 nm) nanoparticles have slower uptake kinetics, besides their total amount inside cells is reduced in comparison to 50 nm particles [81–84]. Shape can also favor or hinder internalization: for example long rod-shaped particles with high aspect ratio, such as carbon multi-walled nanotubes (MWCNTs) can be difficult to incorporate for cells, causing inflammation; a shape effect have been observed for Gold NPs too, showing that, with the same surface chemistry, high aspect ratio nanoparticles have lower uptake ratio in comparison to more symmetrical shapes [72]. Nevertheless, asymmetric

nanoparticles with moderate aspect ratio showed a more effective internalization and a faster uptake kinetics than spherical particles according to Bartneck et al., suggesting that a moderate anisotropy can help cellular uptake but a too high aspect ratio can interfere with it [52]. These contrasting results demonstrate that every single system studied is pretty peculiar and because of the many factors involved in bio-nano interactions it is difficult to extrapolate a general rule. It is important to identify the tunable properties of nanoparticles which can play a role in their biological interactions and test them when studying a new system.

The other actor of the uptake process is important too: not every cell reacts in the same way to the nanoparticle presence. Macrophages and leucocytes are cells dedicated to the removal of infectious diseases and foreign organisms and they are much more efficient in the uptake process than any other cell of the body. Even at very low nanoparticle concentration, the 95% of macrophages internalize NPs while just the 1% of HeLa cancer cells showed uptake, the particle internalization being 80-100 times more efficient in phagocytes than in cancer cells [52]. Thus, on every evaluation made on a drug delivery system, the tests should be made on the targeted cells because the response between various cellular lines can be very different.

I.5.4 Biodegradation

Once drug delivery nanocarriers have fulfilled their purpose, they need to be eliminated from the body, and this is a delicate step, because during the biotransformation they could produce toxic molecules. Generally, organic components such as liposomes, peptides, poly (lactic acid) (PLA) and its copolymers, are completely biodegradable and they are degraded and excreted through standard metabolic pathways, with almost no toxicity. Other materials, such as quantum dots (CdS, ZnS) or Cu and Ag oxides and complexes, form soluble cations ($Ag^{+}, Zn^{2+}, Cd^{2+}, Ni^{2+}$) which have high cellular toxicity because they interfere with cellular metabolism. For this reason, for the moment, they are studied in many research laboratories but don't find many real applications in the nanomedicine field. There are also some materials, particularly sol-gel SiO_2 and iron oxides (Fe_xO_y) which form soluble non toxic species (silicate oligomers and iron complexes) eliminated through metabolic pathways without damaging for the cells. Some nanomaterials, including TiO_2 and Gold NPs, are not soluble in biological conditions and they can be excreted via exocytosis and renal clearance only if their size is small enough. Otherwise, they accumulate in the tissues and they can generate high toxicity. Carbon materials such as carbon nanotubes are potentially biodegradable through enzyme oxidation but often

they contain high amounts of toxic metals, due to their production process, which cause serious level of toxicity.

Oxidative stress

One of the most important mechanism of toxicity of metal oxides nanoparticles is the production, during their biodegradation, of reactive oxygen species (ROS) leading to a condition called oxidative stress. Reactive oxygen species are free radicals containing oxygen, they are produced in small quantities by cells, some of them act as cellular messengers in redox signaling and they are also employed by the immune system to kill pathogens. Usually, cells are perfectly able to balance the production of ROS with the presence of antioxidant defenses, nevertheless when there are too many ROS (coming from an external agent, such as nanoparticles, or because a cellular process is altered) cells are not able to neutralize them or repair the damages efficiently: this situation is what is known as oxidative stress.

ROS are dangerous because they react with proteins, lipids and DNA, modifying their structure and leading to severe alterations of cellular processes. They can damage the membrane lipids impacting physiological functions and eventually causing cellular death. Moreover, ROS activate redox sensitive transcription factors involved in inflammatory response, so when the antioxidants such as glutathione (GSH), are not able to remove all the ROS species, inflammation takes place before apoptotic pathways and cell necrosis would eventually be triggered by very high levels of oxidative species.

There is an interesting study conducted by Zhang et al. screening the toxicity of several metal oxides nanoparticles: from a few sets of data, taken on independent tests, results that a group of metal oxides is highly toxic for cells while others are safe materials [85]. All these metal oxides are theoretically able to produce ROS during their biodegradation, but only a few interfere with biological redox processes, among these toxic oxides there are TiO_2, Ni_2O_3, Cr_2O_3, Co_3O_4, Mn_2O_3, CoO, CuO and ZnO. Except the last two materials mentioned, all the other oxides have something in common: the energy of their conduction band lies in a range between -4.12 and -4.84 eV, which is exactly the gap of redox potential of the main oxidation-reduction pairs in cellular processes.

Basically, almost all the redox reactions involved in cellular metabolism are associated to a redox potential ranging from -4.12 to -4.84 eV and the metal oxides which have a conduction band in this energy span can exchange electrons and in this way interfere with redox cellular signaling. Other oxides such as SiO_2, Al_2O_3, ZrO_2, Fe_2O_3, Fe_3O_4 and CeO_2 don't show toxicity due to interference in redox processes and they have conduction band

placed to lower or higher energies respect to the redox biological active range. There are two oxides which resulted highly toxic even if the energy of their conduction band is out of the critical range: ZnO and CuO. These materials don't owe their toxicity to the redox reactions disturbance but to their high solubility in biological media: they produce cations which easily pass the membranes and enter cells. A high concentration of cations inside the cell alters completely the proton pump activity and causes inflammation, ROS production and mitochondrial damage, which makes ZnO and CuO highly cytotoxic materials.
There are still many aspects of nanomaterials toxicity largely unclear but nanotoxicology is gaining increasing importance, given the growing employ of nanomaterials in many applications: development of a regulation to limit human exposure to harmful levels of nanomaterials is necessary. The therapeutic use of materials at the nanoscale is slightly different and it requires another regulation, which balances the therapeutic effect with potential risks.

I.6 Mesoporous Silica Nanoparticles

Amongst inorganic nanoparticles for drug delivery, particular attention must be given to mesoporous silica nanoparticles (MSNs). These nanomaterials have a silica matrix with a periodically ordered porous structure showing pores diameters from 2 to 50 nm. The advantage of this type of material is its large surface area (500-1000 m^2/g)which allows huge quantities of drugs to be loaded into the particles. Silica nanoparticles are especially suitable for nanomedicine application because they can be easily prepared in large amounts following several protocols, they are chemically stable in air and can be simply functionalized on the surface using well-known silane chemistry. Furthermore, as long as it is made by sol-gel processing, silica is generally recognized as safe and the products of silica degradation, namely orthosilicic acid, are excreted from the body through the renal system.
In recent years many mesoporous silica materials have been synthesized, with different structures, and many efforts have been made to develop them for biomedical application since the first report of MSNs as drug delivery vehicles in 2001 [86], which have been reviewed in two excellent works by Lin et. al. [51] and Argyo and al. [87].

I.6.1 Synthesis

Mesoporous silica is obtained from a solution containing silica precursors (typically silicon alkoxides) and a structuring surfactant: the molecules of surfactant undergo a self-

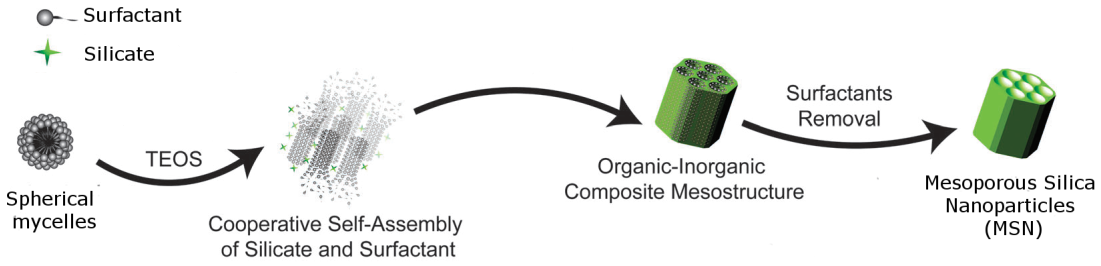

Figure I.11 – Schematic representation of the synthesis process of mesoporous silica. Adapted from [88].

assembling process in which they create micelles and silica precursors place themselves around the formed micelles, interacting with the outer hydrophilic part. The alkoxides hydrolysis/condensation takes place and a shell of silica is formed around the micelles, which have arranged themselves in a liquid crystal phase. Once the surfactant is removed by washing or thermal treatment, a material with pores of accurate size, shape and organization is obtained, as illustrated in figure I.11.

Yanagisawa et al. described in the early 1990s the synthesis of mesoporous materials through intercalation of long-chain alkyltrimethylammonium cations into the layered silicate kanemite [89]. Later, calcination removed the organic species, yielding a porous material where the silicate layers condensed and converted in a silica three-dimensional structure with nanoscale pores. Unfortunately, there were no further characterization data available and the results of Yanagisawa et al. didn't have the regard they deserved.

Few years later, researchers at Mobil Corporation synthesized mesoporous silicate/aluminosilicate using surfactant templates and obtaining very uniform pore sizes [90, 91]. These materials, named MCM (Mobil Composition of Matter), are known as the M41S family which includes materials with three different mesophases: lamellar (MCM-50), cubic (MCM-48) and hexagonal (MCM-41) I.12.

These synthesis were based on the electrostatic interaction between the cationic surfactants and silicates which leads the cooperative self-assembly. Afterwards, Pinnavaia's group described a method based on hydrogen-bonding interactions, to obtain mesoporous silica with neutral amines as a template [92] and shortly after, the first synthesis using non-ionic block copolymers as structuring agents was reported [93]. These materials, templated with non-ionic surfactants, are known as MSU-X (X = 1–4 depending on the nature of the hydrophobic part of the template: alkyl, alkylaryl, block copolymer, or Tween,respectively) and are the subject of an extended review by Prouzet and Boissière [94]. The successful synthesis of 2D-hexagonal SBA-15 silica, templated with neutral

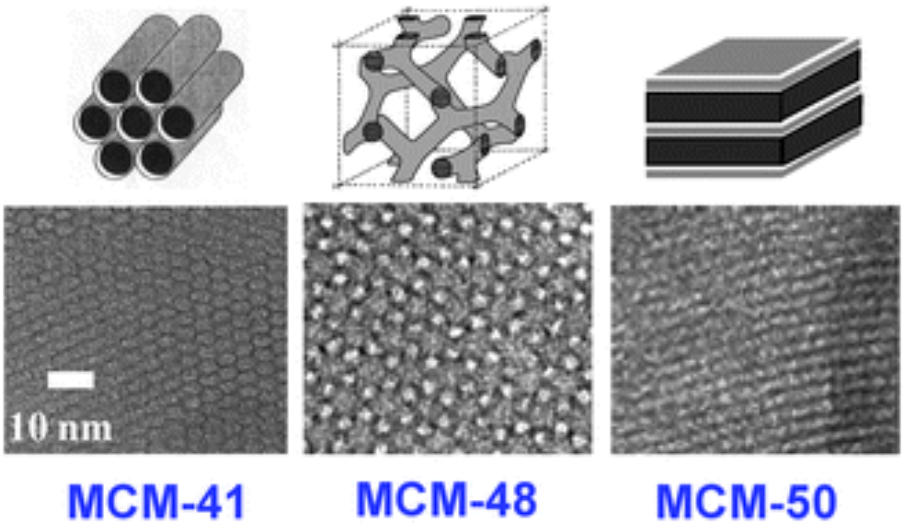

Figure I.12 – The M41S family of mesoporous materials, including MCM-41 where the mesophase have a 2D-hexagonal structure, MCM-48 (cubic) and MCM-50 (lamellar). Reported from [97].

copolymers just followed [95, 96].

Amongst the most common materials employed for therapeutic vectors there are MCM-41 and SBA-15 materials, in which self-assembled micelles of templating surfactant drive the pores ordering in an hexagonal arrangement. Particles from 50 nm to 2 μm of diameter have been obtained, with pores ranging from 2 to 6 nm (MCM-41) or from 4.6 to 30 nm (SBA-15). The surfactant micelles are cylindrical, arranged in an hexagonal structure around which silica condensate. Once the templating surfactant is removed, through calcination or solvent extraction, it leaves well-aligned cylindrical pores parallel to each other (see figure I.12).

MCM-41 and SBA-15 nanoparticles are known for a long time but many progresses have been made to control size and shape of pores and particles, and other synthesis methods, including sol-gel processes, have been studied to obtain mesoporous silica nanoparticles. Sol-gel methods, for example modified-Stöber process, allow a fine control on particle size and pores structure tuning the reaction parameters such as temperature, time, pH and concentration. In the Stöber method, silicates such as tetraethyl orthosilicate (TEOS) and tetramethyl orthosilicate (TMOS), are added to an aqueous solution of alcohol and ammonia, in which the hydrolysis reaction replaces alkoxides groups with hydroxyl groups. Usually, the silanol groups undergo successive condensation reactions producing siloxane bonds (Si-O-Si) and forming polysiloxanes discrete particles. These particles grow and successively aggregate into chains then into networks and eventually evolve into a gel.

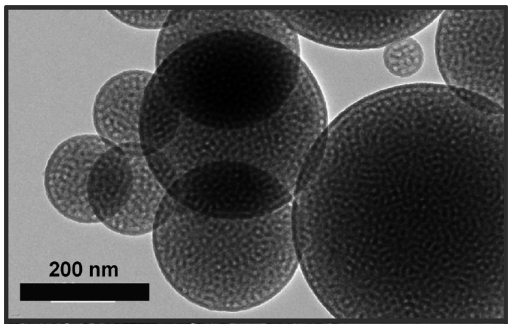

(a)

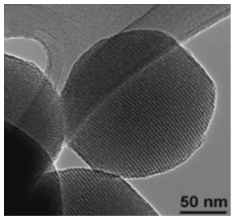

(b)

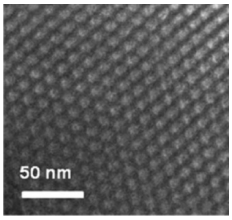

(c)

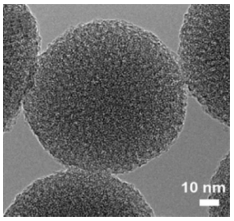

(d)

Figure I.13 – Transmission electron micrographs of (a) silica mesoporous vectors (Adapted from [98]. Copyright 2012 American Chemical Society.)(b) MCM-41-type nanoparticles (Adapted from [99]. Copyright 2011 American Chemical Society.), (c) micrometer-sized SBA-15 material (Adapted from [100] Copyright 2012 Wiley-VCH.), (d) colloidal MSNs with worm-like pore structure (Adapted from [87]. Copyright 2014 American Chemical Society.)

However, under the basic conditions of Stöber process, gel times are long enough for particles to reach a critical size which stabilizes them through electrostatic repulsion effects before gelation can occur. Monodisperse spherical particles of SiO_2 are obtained, their size depending on the reactants concentration, solvent polarity and temperature [101,102].

Adding surfactants as cetyl trimethylammonium bromide (CTAB), or other molecules forming micelles, to the reaction mixture leads to mesoporous particles. The inorganic phase condenses around the micelles which act as a template, once the organic components are removed, a porous structure is obtained. This process is efficient only if there are attractive interactions between the micelles and the inorganic phase, for this reason, in the conditions of Stöber method, only positively charged molecules are valuable templates. Size and structure of the pores depend on the templating material and its concentration. An excess of water and the pH neutralization quench the growth of nanoparticles and the time between the hydrolysis and the neutralization can be modified to tune the particles

size, as reported by Fowler et al. [103]. An overview of the main reported synthesis of NPs by templating techniques using surfactant micelles is given in table I.2.

For mesoporous nanoparticles the template removal is a very critical step: in fact, during high temperature treatment particles can condensate and aggregate irreversibly, resulting in very poor dispersion in aqueous media. Particles aggregation can be an issue even if the surfactant is removed by solvent extraction, because of subsequent cycles of washing and centrifugation, especially on smaller particles. Some methods to avoid aggregation during the surfactant removal step have been elaborated , including dialysis and liquid-phase calcination, in which particles are suspended in high boiling organic solvents and heated at high temperature to degrade the templating agent [112, 114]. Nevertheless, the majority of the studies done on MSNs stability and dispersity are conducted in water, which is not representative in case of biomedical applications. In fact, as discussed in sections I.5.1 and I.5.2, when particles enter in biological environments they find high ionic strength conditions and proteins which adsorb on their surface, modifying to a great extent their aggregation state. Studies on long-term stability of MSNs in physiological conditions are necessary to exploit them as drug delivery carriers, and lately some reports of such type started to appear [115–120].

I.6.2 Toxicity

The hazard for human health represented by silica particles needs to be discussed deeply, given the wide exposure to this material and the growing importance of silica nanoparticles in nanomedicine. In fact, some toxicological studies qualifies silica as safe, but it is well known that a serious disease such as silicosis is provoked by silica nanospheres. Thus, here will be discussed the main factors which can lead to silica toxicity for humans. If silicon dioxide, also known as silica, corresponds uniquely to the chemical formula SiO_2, it exists in several forms with different structures, either crystallines or amorphous. There are several polymorphs of crystalline silica among which the most known and most abundant is quartz. With the exception of stishovite, in all its crystalline forms silica shows tetrahedral SiO_4 units in which a central atom of silicon is coordinated with four oxygen atoms. The SiO_4 tetrahedra share vertices and can arrange themselves in different structures with variable silicon-oxygen bond lengths and Si-O-Si angles. Moreover, silicon dioxide exists in amorphous forms including silica glass and colloidal silica.

About human toxicity of silica particles, in the literature there are many variable results obtained in studies which consider different silica structures, particle size and dose but all the investigations agree that the main toxicity mechanism for SiO_2 is the induction

Table I.2 – Synthesis of mesoporous silica nanoparticles.

Silica Source[a]	Surfactant	pH Condition	Particle Size (nm)	Pore structure	surfactant removal	Reference
TEOS	CTAB	basic (NaOH)	60-100	2D hexagonal	calcination	[103]
TEOS	CTAB, n-dodecylamine	basic (NH_4OH)	60-740	2D hexagonal	calcination	[104]
TEOS	CTAC	basic (NH_4OH)	20-50	2D hexagonal	calcination	[105]
TMOS	$C_nTAC(n = 14, 16, 18)$	basic (NaOH)	150-860	2D hexagonal	calcination	[106]
TEOS	Pluronic F127, P65, P123, F108	acidic (HCl)	100-300	3D cubic	calcination	[107]
TEOS	CTAC	basic (TEA)[b]	45-150	wormlike	solvent extraction	[108]
TEOS	Pluronic P123	acidic (HCl)	50-300	2D hexagonal	calcination	[109]
TEOS	CTAB	basic (NH_4OH)	30-280	2D hexagonal	solvent extraction	[110]
TEOS	CTAB	neutral	100-300	disordered	solvent extraction	[111]
TMOS	CTAB	basic (TEA)	<20	disordered	dialysis	[112]
TEOS and APTS	CTAB	basic (NH_4OH)	100-220	3D cubic	calcination	[113]

a TEOS: tetraethyl orthosilicate; TMOS: tetramethyl orthosilicate; APTS: 3-aminopropyl triethoxysilane

b TEA: triethanolamine

of oxidative stress through production of reactive oxygen species (ROS). As discussed in section I.5.4, an high level of ROS cause citotoxicity through several processes. Looking more in detail the possible paths of ROS generation for silica particles, can be useful to consider the different forms of the material.

In the case of quartz has been evidenced that on the cleaved planes of the crystals are generated some $Si-O\cdot$ and $Si\cdot$ radicals which react with H_2O, O_2 and CO_2 to form ROS such as $OH\cdot, O_2\cdot$ causing acute inflammation. Decreasing the surface reactivity, for example masking silanol groups, leads to a reduction of ROS formed and a critical inhibition of *in vivo* toxicity [121].

Addressing the problem more deeply, Ghiazza et al. compared the toxicity of particles of quartz, silica glass and colloidal silica shaped in spheres of similar dimensions (0.5-5 μm) and equivalent surface area (4-5 $m^2 \cdot g^{-1}$) [122]. They found a similar level of cytotoxicity on macrophages for quartz and silica glass, pointing out that crystallinity is not the source of surface reactivity, given that silica glass is a complete amorphous material. On the other hand, sol-gel amorphous colloidal silica showed no toxicity in all the independent tests evaluated and when analyzed with electron paramagnetic resonance (EPR) it didn't display surface radicals, which are generated from both silica glass and quartz according to EPR spectra. Through reaction with H_2O_2 quartz and silica glass produces $OH\cdot$ radicals while sol-gel silica did not. This process is often associated with particles toxicity and can take place in lysosomes, starting the production of ROS from silicon or silanol surface radicals. Thus, what is the difference between amorphous silica glass and amorphous silica obtained through a sol-gel process which makes the former toxic and the latter safe for human health? It is necessary to analyze the silica production process and its implication in the final structure of the material.

In fact, different amorphous silicas can be obtained through a few procedures, employing high temperatures or mild temperature processes. Among the colloidal silicas synthesized at low temperatures there are the ones obtained through silicate precipitation and silicas produced through hydrolysis of silicon alkoxides, including mesoporous silica materials. Some high temperature processes also produce amorphous silica particles, in particular silica glass, pyrolitic silica and smoked silica. In the high temperature procedures, the materials are cooled down quickly, freezing within them metastable structures. On the contrary, during sol-gel processes the material has enough time to arrange reaching local energy minima.

A study carried out by Zhang et al. [123] investigated the cytotoxicity of pyrolitic silica and Stöber sol-gel silica, finding out through fluorescence microscopy that they accumulate on

different parts of the cells: pyrolitic silica mainly bound to the cell membrane while Stöber silica are localized within the cells. They also confirm that sol-gel amorphous silica is not cytotoxic, but pyrolitic silica show toxicity through oxidative stress mechanism. Also in this case, EPR analysis show high amount of surface radicals in the case of pyrolitic silica and a much smaller amount for Stöber silica. The difference between these two different materials is in the structural organization at a small scale. Raman spectroscopy can provide informations on the various oligomers present in the material structure and when applied to silica particles obtained with high temperature process shows a characteristic peak associated with high strained siloxanes cycles including three silicon atoms. This peak is absent from the Raman spectra of all the silica materials produced through low temperature methods.

So, it seems to exist a correlation between the presence of highly strained cyclic structures which are easily cleavable and the generation of surface radicals which causes the toxicity of silica nanoparticles. These strained cycles are formed because of the fast cooling and are present all over the bulk material, so they generate radicals progressively, along with silica dissolution.

Thus, some silica materials have a high surface reactivity which make them dangerous sources of surface radicals and, subsequently, of reactive oxygen species, capable to damage cells through oxidative stress. Silica nanoparticles obtained through sol-gel process showed almost no cytotoxicity because of their low surface reactivity. Nevertheless, even sol-gel silica particles can reach a certain level of toxicity depending on size, surface charge or anisotropy ratio, for the reasons discussed in section I.5 and reported by Quignard et al. [124]. Porosity can also influence the cytotoxicity of silica nanoparticles, in fact if mesoporous silica has more surface area, a porous particle exposes much less silanol groups to the interaction with cells. This makes mesoporous silica particles less reactive than equivalent dense particle and consequently, safer [125].

I.7 Hybrid organic-inorganic mesoporous silica particles

The versatility of silica nanoparticles is one of their most attractive characteristic, which turns them in powerful tools. In fact, the silica scaffold can be functionalized with many different organic moieties, creating hybrid organic-inorganic materials with peculiar properties [126,127]. External surface functionalization improve colloidal stability and protect nanoparticles from degradation, moreover it can enhance biocompatibility or supply cell targeting moieties or even pores gating moieties, which can release the pore's content

under specific stimuli. Moreover, functionalize the inner pore surface can increase the interaction with the cargo, sometimes even providing a covalent binding site, raising the stability of the therapeutic agent and controlling the delivery kinetics. Making the pore walls hydrophobic [128] will increase their affinity for nonpolar compounds, while lining them with hydrophilic moieties will favor the adsorption of polar substances or metal ions [129, 130].

I.7.1 Functionalization through post-synthetic grafting

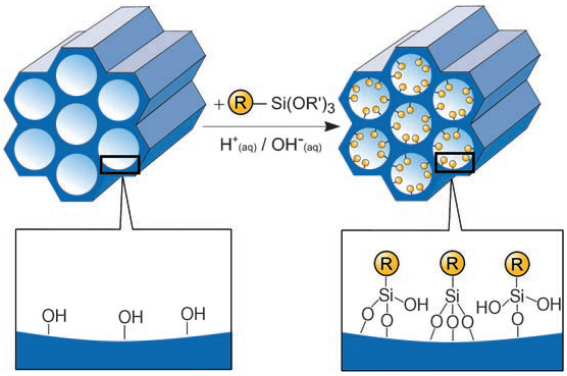

Figure I.14 – Post-synthetic grafting to functionalize silica surface. Reproduced from [126]

Functionalization of silica nanoparticles usually follows two main approaches: post-synthetic grafting or co-condensation. The former method employs alkoxysilanes which react with the silanol groups of silica surface in a condensation reaction, forming Si-O-Si links. The most used alkoxysilane to functionalize silica nanocarriers include 3-aminopropyl triethoxysilane (ATPS), 3-mercaptopropyl trimethoxysilane (MPTS), and various PEG-silanes. The first two allow for easy links with other broadly used moieties such as maleimides and isothiocyanates, while pegylation is widely used to improve biocompatibility and circulation times of nanoparticles *in vivo* (see section I.3).

It is possible to functionalize both the external surface and the inner pore surface, performing the grafting reaction on a material with empty pores; this leads to a reduction of the material porous volume and, in case of very bulky grafting molecules, can induce pore blocking.

On the other hand, it is also possible to functionalize only the external surface of the nanoparticles, removing the template which occupies the pores just after the grafting reaction. With this method, and carefully avoiding template extraction by the reaction mixture, the pores are sealed to the diffusion of grafting species and the functionalization

takes place only on the nanoparticle outer surface. An example of the latter method is given by Mal et al. [131], who grafted coumarin at the pore openings of MCM-41 silica, then removed the templating surfactant by extraction and inserted cholestane molecules in the pores. Irradiation with UV light at 310 nm induce coumarin photodimerization and the dimers act as closing gates obstructing the pores; however irradiating with light at 250 nm causes photocleavage of the dimers, allowing access to the pores, from which cholestane can be released. They manage to create a photochemically controlled gating system for tunable uptake and release.

In many cases controlled release systems involve gatekeepers, which are bulky molecules or nanoparticles sealing the pore entrances, attached to the particle surface through cleavable linkers. When exposed to certain stimuli the links break, unlocking the pore access. Following the same principle, hosted drug molecules can be linked to the pores surface with covalent or coordinative bonds, which can be cleaved to trigger cargo release by competitively binding molecules or reducing/oxidating agents. Platforms which react to many different external triggers, such as temperature [132, 133], pH [134] or redox reactions [135, 136], have been developed. Bein and co-workers employed an interesting method of selective functionalization of the inner and outer surfaces of MSNs, involving multi-step co-condensation and resulting in bi-functional nanoparticles with an onion-shell structure [137].

I.7.2 Co-condensation

Another path to obtain hybrid silica materials is the simultaneous condensation of corresponding silica and organosilica precursors. The co-condensation of alkoxysilanes ($(RO)_4Si$) and trialkoxyorganosilanes of the type $(R'O)_3SiR$ leads to materials in which organic residues (-R) are anchored to the pore walls [138–141]. Using this method, organic moieties have usually a more homogeneous distribution than in post-grafted materials and there's no risk of pore blocking. However, the content of organic functionalities in the matrix affects the mesoscopic order, leading to completely disordered materials when it is too high, thus organic content is usually kept below 40%. In fact, increasing proportion of $(R'O)_3SiR$ in the reaction mixture promotes homocondensation reactions instead of co-condensation reactions with the silica precursors, changing the reaction kinetics and influencing the material structuring process. Obviously, the removal of templating agents should be carried out carefully, to avoid the degradation of organic moieties, thus solvent extraction is usually chosen instead of calcination.

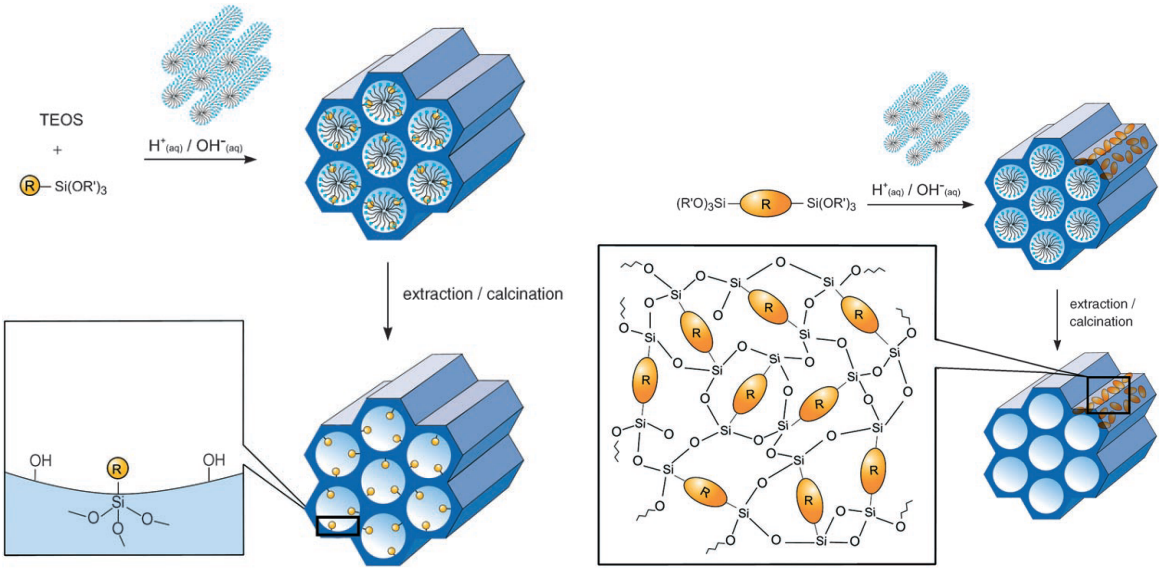

(a) Co-condensation (b) PMO synthesis

Figure I.15 – Co-condensation method to obtain hybrid organo-silica, and its development to obtain periodic mesoporous organosilica materials (PMO) employing organic bridged precursors of the type $(R'O)_3SiRSi(OR')_3$. PMO have organic moieties inside the silica walls, while using non-bridged precursors, such as $(R'O)_3SiR$ the organic moieties are just anchored on the silica pore walls. Images reproduced from [126]

Following the same approach it is also possible to obtain periodic mesoporous organosilicas (PMOs): a new class of mesostructured hybrid materials which have the organic bridges integrated in the silica network, not just anchored on the pore walls [142]. PMO materials are synthesized through hydrolysis and condensation of bridged precursors of the type $(R'O)_3SiRSi(OR')_3$, forming the structure reported in I.15b.

I.8 Conclusions and perspectives

Over the last 15 years, there has been extensive progress toward developing size-controlled, multi-functional nanoparticles for biomedical applications. Several materials have been tested and platforms which can perform more functions in the same time (diagnostic and therapy, for example) have been developed.

Despite the impressive progresses in this field, multiple reviews have highlighted the need for *in vitro* and *in vivo* studies examining biodistribution of NPs and their biodegradation in physiological conditions. These informations would help the design of efficient nanocarriers, capable of reaching their target without harming healthy tissues and being

degraded and excreted with no issue of toxicity.
Nevertheless, even if many encouraging results have been presented, the bio interactions still need to be deeply investigated, in fact many data are collected in media that are far too different from real biological environments, giving informations of limited utility. On the other hand, *in vivo* experiments are often expensive and many parameters play a role, making difficult for scientist to evaluate single contributions. A good way to solve this issue is to perform *in vitro* experiments in conditions as close as possible to biological ones, in order to obtain important informations which would make us able to predict *in vivo* behavior of nanoparticles, limiting the expensive animal tests and inserting each behavior in a general scheme, capable to guide nanomedicine researches.
The work conducted in this thesis follows this idea, focusing on the interaction between mesoporous silica materials and biological environments. In particular, the study addresses the silica degradation process in physiological conditions and the parameters which can have an influence on it.

The main goal of this study is the development of a new and rapid technique for *in situ* analysis of the interface between materials and biological fluids, capable to follow the degradation dynamics of therapeutic vectors and their drug release profile in real biological media (serum, blood). In particular, we want to explore the dynamic nature of bloodstream, which can affect the mechanisms of protein adsorption, particle dissolution and drug release. To do so, ellipsometric analysis has been chosen to follow *in situ* kinetics on 2D therapeutic vectors stack models. Ellipsometry is the ideal method since it is fast, it can differentiate several layers of a stack and can be performed in liquid media. Nevertheless, it works on thin films either than particles, so it is necessary to reproduce the composition and the structure of the nanocarrier on a thin film. Through this approach it is possible to address phenomena which are difficult to assess in colloidal systems. The only difference between nanoparticles and films systems is their surface curvature, which is important in the phenomena of protein adsorption, but its contribution can be investigated later while important detailed informations can be obtained about the silica bio-interfacial structure and its dynamics using in situ studies on films. The aim is to develop a method which can be employed with a large amount of materials, to study nearly any kind of therapeutic vector, but for the fine tune of the technique we started employing a well-known class of nanocarriers: the mesoporous silica nanoparticles.

Thus, we produced mesostructured porous silica and hybrid organo-silica thin films and we performed surface functionalization to provide a PEG-exposing surface (reported in Chapter II).

In parallel, we developed a special setup to perform *in situ* ellipsometry with non transparent fluids, willing to perform analysis in blood. We built a microfluidic cell and coupled it to the sample, in order to monitor the flow influence on silica stability (Chapter IV). This step of the project has been technically challenging, we had to find the best configuration to work, being careful to not modify the analyzed surface during fabrication step. It is a very complex system with many limitations which came from the ellipsometry technique, the microfluidic cell fabrication and coupling and external factors such as temperature control all over the setup parts.

Once the setup has been built, we analyzed mesoporous silica stability in phosphate buffered saline solution. This step was necessary as reference to evaluate the influence of proteins and cells on silica dissolution and it was also mandatory to compare our technique with well-established methods to ensure that it will be accurate and reproducible. Employing phosphate buffered saline as medium, we performed analysis through an ellipsometric standard static liquid cell.

We could then slowly enhance the complexity of the system, adding proteins in solution and then performing the analysis employing serum and blood as liquid media. Through the setup developed we could finally look at the influence of flow on dissolution kinetics in complex media (Chapter V).
The main steps of the project are summarized in figure I.16.
We developed a tool which can simulate a great amount of structures of therapeutic vectors and evaluate their interface dynamics in biological media, obtaining data which can be easily compared when the experiment condition are similar. The versatility of the technique allows the exploration of many different conditions, relevant for different applications (therapeutic vectors for cancer or lung diseases or kidney diseases). Being able to quickly compare materials response for a given environment is crucial to bring drug delivery nanocarriers on the market. Only in this way the fast development of new efficient nanovectors, optimized for their function, will be possible.

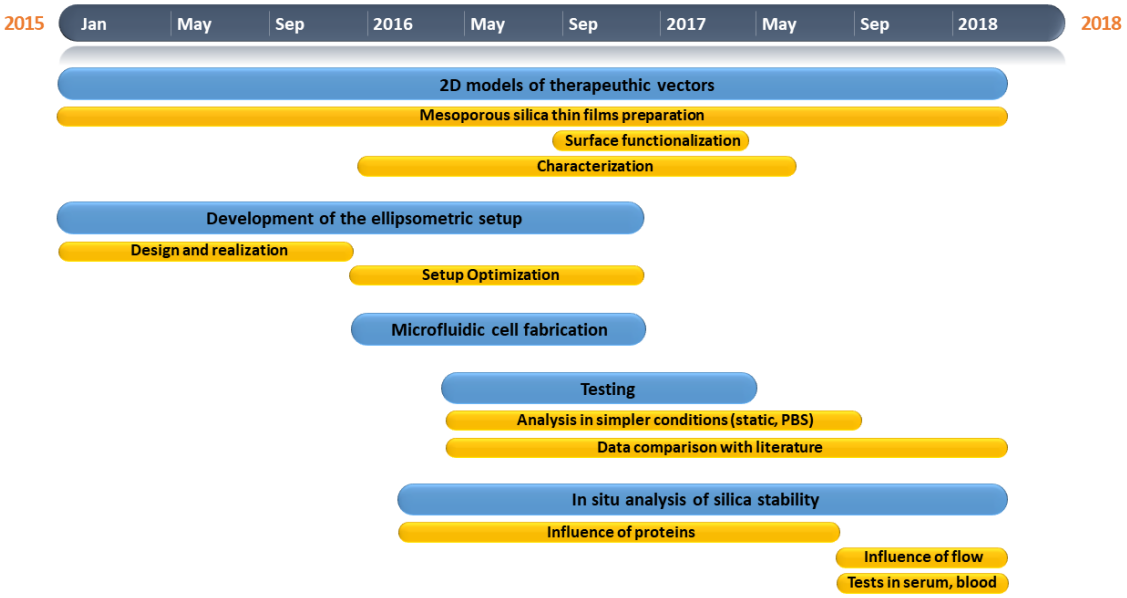

Figure I.16 – Scheme of the project developed during the thesis and its main steps.

Chapter II

Mesostructured sol-gel silica thin films

II.1 Sol-gel chemistry of silicates

The sol-gel method enables the processing of glasses and ceramics starting from molecular precursors, in mild conditions (pressure, temperature) and in presence of solvent. It is based on inorganic polymerization of molecular precursors, which are usually metal alkoxides of general formula $M(OR)_x$, where M is metal and R is an organic group (alkyl, aryl). The precursors undergo hydrolysis in presence of water and two hydrolyzed molecules can link together in a condensation reaction, building a larger molecule and releasing a molecule of water or alcohol.

This process can continue and build huge inorganic polymers into linear chains or three dimensional structures, depending on the monomers functionality, turning the solution of molecular precursors into a *sol*, that is a colloid in which the dispersed phase has dimensions between 1 and 1000 nm. Depending on the nature of the precursors and on the synthesis conditions (pH, concentration, temperature), the colloid can be constituted of discrete particles or extend into a continuous polymer network, in the latter case it is called a *gel*. Gelation can also be produced by fast evaporation of the solvent, as it happens during the processing of films or fibers. Gels continue to condense after their formation, during a period called *aging* and undergo shrinkage during drying by evaporation. The resulting dried gel is called *xerogel* and is usually amorphous and porous. To obtain a non porous material, the xerogel needs to be heated enough to cause sintering, during this thermal treatment many materials also crystallize.

Concerning silicates gels, their synthesis is usually made through hydrolysis and conden-

sation of silicon tetra-functional alkoxides employing a mineral acid (e.g. HCl) or a base (e.g. NH_3) as a catalyst. Alkoxides groups (OR) undergo hydrolysis producing silanol groups (Si-OH) which condense forming siloxane bonds (Si-O-Si) plus the by-products water or alcohol in the following reactions:

$$\equiv \mathrm{Si} - \mathrm{OR} + \mathrm{H_2O} \underset{\text{Water condensation}}{\overset{\text{Hydrolysis}}{\rightleftharpoons}} \equiv \mathrm{Si} - \mathrm{OH} + \mathrm{ROH}$$

$$\equiv \mathrm{Si} - \mathrm{OR} + \mathrm{HO} - \mathrm{Si} \equiv \underset{\text{alcoholysis}}{\overset{\text{Alcohol condensation}}{\rightleftharpoons}} \equiv \mathrm{Si} - \mathrm{O} - \mathrm{Si} \equiv + \mathrm{ROH}$$

$$\equiv \mathrm{Si} - \mathrm{OH} + \mathrm{HO} - \mathrm{Si} \equiv \underset{\text{Hydrolysis}}{\overset{\text{Water condensation}}{\rightleftharpoons}} \equiv \mathrm{Si} - \mathrm{O} - \mathrm{Si} \equiv + \mathrm{H_2O}$$

Usually condensation starts before hydrolysis is complete, thus silanols can react with other silanol groups or with alkoxides groups. Silicon alkoxydes and water are not miscible and a mutual solvent such as alcohol is used as reaction medium, but alcohol is not only a solvent, it can participate in the alcoholysis and condensation reactions. The nomenclature employed has been taken from Brinker and Scherer [102].
The pH is a very important parameter in silica polymerization: in basic solutions particles grow forming stable sols, while in acid solutions or in presence of flocculating salts they aggregate in chains and subsequently in a tridimensional network, forming a *gel*. The particles don't aggregate at basic pH in absence of salt because their surface silanols are ionized, making the particles mutually repulsive. The most employed precursors for silica sol-gel synthesis are: tetraethyl orthosilicate (TEOS) and tetramethyl orthosilicate (TMOS). In order to insert some organic function in the silica network or to reduce the precursor functionality, some organoalkoxysilane of the type $(\mathrm{RO})_3\mathrm{SiR}'$ or $(\mathrm{RO})_2\mathrm{SiR}'_2$ are used, where R' is a nonhydrolyzable substituent (e.g. (3-Aminopropyl)triethoxysilane (APTES), (3-Mercaptopropyl)trimethoxysilane, (3-Chloropropyl)triethoxysilane).

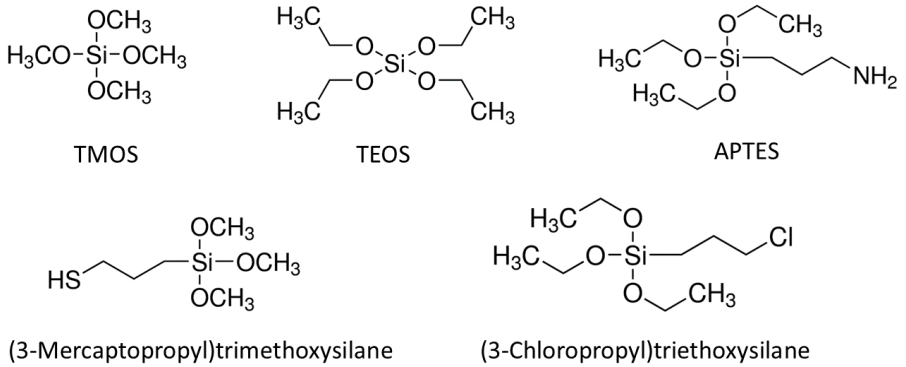

Figure II.1 – Sol-gel silica precursors.

II.2 Mesostructuration

Mesoporous silica thin films can be prepared by evaporation induced self-assembly (EISA), in this method the solvent evaporation causes the spontaneous association of inorganic precursors and surfactants present in solution into an organized structure.
In the case of thin films, solution is deposited onto a substrate through Chemical Liquid Deposition methods such as spin-coating and dip-coating (this method will be discussed deeply in the next chapter). To obtain mesoporous materials, surfactant are added to silica precursors in solution: they will assemble in liquid crystals phases forming the template around which the inorganic network will condensate. In fact, during deposition, the fast evaporation of volatile components (solvent, H_2O, HCl) increases the concentration of inorganic precursors and surfactant molecules, triggering the formation of micelles, when surfactant concentration reaches the critical micellar concentration (CMC) (figure II.2). In a polar solvent micelles have an hydrophobic core and an hydrophilic outer part, while in a non polar solvent the configuration is inversed. When concentration exceeds CMC and depending on the system characteristics, surfactants can assemble in different lyotropic phases (some are reported in figure II.2) and form periodically ordered structures with different symmetries (figure II.3) [143, 144].
Hybrid silica-surfactant mesophases spontaneously co-assemble during EISA process, and the removal of the organic structuring agent leaves periodic mesoporous silica solids, with pore sizes ranging from 1 to 30 nm, depending on the surfactant employed and on the processing parameters. The structuring agents are classically ionic surfactants, such as CTAB (Cetyltrimethylammonium Bromide, $[(C_{16}H_{33})N(CH_3)_3]Br$) or nonionic amphiphilic molecules which aggregates in micelles, bi-layers or liposomes to minimize the exposure of their insoluble domains (hydrophilic or hydrophobic) in a given solvent.

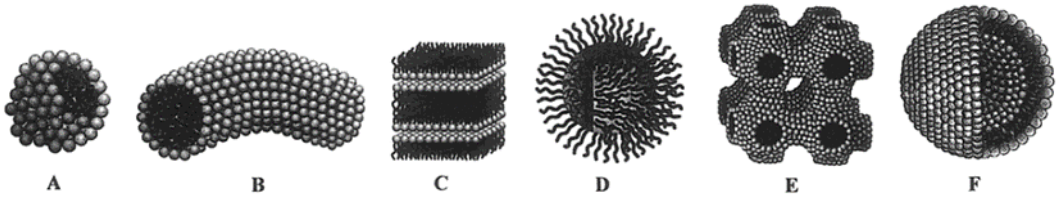

Figure II.2 – Micellar structures: A) sphere, B) cylinder, C) planar bilayer, D) reverse micelles, E) bicontinuous phase, F) liposomes. Reproduced from [144]

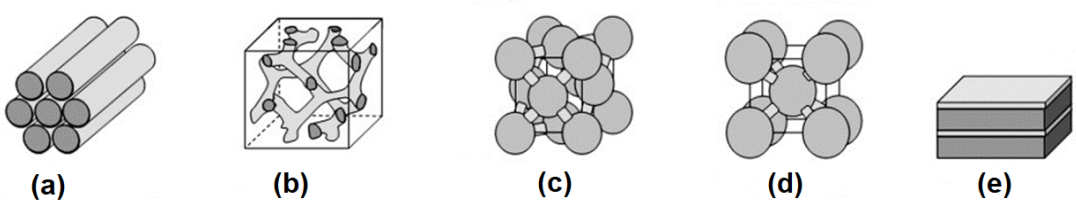

Figure II.3 – Some possible structures of ordered mesoporous materials, including (a) 2d-hexagonal with cylindric pores (p6mm), (b) bicontinuous cubic ($Ia\bar{3}d$), (c) face-centered cubic ($Fm\bar{3}m$) with spheric pores, (d) body-centered cubic and (e) lamellar phase. Reproduced from [145]

These templating agents usually give pore size from 1.5 to 10 nm, depending on the molecule nature and on the presence of species which can swell the micelles to enlarge their size. The structure of the mesophase depends on the packing properties of the surfactant, which result from several parameters such as the steric hindrance of the hydrophobic chain, the polar head volume and charge and the volume ratio between polar and apolar part of the molecule.

Amphiphilic block copolymers are also used as templating agents, being able to self-assemble in different morphologies and allowing pore sizes up to several tens of nanometers, due to the dimensions of the macromolecules which form large micelles. Diblock (AB) or triblock (ABA) copolymers are generally used, in which A represents a hydrophilic block (often polyethylene oxide(PEO) or polyacrylic acid (PAA)) and B, a hydrophobic block (polystyrene (PS), polypropylene oxide (PPO), or polyvinylpyridine (PVP). Pluronic F127 ($PEO_{106}PPO_{70}PEO_{106}$) and Pluronic P123 ($PEO_{20}PPO_{70}PEO_{20}$) or smaller diblock copolymers like Brij58 ($C_{16}H_{33}-PEO_{20}$) are commonly used.
Silica-based mesoporous materials have been obtained using CTAB-like surfactants [146–148], nonionic amphiphilic molecules (mainly alkyl amines and alkyl poly(ethyleneoxides)) [92, 93, 149] and block copolymers [150].

As extensively studied by Brinker et al. [143], during the deposition of a thin layer from a solution, the increasing surfactant concentration drives self-assembly of silica-surfactant hybrid micelles and their further organization into liquid crystalline mesophases. The kinetics of inorganic polymerization and template organization should be adapted in order to obtain an organized hybrid mesostructure. In fact the interaction between the inorganic and the organic components should be fast, and the surfactant organization has to be faster than mineral condensation. Hence, it is essential to fine-tune the reactivity of the inorganic precursors playing on concentration, pH and temperature and to control the interactions between inorganic precursors and surfactants (H-bonding, electrostatic interactions) to generate a well-defined hybrid interface. Changing the initial alcohol/water/surfactant mole ratio leads to different final mesostructures.

Nevertheless, the solution composition is not the only parameter influencing the formation of different mesophases. Grosso et al. [147] reported a modulable steady state (MSS), which lasts some minutes after the evaporation, very important to determine the final mesostructure of inorganic thin films. In fact, in this state the mineral network is still weakly condensed and volatile species (H_2O, EtOH) equilibrate between the environment and the film deposited, affecting the organic-inorganic interface curvature and forming different mesophases depending on their concentration. Being able to control relative humidity or solvent relative vapor pressure during the MSS gives control on the mesostructure organization.

Aging and/or thermal annealing stabilize the structure and condense the inorganic network. High temperature thermal treatments or solvent extraction are employed later to remove the surfactant. The whole process of thin films mesostructuration by EISA during dip-coating deposition is summarized in figure II.4.

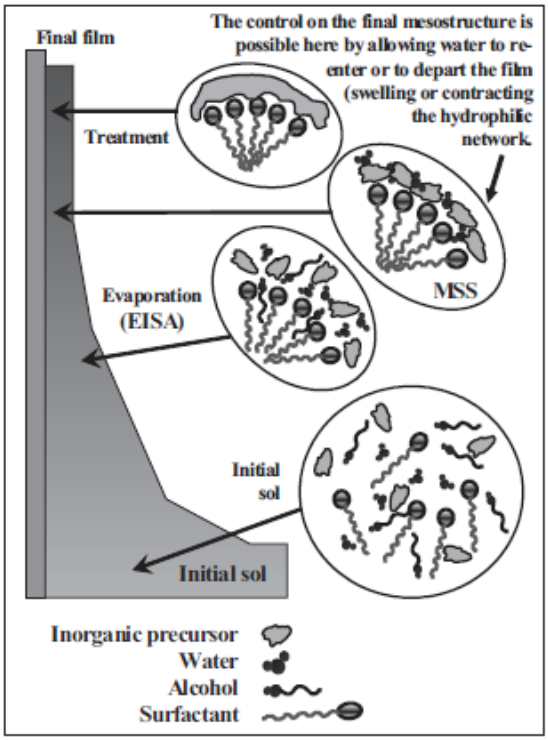

Figure II.4 – Mesostructuration of thin films during dip-coating: the initial sol is isotropic, then the evaporation triggers the surfactant self-assembly to form micelles ($C \geq CMC$), stabilized by the inorganic network which condenses around them. In the MSS the network isn't stiff yet and exchange H_2O and solvent with the environment, varying the organization of mesostructures. In the case of silica, after some minutes the inorganic network is strongly condensed and the mesostructure is fixed. Reproduced from [147]

II.3 Dip-Coating

Sol-gel derived thin films are applied on the substrates by Chemical Liquid Deposition (CLD) techniques and the conditions employed during this step determine the structure of the layer, as discussed previously. In fact, during deposition, inorganic condensation and self-assembly take place, triggered by the fast evaporation of the solvent. Moreover, the deposition conditions influence the final thickness of the film (this aspect will be detailed in the next Chapter). One of the most widely used techniques of CLD is dip-coating.

The dip-coating technique is the simplest method to deposit a thin layer from a solution: the substrate is immersed into the liquid and then retrieved vertically at constant speed, causing the deposition of a layer of solution. The physical chemistry involved in this process is pretty complex and have been deeply investigated.

A first model was proposed by Landau and Levich [151] in 1942 for newtonian and non-volatile systems, taking into account the balance between the adhesion of the fluid to the substrate and the viscous drag induced by gravity. Other studies have been conducted to enlarge the application field of Landau-Levich model to more complex systems, such as sol-gel ones. In these systems the forming layer undergoes continuous polymerization at increasing rate due to the fast solvent evaporation, experiencing a dramatic increase of the viscosity due to non-volatile components concentration.

This technique has been the object of an extensive investigation which is reported in the next chapter. In fact, in the context of this project, it was necessary to properly master the thickness of the silica layer in order to mimic the structure of therapeutic vectors and to easily compare dissolution data. While performing dip-coating to obtain sol-gel silica thin films, we noticed severe reproducibility issues and we decided to address them with a dedicated study, discovering an important influence of the surrounding atmosphere during the dip-coating process, on the films final thickness.

II.4 Surface functionalization

In order to reproduce the structure of particle nanocarriers on thin films as close as possible, it is necessary to functionalize their surface. In fact, silica nanoparticles are almost never introduced in the body as they are, but they often carry different types of surface moieties, as seen in chapter I. In particular, grafting a hydrophilic polymer on the surface is a widely used functionalization for biomedical devices.

Nanoparticles for drug delivery are very often covered with poly(ethylene glycol) (PEG) because of its ability to prevent protein adsorption, hiding the particles from the immune system [152]. Moreover, PEG is biocompatible and not toxic, and it has shown ability to greatly improve the *in vivo* half-life of nanoparticles. Thus, many processes have been developed to create PEG-exposing surfaces. On gold, PEG is usually grafted through thiols binding [153], while on silica and silicon substrates, organosilanes such as amino- or mercapto-trimethoxysilane are employed [154, 155].

If pegylation through organosilanes is common on silica nanoparticles, we experienced difficulties in performing it on silica thin films. In fact, either in vapors or in solution we never obtained an homogeneous layer of polymer on the surface. When a surface modification was evident on the silica films, it was always very irregular and full of defects across the substrate. Thus we turned toward surface-tethered polymers obtained by a controlled *grafting-from* technique, such as atom-transfer radical polymerization (ATRP). In the

literature there are some works discussing the growth of polymer brushes on a substrate from aqueous solutions [156,157]. Nevertheless, in our case, water could not be the solvent of reaction, because mesoporous silica films dissolve fast in aqueous environment. Thus, we investigated the optimal conditions to perform ATRP on mesoporous silica thin films, grafting pegylated polymer brushes onto the surface.
The work presented here on surface functionalization has been conducted in collaboration with Dr. Juan Martin Giussi and Dr. Omar Azzaroni and performed at Instituto de Investigaciones Fisicoquímicas Teóricas y Aplicadas (INIFTA), Universidad Nacional de La Plata – CONICET, La Plata, Argentina.

II.4.1 Atom-transfer radical polymerization

Atom-transfer radical polymerization is a form of living polymerization, that is a reaction in which the chain growth proceeds in absence of chain termination and chain transfer reactions. Usually the rate of chain initiation is fast compared to the rate of chain propagation, resulting in a constant chain growth rate and a very low polydispersity index (chain lengths are all very similar). Living polymerizations are important in materials synthesis because they offer polymers with a well controlled molecular weight and dispersity. Living polymerizations can be anionic, cationic or ring-opening polymerizations. Recently, starting from the 1970s, have been developed several methods of living polymerization which use free radical chemistry. Living radical polymerization is usually defined as *controlled* radical polymerization (CRP) because chain termination pathways are minimized but not completely absent [158].
CRP methods are based on developing a dynamic equilibrium between an active propagating radical and a dormant species. In ATRP dormant species are alkyl halides and propagating radical undergoes an activation/deactivation process with a persistent radical, which cannot propagate. More in details, the active radicals are generated through a reversible redox reaction catalyzed by a transition metal complex ($M^n - Y$/Ligand where Y can be the counterion or another ligand) undergoing a one-electron oxidation. The oxidation of the metal complex causes the abstraction of an halogen atom X from a dormant species R-X, generating a radical R·. This reversible process has its own activation and deactivation rates with associate constants k_{act} and k_{deact} respectively. Polymer chains grow from R· through addition of monomers, similar to a free radical polymerization, with rate constant of propagation k_p. Termination reactions occurs in ATRP, mainly through radical coupling, however under appropriate conditions only a few percent of the polymer chains undergo termination and these radical polymerizations behave as nearly

living systems. Typically, less than 5% of the total growing chains terminates during the initial stage of polymerization.

This process generates oxidized metal complexes, $X - M^{n+1}$, as persistent radicals, meaning that they don't self-terminate and they don't propagate. In fact, the persistent radicals do not react among themselves, but they may couple with the propagating radicals R· in the reverse process (deactivation reaction). On the other hand, R· do not only react with the oxidized metal complex but they also undergo irreversible self-termination through coupling with another R·. Hence, any occurrence of the self-termination of the active radicals induces an excess of the persistent species, which increases continuously as time passes. Therefore, the reaction of the propagating radicals R· with the persistent radicals is more and more favored compared to the self-termination, becoming highly dominant.

A scheme of ATRP mechanism is reported in figure II.5.

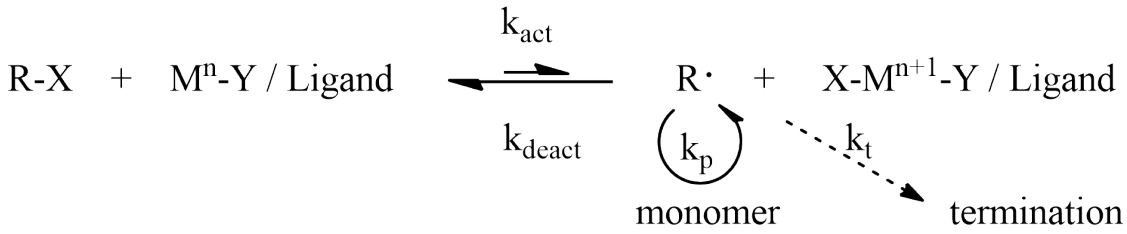

Figure II.5 – General scheme of atom-transfer radical polymerization, mediated by a transition metal complex $M^n - Y$/Ligand and a dormant species R-X where X is an halogen atom.

A successful ATRP will have a small contribution of terminated chains, but also a uniform growth of all the chains, which is accomplished through fast initiation and rapid reversible deactivation. ATRP needs several components: monomer, an initiator with a transferable halogen and a catalyst, which is a transition metal complex. Typical monomers are styrenes, methacrylates, methacrylamides, and acrylonitrile. Each monomer has its own atom transfer equilibrium constant K_{eq} for its active and dormant species, which determines the polymerization rate ($K_{eq} = k_{act}/k_{deact}$). If the equilibrium constant is too small, polymerization will not occur or will occur very slowly . In contrast, too large K_{eq} will lead to a a high radical concentration and consequent large amount of termination. In these conditions a high amount of deactivating metal complex is present, which shifts the equilibrium towards dormant species, making the polymerization slower.

Initiators should provide a fast initiation and, because transfer and termination reactions are negligible, the number of growing chains will be constant and dependent on the initiator concentration. In ATRP, alkyl halides (RX) are typically used as initiators with

the halide group being bromine or chlorine, to assure a rapid and selective migration between the growing chain and the transition-metal complex. Iodine can also work well for acrylate polymerizations but fluorine is not used because the C-F bond is too strong to undergo homolytic cleavage.
The key component of ATRP is probably the catalyst. The metal center should have affinity toward a halogen and its coordination sphere should be capable to selectively accommodate a halogen atom upon oxidation. Various rhutenium and iron complexes have been successfully employed in ATRP, as well as nickel, palladium and copper complexes [158].

II.4.2 Growing PEGylated polymer brushes on silica thin films

A method to create protein resistant surfaces based on poly(oligo(ethylene glycol) methacrylate brushes (p(OEGMA)) was presented by Chilkoti [159] and extended by Brown and co-workers [160]. These brushes exhibit the same surface properties than self-assembled monolayers containing ethylene glycol moieties, being also mechanically and chemically robust. Moreover, through ATRP it is easier to grow co-polymers feeding mixed monomers for polymerization. In this way, it will be possible to introduce on the brushes specific binding sites. We applied the procedure reported by Brown, testing the better conditions for our system. The target density is a brush of a few tens of nm, capable to strongly change the surface properties of the silica layers. The difficulties are: performing the reaction in a solvent different than water and avoiding the pore blocking. In fact, usually this procedure is carried on in water, but mesoporous silica undergoes fast dissolution in aqueous environments, so it is mandatory to find another solvent. Ideally, the polymer brushes are grown on the surface leaving the porosity accessible, but this is not an easy result to obtain. The initiator is grafted on amine moieties, that are uniformly dispersed in the silica matrix. Thus, they are also present onto the pore surface; polymer brushes may grow in the pores and, if they are long enough, they can block the access to the porous network. Probably the easiest way to avoid pore obstruction is to have very short brushes (few nm) which can still provide peculiar surface properties to silica without blocking the pores.

Initiator grafting

As initiator α-Bromoisobutyryl bromide has been chosen, to be grafted on amine moieties. Thus, the choice was either to post-functionalize silica with (3-Aminopropyl)triethoxysilane (APTES) introducing amine groups or co-condensate APTES and TEOS and obtain hy-

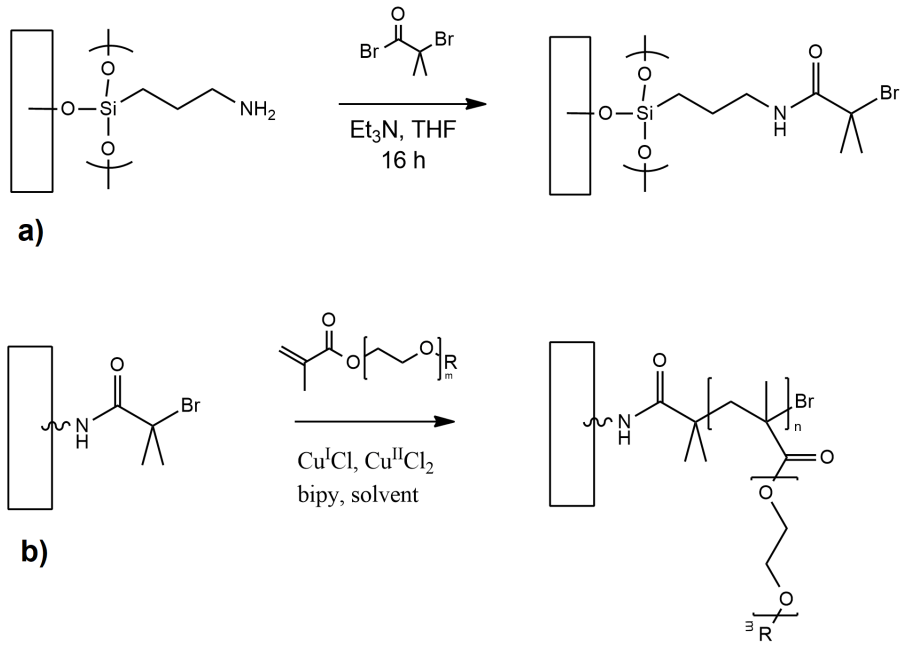

Figure II.6 – Scheme of the growth of pegylated polymer brushes on a silica surface exposing amine moieties. a) In a first step the atrp initiator reacts with the amines on the surface, forming the sites from which polymerization, catalyzed by a metallic complex, will start. b) Polymer brushes are grown from acrylates monomers, bringing poly (ethylen glycol) as side chains.

brid silica bringing amines. Because post-functionalization with APTES could lead to pore blocking in the mesoporous silica material, we chose to employ co-condensation in order to obtain hybrid mesoporous silica exposing amine moieties. The employed sol composition is reported in table II.1 and samples were dip-coated on silicon or glass substrates (2 mm·s^{-1}, RH=35 %, T=21° C) to obtain mesoporous layers of about 120 nm of thickness. Hexadecyltrimethylammonium bromide (CTAB) was used as templating agent. After deposition the films were stabilized 1 night at 130 °C and washed in Ethanol to remove the templating surfactant.

Table II.1 – Composition of mesoporous hybrid silica sol.

Molar ratio	TEOS	APTES	HCl	H_2O	Ethanol	CTAB
Hybrid silica	0.85	0.15	0.09	5	40	0.14

The ATRP initiator α-Bromoisobutyryl bromide is grafted on the surface of silica films in anhydrous conditions, it is thus important to dry glassware and samples in oven at

120 °C for 15 minutes before starting the reaction. Under nitrogen flow, samples are placed in anhydrous tetrahydrofuran (THF) and triethyl amine is added, to activate the substitution and neutralize the formed HBr. The initiator α-Bromoisobutyryl bromide is added at 0 °C and under N_2 flow. The samples are then kept under nitrogen at r.t. overnight. The work-up is done the day after, scavenging residual radicals by adding 30 mL of ethanol and then washing the samples in ethanol. The static contact angle of water on the surface passes from $\theta = 15°$ before the reaction to $\theta = 49°$ after the initiator grafting.

Table II.2 – Experimental conditions of α-Bromoisobutyryl bromide grafting on 30 cm^2 of total surface.

	MW (g/mol)	mmol	g	d (g/mL)	mL
α-Bromoisobutyryl bromide	229.90	15	3.448	1.86	1.86
Triethyl amine	101.19	15	1.518	0.726	2.10
THF anhydrous					60

The success of the grafting reaction has also been confirmed by the presence of Br centers on the surface through X-ray photoelectron spectroscopy (XPS) analysis (figure II.7b and II.8g). The peak of bromine (3d orbital level), centered at 70.4 eV, appeared after the grafting reaction, while it was absent in the aminated silica analysis (figure II.7a). The second bromine peak, centered at 68.3 eV is attributed to bromide ions Br-, which are formed during the analysis. Bromine peaks show spin orbit splitting, as every orbital level except 1s does. For 3d orbital level, two possible spin states are possible (j = 3/2 and 5/2) and they have different binding energies. The $3d_{3/2}$ and $3d_{5/2}$ doublet has a 2:3 peak area ratio.

After the grafting reaction, the Br/N ratio, obtained from XPS data, is 0.48, meaning that the reaction takes place on half of the amine moieties. This could be due to the fact that not all the amines were available for the grafting reaction, some may be embedded in the silica walls or not accessible because of closed pores. Moreover, amines grafted on silica surface can interact through hydrogen bonding with -OH group and the proton can eventually be transferred on the amine, forming a ion pair $NH_3^+SiO^-$. This two forms of the amine groups are most probably in equilibrium, as reported by Graf et al. [161] but anyway, they are not good nucleophiles for the reaction with α-Bromoisobutyryl bromide, because their lone pair of electrons is involved in the interaction with silanols.

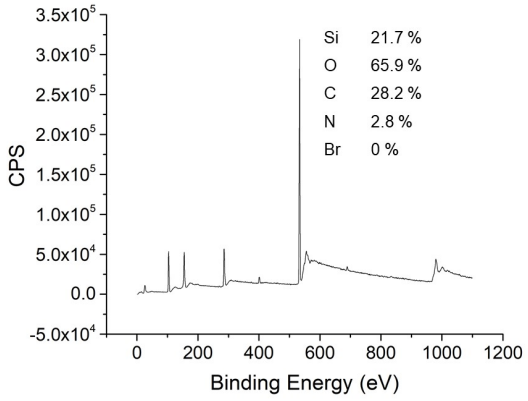

(a)

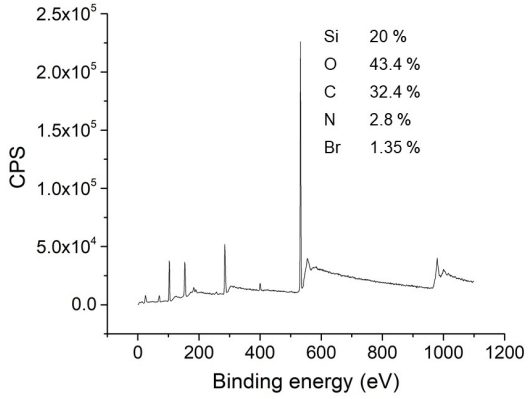

(b)

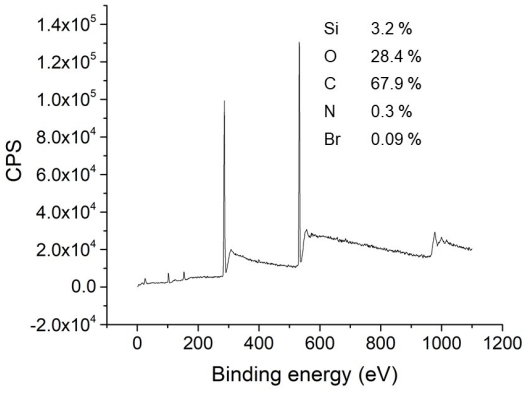

(c)

Figure II.7 – XPS survey spectra of hybrid aminated silica (a) pristine, (b) after the α-Bromoisobutyryl bromide initiator grafting, and (c) after ATRP reaction using PEGMA as monomer. The atomic percents reported include carbon, thus they contain an error which is due to contamination by adventitious carbon. In fact, a thin layer of carbonaceous material is usually found on the surface of every air exposed sample. The contribution of this contamination layer can't be removed and it is not constant for every sample, thus we will mainly employ atomic percent ratio between elements to compare samples, and not absolute atomic percent.

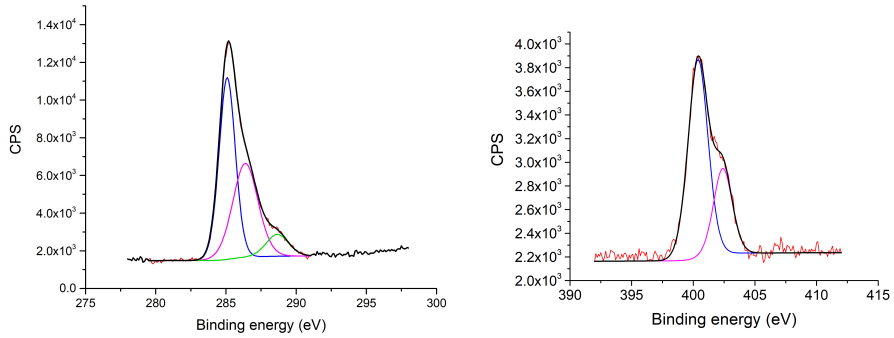

(a) Carbon 1s

(b) Nitrogen 1s

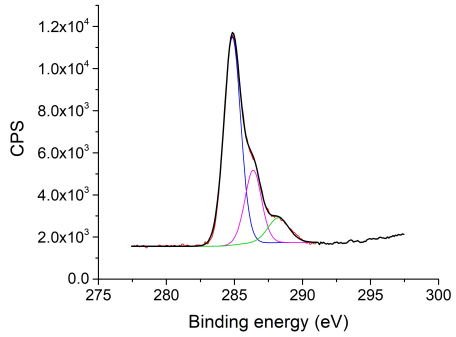

(c) Carbon 1s

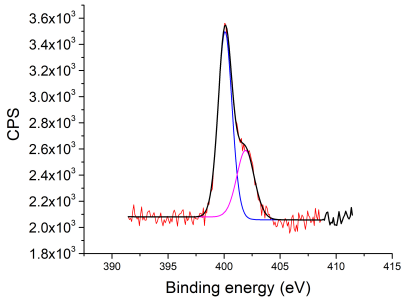

(d) Nitrogen 1s

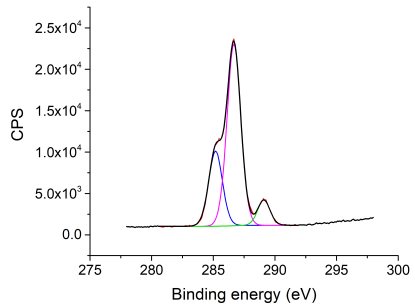

(e) Carbon 1s

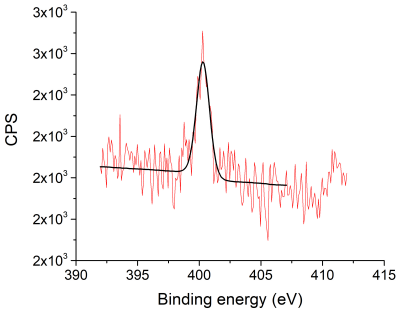

(f) Nitrogen 1s

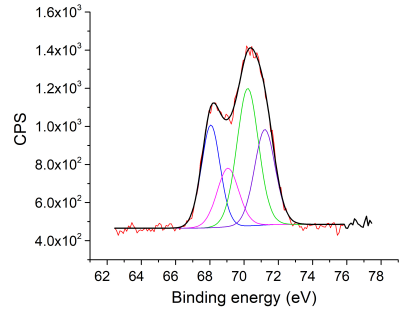

(g) Bromine 3d

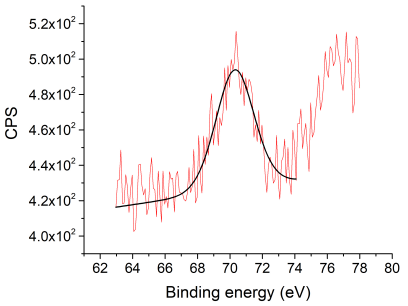

(h) Bromine 3d

Figure II.8 – Lorentzian distribution fitting curve of C1s and N1s peaks for thin films of (a-b) hybrid aminated silica, (c-d) α-Bromoisobutyryl bromide grafted silica, and (e-f) silica with PEGMA brushes. The bromine Br3d peaks of (g) α-Bromoisobutyryl bromide grafted silica and (h) silica grafted with PEGMA brushes are also reported.

Surface initiated polymerization

The ATRP was catalyzed by a copper complex with 2,2'-dipyridyl (bipy) as ligand. The polymerizations were carried out in methanol or in mixtures of methanol and water with a percentage of water not higher than 20% v/v. Three methacrylate monomers, carrying poly(ethylen glycol) as side chain have been tested. We used both poly(ethylen glycol) methacrylate and its methyl ether, obtaining very similar results. In the case of poly(ethylen glycol) methyl ether methacrylate, two different molecular weights (MW = 500 and MW = 950) have been investigated, because chain length may influence the grafting density and the length of the brushes. In fact, longer chains can have a huge steric hindrance which favors shorter brushes and a lower grafting density. The structure of monomers and initiator employed are reported in figure II.9.

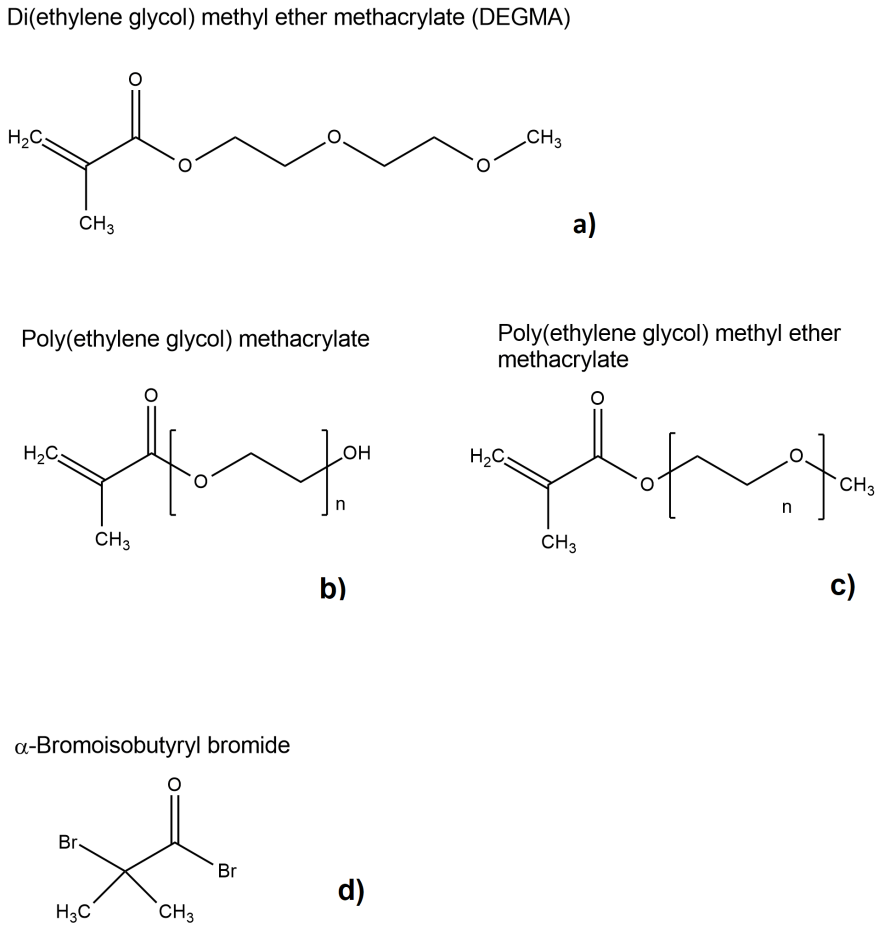

Figure II.9 – Molecular structures of the monomers (a-c) and the initiator (d) employed in the atrp reactions to graft pegylated polymer brushes on silica surface.

Monomer was dissolved in solvents (70 mL) at room temperature and degassed by passing a continuous stream of dry N_2 through the solution whilst being stirred (30 min). To this solution was added in succession bipy (1.65 mmol), $Cu^{II}Cl_2$ (0.07 mmol) and $Cu^{I}Cl$ (0.7 mmol) to form the catalyst complex. The addition of a small amount of Cu(II) halides at the beginning of the polymerization reduces the proportion of terminated chains and helps fast establishment of the atom transfer equilibrium [158]. After every addition, the mixture was further stirred and degassed with a stream of dry N_2 for 15 min. Separately, initiator coated samples (10 cm^2 each) were sealed in Schlenk tubes, degassed (5 · high-vacuum pump/N_2 refill cycles) and kept under N_2 atmosphere. The polymerization solution was then syringed into each Schlenk tube, submerging each sample completely. After various polymerization times the samples were removed, washed with methanol, then with ethanol and dried.
Polymerizations under different conditions were carried out following the above procedure, changing the monomer, reaction times and solvent. The different experimental conditions used are listed in table II.3 and are referred to throughout the text. A scheme of the surface initiated polymerization was given in figure II.6.

Table II.3 – Experimental conditions of ATRP reactions, for 30 cm^2 of total surface

Monomer	Solvent	Time (hours)	Thickness (nm)	$\theta(^\circ)$
DEGMA ME*	MeOH	1.5	1-2	44
DEGMA ME	MeOH	24	35	39
DEGMA ME	MeOH/H_2O 80:20	1.5	1-2	39
DEGMA ME	MeOH/H_2O 80:20	24	60	39
PEGMA ME (500 MW)	MeOH	24	-	49-50
PEGMA ME (500 MW)	MeOH	72	-	49-50
PEGMA ME (500 MW)	MeOH/H_2O 80:20	72	10	35-41
PEGMA ME (950 MW)	MeOH	72	-	49-50
PEGMA ME (950 MW)	MeOH/H_2O 80:20	24	5	22-27
PEGMA (500 MW)	MeOH/H_2O 80:20	72	1-5	41

* ME= Methyl ether.

The reaction times control the length of the polymer brushes: using DEGMA methyl ether as monomer, we observed that after 1.5 hours the reaction didn't produce a uniform

monolayer of polymer on the surface, even if brushes started to grow.
In fact, the contact angle θ decreases in comparison to the sample with only the initiator grafted (θ = 49-50°) but it's not possible to establish the thickness of the brushes by ellipsometry because they are probably very short (1-2 nm) and these values are in the range of thickness fluctuation of the sample. Performing the reaction for longer times (24h) the brushes grow more and ellipsometry measured their thickness as more or less 35 nm. In this case θ further decreased to 39°. Adding a percentage of water in the solvent helps the polymerization, giving longer brushes for the same reaction time.

Using PEGMA methyl ether as monomer the mixture methanol/water as solvent became mandatory. In fact, in this case the catalyst-monomer complex is not stable in methanol and a green precipitate of copper salts is observed at the bottom of the Schlenk tubes at the very beginning of the reaction. Thus, polymerization does not occur in this solvent. Adding the 20% of water the polymerization takes place with no issues, covering the silica surface with polymer brushes with length between 5 and 10 nm. When the monomer employed had a lower molecular weight the brushes grew longer, while increasing MW leads to shorter brushes but a more hydrophilic surface (contact angle passes from θ = 35-41° to θ = 22-27°), as summarized in table II.3.
Contact angles were consistent with that reported in literature for ethylene glycol coated surfaces [160] and very similar to values of ethylene glycol monolayers [153]. In fact, employing PEGMA methyl ether with MW = 950, the contact angle on the surface reaches the smaller values obtained for ethylene glycol monolayers (θ = 22-27° compared to θ = 22-25° for the monolayers). Using the other monomers we found θ values around 40°, observing a clear dependence on molecular weight of monomer for reactions performed in the same conditions. In particular, comparing PEGMA methyl ether polymerizations we noticed a decrease in static contact angle for higher MW.

The XPS analysis (figure II.7 and II.8) confirms the successful grafting of the polymer brushes. The C/Si ratio passed from 1.30 (hybrid aminated silica sample, figure II.7a) to 1.62 after the initiator grafting (figure II.7b) and reaches a value of 21.1 after the ATRP reaction (figure II.7c). Looking at the carbon signals (figure II.8) we can see an important increase of the C-O bond peak centered at 286.3 eV, after the ATRP (figure II.8e), due to the PEG chains. The other peaks of carbon are those of C-C (284.9 eV) and of C=O (288.2 eV). All these moieties are present in initiator-grafted and PEGMA-grafted silica samples. Nevertheless, we can observe them even in the pristine aminated silica sample, which should show only the C-C functionality. This is due to an inevitable contamination by adventitious carbon. In fact, every sample which has been exposed to air, even for

very short times, presents a thin layer of carbonaceous materials. This layer is known as adventitious carbon and generally includes a variety of hydrocarbons species with small amounts of both C-O and C=O bonds (286.3 and 288.2 eV, respectively), producing a main peak of C-C bonds at 284.9 eV. In our case, the contribution of this contamination layer to the carbon signal can't be separated from the sample contribution. A reference sample without carbon can't be used to evaluate the contamination percent because it can't be assumed constant for every sample. Thus, to compare different samples it will be used an atomic percent ratio between elements and not absolute atomic percents.

The ratio between carbon and silicon increased so abruptly after the polymerization that it's not possible to doubt about the increased presence of carbon atoms on the sample. It has to be pointed out that XPS is a surface technique and it gives information on the first 10 nm below the surface. With a polymeric surface layer of some nm, silicon atoms are masked and the amount of silicon seen by the instrument results much lower than before the polymer grafting.

It is also interesting to observe the nitrogen signal (figure II.8b, II.8d and II.8f). In the hybrid aminated silica sample and in the initiator-grafted sample (figures II.8b and II.8d respectively) the N signal presents two peaks: the main one is the primary amine NH_2 signal at 400 eV. There is also another peak, centered at 402 eV which is attributed to hydrogen bonded or protonated nitrogen, as already reported [161]. Aminosilane molecules may form hydrogen bonds with silanol groups while bending down toward the surface and they may undergo protonation, being in a tautomeric equilibrium as illustrated in figure II.10. This chemical state of nitrogen originates the signal observed at 402 eV. When the amines become hindered by the presence of the polymer brush, we observe the disappearance of this peak (figure II.8f).

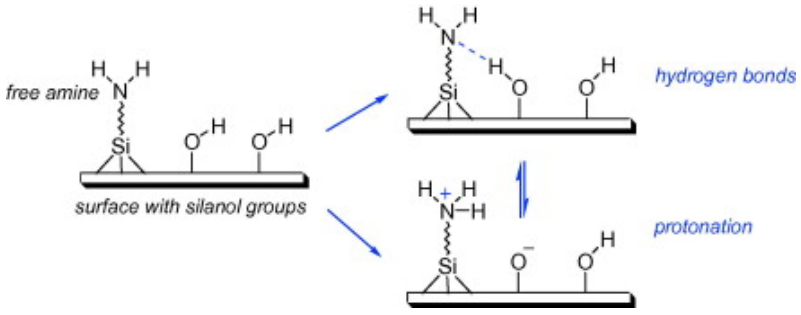

Figure II.10 – Free amines from aminosilane groups can form an hydrogen bond with surface silanol groups, establishing a tautomeric equilibrium between the hydrogen bonded nitrogen and the protonated nitrogen. Reproduced from [161].

From atomic force microscopy (AFM) II.11 and scanning-electron microscopy (SEM) II.12 images we can see a smoother surface when polymer brushes have grown compared to bare silica surface.

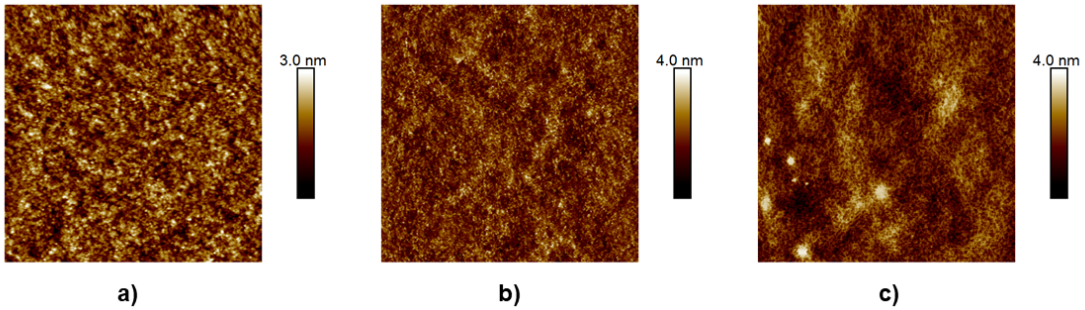

Figure II.11 – Atomic force microscopy images of: a) Mesoporous silica exposing NH_2 moieties, before polymer growth b) Surface coated with polymer brushes, PEGMA methyl ether MW 500 c) surface coated with polymer brushes, PEGMA methyl ether MW 950. These images have been obtained in tapping mode in nitrogen and the analysis has been performed by Catalina von Bilderling, researcher at Instituto de Investigaciones Fisicoquímicas Teóricas y Aplicadas (INIFTA), Universidad Nacional de La Plata – CONICET, La Plata, Argentina.

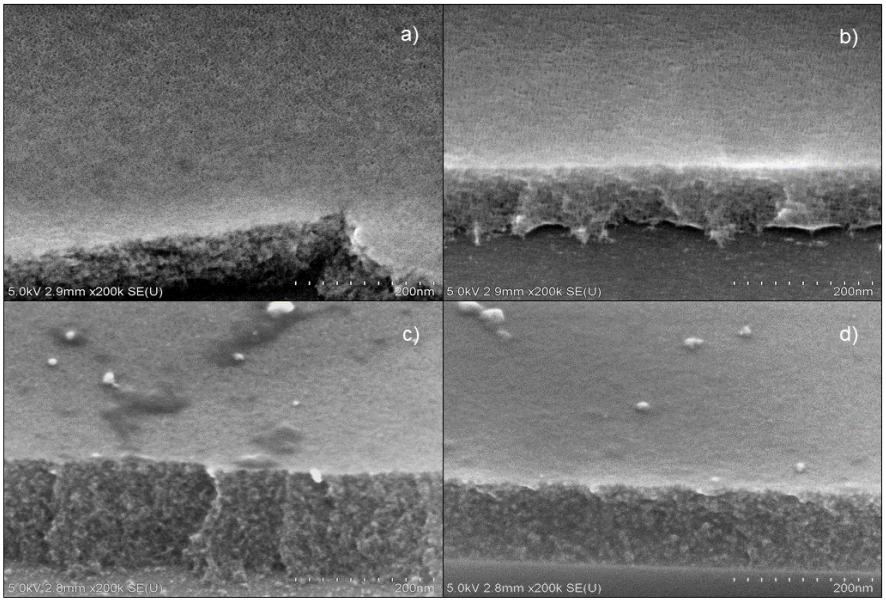

Figure II.12 – Scanning electron microscopy images of: (a-b) Mesoporous silica exposing NH_2 moieties, before ATRP reaction (c-d) Mesoporous silica surface coated with polymer brushes, PEGMA MW 500.

Thus, we can infer that p(OEGMA) brushes could have blocked the pores, at least in the

superficial layer of the silica film. This hypothesis has been confirmed by Environmental Ellipsometric Porosimetry (see section II.5.2 below), in which the surface-PEGylated samples doesn't show the typical curve of mesoporous materials, their pores remaining unaccessible to water vapors (figure II.13). Anyway, by transmission electron microscopy (TEM) we can see pores in these functionalized thin films, meaning that the film conserved its mesostructure. This is a great result, demonstrating that the little quantity of water we had to add in the reaction mixture didn't alter the mesostructure through dissolution. Anyway, we aren't able to say if the polymer brushes only block the pores on the surface of the sample, but not through its overall thickness or if the pores are completely full, because the optical contrast on carbon atoms is poor in TEM analysis (figure II.14).

Thus, when analyzing the dissolution of these hybrid silica films (chapter V) we must also consider a barrier effect to water penetration, due to the occluded pores on the surface. This effect will overlap the contribution of polymer brushes functionalization, but it was not possible to eliminate it. In fact, to avoid blocking the pores it would be necessary to graft polymers only on the external film surface and not on the inner surface of pores. Thus, ATRP initiator should be grafted only on the external surface, carrying out the reaction with pores still full of surfactant, to minimize the possibility of grafting inside the pores. These procedure could take months to be optimized and, because it was not the main subject of this work, we didn't develop it any further.

For future perspectives, it would be interesting to obtain similar PEGylated silica thin films, functionalized only on the external surface. Then, it will be possible to study how much of the brushes impact on dissolution is due to the reduction of exposed surface, caused by the pore blocking.

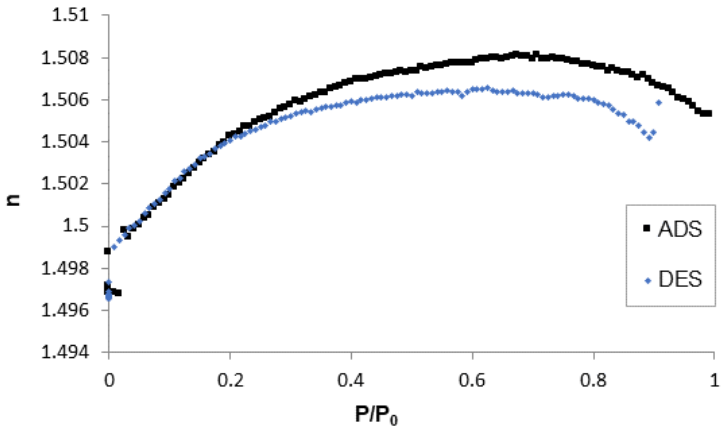

Figure II.13 – Refractive index at 632 nm of a PEGMA-coated silica film vs P/P_0 of water for the adsorption-desorption cycle. The steep change of refractive index associated with capillary condensation is absent, meaning that pores are not accessible to water vapors.

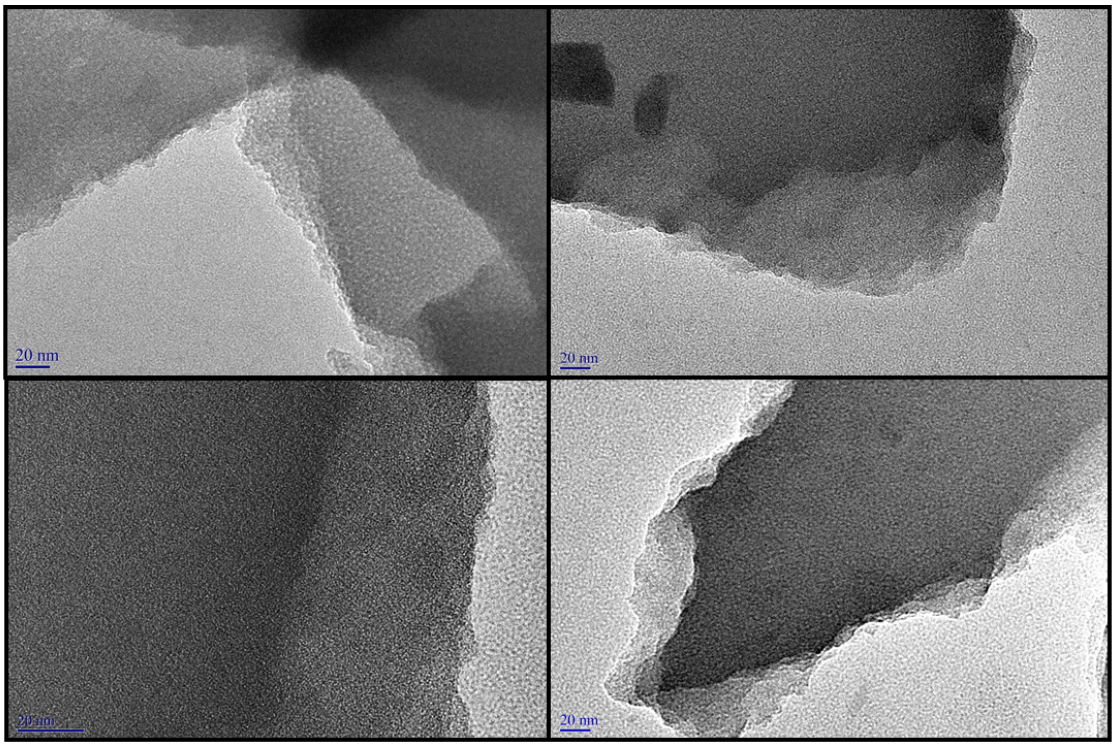

Figure II.14 – Transmission electron microscopy images of: (a-b) Mesoporous silica exposing NH_2 moieties; (c-d) Mesoporous silica coated with polymer brushes, PEGMA MW 500. The PEGylated sample appears still mesostructured.

II.5 Thin films characterization

II.5.1 Variable Angle Spectroscopic Ellipsometry

The refractive index and the thickness of final films were measured, after the stabilizing thermal treatment, by spectroscopic ellipsometry performed on a UV-IR (193 1690 nm) variable angle spectroscopic ellipsometer (VASE) M2000DI from Woollam. Measurment were performed at an incidence angle of 70°, and the data analysis was performed with the CompleteEASE software.

Ellipsometry is an optical technique based on the fact that a polarized light wave change its polarization state when reflected by a surface. This change depends from the optical properties of the reflecting material, which can be extrapolated from the ellipsometric measurement, along with its thickness. This can be done through an optical dispersion model of the analyzed film, whom parameters are varied to match as closely as possible the experimental data. For dielectric transparent materials, the most common employed model is a Cauchy dispersion, described by the equation:

$$n = A + \frac{B}{\lambda^2} \tag{II.1}$$

where A and B are the variable parameters and n is the refractive index. This is the model employed, during ellipsometric analysis, to describe the silica and hybrid silica films prepared in this thesis, deposed on silicon or glass substrates.

The basis of ellipsometry and its mechanism will be extensively treated in chapter IV.

II.5.2 Environmental Ellipsometric Porosimetry

Environmental Ellipsometric Porosimetry (EEP) is a characterization technique for thin porous films which has gained more and more importance. It monitors *in situ* gas sorption within the film, through which it is possible to evaluate open porosity, pore radius distribution and the film backbone refractive index [162, 163].

Thin porous films cannot be considered as a completely homogeneous material, in fact they alternate the backbone material with empty volume (pores). Therefore, Effective Medium Approximations (EMA) models can be applied to calculate the porous volume of the layer. EMA treats the optical layer properties as a mix of the properties of its constituents, considering the respective volume fractions. The Bruggemann-EMA is frequently used, which allowed the determination of the relative volumetric fractions f_A and f_B of two materials A and B of known dielectric constants $\tilde{\epsilon}_A$ and $\tilde{\epsilon}_B$ within a volume unit of

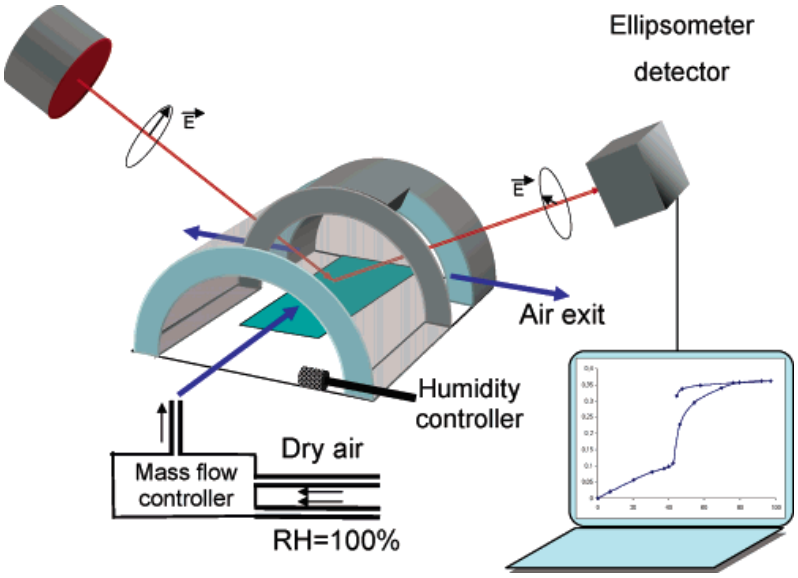

Figure II.15 – Experimental setup employed in environmental ellipsometric porosimetry, reproduced from [162]

measured dielectric constant $\tilde{\epsilon}$. This equation is very accurate for a two component system:

$$f_A \frac{\tilde{\epsilon}_A - \tilde{\epsilon}}{\tilde{\epsilon}_A + 2\tilde{\epsilon}} + f_B \frac{\tilde{\epsilon}_B - \tilde{\epsilon}}{\tilde{\epsilon}_A + 2\tilde{\epsilon}} \tag{II.2}$$

Thus, the dielectric constant of the porous film $\tilde{\epsilon}$ is measured by ellipsometry under dry air atmosphere: the dielectric function in the pores $\tilde{\epsilon}_A$ equals to the one of dry air and the walls have a known $\tilde{\epsilon}_B$, previously measured on a dense film of the same material. The porous volume V_p of the mesoporous thin layer is determined with the Bruggerman EMA by fitting the volumetric fractions of air f_A and of the matrix f_B within the mesoporous film. Flowing wet air in the atmosphere, water adsorbs in the pores forming a multi-layer coverage, until water capillary condensation. The Kelvin equation:

$$RT \ln \frac{P}{P_0} = -\frac{\gamma V_L \cos\theta G}{r_m} \tag{II.3}$$

where P/P_0 is the partial pressure, assumed equal to atmospheric relative humidity RH, gives the value of P/P_0 for which water condenses inside the pores, in a process called capillary condensation. When P/P_0=1 the pores are completely full of liquid water. In the Kelvin equation γ is the surface tension, V_L is the molar volume of water, θ is the wetting angle and r_m is the curvature radius of the liquid/vapor interface. G is a geometric factor accounting for the pores shape, it has a value of 2 for a sphere and 1 for a cylinder. The

geometric factor can be calculated also for elliptic pores, knowing their anisotropy factor, as reported by Boissière et al. [162].

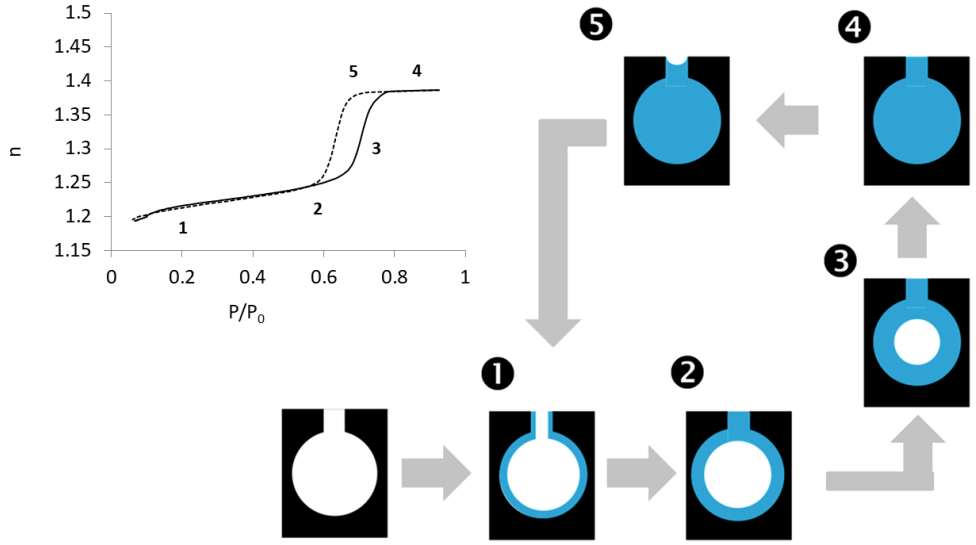

Figure II.16 – Representation of sorption isotherms and scheme of respective situation in the pore system. The capillary condensation corresponds to phase 3. Adapted from [163].

In a smaller pore r_m is small, so P/P_0 is small, in fact capillary condensation happens first in smaller pores. It is to mention that the measured radius r_m is not exactly equal to the pore radius since the capillary condensation occurs only after the adsorption of a water layer completely covering the pore walls. The thickness t of this deposit can be measured on non-porous samples of the analyzed material. And the pore radius r can be calculated as follows: $r = r_m + t$.

The evolution of film refractive index n and thickness d as a function of the environmental relative humidity (RH =P/P_0), are measured by EEP. In this way the capillary condensation pressure P/P_0 is measured and the pore radius distribution can be obtained. Registered isotherms will present hysteresis, meaning that two different values of P/P_0 are associated with adsorption and desorption.

Hysteresis is originated from the fact that the interface curvature is not the same at adsorption and desorption, in fact, after capillary condensation a liquid meniscus is formed inside the pores, and it has a different curvature compared to the starting adsorbed layer. Thus, the desorption curve is shifted towards smaller P/P_0.

Another reason that causes hysteresis in the porosimetry curves is that in many cases the access to larger pores is limited by smaller pores and they are not drained until the

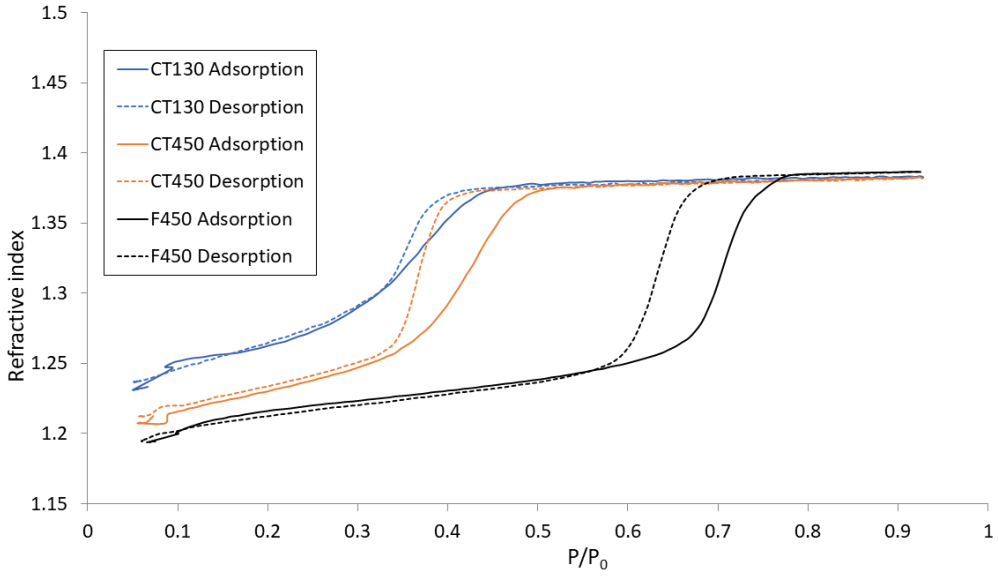

Figure II.17 – Evolutions of refractive index n of CT130, CT450, F450 films as a function of P/P_0 of water adsorption-desorption cycle. All the films reported are mesoporous silica films, templated with CTAB (CT130 and CT450) or with Pluronic F-127 (F450). They have been thermally treated at 130 °C or 450 °C, as indicated in their identification name.

desorption condition of the bottleneck is met. Then both the neck and the large pore are rapidly emptied. From the desorption isotherm it is thus possible to obtain the pore radius of the restrictions that access the larger cavities, also called bottlenecks.

The condensation into pores induces capillary forces, which trigger a shrinkage of the film network during adsorption and desorption, both reversible. Based on these data the mechanical properties of the porous film network can be calculated, as reported by Boissière et al. [162].

From EEP data it is possible to obtain surface area values using a t-plot analysis (figure II.19). In fact surface area S can be obtained from the measurement of slopes β of the t-plot curve, with equation II.4.

$$S_{tot} = S_{ext}\frac{\beta_{tot}}{\beta_{ext}} \tag{II.4}$$

External surface area is known. This method had an uncertainty (about 20-40%) because the β_{ext} value is always very small for films and thus difficult to measure with a good accuracy. Anyway, it is a good option to estimate total surface area when geometric calculation from the total mesoporous volume and mesopores dimensions is not possible. In

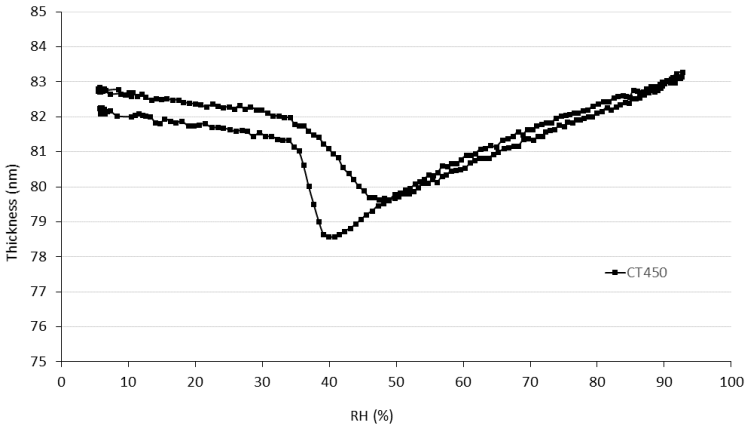

Figure II.18 – Evolution of film thickness of a mesostructured silica film, as a function of P/P_0. The capillary contraction due to condensation and the relaxation due to water desorption are clearly visible.

fact, this calculation required the knowledge of the mean number of connections between pores and when several pore environments exist or when the porous network hasn't an ordered structure, it can't be used. The values of t at each partial pressure P/P_0 have been previously measured by ellipsometry on a dense silica layer.

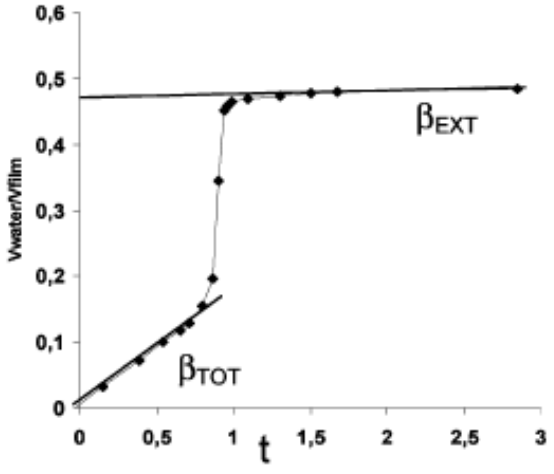

Figure II.19 – Plot of the adsorbed water volume as a function of water layer thickness t (in angstroms).

II.5.3 Small-angle X-ray scattering (SAXS)

Grazing incidence small-angle X-ray scattering has been performed on silica thin layers to check their mesostructures. The GI-SAXS experiments have been performed by Pierre-Antoine Albouy, researcher at Laboratoire de Physique des Solides, Université Paris Sud (Orsay, France).

The mesostructuration of thin films obtained through Evaporation Induced Self Assembly depends on several chemical and processing parameters, as previously explained (see sections II.2 and II.3). In a very detailed study, Grosso et al. analyzed the mechanisms involved in the mesostructuring process during EISA, performing SAXS experiments *in situ* [147]. They pointed out that the final mesostructure is achieved during the modulable steady state (MSS) where the film is exchanging volatile components with its environment before fixing its composition. So, the initial chemical composition of the *sol* is one of the parameters which defines the final material mesostructure, along with temperature and vapor pressures around the sample during deposition. In fact, these two processing parameters modulate the content of volatile species (water, ethanol) in the wet film during its equilibration with the environment.
Thus, at a given temperature, playing on precursor/surfactant ratio and relative humidity during the deposition step, one can obtain different mesostructures in a reproducible way. For the silica thin layers studied in this thesis, we had a Pm3n cubic structure on pure silica films obtained with TEOS as silicon precursor and CTAB as templating surfactant, with a molar ratio CTAB/Si = 0.14 (figure II.20 a). These films were dip-coated at 26 °C with a relative humidity of 30-35 % in the atmosphere. The obtained structure is consistent with the results reported by Grosso et al. in their study [147].
In the same processing conditions (T = 26 °C, RH = 30-35 %) the hybrid silica films, obtained through co-condensation of TEOS and APTES (molar ratio 0.85:0.15) with CTAB as template, self-organize in disordered structures (figure II.20 b). The system of TEOS/Pluronic F127, with a molar ratio F127/Si = 0.005, dip-coated at T = 26 °C and RH = 35-40 % forms a p6m 2D-hexagonal structure (figure II.20 c).

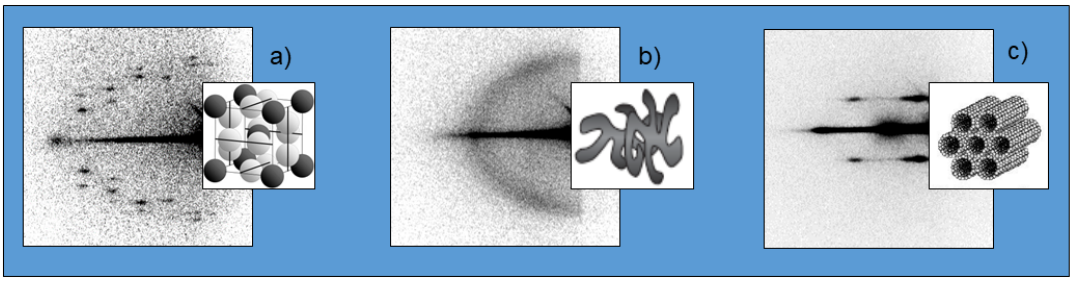

Figure II.20 – Saxs patterns and the related mesostructures obtained: a) Mesoporous silica, CTAB templated, CTAB/Si molar ratio = 0.14 b) Hybrid mesoporous silica exposing NH_2 moieties, CTAB templated, CTAB/Si molar ratio = 0.14 c) Mesoporous silica, Pluronic F127 templated, F127/Si molar ratio = 0.005. The films have been obtained by dip-coating from solution at 26 °C and 30-35 % relative humidity for CTAB systems and 35-40 % RH for Pluronic F127 system.

II.5.4 Scanning-electron microscopy (SEM) and Transmission Electron microscopy (TEM)

The SEM images presented in this thesis are made on a Hitachi SU-700 operated by Mr. David Montero, research engineer at the Institut des Matériaux de Paris Centre from the Université Pierre et Marie Curie (Paris, France).
The TEM images are made on a Cryomicroscope Tecnai spirit G2, operated by Mr. Patrick LeGriel, at Laboratoire Chimie de la Matière Condensée de Paris from Université Pierre et Marie Curie.

II.5.5 X-ray photoelectron spectroscopy (XPS)

In order to study the chemical composition of thin films surfaces, XPS has been performed on samples. The XPS experiments have been performed by Christophe Méthiviers at Institut des Matériaux de Paris Centre (IMPC) from the Université Pierre et Marie Curie (Paris, France) on a spectrometer by Omicron Scienta.
Kinetic energies of electrons are measured through an Argus hemispheric analyzer. The XPS analyses were carried out using a monochromatic Al K(α) source (1486.6 eV, 300 W). XPS probes the surface of the sample to a depth of 5-10 nanometres, and has detection limits ranging from 0.1 to 0.5 atomic percent depending on the element. The instrument was calibrated to give a binding energy (BE) of 103.3 eV for the Si 2p corresponding to Si in SiO_2 samples. An electron gun (1 eV, 5 mA) was used on all specimens as charge neutralizer system. Peak fitting of XPS spectra was performed with CasaXPS.

Chapter III

Study of dip-coating deposition process

Dip-coating from solution is a widely used method to deposit both organic and inorganic thin films onto various substrates. With this liquid-coating process, a homogeneous layer is easily spread onto the substrate surface and the solvent evaporation leads to the formation of a solid film with good control of its structure and thickness. In this thesis we always used dip-coating as deposition technique since it is simple and it was previously extensively studied in our laboratory, to control several important parameters.

Nevertheless, we often noticed a lack of reproducibility in certain conditions, particularly when exploiting a withdrawal speed regime so-called "capillarity regime" (it will be described later in this chapter). Particularly, we noticed important thickness fluctuations of films deposited at the same temperature and humidity. Thus, we decided to conduct a systematic study, in parallel with the main subject of the thesis, to address this issues and understand their origins. The results of this study are reported in this chapter and have been published recently [164]. The mastering of the technique was required to prepare thin mesoporous silica layers of very well controlled thickness, which will be shown in next chapters. The effect of solvent relative pressure around the meniscus on final thickness was deeply investigated, identifying some parameters which can affect it. We found that the solvent evaporation rate is not constant but strongly depends on the geometric configuration of the dip-coating experiment. The first part of the chapter is dedicated to a general study of physico-chemical phenomena involved, while the last part is focused on exploiting the effect of solvent relative vapor pressure to provide a very good control on layer thickness or to obtain giant thickness gradient profiles.

We carried on this investigation for various solutions (of sol gel or polymer) and found that

they all stick to a general common trend. The as-dipped sol-gel films were then stabilized by thermal treatment and the final thickness h_0 and refractive index n were measured by spectroscopic ellipsometry. Polymer films and colloid films were not thermally treated before measurement.

III.1 Fundamentals of dip-coating

The first description of draining and dragging phenomena involved in dip-coating was published in 1942, for polymeric systems, by Landau and Levich (LL) [151], who built a theoretical model to describe the film formation mechanism and predict the final thickness in certain conditions. They find that the thickness of the layer deposited depends on the withdrawal speed u at which the substrate is retrieved from the solution. Nevertheless, the LL model can't apply to every system. For example, whenever solvent evaporation is taking place, several critical parameters, assumed constant in LL model, may change with time (like rheological properties and surface tension) due to the increase of concentration of non-evaporating components. For this systems, including colloidal suspensions and polymeric solutions, exist two distinct behaviors: at low withdrawal speeds ($u< 0.1$ mm $\cdot$ s^{-1}) the thickness of the final layer deposited h decreases with u until a minimal value, whereas at high withdrawal speeds ($u>$ 0.5mm $\cdot$ s^{-1}) the thickness start to increase again, as showed in figure III.1.

In the low dragging speed deposition regime (so-called capillarity regime, CR) solvent evaporation significantly affects the deposition process, its rate E becoming a critical parameter that radically influences the deposited film thickness, while in the high speed regime (so-called draining regime) this parameter is negligible and the film formation follows the LL theory.

A global, semi-empirical model giving a satisfactory description of the dip-coating process, covering a broad withdrawal speed range (from 0.001 to 10 mm $\cdot$ s^{-1}) was published by Faustini et al. [165], combining in a single equation the contributions of both capillarity and draining effects:

$$h_0 = k_i\left(\frac{1}{u}\frac{E}{L} + Du^{2/3}\right) \tag{III.1}$$

where k_i and D are constants characteristic of the solution, L is the width of the deposited layer, and u is the withdrawal speed. This model matches very well with experimental results, as reported in figure III.1.

At low withdrawal speeds, solvent evaporation takes place at the liquid meniscus, which

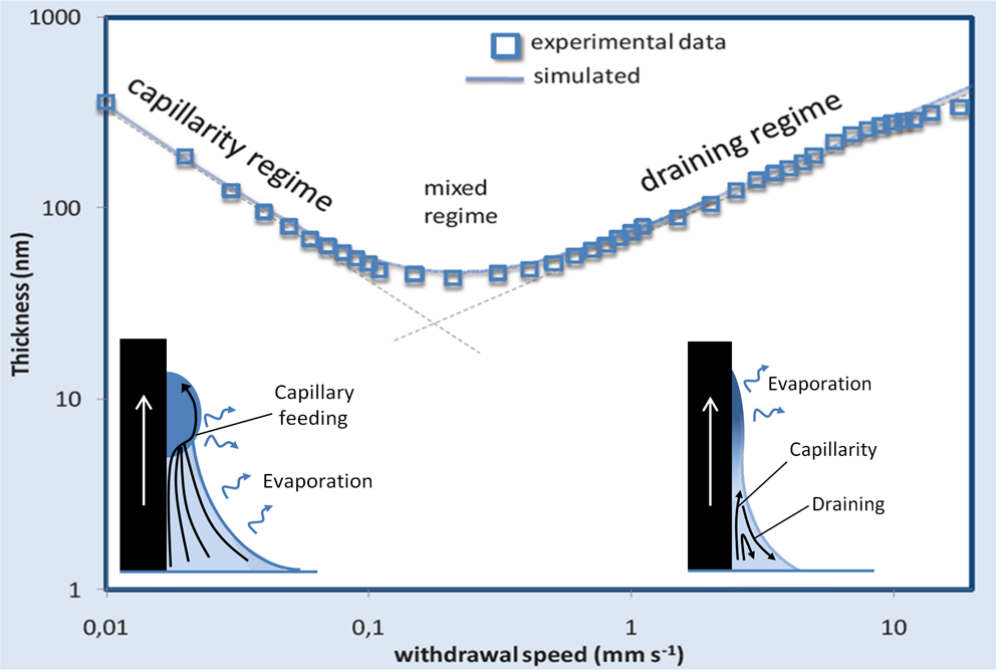

Figure III.1 – Plot of the thickness versus withdrawal speed (log-log scale) for a thin sol-gel film deposited by Dip-Coating. Experimental points match with the thickness predicted through equation III.1 for a wide span of withdrawal speeds. Inside the plot: schemes of the meniscus region for both capillary (left) and draining (right) regimes which dominate the dip-coating process at slow and fast withdrawal speeds, respectively. Adapted from [166]

is continuously fed through capillary rise from the solution. In this capillarity regime no solution dragging is involved, and the film thickness is directly related to the solvent evaporation rate E. Capillarity regime can be very useful in the case of high surface tension solutions because it avoids dewetting problems, otherwise encountered using draining regime; moreover, it enables deposition of thick films from highly diluted solutions, which can be interesting if species to deposit cannot be dissolved or dispersed in high concentrations. At high withdrawal speeds the final thickness is mainly dependent on the viscous drag and the film formation is well described by the Landau-Levich model. At intermediate speeds, both regimes of film formation are overlapping, summing their contributions. The speed range of this intermediate domain strongly depends on both solution composition and processing conditions such as temperature.

Thus, to resume: in the dip-coating process 3 different speed ranges exist, in which the film formation follows different speed dependencies: capillarity regime concerns low speeds and draining regime, in which is valid the Landau-Levich model, takes place at high speeds,

while they combine into a third regime at intermediate speeds. The boundaries of these three regions are not fixed but shift, depending on the system examined.

III.2 Irreproducibility issues

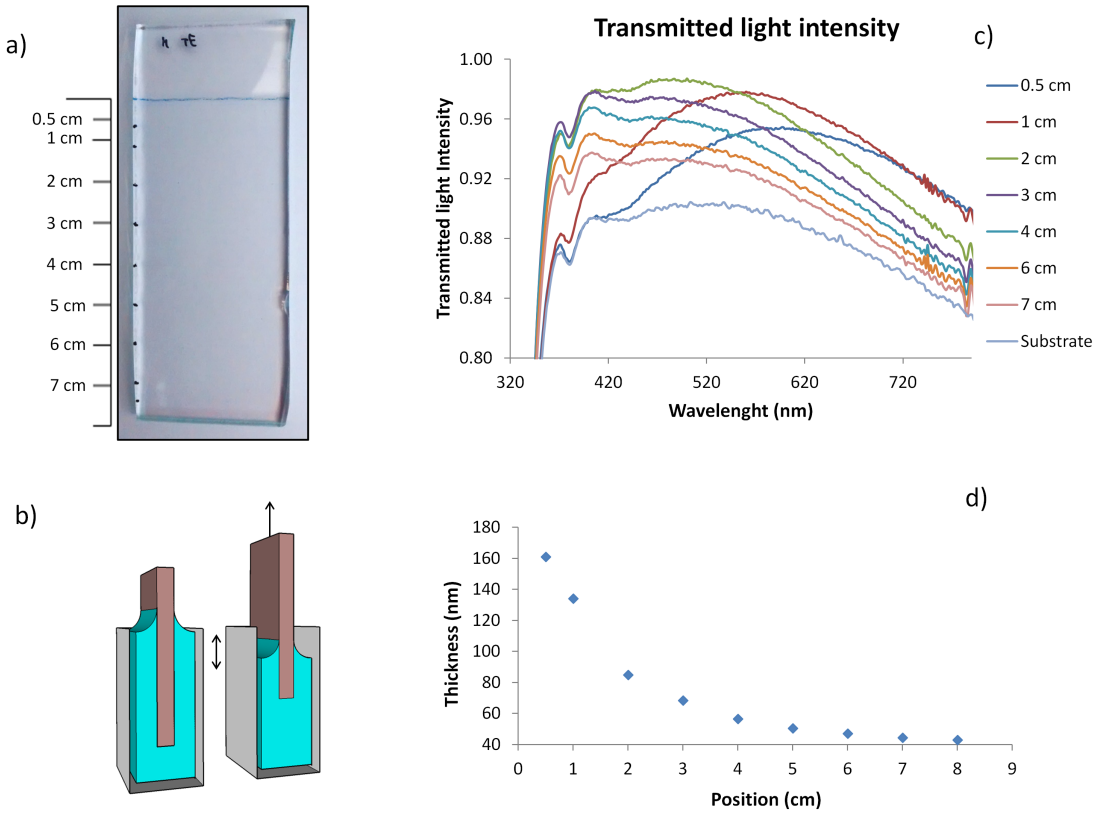

Figure III.2 – (a) Glass substrate coated with a single anti-reflective layer; various positions on the sample for which transmission and layer thickness have been measured are reported. (b) Dip-coating conditions: the liquid level inside the container decreases during the process because of substrate dragging. Withdrawal speed used: 0.3 mms^{-1}. (c) Transmission spectra taken at different distances from the top edge of the coating layer. (d) Thickness profile of the sample.

All the cited theoretical models assume that the processing conditions do not change during coating. Anyway, conditions may not be identical over the entire substrate surface, and thickness non-uniformity is often noticed on the samples, for example when relatively large surfaces have to be covered.

As an example, in figure III.2 is shown a glass substrate coated with a mesoporous methylated silica-based anti-reflecting layer, made by a dip-coating process at constant temper-

ature and withdrawal speed (T= 22 °C, u=0.3 mms^{-1}). The solution composition is reported in table III.1. After deposition, samples were cured at 450 ∘C for 10 min.

The transmission spectra along the sample point out that, the intensity of transmitted light changes, which means that the anti-reflective layer thickness is not uniform from the top to the bottom of the sample. By measuring the film thickness at several heights, we evidenced that the coating layer becomes thinner when the distance from the top increases. This behavior has been noticed quite often: layer thickness decreases along the sample with distance from the top.

We think that this is mainly related to the variation of the level of the solution with respect to the reservoir top limit during withdrawal. Retrieving the substrate lowers the liquid level, changing the evaporation conditions along the substrate due to vapor confinement. Other evidence of such an effect is reported in figure III.3 where the variations of thickness with respect to the withdrawal rate are plotted for a TiO_2 sol gel solution prepared under similar conditions but with different reservoir geometries or filling levels. One can notice that filling the container at various levels or using different containers could lead to very different thicknesses of the final film obtained. Thus, these processing parameters seem to have a strong impact on the amount of material deposited, causing thus very significant thickness non-homogeneity. Because the reservoir geometry and filling level mainly influence the local vapor pressure governing the evaporation rate, we chose to investigate the influence of solvent relative vapor pressure in the atmosphere on the final layer thickness. It is known that the relative solvent vapor pressure during film formation can impact the material structure [167,168], but until now, the effect of a solvent-enriched atmosphere on the amount of material deposited was never extensively investigated.

The purpose of this work is to give an overview of the phenomenon and its mechanisms to be able to better handle and control the dip-coating process. Several systems were investigated to obtain dense TiO_2 or mesoporous SiO_2 films from ethanol-based sol gel solutions, porous SiO_2 films from water-based colloidal solution, and PS PEO copolymer films from THF solution.

The TiO_2 solution was prepared with a molar ratio of 1:55:10 $TiCl_4$/EtOH/H_2O and used fresh. The experimental investigation was performed using dense titania as a model system since the film formation mechanisms are well-known and titania thin films are widely employed for many applications. Dip-coating was performed at 26°C and RH $<$ 5%.The final films obtained were cured at low temperature (130 ∘C) to stabilize them, keeping an amorphous structure in order to avoid uncontrolled crystallization followed by $>$ 50 nm surface roughness, not suited for ellipsometric analysis [169]. All TiO_2 films

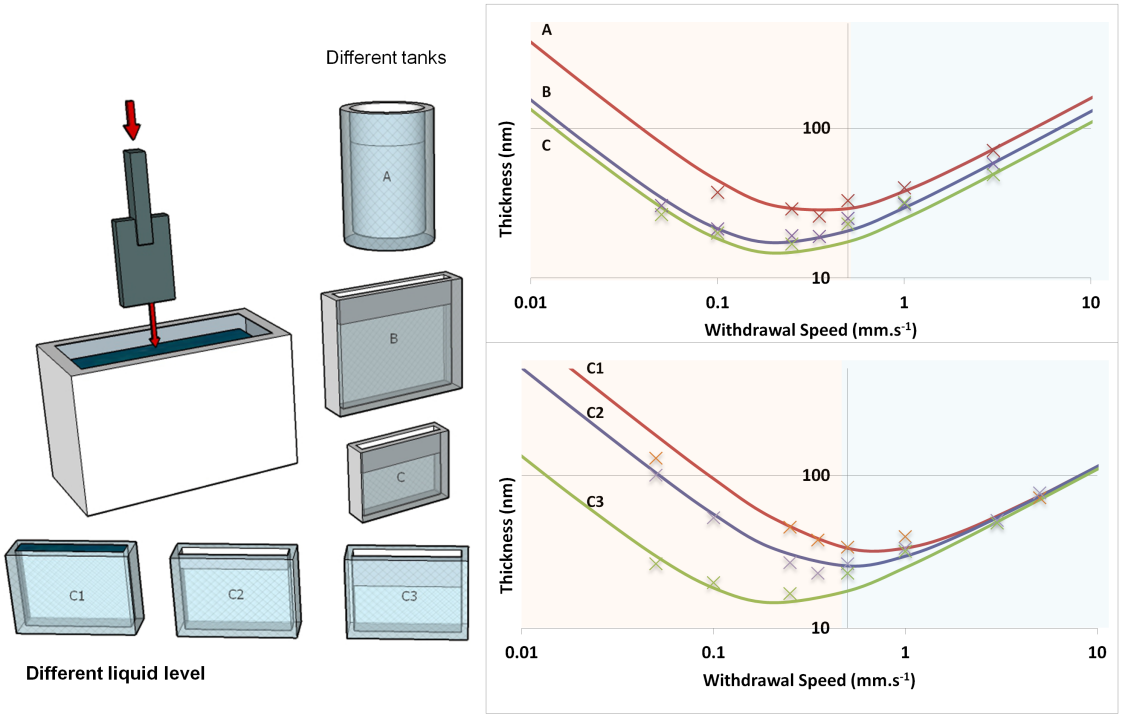

Figure III.3 – Scheme of the dip-coating method and plot of the thickness versus withdrawal speed (log-log scale) when the dip-coating is performed with different reservoirs (curves A-C) or the same reservoir but different level of liquid (curves C1-C3) for a TiO_2 solution in EtOH. The reported graphs are the fits obtained from experimental data points (reported in figure III.5) following equation III.1. The data points were acquired at 0.5 cm from the top of the film.

analyzed had a refractive index at 700 nm between 1.985 and 2.020.The thickness values were obtained by using a regular beam (3 mm) that allows the thickness fluctuation (typically 7%) due to stick and slip phenomena in the capillarity regime to be averaged.

The mesoporous SiO_2 solution was prepared using tetraethyl orthosilicate (TEOS) as inorganic precursor and hexadecyltrimethylammonium bromide (CTAB) as template surfactant. TEOS and CTAB were added to EtOH and in the end was added the aqueous acidic solution (pH = 2 by HCl addition); the molar ratio used is reported in table III.1. The solution was stirred at room temperature for 72 h before use. Dip-coating was performed at 26°C and samples were stabilized at 130°C for 1 hour.

The PS-b-PEO polymer solution was prepared in a concentration of 3.33 g/L using THF as solvent. PS-b-PEO (polystyrene-b-poly(ethylene oxide)) had Mn = 16400, Mn = 36400 Mw/Mn: 1.06. Dip-coating was performed at 40°C.

A ludox silica nanoparticle suspension, named HS40, was purchased from Aldrich. The

original stock of colloidal suspension was diluted 10 times with water. Dip-coating was performed at 40°C.
The refractive index and the thickness of final films were measured, after the stabilizing thermal treatment, by spectroscopic ellipsometry at an incidence angle of 70 °C on a UV-IR (193 1690 nm) variable angle spectroscopic ellipsometer (VASE) M2000DI from Woollam , and the data analysis was performed with the CompleteEASE software.

Table III.1 – Molar composition of solutions.

Molar ratio	TEOS	MTEOS	TiCl4	EtOH	HCl	H_2O	F127	CTAB
Anti-reflective (fig. III.10 a-c)	0.5	0.5	-	40	0.006	5	0.006	-
Anti-reflective (fig. III.10 d)	0.5	0.5	-	20	0.007	4	0.006	-
TiO_2	-	-	1	55	-	10	-	-
Mesoporous SiO_2	-	-	1	40	0.009	5	-	0.14

III.3 The role of solvent relative vapor pressure

Analyzing figure III.3 we can see that the curve of film thickness versus withdrawal speed shifts between different experiments, meaning that, for the same experimental conditions and the same speed, we obtain films with different thicknesses. The gap in thickness is huge in the ultra-low speeds regime and is progressively reduced with increasing speeds. The factor responsible for this behavior is likely to be the partial vapor pressure of the solvent in the atmosphere, originating from the solution evaporating from the reservoir and from the deposited layer. In fact in the capillarity regime the film thickness is directly related to the evaporation rate while for faster speeds this parameter has minor impact.
To investigate this hypothesis, we performed a first set of dip-coating with an ethanol-based TiO_2 sol gel solution in which the dip-coater atmosphere was progressively enriched with ethanol, employing the gas injection system described in figure III.4.
Briefly, dry air was bubbled into hot ethanol at 50 °C to be saturated with the solvent vapors and then passed through cold ethanol at 25 °C before entering in the dip-coater chamber. After the passage in ethanol at ambient temperature, the solvent-saturated air was mixed with dry air in different proportions, regulated by mass flow controllers, and injected within the dip-coater. The passage in EtOH at ambient temperature is

mandatory to avoid the condensation of solvent in the tubes and within the dip-coater chamber, which cause severe irreproducibility issues. Moreover, it is important to control the temperature of ethanol throughout the experiment and keep it constant (in fact when a higher flow of hot EtOH-enriched air passes through the second tank, it heats up the solvent quickly). The temperature of ethanol was checked before and after every experiment, using an ice-bath when necessary to keep it at 25 °C. A total air flux of 2.5 L/min is maintained during the deposition process; otherwise, especially for slow withdrawal speeds, the ethanol relative vapor pressure in the atmosphere changes too fast, leading to irreproducible results, since the chamber is not a hermetically closed system but communicates with the external environment. The experimental points obtained are presented in figure III.5, from these data we draw the curves of figure III.6.

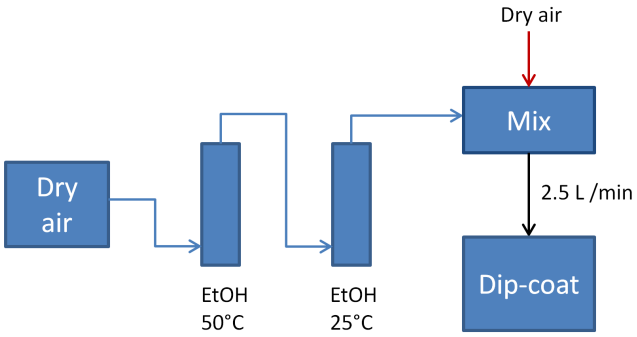

Figure III.4 – Experimental apparatus used to perform dip-coating with increasing solvent vapor pressure.

From the ratio between dry air and EtOH-enriched air, we inferred the ethanol relative pressure injected into dip-coating chamber. The relative vapor pressure values reported in figure III.6 are values related to the air injected in the chamber; they are not the effective ethanol vapor pressure values of the atmosphere within the chamber. In fact, probably full saturation in EtOH (100%) is never reached because the system is not perfectly sealed and exchanges always some air with the outside. All of the experiments were performed with a reservoir filled to the top with solution.

Plotting the thickness versus withdrawal speed by equation III.1, we can see a shift of the point of minimum thickness toward lower withdrawal speed values with increasing solvent vapor pressure, as shown in figure III.6, going from a minimum thickness of 62 nm in dry air until 29 nm when injecting EtOH-saturated air. There is a linear correlation between minimum thickness and solvent partial vapor pressure increase, as reported in figure III.6.

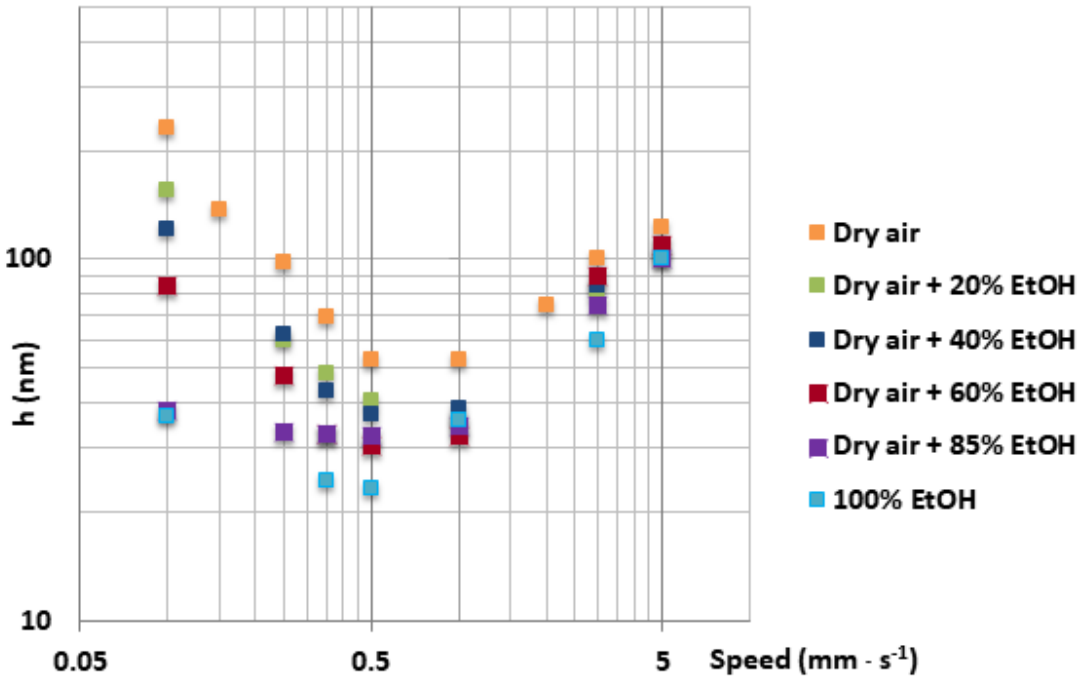

Figure III.5 – Plot of the thickness versus withdrawal speed (log log scale) for different solvent vapor pressures injected in the dip-coater chamber (the data points were acquired at 0.5 cm from the top of the film). From these data we draw the curves of image III.6.

As expected, the influence of higher vapor pressure atmosphere is stronger in the capillarity regime where the thickness of the deposited layer is directly proportional to the evaporation rate E [165]:

$$h_0 = k_i \frac{1}{u} \frac{E}{L} \tag{III.2}$$

The evaporation process of a solution could be a complex phenomenon to discuss because it is influenced by several parameters. In the most simple case for which no convection is involved, the evaporation rate E of a solvent can be described following the Hertz Knudsen equation (eq.III.3) [170, 171]:

$$E = A\alpha(KT)^{-1/2}(P^*_{(T)} - P_{amb}) \tag{III.3}$$

where$A$ is the evaporation surface area, T is temperature, α is the sticking coefficient of a gas molecule onto the surface, and K is a constant including the molecular mass, the Boltzmann constant, and a numeric prefactor. Both α and K are determined by solvent

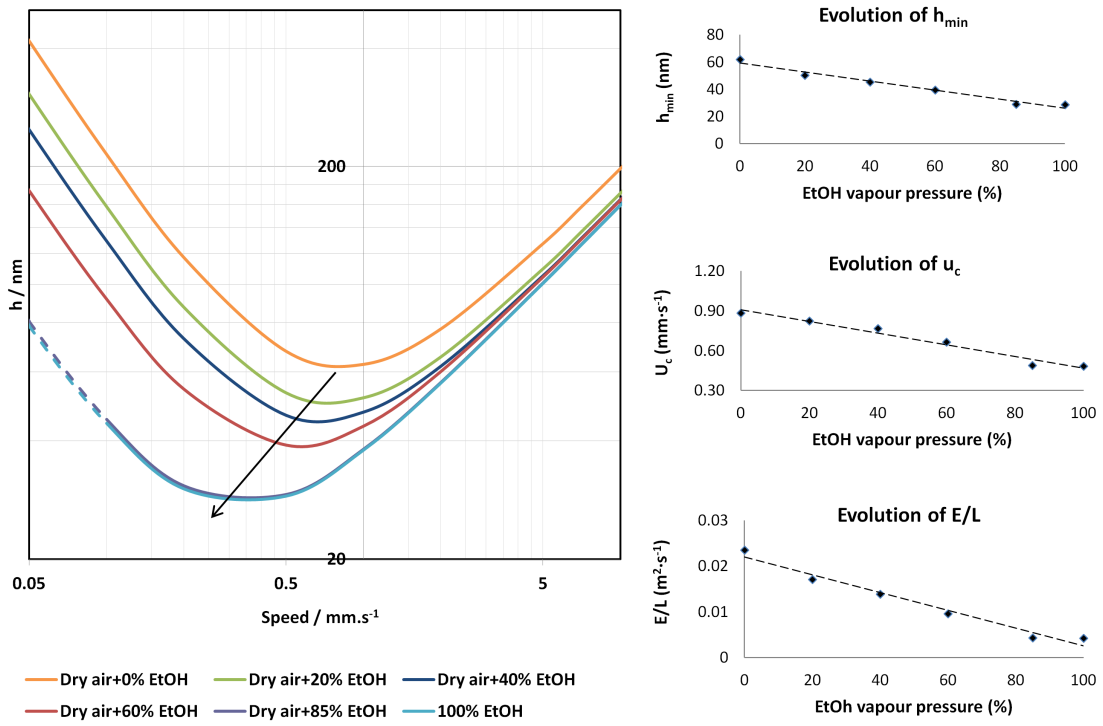

Figure III.6 – Plot of the thickness versus withdrawal speed (log/log scale) for different solvent vapor pressures injected in the dip-coater chamber (the data points were acquired at 0.5 cm from the top of the film.). Dashed lines are the theoretical trends, which are not possible to verify because dewetting from substrate surface occurs at speeds smaller than 0.1 mm s^{-1} for high values of EtOH vapor pressure. To have a clear image, we report here just the curves fitted with equation III.1 from experimental data points reported in figure III.5. On the right are shown evolutions of the minimal thickness h_{min}, the critical withdrawal speed u_c (at which h_{min} is obtained), and the solution deposition rate E/L (from equation III.1) versus solvent vapor pressure injected into the dip-coater chamber.

characteristics. Equation III.3 shows that E depends on the difference between the solvent saturation vapor pressure P^* at the temperature of the solution and its relative vapor pressure in the gas phase P_{amb}. Including E in equation III.2, we obtain:

$$h_0 = \Gamma A T^{-1/2}(P^*_{(T)} - P_{amb})\frac{1}{u} \tag{III.4}$$

where Γ combines all of the previously described constant factors. By increasing the solvent relative vapor pressure in the atmosphere P_{amb}, the evaporation rate E is reduced, and, as it is evident from equation III.4, the thickness of the deposited layer h_0 will be smaller. The surface of the interface A which, in our case, is the surface of the liquid meniscus at the contact with the substrate, also plays a role in the kinetics of evaporation.

As a direct consequence, every parameter which can lead to a different shape of the meniscus, such as the reservoir geometry, the contact angle between the substrate and the solution, and the distance of the sample from the reservoir's edge, will also influence the evaporation rate and, consequently, the film thickness.
In the draining regime, the system quickly reaches the equilibrium thickness, meaning that the variations in viscosity and surface tension, caused by the presence of solvent vapors in the atmosphere, are small and that the evaporation process is slower than the time needed for the layer deposition. Thus, the contribution of E is negligible and the film formation follows the Landau-Levich model, in which final thickness is related only to withdrawal speed u by equation III.5.

$$h_0 = k_i D u^{2/3} \tag{III.5}$$

The effect of higher ethanol relative vapor pressure in the atmosphere can easily explain the behavior observed in real experimental conditions, reported in figure III.3. In fact, changing the reservoir shape and dimension leads to a modification in the shape of meniscus, which is the surface of the interface, directly affecting evaporation rate and, consequently, layer final thickness h_0. On the other hand, lowering the liquid level inside the container places the meniscus in an atmosphere richer in solvent vapors (P_{amb} is higher), decreasing evaporation rate E and leading to thinner films.
We notice a huge thickness fluctuation along samples linked to the meniscus position during dip-coating process, which can be explained as an effect of solvent relative pressure. When the liquid meniscus is above the container, the evaporation speed is controlled by the relative solvent vapor pressure within the dip-coater; as soon as the meniscus is positioned within the solution's container, the relative solvent vapor pressure increases, following a gradient from the external edge toward the inside. In such an experimental situation, the P_{amb} parameter of equation III.4 is not a constant anymore but becomes a function describing the local evolution of the relative solvent pressure above the solution meniscus. Performing dip-coating without paying attention to the meniscus position can lead to huge thickness non-uniformity.
Plotting the thickness of a film deposited a constant speed versus the position Δz of the liquid level within the container, it is evident that a small variation in the solution height leads to huge differences in the amount of material deposited, up to a decrease of 80 90%, in capillarity regime. We performed experiments at constant temperature, humidity and withdrawal speed, changing the starting level of solution within the reservoir. Lowering the liquid level we obtained thinner films for every studied system, as reported in figure

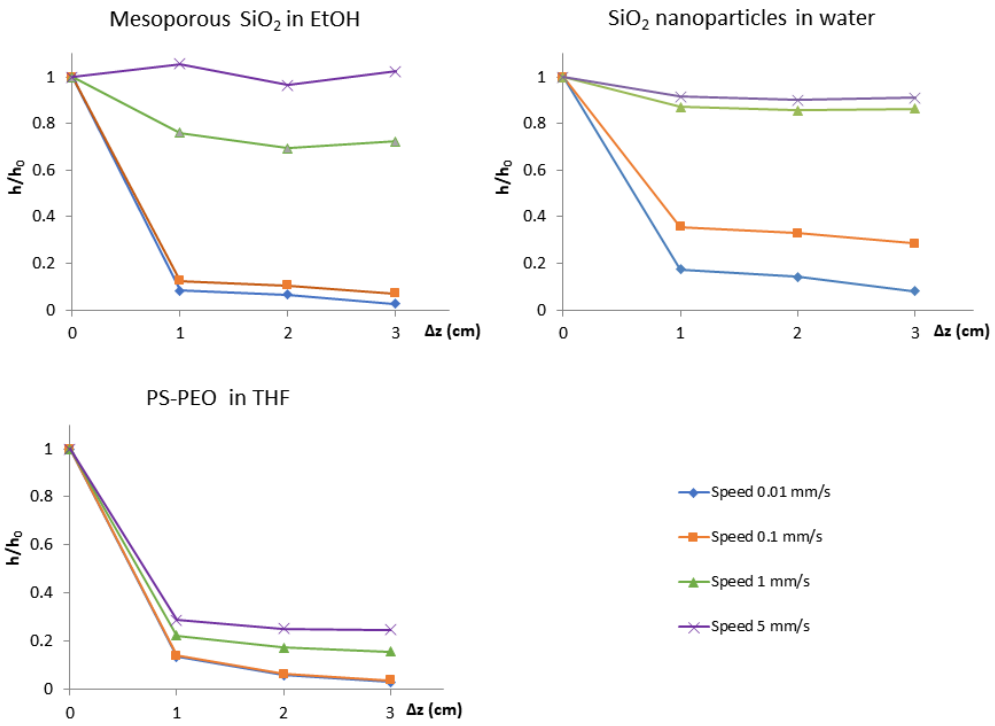

Figure III.7 – Evolution of h/h_0 with the difference in liquid level Δz for different speeds for (a) ethanol-based sol gel SiO_2 solution, (b) water-based colloidal SiO_2 solution, and (c) THF-based PS PEO block copolymer solution. The $h/h0$ is the ratio between the thickness of a film dip-coated with a liquid level within the reservoir lowered by 1, 2, or 3 cm and a sample dip-coated at the same speed but with the liquid level reaching the top edge of the container (level 0).

III.7.

In order to compare different solutions, the final film thickness h was normalized on h_0, which is the thickness of a film deposited in the same conditions but with a completely full container (level 0). In the latter conditions, the liquid is up to the edge of the container and, when substrate is immersed, the meniscus is above the container.

Below a given Δz value, we observe that lowering further the liquid level does not bring any additional thickness variation. We assume this is due to the fact that within the solution reservoir the atmosphere is nearly saturated; thus, that evaporation speed is the minimum. How steep the initial thickness decreases (in other words, how high P_{amb} value increases) with solution lowering depends experimentally on the solvent volatility, on the withdrawal speed, and on the reservoir dimensions and shape. It can be determined

experimentally in figure III.7 by assuming that h/h_O is proportional to $P_{amb}(\Delta z)/P_{amb}(0)$. This effect is visible even at high withdrawal speed and can be very strong when a highly volatile solvent, such as THF, is used. This is exemplified with the polymeric system polystyrene-block-poly(ethylene oxide) in figure III.7, which reveals a thickness variation of 70-75% even at a withdrawal speed of 5 mm $\cdot$ s^1 that is usually considered in a "pure" LL regime. Thus, in this case, even for a high withdrawal speed, the evaporation process is faster than the liquid layer deposition.

One could argue that passing from outside the container to within it, meniscus change its shape and this could be the explanation of the thickness difference observed along the sample. Anyway, we verified that the meniscus shape changes noticeably only in the first 0.1 cm (the experiment is illustrated in figure III.8 and III.9 and results are reported in table III.2), but we can observe thickness variations during the first 2-3 cm on the film (figure III.7), meaning that the solvent vapor pressure variation is mainly responsible for the described behavior.

From these results, we can infer that, to gain reproducibility, it is better to keep the liquid level some centimeters below the top of the reservoir to be on the plateau of vapor pressure profile. In such a case, obtaining the targeted thickness of 80 nm for an anti-reflective layer, implies re-adaption of the concentration of the solution, as shown in figure III.10. Moreover, it is better to use a large reservoir with respect to the volume of the substrate; in this way, the dragging will impact less the level of the solution within the container than in the case of a smaller reservoir, but this may demand a large volume of solution for large substrates.

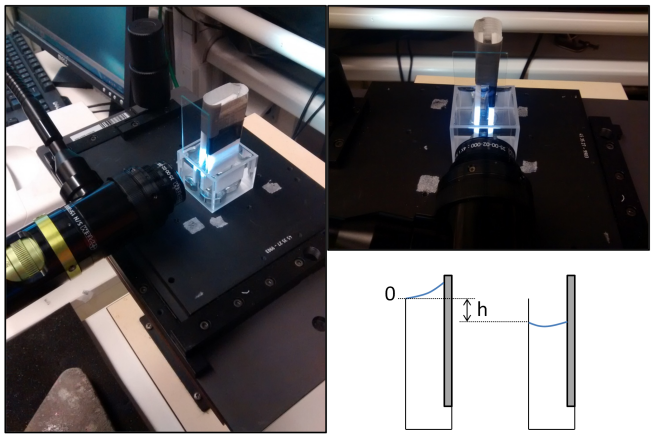

Figure III.8 – Setup used to observe meniscus shape variations: with a camera perpendicular to the meniscus plane we observe its shape evolution while slowly lowering the liquid level inside the tank employing a peristaltic pump (not shown in the pictures). We build a tank with two PTFE walls spaced 0.5 cm. We attached a Si wafer at one of the PTFE walls (white in the pictures) making it exceed the height of the opposite wall. We submerged everything in a transparent glass container and filled it with water. We observed the meniscus of water on the Si surface; at the starting point the liquid reached the top of the PTFE wall, and the meniscus is higher than the tank top, as sketched in the figure.

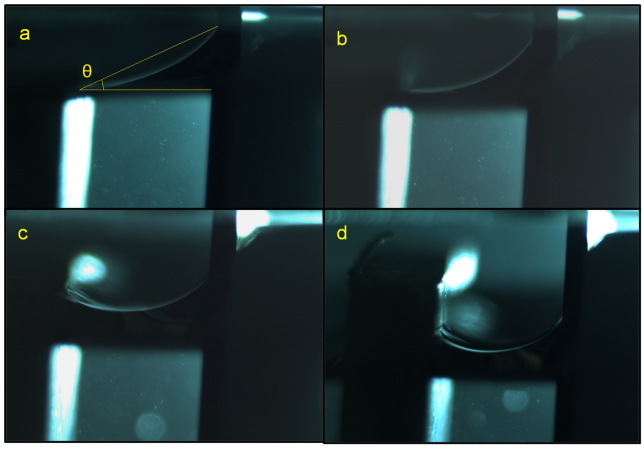

Figure III.9 – Evolution of the meniscus shape. a) h = 0 mm b) h = 0.42 mm c) h = 0.84 mm d) h = 3.57 mm. Angles have been drawn and measured with ImageJ software.

Table III.2 – Angle Θ variation with distance from the top of the reservoir.

Distance from the top h (mm)	**Angle** $\theta(\pm 1)^\circ$
0	27.0
0.21	25.5
0.42	24.9
0.63	21.5
0.84	20.6
1.26	19.7
1.68	20.4
1.89	22.2
2.1	20.9
2.52	21.3
3.57	20.7
4.41	19.9
5.04	20.5
7.98	20.7
10.08	20.8

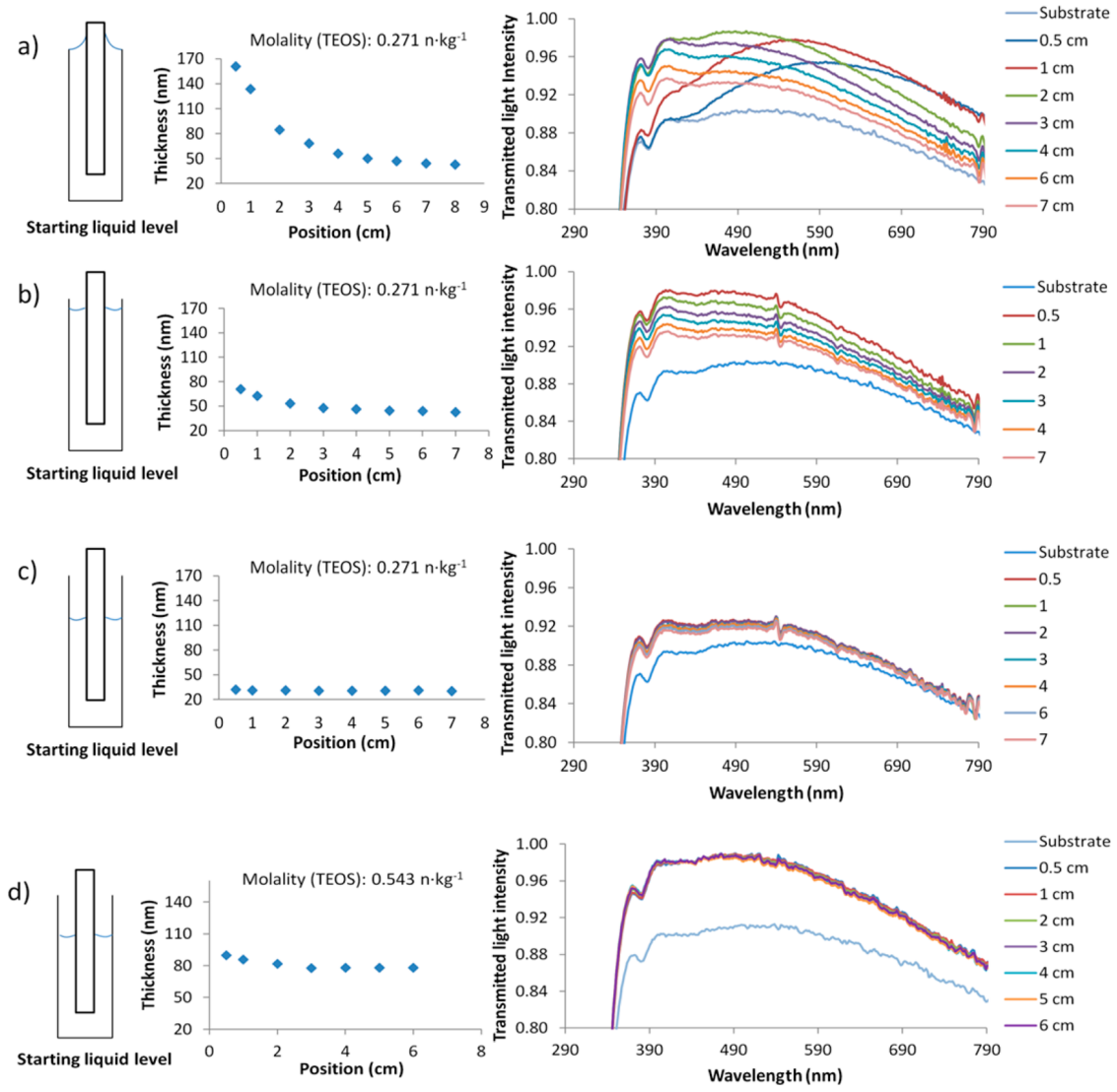

Figure III.10 – Dip-coating of an anti-reflective layer on a sodalime glass ($u = 0.3$ mm s^1). (Left) Film thickness profile obtained at different positions of the substrate. (Right) UV vis transmission spectra at similar positions of the substrates. The films are obtained by dip-coating a mesoporous silica sol gel solution (TEOS/MTEOS 0.5:0.5); (a c) Lowering the liquid level within the container leads to more uniform film deposition, but the layer becomes too thin to have good anti-reflective properties with the original solution. (d) By readapting the solution concentration and dip-coating with the meniscus inside the reservoir, we obtain quasi-homogeneous film thickness and good anti-reflective properties along the whole sample. $\Delta z = 0.5$, 2 and 2 cm for figure b, c, d respectively.

III.4 Towards controlled gradients

In the previous section, we observed the variation of the solvent relative vapor pressure in the atmosphere during the dip-coating process, verifying that it may cause a huge thickness gradient on the deposited films. We proposed some solutions to compensate it when the thickness uniformity of the layer is required. Nevertheless, considering that in some processing conditions the thickness decrease can be as important as 90%, it would be very interesting to exploit this effect to fabricate graded films with a controlled thickness profile. The huge potential of thin films exhibiting functionality gradients obtained from films thickness gradient is well illustrated in the work of Faustini et al. [172]. In this study, thickness gradients were produced by employing the dip-coating technique with increasing withdrawal speeds. However, with this procedure, the maximum thickness obtained is about two times the value of the initial thickness. In contrast, partial vapor pressure gradient can promote much larger relative thickness variations. Moreover, exploiting the effect described in this work to produce controlled thickness gradient allows preparation of graded films at a constant withdrawal speed in a very simple process that does not require elaborate dip-coating equipment.

As highlighted in equation III.4, the factor that has to be controlled is the relative solvent vapor pressure in the atmosphere P_{amb}. If one target is building a linear film thickness profile, we are facing the fact that a linear evolution of Δz caused by the substrate dragging induces at the solvent/air interface a $P_{amb}(\Delta z)$, which does not have a linear evolution inside the container. Hence, ideally, one should find a way to promote a linear solvent relative pressure within the reservoir.

A simpler method consists of playing on the ratio between the substrate volume and the solution volume V_{sample}/V_l. The goal is to maintain the total solution lowering Δz (promoted by substrate dragging) within the range in which the surrounding atmosphere is far from saturation (the first centimeter of Δz in figure III.7 experiments for example). In this Δz range, the diffusion profile of P_{amb} can be considered as a reasonable linear approximation. This could lead to the preparation of graded layers exhibiting large thickness gradient along the specimen.

We tested this method (cf. figure III.11) by varying the solvent to substrate volume ratio in order to vary the solution total lowering Δz. For a small volume ratio of 0.21, resulting in a small Δz, the deposited layer has a thickness gradient which is perfectly linear but of moderate amplitude. A too high volume ratio of 0.43 does not allow a linear thickness gradient to be obtained. With an intermediate volume ratio of 0.32 however, one obtains an almost regular thickness gradient decreasing from 74 to 16 nm on 5 cm

length. Thus, controlled thickness gradients can be obtained with a very simple constant speed dip-coating process by knowing and compensating the solvent vapor pressure variations around the meniscus. Remarkably, the thickness variation observed here (4.6-fold between smaller and larger thicknesses) is larger than that previously obtained by using an accelerating dip-coating process (2.5-fold) [169].

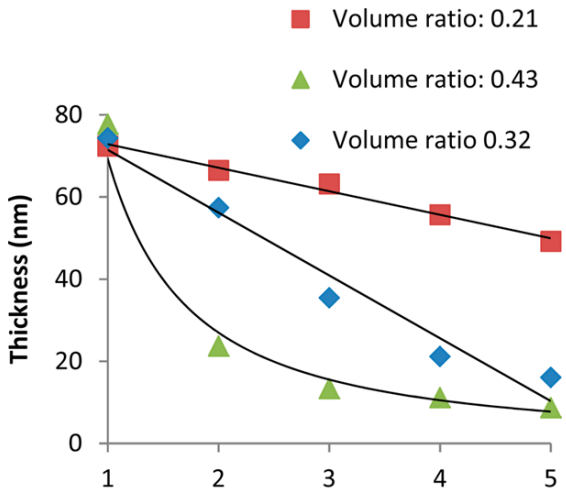

Figure III.11 – Plot of the thickness of graded mesoporous SiO_2 films for different volume ratios between the sample and the solution. The ethanol-based solution was dip-coated at a withdrawal speed of 0.1 $mm \cdot s^{-1}$. Black lines are given as guides for the eyes.

Chapter IV

Ellipsometry as a tool to study thin films dynamics in biological fluids

IV.1 Spectroscopic ellipsometry

Ellipsometry is a non-destructive measurement technique to obtain optical properties of a sample material through the reflected light waves. The technique measures a relative change in polarization and is therefore not dependent on absolute light intensity, which makes ellipsometric measurement very accurate and reproducible. An ellipsometer sends linearly polarized light at an oblique incidence on a surface, this light changes its polarization state when it is reflected, becoming elliptically polarized. In some cases the incident light can be circularly or elliptically polarized. A general scheme of ellipsometry is given in figure IV.1.

When a plane light wave is directed at a surface at oblique incidence, there is a vector which points in the direction of propagation of the light wave, called the wavevector k_{in}. This vector is contained in a plane perpendicular to the surface defined as the plane of incidence. Perpendicular to k_{in} is the E-vector for the electric field E of the light wave, which can be decomposed into two components, which are mutually perpendicular and perpendicular to k_{in}. The two components of E are parallel and perpendicular to the plane of incidence and are named p and s respectively.

When a light wave is linearly polarized it means that the p- and s-component of E oscillate with an amplitude and mutual phase causing the endpoint of E to move in a straight line in the plane of p- and s-components (see figure IV.2). When the light wave reflects off the

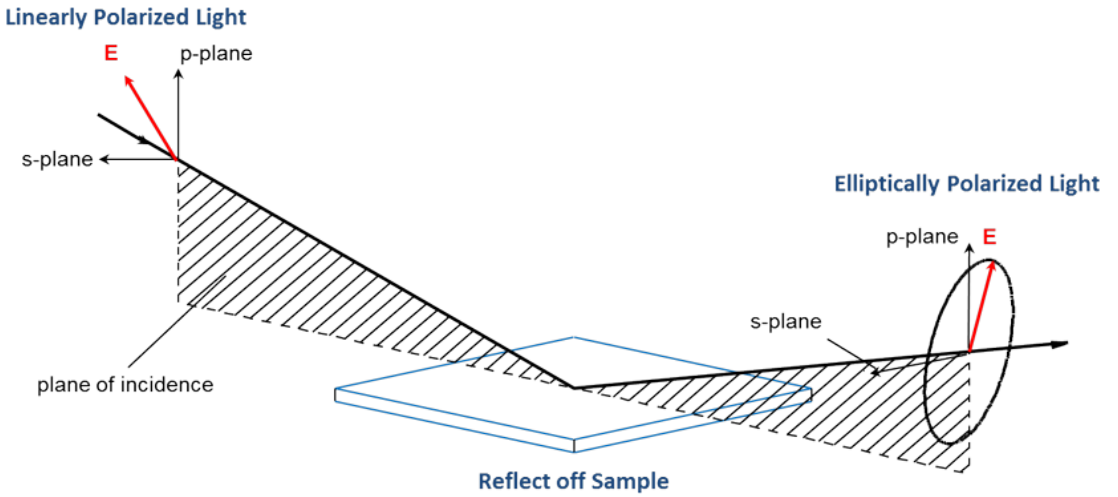

Figure IV.1 – The general principle of ellipsometry. A linearly polarized light beam is reflected by a surface, changing its state of polarization to an elliptical one.

surface, the polarization changes to elliptical polarization. This means that the amplitude and mutual phase of *p*- and *s*-component of E have been modified, causing the endpoint of E to move describing an ellipse. Elliptic polarization can be rather right-handed or left-handed, if, observing from a point towards which the wave is advancing, the vector E moves in clockwise or counter-clockwise direction, respectively.

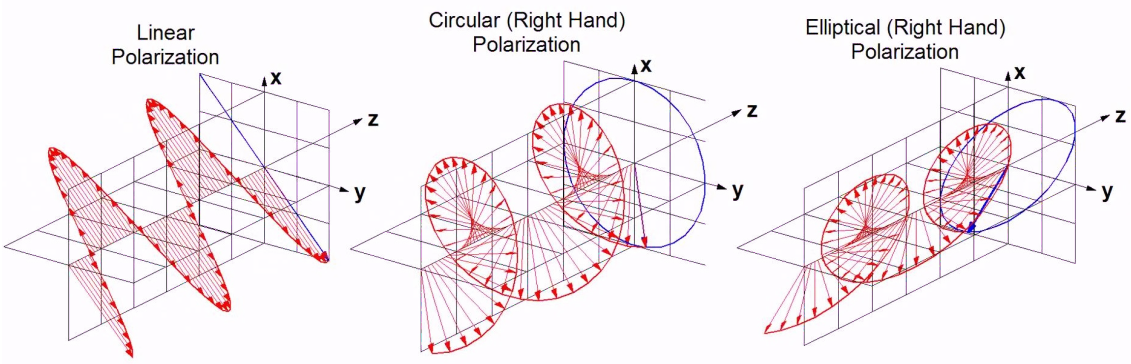

Figure IV.2 – General representation of polarized light waves: when plane light propagates along z direction, the electric field vector E (represented in red) oscillates in the plane xy, perpendicular to the wave propagation direction, describing a line (linear polarization), a circle (circular polarization) or, in the most generic case, an ellipse (elliptical polarization). In the case of an incident beam on a surface, x and y are the directions of the two components of the electric field *p* and *s*, respectively parallel and perpendicular to the plane of incidence.

Between the p- and s-components of the electric field there is a relative phase shift Δ which is $\Delta = 0$ for linearly polarized light, $\Delta = \pi/2$ for circularly polarized light and can span from 0 to 2π in elliptic polarization. In ellipsometry, the Δ phase shift of the reflected beam is directly measured. The other parameter measured by ellipsometry is the angle Ψ, which is defined to satisfy the following:

$$\tan \Psi = X/Y \tag{IV.1}$$

This is illustrated in figure IV.3.

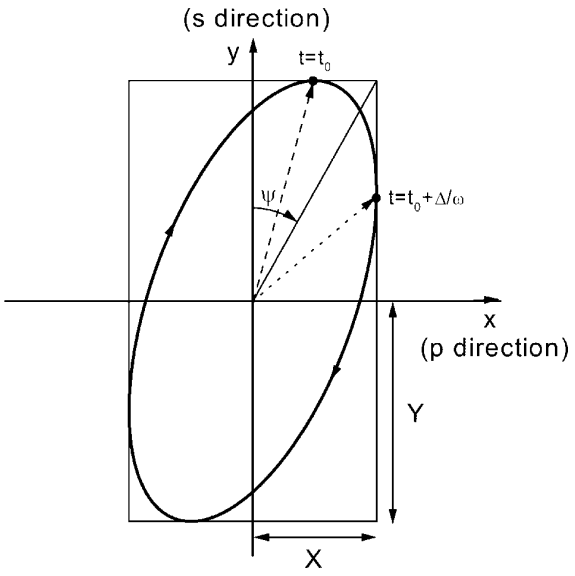

Figure IV.3 – Polarization ellipse, described by the ellipsometric angles Ψ and Δ. The polarized wave propagates on z axis, which points towards the reader.

Only relative amplitude X/Y is relevant in ellipsometric analysis, this makes the measure independent from intensity (bigger or smaller ellipse as beam spot), assuring a very precise and reproducible measurement.
The measured values Ψ and Δ are related to the ratio of Fresnel reflection coefficients R_p and R_s for p- and s- polarized light, through what is called the fundamental equation of ellipsometry IV.2:

$$\rho = \frac{R_p}{R_s} = \tan(\Psi) e^{i\Delta} \tag{IV.2}$$

The ratio of the reflection coefficients R_p and R_s is maximized at a specific angle of incidence, called Brewster's angle θ_B for which R_p is minimal. The value of this angle depends on the refractive indexes of the media in which light is traveling (n_1) and of the

material which reflects it (n_2) and can be calculated with the formula IV.3:

$$\theta_B = \arctan \frac{n_2}{n_1} \tag{IV.3}$$

Because the sensitivity of ellipsometry is higher at this particular angle of incidence, measurements are usually performed at angles close to Brewster's angle.

An ellipsometer is generally made of the following main parts:
-**The light source**, emitting unpolarized light
-**The linear polarizer**, converting the light in linearly polarized light.
-**The compensator**, not always present, which delays the two perpendicular components of the electrical vector by different amounts. This delay occurs because of the optical anisotropy of the element acting as a retarder. Basically, each of the orthogonal electric fields of the incident light experience a different refractive index and so they have different phase velocity. A compensator is a retarder element that introduces a 90° phase change. Therefore, linearly polarized light becomes circularly polarized when passes through it.
-**The analyzer**, which is a linear polarizer collecting the light beam reflected by the sample.
-**The detector**, measuring the intensity of the light passed through the analyzer.

Polarizer, compensator and analyzer can be either fixed or rotating depending on the configurations. The most employed are the rotating polarizer ellipsometer (RPE), the rotating analyzer ellipsometer (RAE) and the rotating compensator ellipsometer (RCE). Ellipsometers can be generally classified in two families: null ellipsometers and photometric ellipsometers. In null ellipsometers the components settings are adjusted to extinguish the light collected by the detector. So, polarizer and compensator are rotated to obtain linearly polarized light after reflection, extinguished by rotating the analyzer to a suitable angle. Anyway this procedure, usually performed manually, is pretty slow and not very suitable for spectroscopic studies across broad spectral ranges. Photometric ellipsometers on the contrary, measures light intensities for several properly chosen conditions, which can be rotational azimuths angles of the polarizer, compensator or analyzer or angle of incidence. The general principle behind a photometric ellipsometer is thus to measure the intensity at different analyzer (or polarizer or compensator) rotational angles, and from these measurements calculate the ellipsometric parameters Ψ and Δ. These systems don't necessarily need a retarder but they are not very sensitive when Δ approaches to 0 or π values. This issue can be solved adding a variable retarder (compensator) after the polarizer and before the sample. In this configuration any input polarization can be generated before the reflection on the sample, adjusting it to obtain a reflected beam with

Δ close to $\pi/2$ where the sensitivity of the system is maximized. Light intensity can be measured at predetermined fixed azimuthal positions or while periodically varying the azimuth angle of either or both the analyzer and polarizer with time.

IV.2 Light and materials

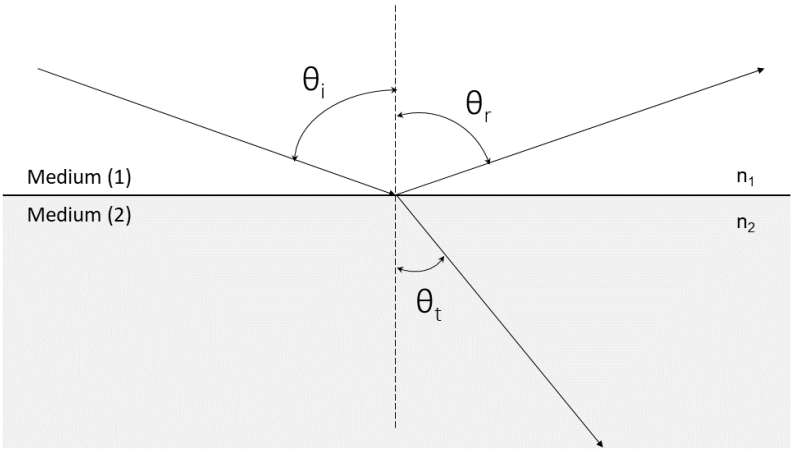

Figure IV.4 – Reflection and transmission of an incident light wave at a surface boundary between a medium (1) with refractive index n_1 and another material (2) with refractive index n_2. $\theta_i = \theta_r$.

Physical properties of materials such as refractive index and thickness can be obtained by ellipsometry on thin films. This section describes the relation between the ellipsometric function Ψ and Δ, directly measured, and the complex index of refraction $\tilde{n}_2$ of the material analyzed.

The fundamental equation of ellipsometry (eq.IV.2) contains Fresnel reflection coefficients $\widetilde{R}_p$ and $\widetilde{R}_s$ which can be given as function of refractive indexes, angle of incidence θ_i and angle of refraction θ_t. In fact, $\widetilde{R}_p$ and $\widetilde{R}_s$ are expressed as the ratio between the amplitude of the reflected electric field E_r and the amplitude of incident electric field E_i, for the p- and s- component, respectively (eq. IV.4). Using the notation employed in figure IV.4 the Fresnel coefficients for reflection are defined as follows:

$$\widetilde{R}_s = \frac{E_{rs}}{E_{is}} = \frac{\tilde{n}_1 \cos(\theta_i) - \tilde{n}_2 \cos(\theta_t)}{\tilde{n}_1 \cos(\theta_i) + \tilde{n}_2 \cos(\theta_t)}$$

$$\widetilde{R}_p = \frac{E_{rp}}{E_{ip}} = \frac{\tilde{n}_2 \cos(\theta_i) - \tilde{n}_1 \cos(\theta_t)}{\tilde{n}_2 \cos(\theta_i) + \tilde{n}_1 \cos(\theta_t)} \tag{IV.4}$$

where $\tilde{n}_1$ and $\tilde{n}_2$ are the complex refractive indexes of the media and the reflecting material, respectively. Thus, inserting the expressions for $\widetilde{R}_p$ and $\widetilde{R}_s$ in the equation IV.2 we obtain the relation between Ψ and Δ and the complex refractive index of the analyzed material $\tilde{n}_2$. The data from spectroscopic ellipsometry are values of Ψ and Δ as a function of wavelength. These data can be used to calculate the complex index of refraction as a function of wavelength, which is defined as $\tilde{n} = n - ik$ where n is the real part and k is the extinction coefficient.

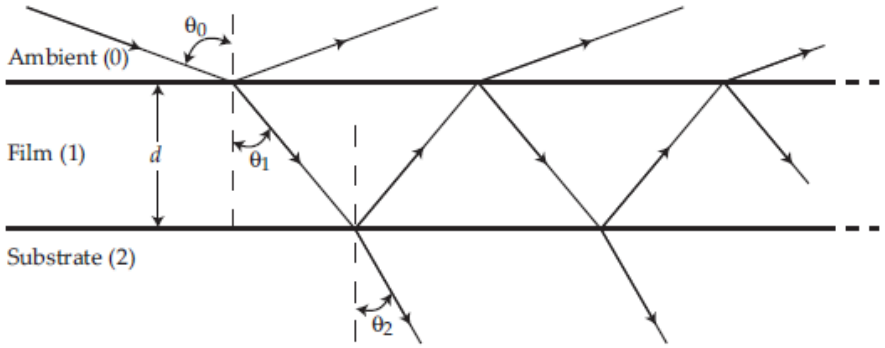

Figure IV.5 – Multiple reflected and transmitted beams for a single film on a substrate.The incident wave is partially reflected and partially transmitted at each boundary, between the ambient and the film and between the film and the substrate.

In a three phase optical system as the one represented in figure IV.5 (ambient-film-substrate structure), it is possible to determine the thickness of the thin film by ellipsometry, if the refractive indexes of the three materials are known. In fact, the incident wave is partially reflected at the first interface and partially transmitted. The transmitted wave travels through material 1 until the boundary with the substrate where it is again partially reflected through the film until the interface with ambient. At this point one wave is reflected back inside the film and one wave is transmitted in the ambient medium. Thus, in such a system there are several reflected beams with a phase difference between them which depends on the film thickness. The quantity measured in ellipsometry is in this case the ratio between the total reflection coefficients P_p and P_s, which contains the contributions of all the reflected beams and their phase difference factor β. Knowing the refractive indexes and the angle of incidence, β can be calculated and, from it, the value of thickness can be determined.

So, how do we get layer thickness and optical constants of the material analyzed from the measured ellipsometric parameters Ψ and Δ? Ellipsometry is a model-dependent

technique, meaning that a numerical analysis of the experimental data, based on mathematical models, is required to obtain the physical properties of the studied sample. The ellipsometric data as function of wavelength and angle of incidence are measured, then an optical model representing the studied system is built, with several layers, each one with its own refractive index and thickness. Some parameters of this model are adjusted such that the experimental data match the data calculated from the model as closely as possible.

The quality of the match between the data calculated from the model and the experimental data can be evaluated through the mean-squared error (MSE), which should be as close as possible to zero when the model fit well with experimental data:

$$MSE = \frac{1}{2N - M} \sum_{i=1}^{N} \left[\left(\frac{\Psi_i^{mod} - \Psi_i^{exp}}{\sigma_{\Psi,i}^{exp}} \right)^2 + \left(\frac{\Delta_i^{mod} - \Delta_i^{exp}}{\sigma_{\Delta,i}^{exp}} \right)^2 \right] \tag{IV.5}$$

where N is the number of Ψ and Δ pairs (the number of wavelengths in spectroscopic mode) and M is the number of variable parameters and σ is the standard deviation of experimental data points. To analyze data we used CompleteEASE software, where some multiplicative factors are included to the MSE formula, thus an ideal model fit should have an MSE of ≈ 1. This could be achieved on single thin films with good optical quality on Si substrate, while with more complex samples such as multilayers the MSE is usually larger and a MSE around 10 is still considered acceptable.

The refractive index of transparent films in the visible range can be modeled using the Cauchy dispersion relation:

$$n = A + \frac{B}{\lambda^2} + \frac{C}{\lambda^4} \tag{IV.6}$$

where the A parameter defines the amplitude of the material index and B and C parameters provide the shape of the index curve versus wavelength, λ values in equation IV.6 are expressed in μm. For this materials extinction coefficient k is very close to zero in the considered spectral range.

For absorbing materials other models are employed, including classical Lorentz oscillator and Drude expressions for the real and imaginary parts of the complex dielectric functions $(\tilde{\epsilon_1}, \tilde{\epsilon_2})$, or the real and imaginary parts of the complex index of refraction (n, k) [173].

Often one would like to model the optical functions of thin films using an average of two or more other sets of optical functions, because the material is a non-homogeneous mixture of other materials. It exists some theories, called effective medium approximation theories (EMA) which calculate the dielectric function for the composite film based on the

dielectric functions of two or more other materials. One of the most known and employed EMA theories has been developed by Bruggemann and for a two-component system it calculates the effective dielectric function $\tilde{\epsilon}$ from the following:

$$f_A \frac{\tilde{\epsilon}_A - \tilde{\epsilon}}{\tilde{\epsilon}_A + 2\tilde{\epsilon}} + f_B \frac{\tilde{\epsilon}_B - \tilde{\epsilon}}{\tilde{\epsilon}_A + 2\tilde{\epsilon}} \tag{IV.7}$$

being f_A and f_B the volume fraction of the two components and $\tilde{\epsilon}_A$ and $\tilde{\epsilon}_B$ their dielectric functions.

The silica films studied during this thesis were modeled through a Bruggeman-EMA layer constituted by dense silica and air or dense silica and PBS. The refractive index of the dense silica and the PBS had been previously measured and modeled through a Cauchy dispersion.

IV.3 Total Internal Reflection Ellipsometry

Several biological fluids are opaque and will not allow ellipsometric studies at a solid/liquid interface in external reflection mode. However, if the substrate is transparent the interface can be probed by internal reflection. Internal reflection setups in combination with spectroscopic ellipsometry (total internal reflection ellipsometry, TIRE) [174, 175] have been used to study protein adsorption and other biological processes *in situ* [176–178], displaying high sensitivity. The technique is similar to the most known surface plasmon resonance (SPR) in which a *p*-polarized light beam is used to excite a surface plasmon in a metal layer and reflectivity is monitored.

Surface plasmon polaritons (SPPs) are charge density oscillations caused by coherent oscillations of free electrons in the metal conduction band. SPPs are excited by an electromagnetic field at the interface between the metal layer and a dielectric layer, often through a prism coupler. The SPPs form an electric field that exponentially decays into its surrounding medium, with a penetration depth of hundreds of nanometers. This evanescent field is highly sensitive towards the refractive-index change of the surrounding environment. Thus, when the refractive index of the sensing medium changes, the incident light which excites SPR will have different characteristics (a different angle if we are looking at a fixed wavelength, or a different wavelength if we fixed the angle). In practical terms, this means that we will observe a shift in the peak of plasmon resonance, for every change in the refractive index of the medium surrounding the metal/dielectric interface.

In the most common Kretschmann configuration of SPR [179] a thin film (30-50 nm) of metal (usually Au, Ag or Cu) is deposited on the base of the prism, which provides the

conditions of total internal reflection. Alternatively, the metal layer is deposited on a glass substrate, which is put in optical contact with the prism through an index matching fluid (see figure IV.6).

A polarized light beam passes through the prism and the in-plane component k_x of its wave-vector can be varied by changing the angle of incidence (see figure IV.6).

When the angle of incidence exceeds the critical value θ_r for total internal reflection of the glass/air interface, the light is almost completely reflected (reflectivity $\approx 100\%$). The value of θ_r can be calculated from equation IV.8 for the interface between two materials with different refractive index, in which n_0 is the refractive index of the medium in which light propagates (the prism, in Kretschmann configuration). Employing a BK7 prism the θ_r value is 41° for the interface with air and 61° for the interface with water.

$$\theta_r = \arcsin \frac{n_1}{n_0} \qquad n_0 > n_1 \tag{IV.8}$$

If the in-plane wave vector k_x of incident light matches the value of the wave vector k_{sp} of electron plasmon oscillations in the metal layer, the energy of the light beam is partially transferred to surface plasmons (reflectivity drops in a sharp peak), as sketched in figure IV.6. Light beam in this special conditions excites the SPPs on the prism/metal interface but if the metal film is thin enough (less than 100 nm for visible and near-infrared light), the evanescent wave penetrates through the metal film and couples with a surface plasmon at the outer boundary (metal/air or metal/water interface).

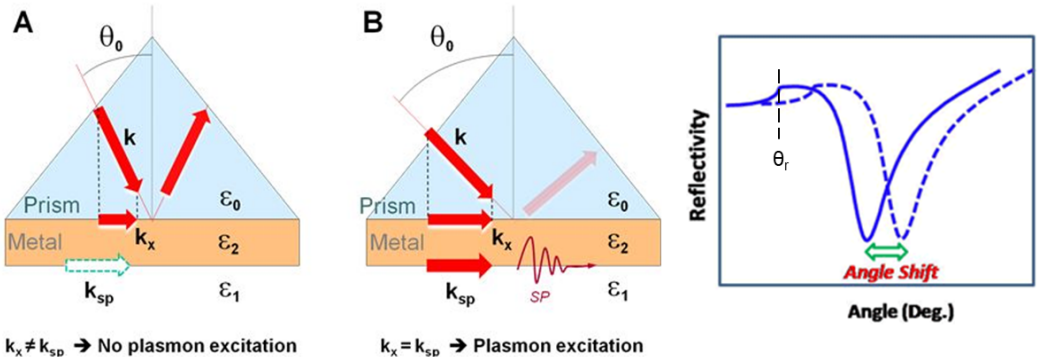

Figure IV.6 – Kretschmann configuration of surface plasmon resonance. With a monochromatic light source, SPPs can be excited when the in-plane wave vector of the incident light k_x matches the value of k_sp (B) and in this case the energy of the incident beam is partially transferred to plasmons causing a drop in reflectivity, as showed on the right. This plasmon resonance peak can shift depending on the refractive index of the surrounding medium.

When ellipsometry is performed in internal reflection mode, the ellipsometric function Ψ exhibits a peak similar to the one seen in surface plasmon resonance (SPR) experiments (figure IV.7). At the corresponding resonance conditions Δ displays a very large drop – from 10 to 20 degrees when a dielectric layer is deposed on gold and until 90° analyzing bare gold surface. This is a remarkable change when compared to the change in external reflection which at maximum is a few degrees. Conventional SPR is based on monitoring the intensity of reflected p-polarized light, while TIRE measures two parameters, Ψ and Δ carrying informations on the intensity and the phase of reflected polarized light. The two ellipsometric parameters in fact, are linked to Fresnel coefficients for p- and s-polarized light, as explained previously (equation IV.2). Several authors have pointed out that TIRE enhances sensitivity with respect to external reflection ellipsometry and also with respect to SPR technique. In fact, it has been reported that the phase function Δ (absent in SPR) is more sensitive than intensity function Ψ [175, 180].

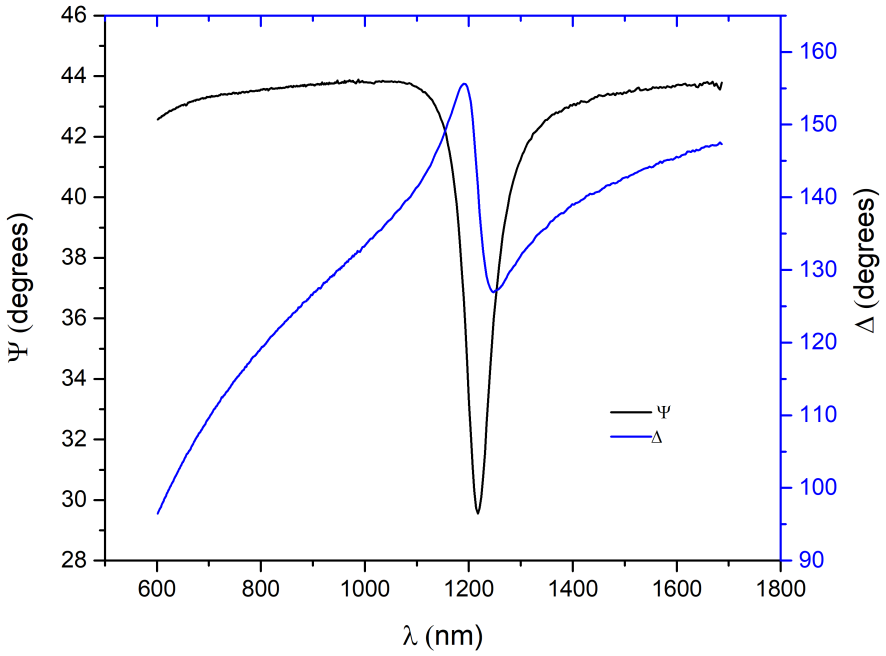

Figure IV.7 – Ellipsometric functions Ψ and Δ in TIRE technique employing a Kretschmann configuration and measuring at a fixed angle. The *Psi* function exhibits a peak at the wavelenght of surface plasmon resonance, while the *Delta* function displays a sharp drop.

IV.4 Development of TIRE setup including a microfluidic device

An experimental setup to perform TIRE requires an ellipsometer, a prism and a flow cell designed to be attached to the prism (or to the glass slide coupled with it). Employing a glass slide as a support for the metal layer is usually preferred because it avoids complicated regeneration of the metal layer for repeated use. When using metal covered glass slides, the substrate is simply replaced for each experiment.

The prism should be chosen with an opening angle assuring perpendicular incident light beam. Once settled the total internal reflection condition for the probed interface, the opening angle can be calculated. If the incident polarized light beam isn't perpendicular to the prism face, refraction phenomena will modify the incident angle on the metal layer and this angle offset needs to be considered when modeling the surface plasmon resonance position.

We decided to build a TIRE setup in which the flow cell was constituted by a microfluidic channel, to study mesoporous silica dissolution in biological, non-transparent fluids under controlled flow conditions. In the last years, coupling plasmonics with microfluidics has been indicated as a very promising path for biosensing and point-of-care diagnostics [181, 182]. The microfluidic cell allows the controlled reproduction of *in vivo* flow conditions employing small volumes of liquids, which is ideal when working with biological fluids such as blood, being the available amounts usually very limited.

We designed a setup to work at fixed angle (70°) in a spectroscopic mode, at the interface with aqueous media. We employed a BK7 triangular prism with an opening angle of 45°. This means that the incident light beam was not perpendicular to the prism face and a correction to calculate the real angle of incidence was made, because of refraction phenomena at the air/prism interface. We deposited a 50 nm gold layer on a glass slide which we coupled with the prism through an index matching liquid (Cargille BK7 matching liquid). A chromium layer of 1 nm between glass and gold was necessary to assure adhesion. The surface to probe is a sol-gel mesoporous silica layer which we deposed directly on gold through dip-coating. The setup is displayed in figure V.41 and was used with a UV-IR (193 1690 nm) variable angle spectroscopic ellipsometer (VASE) M2000DI from Woollam.

We also needed a syringe-pump to manage the flow in the microfluidic device, and a heating element (Kapton flexible heater by Omicron) to bring the system at 37 °C along with a thermocouple placed on the PDMS cell to check the temperature (showed in figure

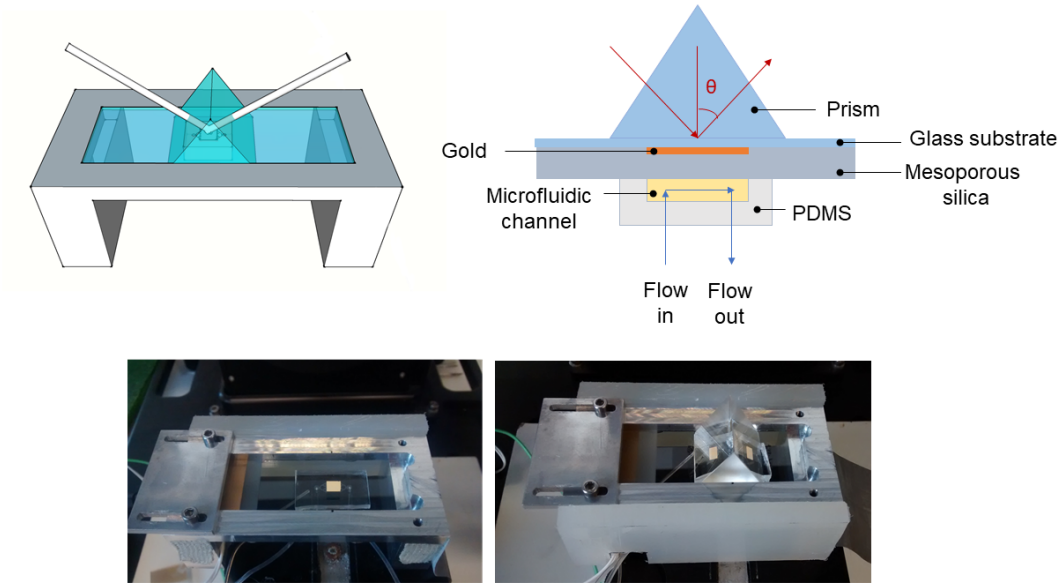

Figure IV.8 – Setup to perform total internal reflection ellipsometry under flow conditions employing a microfluidic channel. The mesoporous silica film is deposited onto a glass substrate previously covered with a gold layer, the liquid is flowed through the microfluidic cell.

IV.9). To hold the sample we built a support in aluminum, sealed with PTFE windows which had a hole for the microfluidic tubes, and the heating element connections (figure IV.9). The temperature controller displayed a stable temperature of 37 °C on the PDMS cell (figure IV.10). The complete setup mounted on the ellipsometer platform is showed in figure IV.10.

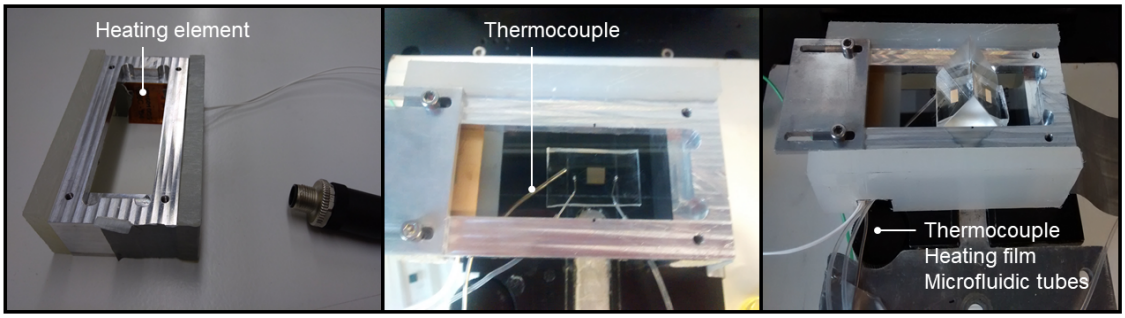

Figure IV.9 – The aluminum support for the sample is heated at the desired temperature through a heating thin film and it is sealed with PTFE windows to assure uniform temperature, which is controlled through a thermocouple on the PDMS microfluidic device. The PTFE windows had an opening to pass microfluidic and heating system connections.

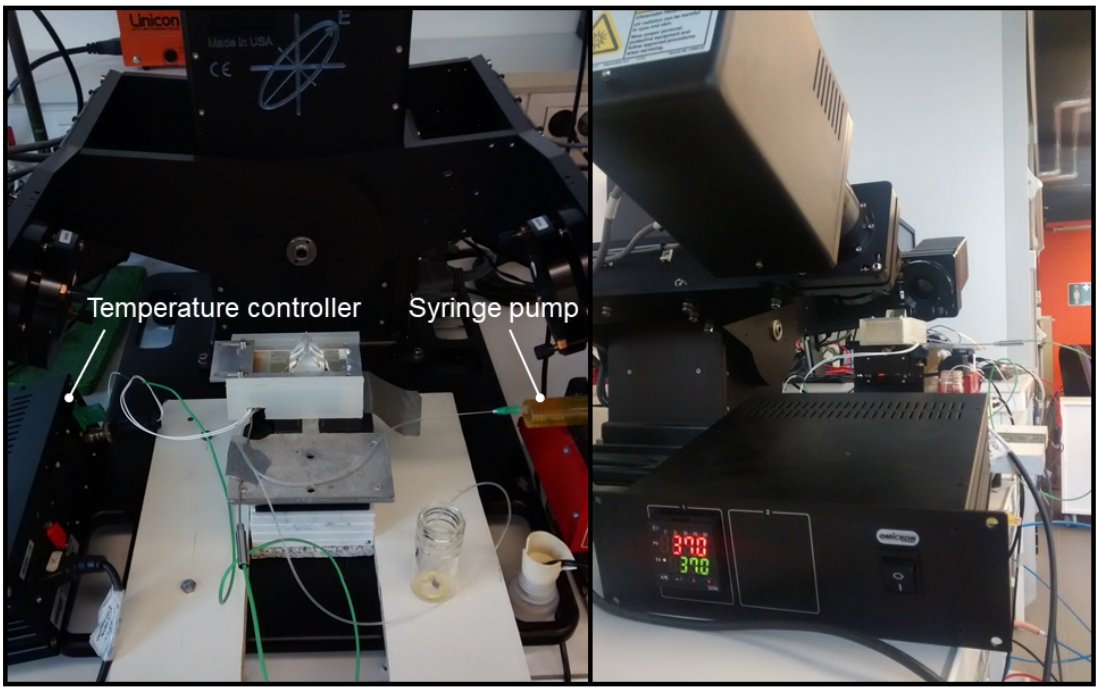

Figure IV.10 – Setup for TIRE mode mounted on the ellipsometer platform, including the syringe pump for the liquid flow control and the temperature controller.

We tried to study silica dissolution kinetics through an SPR commercial system (Bionavis, SPR Navi 210A), performing experiments in collaboration with Dr. Omar Azzaroni at Instituto de Investigaciones Fisicoquímicas Teóricas y Aplicadas (INIFTA), Universidad Nacional de La Plata – CONICET, La Plata, Argentina. Nevertheless, we faced some difficulties in studying long kinetics with media more complex than PBS. In fact, the volume of the injected fluid is limited and to have a fast flow it is necessary to re-load the loop many times. Unfortunately, every time that the loop is re-loaded, a buffer solution is flushed on the sample, removing eventually adsorbed proteins and changing the interfacial dynamics. Moreover, this system could only give kinetic informations while we wanted to model the refractive index variation of the silica layer. Thus, we came back to the more versatile TIRE technique coupled with a microfluidic channel.
Nevertheless, being a home-made system, it suffered of many problems due to a lack of calibration. In fact, nor the support for the sample, the microfluidic cell or the prism were in a fixed position and alignment should be found for every experiment. The presence of the prism induced some shifts in Ψ and Δ functions which can be corrected setting some offsets, but since the positions were not fixed, offsets needed to be defined every time. Moreover, if it happened to move the setup during the experiment (to solve a liquid

leakage for example) the offset were not valid anymore. Ψ and Δ shifts along with incident angle correction introduced many parameters to adjust when fitting experimental data with optical models. For this reason, often the refractive index evolution was difficult to model, considering that in our system nor thickness or refractive index stayed constant in time. We thus decided to analyze in priority the raw data of plasmon resonance shift to evaluate kinetics.

In order to fully exploit this kind of system it would be necessary to build a fixed, calibrated setup including prism and liquid cell, leaving layer optical constants and thickness as the only variable parameters in the measurements.

IV.4.1 Microfluidics

Microfluidics is the manipulation of liquids in channels with cross-section of 10-100 μm and has been greatly developed in recent years for many miniaturized systems for chemical, analytical and biomedical applications. Microfluidics allows the reduction of samples and reagents volumes, reducing the global fees of analysis. Because of their compact, small size microfluidic devices can integrate many following operations, shortening the time of experiment, on platforms now called *lab-on-a-chip* [183–186]. Microfluidics is particularly important in biomedical studies, in fact, microfluidic channels have sizes in the range of blood capillaries and flow patterns can approximate *in vivo* conditions [187].

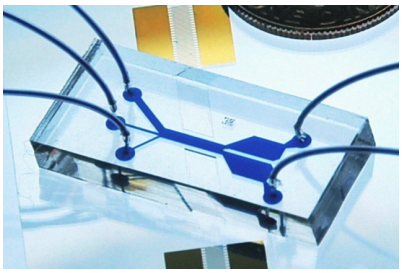

Figure IV.11 – Example of a microfluidic device in PDMS.

IV.4.2 Microfluidic cell fabrication

The simplest microfluidic device is constituted by micro-channels molded in a material that is bonded to a flat surface (such as a glass slide). Several materials, such as glass, silicon and polymers, have been employed to manufacture microfluidic devices. Conventional methods rely on etching in glass and silicon the micro-channels but fabrication of

polydimethylsiloxane (PDMS) devices by lithography and replica molding is faster and cheaper and it became the most employed technique to realize microfluidic chips.
PDMS is a biocompatible, mineral-organic polymer of the siloxane family, it is deformable and cheaper compared to glass or silicon. Moreover, it is transparent in the visible region so that micro-channels can be observed directly and their content analyzed with optical techniques. It is a linear polymer with a structure reported in figure IV.12 which can have different viscosity depending on the chain length and can be poured into a mold. PDMS can also form cross-linked elastomer materials. Typically, linear PDMS polymers containing two vinyl end groups react with a multifunctional cross-linker leading to a three-dimensional cross-linked network [188].

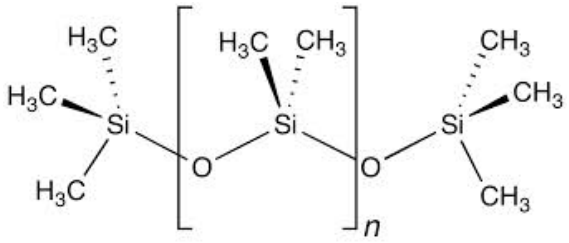

Figure IV.12 – General structure of PDMS linear polymer. Terminal groups can be substituted with hydroxyl or vinyl groups to allow further functionalization and cross-linking to obtain an elastomer.

It is often employed for microfluidic applications employing water but can't be used with some organic solvents. In fact, PDMS swells in organic solvents changing the cross-sectional area of the channel and, therefore, the rate and profile of flow [189]. Sometimes swelling can cause a detachment of the device from its substrate. For this reason, applications involving organic solvents usually employ microfluidic platforms made of glass.
The fabrication of microfluidic chips in PDMS requires several steps and starts with designing the microfluidic channels with a dedicated software (AUTOCAD, Illustrator, etc..) and then transfer the scheme on a photomask. The channels pattern is then transfered on a photo-sensible SU-8 resin, supported on Si, by photo-lithography. The thickness of the resin determines the height of the final channels. Once removed the non-cured resin, a mold is obtained from which microfluidic channels can be reproduced in PDMS many times. A scheme of the process is reported in figure IV.13. Once obtained the mold, a mixture of PDMS and cross-linking agent is poured into the mold and heated to accelerate the cross-linking reaction. Once the polymer is hardened, it can be taken off the mold and it will show a replica of the mold pattern carved in the PDMS. We employed PDMS polymer and cross-linker from Momentive (RTV 615 kit) mixing them in a ratio

of 10:1 w/w. After the mixing the material needed to be degassed under vacuum to avoid air bubbles to remain trapped in the crosslinked structure. Then we poured the PDMS mixture in the mold and cured it for one night at 60°C. When removed, we punched holes (diameter 0.75 mm) to allow the injection of fluids, being careful not to crack the polymer in any point (cracks in the drilling holes can cause liquid leaks). Our microfluidic pattern was a single channel of 4.8 x 4.8 mm and 30 μm of thickness.

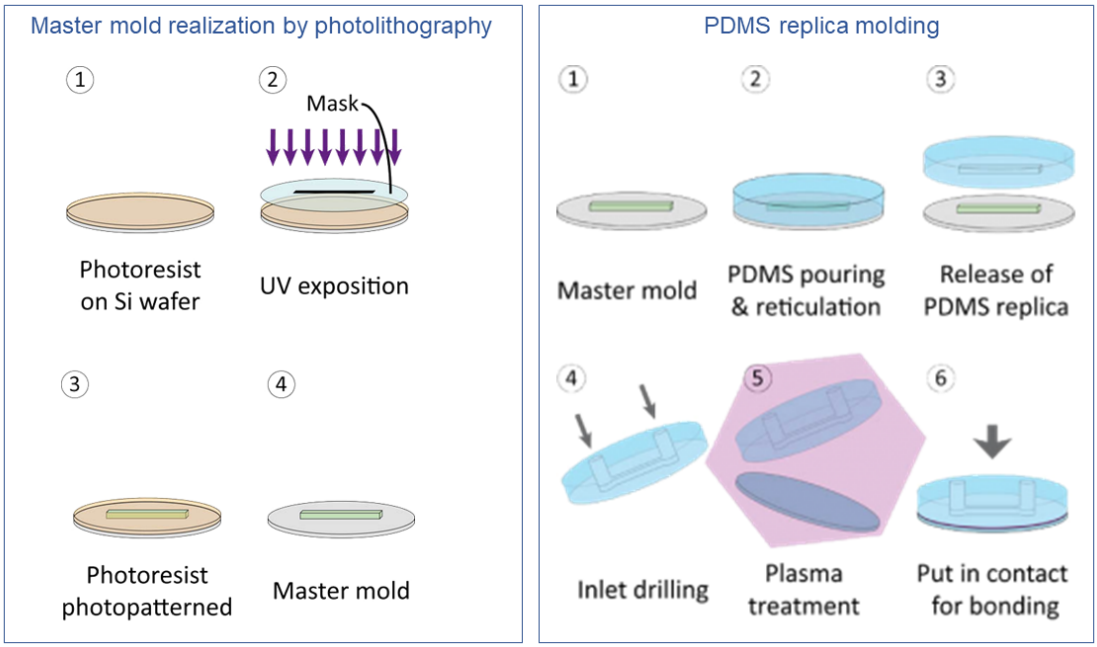

Figure IV.13 – Scheme of microfluidic chips fabrication. First, a master mold is realized in SU-8 resin supported on silicon through photo-lithography (left). Then, PDMS is poured on the master mold and crosslinked to reproduce the channel pattern of the mold. Once removed from the mold, the PDMS device is bonded with substrate through a plasma treatment.

IV.4.3 Sample fabrication

Glass slides (RS, 26x76 mm) were cleaned in water and ultrasonic bath for 5 min, then cleaned with acetone. A bonding layer of 1 nm of metallic chromium have been deposited (deposition rate 0.1 nm/s) on the glass slides by an electron-beam physical vapor deposition Plassys 550 SL, followed by a 50 nm gold layer (deposition rate 1 nm/s).
A silica sol constituted by TEOS, CTAB, H_2O in ethanol has been dip-coated on the metal layer. Silica solution has molar ratio of 1:0.14:5 for TEOS:CTAB:H_2O and 1:40 TEOS:EtOH, it is acidified by HCl 37% (0.09 molar ratio with respect to TEOS). Samples

have been dip-coated at 21°C and 30%RH and stabilized at 130°C for one night, to obtain a final thickness value around 120 nm. Silica deposited on gold can't be heated to higher temperature than 200°C, because the gold layer modifies its optical properties when heated and the optical quality of the film is compromised.
Samples were then washed with ethanol to remove CTAB surfactant from the pores (3x5min).

IV.4.4 Bonding

The PDMS microfluidic device needed to be bonded to the silica surface to allow the analysis of the latter in moving fluids. Usually both surfaces (PDMS and glass to bond) undergo a plasma treatment before the sticking, to introduce silanols on the surface, allowing a permanent bond between the PDMS device and the substrate. In our case the bonding step was more delicate because the surface to bond was also the surface to analyze and we didn't want to modify it with a plasma treatment, especially thinking about silica functionalized with organic groups. We tried to treat with plasma an hybrid silica film carrying aminopropyl moieties and just after the treatment they emanate the typical smell of amines, meaning that organic moieties had been cleaved by the plasma treatment.
Thus, we tried some mechanical pressing methods to bond the PDMS and the silica surface without plasma treatment, but this kind of method wasn't effective. We found that performing the plasma only on PDMS surface (80 s, 1000 mTorr) was enough to assure a perfect bonding when sticking on silica surface. We used an air plasma cleaner from Harrick (Expanded Plasma Cleaner PDC-001). After the sticking the samples were kept at 60 °C for 1 hour.
However, while flowing liquids through the microfluidic devices we encountered some problems. Sometimes, due to some channel blocking or air bubble, or even some blockage of the microfluidic tubes the pressure in the channels reached high values and the PDMS cell quickly detaches from the sample, making it not employable anymore. We noticed that the fragile interface wasn't the one between silica and PDMS but the one between gold and silica, as evident from figure IV.14.
The adhesion between gold and silica is not very good, and to solve this problem we added a second layer of 1 nm of chromium between the gold and the sol-gel layer. The glass substrates were then covered with Cr/Au/Cr and then dip-coated with the sol-gel silica. This didn't solve the problem, so we decided to depose the metal layers only on the center of the micro-channel (where TIRE analysis will be performed) covering the

Figure IV.14 – Picture of a PDMS microfluidic device which detached from the silica sample because of a sudden pressure jump in the channels. It can be seen that the interface which give way is the one between sol-gel silica and gold.

sample with a mask during metal deposition. In this way, metal will be where it is needed for surface plasmon resonance but PDMS will stick on silica deposited on glass, avoiding fragile interfaces. This design,displayed in figure IV.15, avoids detachment with sudden pressure peaks.

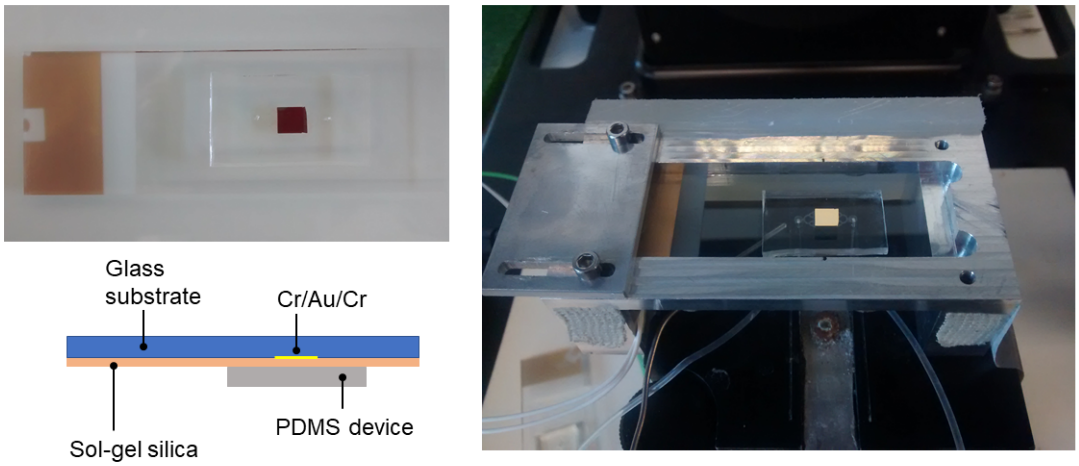

Figure IV.15 – Samples employed with TIRE technique: Cr/Au/Cr layer was deposed on a glass substrate through a mask, then the sol-gel silica layer was deposed on all the substrate and then the PDMS microfluidic device was bonded to the silica surface. The sample is analyzed from the back side, thus is mounted on the support with microfluidic cell towards the bottom, while light beam comes from the top and passes through a prism before hitting the sample. The prism will be positioned on the top of the sample while it is disposed as in the picture on the right.

IV.4.5 Oligomers release

PDMS is hydrophobic and it easily adsorbs hydrophobic molecules, which has been identified as a problem for some biological sensing applications. Moreover, it can release oligomers into the channels [190, 191]. This was a major problem for us, because PDMS oligomers contaminated the silica surface affecting the analysis. We verified that the static water contact angle on silica surface was around 15-28° before the microfluidic device bonding, while it passed to 86-90° after (figure IV.16 a,b). To check this change we bonded a microfluidic PDMS cell to the silica sample and then removed it with the help of a razor blade.

We tried to flow some ethanol and water after the sticking of the device, but solvents didn't remove the oligomers. We tried also to cure PDMS for longer times before sticking (24hours) but it wasn't effective. We deposited a surfactant layer only in the channels before bonding, making it act as a sacrificial layer on which the oligomers would adsorb. After bonding, we washed out the surfactant and the oligomers adsorbed on it flushing water in the channels. This method reduced the oligomers on the silica surface but the static contact angle still passes from 15-22° to 35°. If heated at 60°C after bonding, the surfactant started to decompose and sticked to the surface, causing contact angle to be 90° (figure IV.16 c-e).

We finally found that solvent extraction of the PDMS devices after curing removed the oligomers in an efficient way before the bonding. We used the following protocol: after curing PDMS cells one night at 60°C we swelled them in diethyl ether for 24 hours, then replace diethyl ether with toluene for 24 hours and finally replace toluene with 1-propanol for further 24 hours, changing the last solvent with fresh one after 6 and 16 hours. The passage in three solvents of decreasing swelling ability for PDMS is done to avoid cracks in the material which happen when dried too fast from a highly swollen state. The devices were then dried in oven at 70°C for 1 hour and then at 130 ° for 1 hour. Bonding on silica leaved the static contact angle unchanged as displayed in figure IV.16 f,g.

Generally, once optimized every step of fabrication, it took from 5 to 8 days to realize a complete sample.

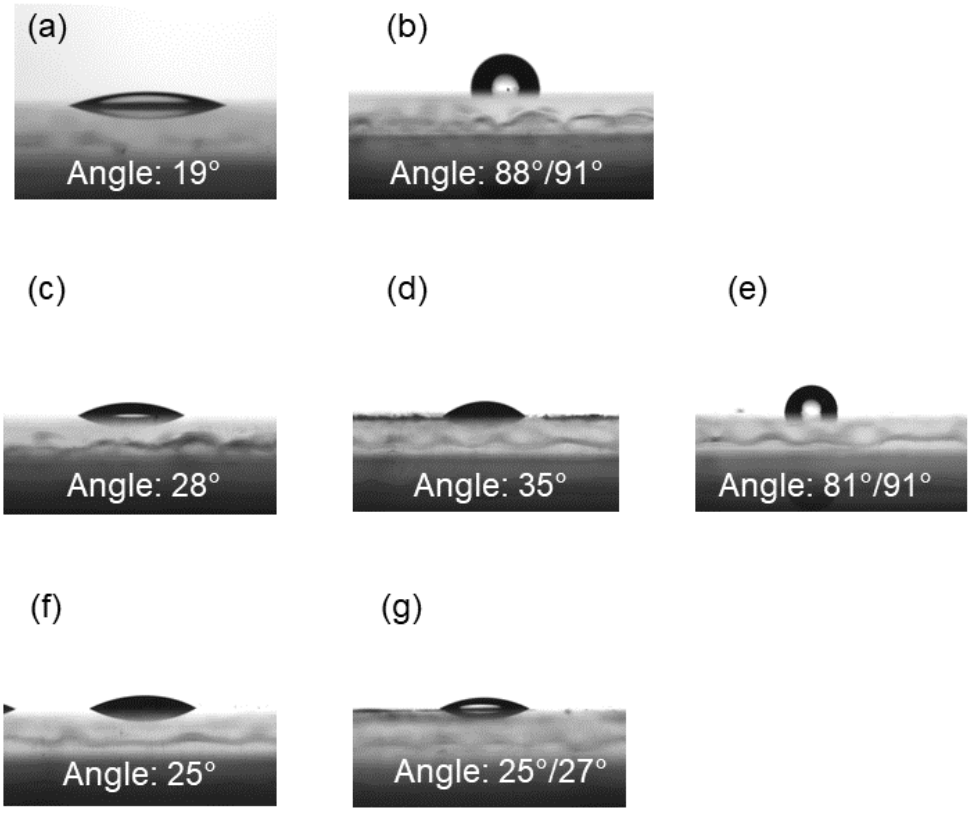

Figure IV.16 – Static contact angle of water on silica surface: (a-b) before and after bonding of PDMS device + 1 hour at 60°C; (c-e) before and after the bonding with PDMS using a sacrificial layer of surfactant, without heating (d) and with heating treatment after bonding (e); (f-g) before and after bonding with PDMS, employing solvent-extracted PDMS devices from which oligomers have been removed. The angles after bonding have been measured in the channels, after removal of the PDMS device.

IV.4.6 Setup issues

Once found a robust protocol to prepare samples, we tested the setup. The main issues encountered involved air bubbles and temperature control. In fact, the plasmon resonance for our samples was placed at a wavelength of 720-760 nm in air and it shifts at 1180-1240 nm in PBS and at 1260-1312 nm in serum. When the microfluidic channel was full of liquid, the plasmon resonance was clearly visible over 1100 nm. Its shift towards smaller wavelengths due to silica dissolution could be followed. However, if air bubbles entered in the channel the plasmon resonance lost intensity and in some cases completely disappeared because of the energy transfer to the plasmon resonance at gold/air interface (see figure IV.17). Until the air bubbles were removed, the TIRE was blind and we couldn't have

uniform kinetic data. Air bubbles were a regular issue, in particular when high flow rates required to load the syringe several times. Moreover, the hydrophobic surface of PDMS retained them, making it complicated to flush them away.

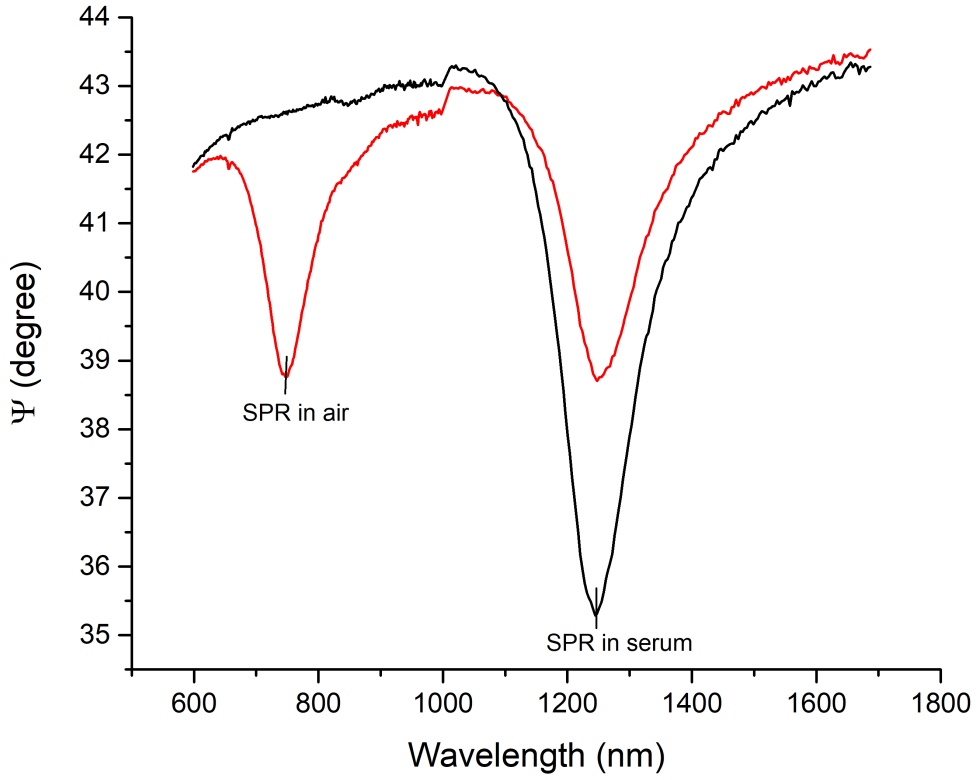

Figure IV.17 – Surface plasmon resonance of a 50 nm gold layer coated with 120 nm of mesoporous silica in serum, without air bubbles (black line) and with air bubbles in the microfluidic channel (red line). The red line shows two plasmon resonance peaks: the one corresponding to the gold/air interface (smaller wavelength) and to the gold/serum interface (bigger wavelength).

Anyway, the biggest issue of the setup was the temperature control. If heating the sample and microfluidic cell at 37°C was simple and quick, it was very difficult to maintain the temperature constant during dissolution. In fact, the liquid injected in the microfluidic device couldn't be heated up, and when it flowed in the channel, it cooled the channel down (a temperature decrease of several degrees was revealed by the thermocouple on the PDMS, the channel should be even colder). We passed the microfluidic wires in water at 40, 60 or 80 °C before entering the device but it didn't solve the problem. The heating transfer with the ambient was very efficient also because the laboratory was at a particularly low temperature when we performed the experiments (12 °C).

We solved this problem by passing the wires through a metal tube, heated to have an internal temperature of 42-44°C (depending on the flow rates). The metal tube finished just before the sample leaving a very short path between itself and the space heated at 37°C, not sufficient to cool down the fluid (figure IV.18). The temperature was measured at the exit of the microfluidic channel and was found to be 37 ±0.5°C. Unfortunately, we didn't have time to repeat the experiments with this new configuration and they are scheduled in the next months. Only the dissolution experiments in serum and blood were performed without temperature fluctuations.

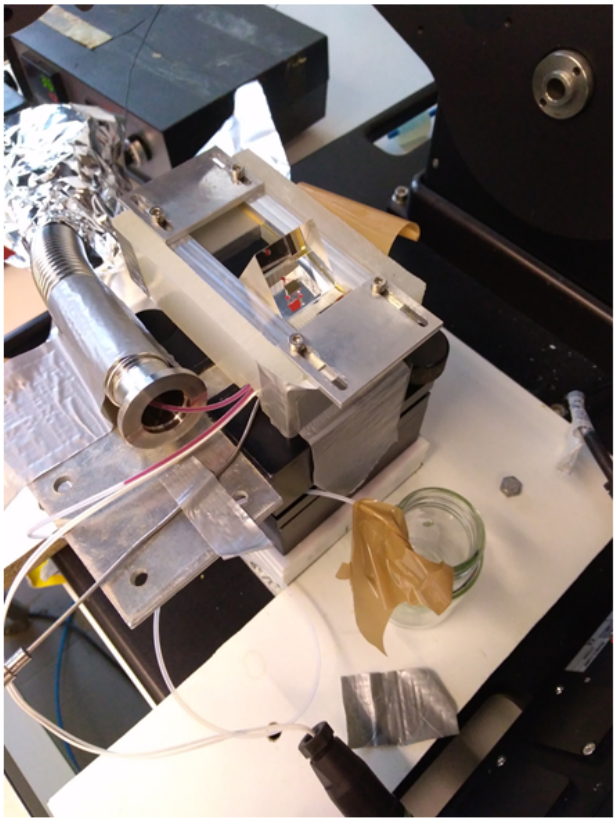

Figure IV.18 – Heating system for the microfluidic tube bringing the fluid to the PDMS device. The tube is passed inside a metal tube heated at 42-44°C from the syringe to the sample.

IV.4.7 Concluding remarks

Total internal reflection ellipsometry is a non-destructive technique very promising for *in vitro* studies of biological system. It can be performed in real time and in opaque media,

allowing analysis of real biological fluids. It has a high sensitivity due to the us of phase information in the reflected light. Nevertheless, it is technically more complex than other techniques such as SPR analysis, and it requires a very good knowledge of the sample to build the correct optical model and a very well calibrated experimental system.
Coupling TIRE with microfluidics is extremely interesting to probe *in vivo*-like dynamics and it brought important results during this thesis work, on the silica degradation dynamics under controlled flow conditions. Anyway, it added some complexity to the system, in particular regarding sample fabrication and temperature control.
An optimization of system and sample parameters should be performed for future technical developments, in order to make TIRE more competitive for biomedical applications.

Chapter V

Mesoporous silica dissolution in physiological conditions

V.1 State of the art

The last decade has seen the fast development of mesoporous silica nanoparticles as a platform for drug delivery and along with the increasing employment of these engineered nanomaterials, their toxicity on human health has become of concern. A good understanding of silica nanoparticles biodegradability is required not only for their risk assessment but also to control their drug release properties and design efficient nanocarriers. The degradation of mesoporous silica under physiological conditions has been studied *in vitro* using simulated body fluids, nevertheless results are sometimes conflicting and difficult to compare. On the other hand, *in vivo* tests are expensive and it's usually complicated to follow the dynamics taking place in this kind of experiments. Determining the key parameters which influence the dissolution kinetics of mesopourous silica nanoparticles is of high interest and could mark a decisive step towards their employ as drug delivery vectors.

This research work wants to determine the dissolution rate of mesoporous silica under physiological conditions and identify some of the factors affecting silica behavior in biological media. The conducted study leads to results which, if they can't be directly extrapolated towards *in vivo* conditions, can anyway provide useful informations about trends and can be used to design *in vivo* tests.

Silica is not chemically stable in water media, it undergoes hydrolysis forming silicic acid, the breaking of Si-O bonds being the rate-limiting step of the reaction. Anyway its solubility strongly depends on its structure, surface area and on the properties of surrounding

media. The stability of mesoporous silica particles and films has been tested in several simulated body fluids and physiological buffers [98, 117, 119, 192–194] finding dissolution rates going from several hours to several days depending on experiment conditions and silica structure.

Thermal treatments can increase silica stability in aqueous media, as reported by Bass et al. [195] and modifying the inorganic network introducing heteroatoms such as Zr or Al, also results in an effective way to increase silica hydrolytic stability [98, 195]. The bulk composition influences dissolution kinetics and so does the material structure, since the Si-O bond length and energy vary in different silica materials causing hydrolysis to happen at different rates [196].

Moreover, the structural organization of silica at a small scale can influence its surface reactivity, as discovered by Zhang et al. [123] and, consequently, its dissolution rate. This can explain some of the conflicting data found in literature about silica dissolution, in fact different methods of synthesis can produce silicas with different bulk structures (e.g. presence or absence of strained cyclic species or predominance of highly connected species [197]), which don't react with the same kinetics.

The surrounding medium characteristics determine dissolution as well, in particular pH is known to be an important parameter to tune silica solubility, which starts to increase abruptly above pH 9 [198]. Moreover, if silica is grafted with polymers or ligands, or presents adsorbed molecules on the surface, its dissolution kinetics is altered.

This is the reason why dissolution behavior can be significantly different in different media, for example He et al. showed that in presence of Ca and Mg ions, calcium/magnesium silicates are formed at the silica surface, protecting underneath silica from further dissolution [117]. Icenhower showed that the presence of NaCl in solution can increase dissolution rates up to a factor of 20x [196]. In the case of particles, another factor that has to be considered is aggregation, which reduces the exposed surface area, slowing down dissolution.

The driving force of dissolution is the undersaturation in silicon species of the medium in contact with the surface: when silicic acid saturation is reached, silica can randomly nucleate and precipitate, getting to an equilibrium in which silica dissolution and precipitation happen at the same rate and hindering the complete dissolution of solid silica particles. In porous materials this behavior can lead to pores occlusion due to precipitation, further inhibiting dissolution by reduction of accessible reactive surface [199]. The presence of ions or molecules able to form soluble complexes with the released ions alters the saturation level, enhancing dissolution.

The saturation level of biodegraded silicon species is a very important issue and causes some problems in evaluating dissolution rates: in fact, depending on the experiment conditions, an equilibrium of dissolution-precipitation can be reached more or less quickly, blocking dissolution. This leads to easy misunderstanding on the degradation of mesoporous silica in biological environments, since some works reported hour-scale dissolution while other studies showed stability over many days. As pointed out by He et al. [117] and also verified during this thesis work, in a undersaturated medium mesoporous silica is degraded within few hours. Nevertheless, in previous literature reports, degradation is investigated with a silica concentration between 0.2 and 1 mg/mL (or even higher), conditions for which the saturation limit is reached soon or later, while monitoring silica concentrations below 0.1 mg/mL leads to complete dissolution within few hours. This hour-scale degradation is observed in all the studies conducted on mesoporous silica thin films [98, 195, 200], where the small amount of matter involved avoids silica saturation in the medium, the same kinetics have also been observed during the studies which will be presented here, carried out on mesoporous silica thin films.

V.2 Dissolution of mesoporous silica thin films

The main goal of this work is to investigate mesoporous silica dissolution *in situ* under physiological relevant conditions. Because the biological fluids are complex media, to have a reference in simplest conditions the first experiments have been performed in a phosphate buffered saline solution (PBS) containing 0.01 M phosphate buffer, 0.0027 M potassium chloride and 0.137 M sodium chloride, at 37 °C and pH=7.4. Amorphous silica solubility can reach 145 mg/L at 37 °C in pure water, according to the equation V.1, elaborated by Fournier and Rowe [201] and valid between 0 and 250 °C:

$$\log C = -\frac{731}{T} + 4.52 \tag{V.1}$$

where C is silica concentration in mg/L and T is temperature in Kelvin. This value can be alterated by the presence of salts in solution and by the variations of pH, but can be a good starting point to settle the saturation value and design the experiments conditions accordingly.

As previously pointed out, silica saturation in solution stops dissolution and, if it is interesting to understand the behavior of silica material in saturated conditions, it is also necessary to assess the silica dissolution kinetics in a non-saturated media. In fact, concerning biomedical applications, silica nanoparticles can be confined in small compart-

ments such as cells and vesicles, where high local silica concentration in the surrounding media can be attended, finding themselves in a saturated environment. On the other hand, before being uptaken, nanoparticles travel in the blood stream and undergo degradation in an undersaturated media. This first stage of their permanence in the body is crucial, because they need to reach their target intact, delivering encapsulated drugs where is needed and not releasing them previously, in an uncontrolled process.

Thus, we decide to perform our experiments in non-saturated conditions, working on thin mesoporous silica films of 100-120 nm thickness, looking more deeply into the dynamics involved during dissolution in this regime. We analyzed the film degradation in PBS solution at 37 °C in a liquid cell of 5 mL volume, in static condition or with a weak flow. In any case, we are far below the saturation limit calculated from eq. V.1, being the silica mass involved in every experiment around 0.015 mg/mL.

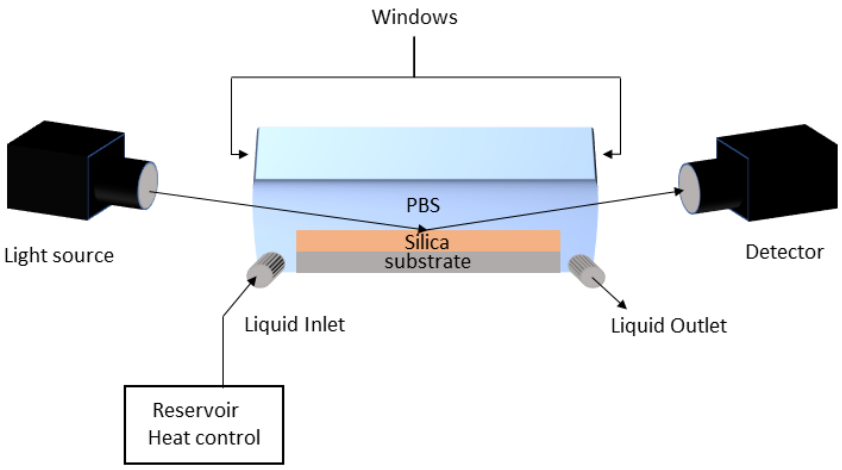

Figure V.1 – Schematic representation of experimental setup to investigate mesoporous silica thin film dissolution in PBS, through ellipsometric *in situ* measurement. Both the liquid cell and the liquid reservoir are kept to a constant temperature of 37 °C during analysis.

Thin layers of mesoporous silica were obtained by dip-coating at u= 2mm $\cdot$ s^{-1}, 26 °C and 30% RH from sols whose compositions are given in table V.1. Tetraethyl orthosilicate (TEOS) was used as precursor and hexadecyltrimethylammonium bromide (CTAB) and Pluronic F127 as templating agents. Sols have been stirred at room temperature for 72 h before use. After deposition the films were stabilized 1 night at 130 °C and, in the case of F450 and CT450, further calcined at 450 °C for 15 minutes. In films stabilized at 130 °C the templating surfactant was removed by cold extraction in ethanol. As reported in

section II.5.3 the silica films templated with CTAB have a Pm3n cubic mesostructure, while the films templated with Pluronic F-127 showed a p6m 2D-hexagonal structure V.2. Their porous volume, specific surface area and pore sizes distribution have been obtained through Environmental Ellipsometric Porosimetry (EEP) and are reported in table V.2. From GI-SAXS experiments we obtained the cell parameters of both materials and, comparing them with pore sizes acquired trough EEP, we calculated the silica wall thickness w_t.

Table V.1 – Composition of mesoporous silica sols (molar ratios).

Molar ratio	TEOS	Ethanol	HCl	H_2O	F127	CTAB
CT SiO_2	1	40	0.09	5	-	0.14
F SiO_2	1	40	0.09	5	0.005	-

Table V.2 – Structure parameters such as semi-major axis (r_l) and semi-minor axis (r_s) of the elliptical pores, thickness of silica walls w_t, specific surface area and porous volume for the investigated silica mesostructured films.

sample	r_l (nm)	r_s (nm)	w_t (nm)	S (m^2/cm^3)	V_p (%)	Structure	Surfactant
CT130	1.61	1.55	1.2	700	0.455	Pm3n	CTAB
CT450	1.63	1.44	1.0	750	0.510	Pm3n	CTAB
CT450				800	0.562	wormlike	CTAB
CT450	1.62	1.44	1.1	850	0.620	Pm3n	CTAB
F450	2.91	1.98	5.7	370	0.554	p6m	Pluronic F-127

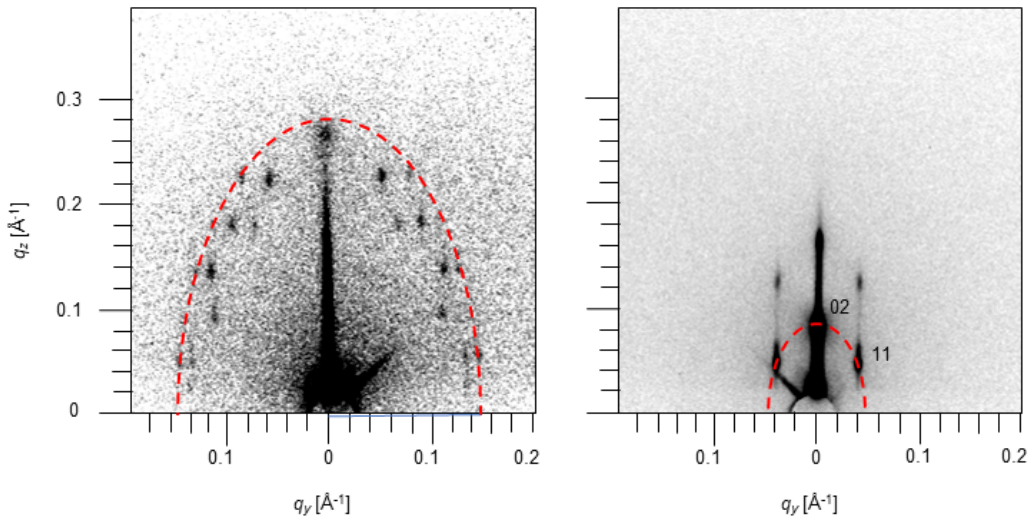

Figure V.2 – GI-SAXS pattern of the CTAB templated (left) and Pluronic F-127 templated (right) silica films, showing peaks of Pm3n cubic structure (left) and (11) and (02) peaks of the 2D-hexagonal structure (right).

V.3 Dissolution in PBS

Monitoring the refractive index of mesoporous silica thin films during dissolution we observe a linear decrease which ends up on a plateau approaching the medium refractive index, as reported in figure V.3. In fact, silica refractive index is higher than PBS one, and the optical properties of the porous layer are proportional to its PBS content (which is equal to the porous volume of the film in air) following equation V.2. Thus, during dissolution porous volume is increased and refractive index diminishes progressively (see figure V.3).

Thermal treatment doesn't influence much the dissolution kinetics, as can be seen comparing the data of CT450 and CT130, films obtained from the same sol and thermally treated at 450 °C and 130 °C, respectively. The dissolution of silica calcined at 450 °C is slightly slower than the one of silica stabilized at 130 °C, very probably because highest temperatures allow for further silica condensation, building a more cross-linked network, as already reported by Bass et al. [195] in previous studies. Anyway the high temperature treatment doesn't seems to improve silica stability towards hydrolysis to a great extent.

The film thickness remains constant at early times while refractive index decreases, con-

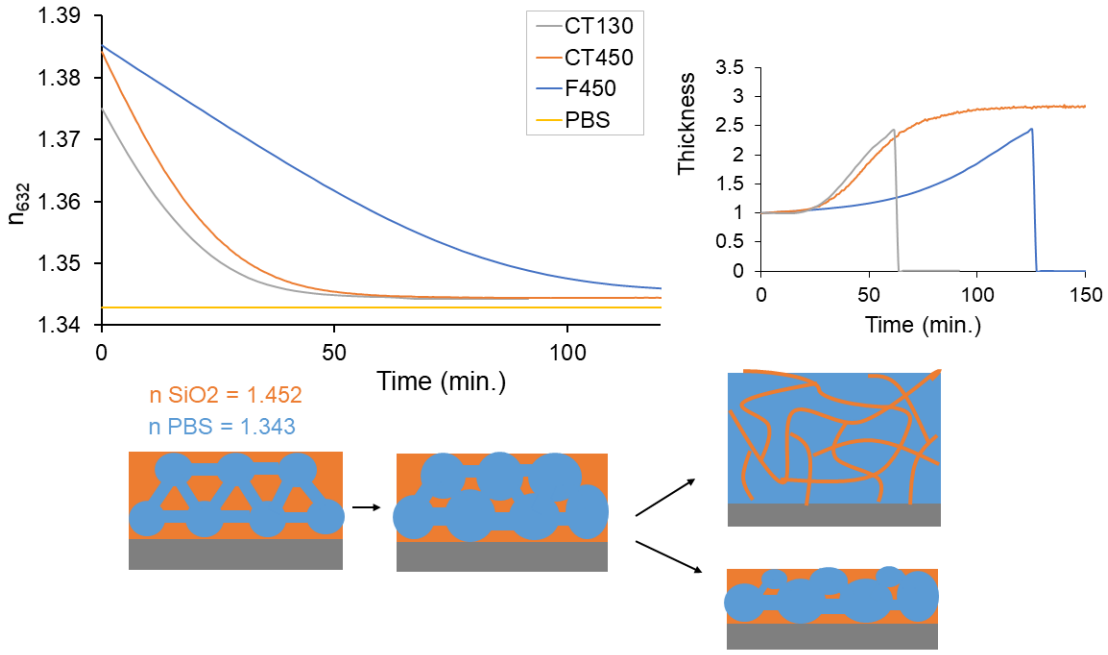

Figure V.3 – Refractive index and thickness variation during dissolution in PBS at 37 °C, static conditions. In yellow is reported the refractive index value of PBS in the same conditions, previously measured. Thickness is normalized on the thickness value at t=0. In early times dissolution enlarge the pores while thickness remains constant, causing a decrease in the refractive index of the mesoporous layer. Two mechanisms are possible for the advanced stages of dissolution: either thickness starts to diminish homogeneously or a highly swollen silica gel is formed and later degraded. The data seemed to confirm the latter hypothesis, showing a remarkable thickness increase.

firming the mechanism in which dissolution starts in the pores, leading to a progressive increase of pore volume in a so-called bulk dissolution mechanism [98, 195]. Refractive index of the silica layer reaches the value of PBS after only 50 minutes in the case of CTAB-templated silica, meaning that almost all its volume is replaced by PBS. In the case of F-127 templated silica this point is reached after 100 minutes, doubling the dissolution time.

At the moment in which the refractive index of the silica layer matches the one of the medium, the ellipsometer showed limitations in measuring layer thickness accurately, finding a huge swelling as the best fitting solution. We can't verify the in-situ thickness with independent experiments, so it is not possible to know if at a certain value of porous volume the silica layer becomes an highly swollen gel of if it is just an artifact due to the very small optical contrast between the mesoporous film and the surrounding medium. The formation of a porous gel layer at the surface is possible and it has been proved in

the case of dissolution of nuclear glass [202, 203], anyway the material and the conditions of dissolution in the latter case are pretty different from ours, thus the material behavior could differ sensibly. When retired from liquid media, samples showed no visible silica layer and by ellipsometry we measured a residual layer of 1-5 nm. We can thus assume that mesoporous silica dissolution is complete in these conditions and saturation of the liquid medium is never reached, as expected.

The volume fraction of silica in each film was calculated from ellipsometric data using a Bruggeman effective medium approximation, considering the layer optical constants as a two-phase mix of the optical constants of silica walls and optical constants of PBS.
Bruggemann effective medium approximation (BEMA) model allows determining the relative volumetric fractions f_a and f_b of two materials A and B of known dielectric constants ε_a and ε_b within a volume unit of measured dielectric constant ε (eq. V.2). In our case ε is the dielectric constant of the porous film, measured by ellipsometry, ε_a and ε_b are the dielectric constants of PBS and dense silica, respectively. Both the optical properties of silica and PBS have been measured previously by spectroscopic ellipsometry (the ones of silica have been evaluated on a dense film of similar composition). Thus the volumetric fraction of PBS (f_a) and silica (f_b) can be obtained by fitting the experimental data. Remaining silica mass was calculated from the silica volumetric fraction and the thickness of the film, assuming the walls as chemically homogeneous with a density of 2.2 $g \cdot cm^{-2}$, usually accepted for amorphous silica.

$$f_a \frac{\varepsilon_a - \varepsilon}{\varepsilon_a + 2\varepsilon} + (f_b) \frac{\varepsilon_b - \varepsilon}{\varepsilon_b + 2\varepsilon} = 0 \qquad f_a + f_b = 1 \tag{V.2}$$

V.3.1 The Noyes-Whitney model of dissolution

The evolution of the dissolved silica amount versus time is reported in figure V.4. We observed that more than 85% of silica was dissolved in the first 40 minutes for some films and in about 2 hours for more stable materials. From figure V.4 we can also notice that films templated with pluronic F127 dissolve slower than films templated with CTAB, suggesting that porous volume and surface area play an important role in dissolution kinetics. To address this aspect deeply we investigated samples presenting different structure, surface area and porous volume. In fact, dissolution is proportional to the surface area exposed to the solvent, according to Brunner modification of the Noyes-Whitney equation, which describes the dissolution of a solid in a liquid:

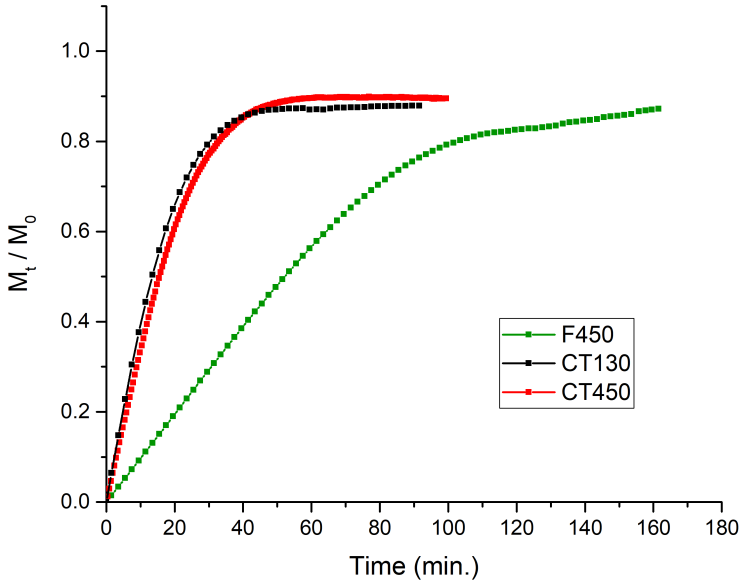

Figure V.4 – Dissolved silica mass normalized on initial silica mass (M_t/M_0) during dissolution in PBS at 37 °C.

$$\frac{dC}{dt} = kS(C_s - C)$$
$$with\ k = \frac{D}{Vh} \tag{V.3}$$

where the concentration of the dissolved species in solution C follows a first order kinetics, being S the surface area of the solid, C_s the solubility at equilibrium and k a constant factor gathering the diffusion coefficient of the dissolved species D, the volume of the solution V and the width of the diffusion layer h. Practically, dissolution is driven by the concentration gradient between the surface of the solid material (where C is assumed equal to C_s) and concentration in the bulk solution, with a rate which depends on the exposed surface. The concentration gradient is controlled by the diffusion process between the surface and the bulk solution, which, in this model, is the rate limiting step.
After integration, eq. V.3 gives the value of concentration at any given time $t \geq 0$:

$$C(t) = C_s(1 - e^{-Kt}) \tag{V.4}$$

where $K = kS$ and from which we can develop the expression for the amount of dissolved silica M_t, normalized on initial silica mass M_0:

$$\frac{M_t}{M_0} = \frac{C_s V}{M_0}(1 - e^{-Kt}) \tag{V.5}$$

Anyway, it has to be pointed out that equation V.3 is derived from Fick's laws assuming special boundary conditions: the solution concentration in the bulk is assumed to be zero (perfect sink condition) at t=0, and the surface and the diffusion coefficient are considered constant with time. This model assumes that saturation is rapidly achieved at the solid-liquid interface and then diffusion takes place across a layer of stagnant solution, called diffusion layer, towards the bulk solution. This concept of a stagnant diffusion layer is not perfectly realistic but it allows easier calculations [204], in reality the boundaries of the diffusion layer are not sharp and it exists a region where concentration decreases gently towards the bulk one (see figure V.5).

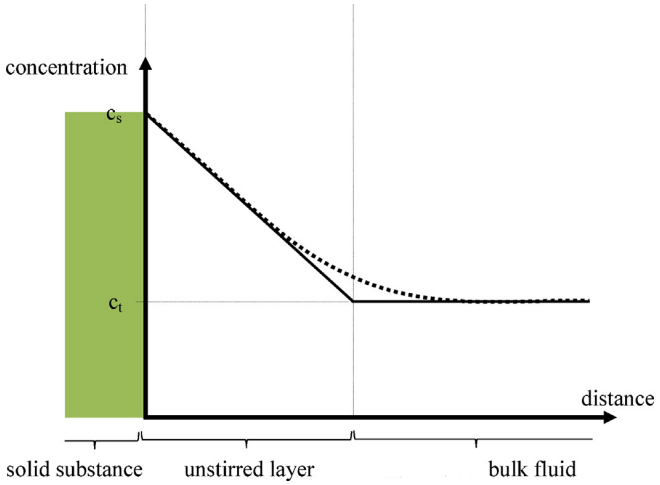

Figure V.5 – Scheme showing the model concentration–distance-profile through the unstirred liquid boundary layer surrounding a solid substance, which dissolves in its own solution, by Nernst-Brunner. The theoretical trend is represented by the solid line, while the dotted curve represents a more realistic trend in which concentration decreases less abruptly towards the bulk value, through a zone in which convection gains more and more importance on diffusion as transport mechanism.

In our system dissolution happens fast, following Noyes-Whitney kinetics, nevertheless, the boundary conditions of this model are not valid in our conditions. Indeed, in our system we will never reach saturation, while the Noyes-Whitney model assumes that the dissolving solid constitutes an amount of material equal or greater than the saturation limit. Thus, it is reasonable to think that the silica dissolution kinetics will follow equation V.3 as long as the amount of solid material will be enough to sustain the kinetics.

Moreover, mesoporous films surface area evolves with time due to the bulk dissolution of the material and D may not be considered constant. In fact, inside the porous network, diffusion is limited by the accessible volume and its tortuosity, which means that a diffusing molecule in a porous solid will have a diffusion coefficient $D_{eff} \leq D$, where D is the diffusion coefficient in the selected medium when diffusion is not hindered. A model for molecular diffusion in porous matrices was developed by Higuchi in 1963 [205] for drug release devices, where D_{eff} is defined as follows:

$$D_{eff} = \frac{\epsilon}{\tau} D \tag{V.6}$$

where ϵ is the porous volume of the solid and τ is the tortuosity of the porous network. Higuchi assumed tortuosity and porosity to stay constant, because he developed his model for porous matrices which don't evolve with time. This may not occur when the porous solid undergoes bulk degradation. In fact during the dissolution/erosion of the matrix the porous volume increases and the morphology of the pores changes, along with their surface curvature and the number of open connections with contiguous pores, until it reaches a configuration in which the channels can be considered completely interconnected. It is very difficult to follow the evolution of the tortuosity factor τ but it is reasonable to assume that it is decreasing during dissolution. At the same time the porous volume ϵ increases continuously, and we can follow its trend fitting the ellipsometric data with a Bruggerman-EMA model.

The differences between conditions of our experiments and the Noyes-Whitney dissolution model mean that mesoporous silica layer dissolutions can deviate from Noyes-Whitney kinetics.

If we fit the silica concentration data with the corresponding equation V.4, we can see a good agreement between the model and the experimental data in the first part of the experiments, while after the 50% of silica is dissolved, the kinetics of release starts to slow down (figure V.6). Considering the first half of the dissolution experiments and a value of $C_s = 145$ μg/mL, we found $K = 2.5 \cdot 10^{-3}$ s^{-1} for CT450, $K = 2.78 \cdot 10^{-3}$ s^{-1} for CT130 and $K = 9.6 \cdot 10^{-4}$ s^{-1} for F450.

Because of the difference in boundary conditions between our systems and the theoretical model, the description of the constant K needs some further considerations. We know that K gathers the surface factor S and the coefficient of diffusion D, which are treated as constants in the model but in our system this assumption may not be true. In fact, surface is evolving with time during dissolution, and towards the end its value will surely drop. Concerning the diffusion coefficient D we don't know if the porous network limits

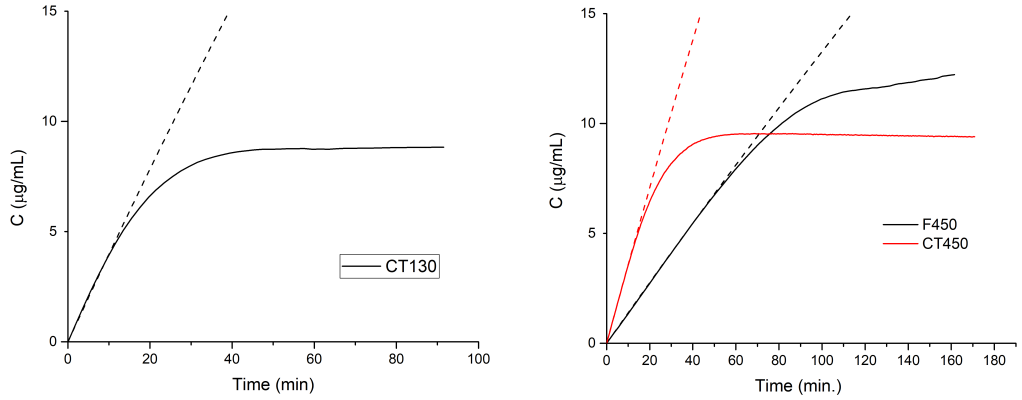

(a) (b)

Figure V.6 – Silica concentration growth during dissolution process is reported for mesoporous silica films templated with CTAB (CT130 and CT450) and with Pluronic F-127 (F450). The three samples have equivalent porous volume (61-62%). Dashed lines are the theoretical trends according to equation V.4.

the diffusion causing D_{eff} to be smaller than D or if it is permeable enough to consider $D_{eff} \approx D$. If the diffusion is limited at the beginning, D_{eff} will increase gradually during dissolution (because porosity ϵ will increase and network tortuosity τ will decrease) until it will reach the value of D. Thus there will be 3 scenarios for K evolution during dissolution, summarized in figure V.7:

1- S stays constant at the beginning and starts to diminish in advanced phases of dissolution, D stays constant throughout the process. Thus, K is directly proportional to the exposed surface and it will decrease in the last part of the dissolution experiments, shaping an inverse exponential release curve.

2- S stays constant at the beginning and then increases, due to the modified morphology of the porous network after the initial stages of dissolution, towards the end of dissolution it decreases. D stays constant. Another scenario could consider S constant in the first part of dissolution and D_{eff} increasing due to an evolution of the porous network towards a more open and interconnected system. In both these cases, K increases after the first phases of dissolution (due to an increase of S or of D_{eff}, or both) and decreases in the end, due to a decrease of the surface involved, shaping a sigmoid release curve.

3- D_{eff} increases and S decreases but they compensate each other, giving a K which stays constant for the majority of dissolution process, before slowing down at the end, when surface factor S drops. In this case the release plot is linear and the concentration

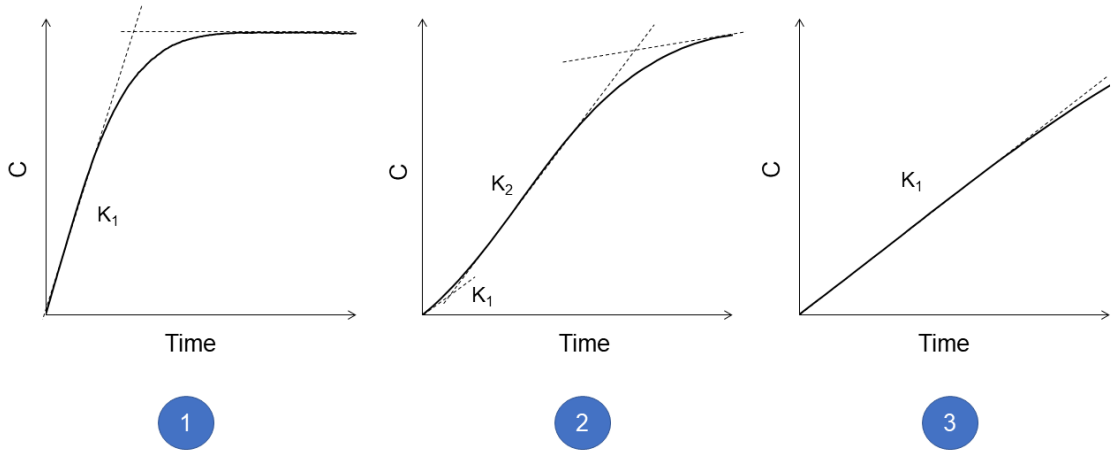

Figure V.7 – Possible scenarios of silica release considering the evolution of surface and diffusion coefficient with time. 1- Diffusion is never hindered and D is constant throughout the process. Surface stays constant for the first 50% of dissolution, then starts to diminish. 2- Reactive surface or D (or both) increase shortly after the beginning and decrease towards the end of dissolution. 3- Changes of S and D compensate and dissolution happens at a constant rate. In any case, towards the end, when almost all silica is dissolved, surface value drops and so does the rate of dissolution. The release curve always ends on a plateau when silica concentration reached its maximum value.

in solution increases at a constant rate until it reaches a plateau when all the silica is dissolved.

Influence of the mesostructure

Surface area and porous volume, which are interconnected, are crucial parameters to tune the rate of dissolution. The structure of the porous network can play a role, but if the values of porosity and surface area are similar, the difference in dissolution rate are very small as showed in figure V.8 for two similar silica layer templated with CTAB, one having a Pm3n cubic mesostructure and the other having a disordered wormlike porous network. The CTAB-templated silica presenting a Pm3n structure (sample CT450-1) dissolves at the very same rate than the wormlike structure (sample CT450-3) for more than 70% of the dissolution process (for similar values of V_p and S). Towards the end of the dissolution process the wormlike structure dissolved faster than the Pm3n, probably because of the very interconnected geometry of the porous network, which causes faster diffusion and surface evolution.

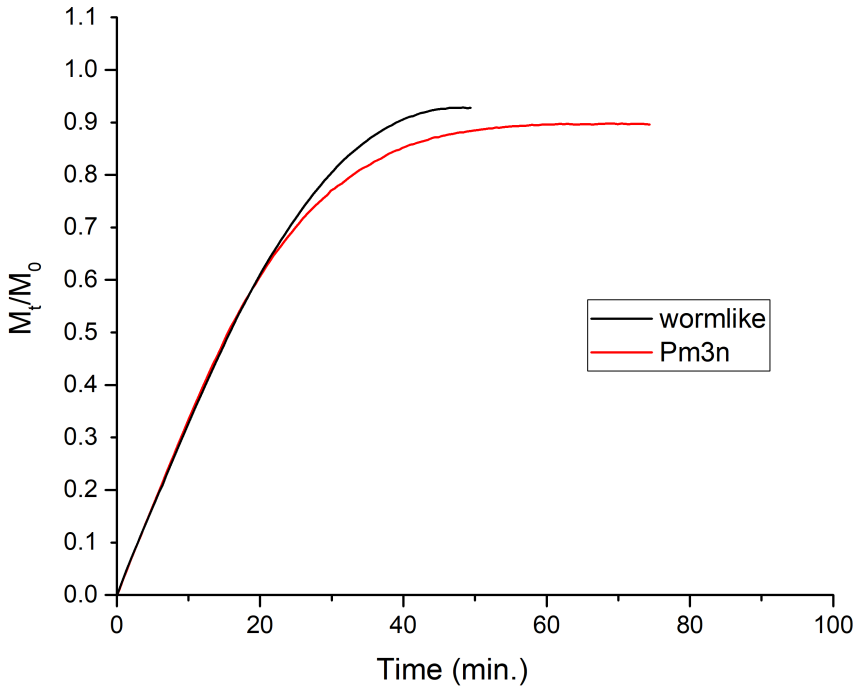

Figure V.8 – Dissolved silica mass M_t normalized on initial silica mass M_0 during dissolution in PBS at 37 °C. Both samples are mesoporous silica layer templated with CTAB and exposed to the same thermal treatment (450°C, 15 min). They have similar porosity (0.56 for the wormlike structure and 0.62 for the Pm3n) and surface area (800-850 m^2/cm^3).

Influence of specific surface and porous volume

On the contrary, Pluronic F-127-templated films dissolve two times slower than CTAB-templated ones, for similar values of V_p (figure V.9). This happens because they present a much lower surface area (370 vs 850 m^2/cm^3). Moreover, not only their starting exposed surfaces are significantly different but also their evolutions don't happen at the same rate. In fact, Pluronic F-127 templated films presented thicker silica walls than CTAB-templated ones, so their porous volume and surface evolve at a slower rate. Anyway this structural contribution is someway included in the surface factor and we can say that dissolution rate of mesoporous silica depends linearly on specific surface area of films (figure V.10).

Analyzing two equivalent films (CTAB templated, calcined at 450 °C, Pm3n cubic mesostrucure) with different porous volume we notice a different shape in the release curve (figure V.11). The sample CT450-1 has a porous volume of 62% while CT450-2 has a porous volume of 43%. The CT450-1 silica release curve belongs to case 1, where K follows the

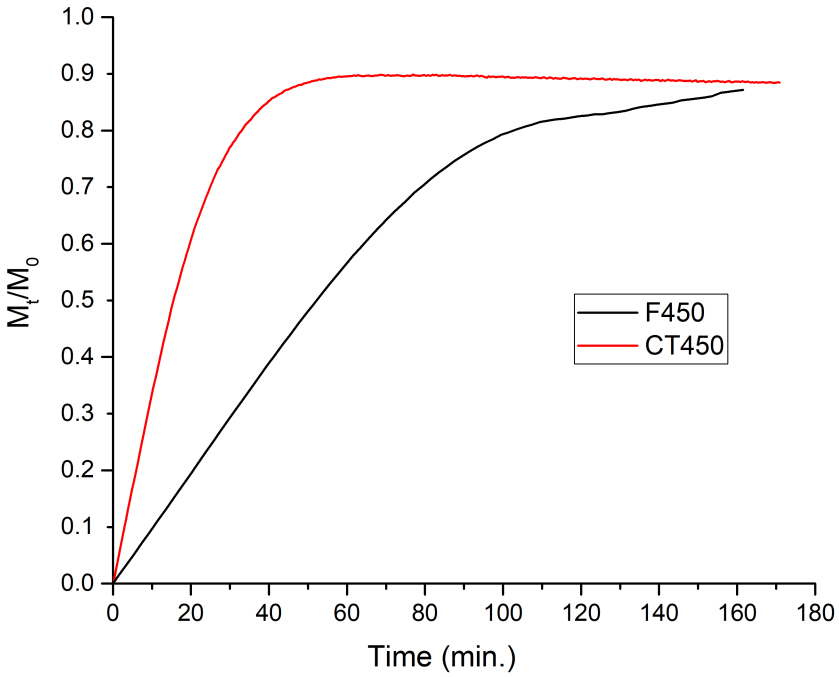

Figure V.9 – Dissolved silica mass M_t normalized on initial silica mass M_0 during dissolution in PBS at 37 °C for mesoporous silica films treated at 450°C for 15 min. CT450 is templated with CTAB and F450 with Pluronic F-127. They have similar porosity (0.62 for CT450 and 0.61 for F450) but very different surface area (850 vs 370 m^2/cm^3 for CT450 and F450, respectively).

evolution of the surface which stays constant for a while and diminishes in the second part of dissolution. It is reasonable to assume D as constant, given that the porosity is already high when dissolution began.

Starting from a lower porosity value, the curve of silica release assumes a sigmoid shape, as described in case 2. We can attribute this behavior to a starting rate which increases shortly after the beginning and decreases again towards the end of dissolution. This could be due to an initial increment of surface or to a raise in the value of D_{eff}, or both. In fact, for lower porosity values, the porous network may hinders molecules diffusion, in this case when V_p increases D_{eff} rises, accelerating the release. Another possibility is that not all the surface is available to react with water at the beginning of dissolution, because of pore blocking. In the latter case, the increment of V_p due to dissolution can trigger an acceleration of the release rate, due to an increase of reactive surface. This effects can also combine. Towards the end of dissolution the surface value drops inevitably and the release rate slows down.

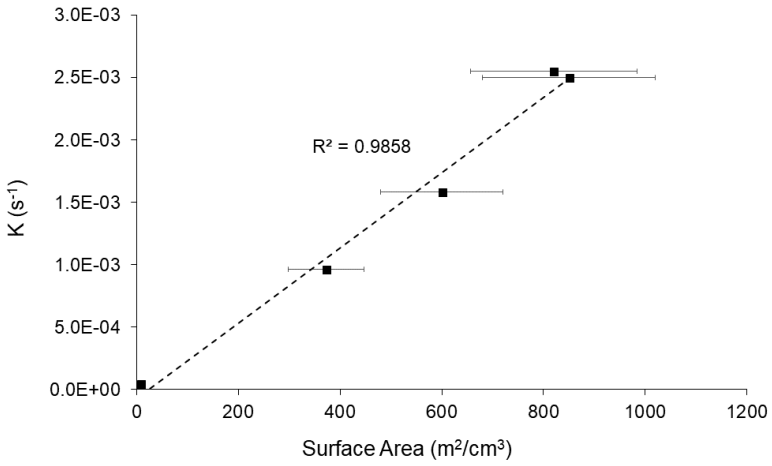

Figure V.10 – Rate of dissolution K derived from equation V.4 vs surface area for mesoporous silica thin films. All the samples have been obtained in the same conditions (deposition speed $= 2\text{mm} \cdot \text{s}^{-1}$, 26 °C and 30% RH) and treated at 450°C for 15 min. The point at the lowest surface value refers to dense silica while the porous samples have porosity values ranging from 0.43 to 0.62. The surface has been evaluated from porosimetry measurements with t-plot method, the error bars reported corresponds to an error on the surface value of 20%.

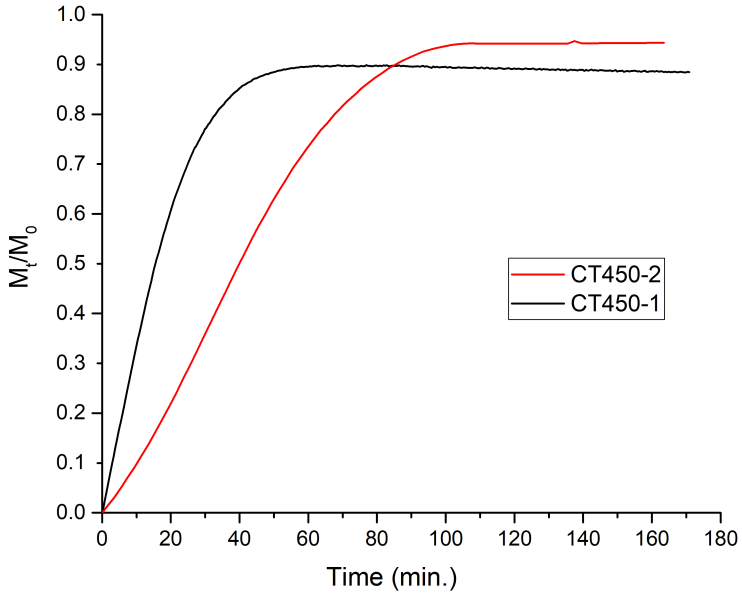

Figure V.11 – Dissolved silica mass M_t normalized on initial silica mass M_0 during dissolution in PBS at 37 °C for mesoporous silica films (CTAB templated, Pm3n structure) treated at 450°C for 15 min. The sample CT450-1 has a porous volume of 62% and a surface area of 850 m^2/cm^3, while CT450-2 has a porous volume of 43% and surface area of 600 m^2/cm^3.

V.3.2 Alternative models of dissolution

There are some other models which concern molecular release process from a solid device, and they are usually employed in pharmaceutical studies. Nevertheless, the most of them only consider the diffusion process of a soluble drug encapsulated in a matrix (dense or porous). This situation doesn't correspond to our case of study, in fact, mesoporous silica dissolution implies the hydrolysis of silica network and then the diffusion of the dissolved species. The models used in pharmaceutics only accounts for the second step of the process so, most likely, they will not fit with the silica dissolution kinetics. We tried some of them, verifying the mismatch between our data and the models.

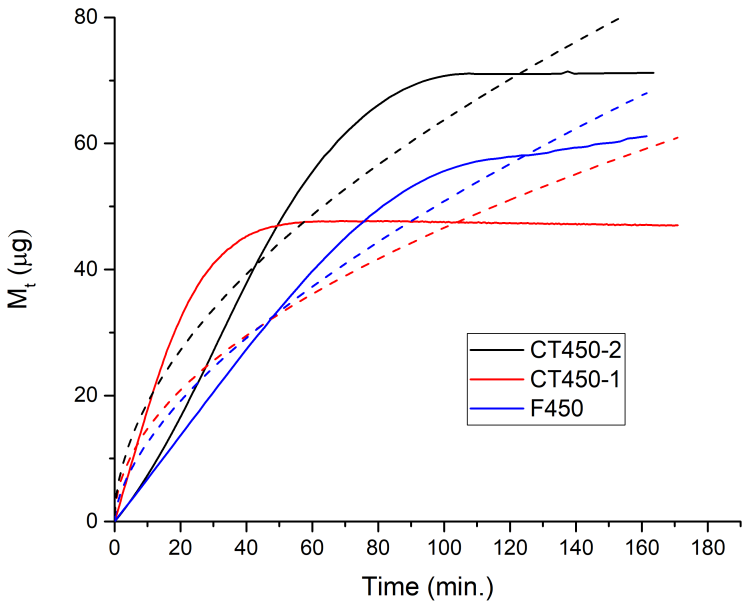

Figure V.12 – Dissolved silica mass M_t during dissolution in PBS at 37 °C. CT450-1 and CT450-2 have different values of surface and porous volume. Data have been fitted with Higuchi equation V.7 (dashed lines).

The already cited Higuchi model [205] describes a square-root dependence of the released amount with time (V.7):

$$M_t = \sqrt{D_{eff}(2C - \epsilon C_s)(C_s t)} \tag{V.7}$$

This kind of kinetics can't describe satisfactorily our systems, as evident from figure V.12. The silica mass release of mesoporous films seems rather to follow a zero-order kinetics where M_t increases at a constant rate (eq. V.8), as showed in figure V.13.

$$\frac{M_t}{M_0} = \beta t \tag{V.8}$$

where β includes the surface parameter S and the diffusion coefficient D_{eff}, which is dependent on porous volume and morphology. Thus, β gathers some parameters which aren't constant during dissolution, but their combined evolutions account for a constant rate of silica release. Zero-order release kinetics have already been observed for swellable polymeric devices [206–209]. Ritger and Peppas presented an empirical equation, valid for $\frac{M_t}{M_0} \leq 0.60$, useful to analyze data from Fickian and non-Fickian diffusional release for this kind of systems [206, 207]:

$$\frac{M_t}{M_0} = \beta t^n \tag{V.9}$$

where n describes the transport mechanism involved, being equal to 0.5 for Fickian diffusion and to 1 for the so-called case II transport, which provokes a zero-order release kinetics. If n assumes values between 0.5 and 1 the transport mechanism is a combination of Fickian and non Fickian behavior, with the latter dominating. Fitting our release data with equation V.9 we find for all the systems a dominance of non-Fickian transport, with values of n close to 1, indicating a condition in which silica release is almost linear with time (zero-order kinetics), as showed in figure V.14.

Nevertheless, we can notice that there is a case in which n is higher than 1, which is not possible. This is an indication of a discrepancy between the model assumptions and our system conditions: in fact, also in this case the only part of the dissolution process considered by the model is the transport outside the matrix of a species which is already dissolved, without taking into account the hydrolysis of silica.

Moreover, for polymeric swellable matrices it was pertinent to imagine a non-Fickian transport mechanism, due to chains relaxation processes which modify molecules diffusion, but for mesoporous silica there's no reason to assume this kind of transport mechanism.

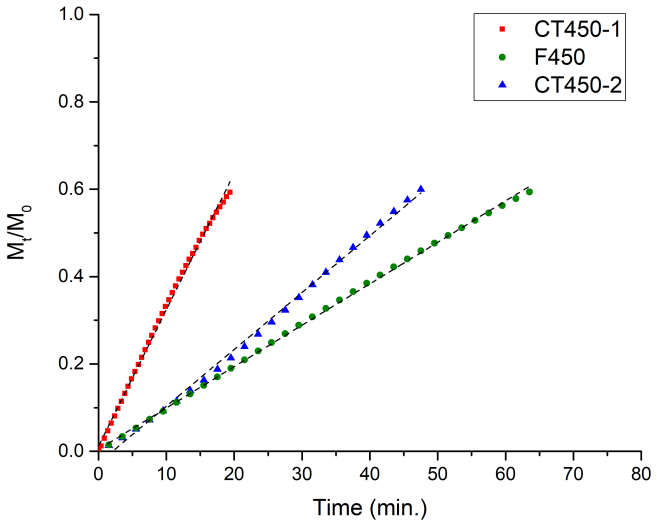

Figure V.13 – Dissolved silica mass normalized on initial silica mass (M_t/M_0) during dissolution in PBS at 37 °C. Data are reported for the first 60% of dissolution process ($\frac{M_t}{M_0} \leq 0.6$) and have been fitted with linear equation V.8 (dashed lines).

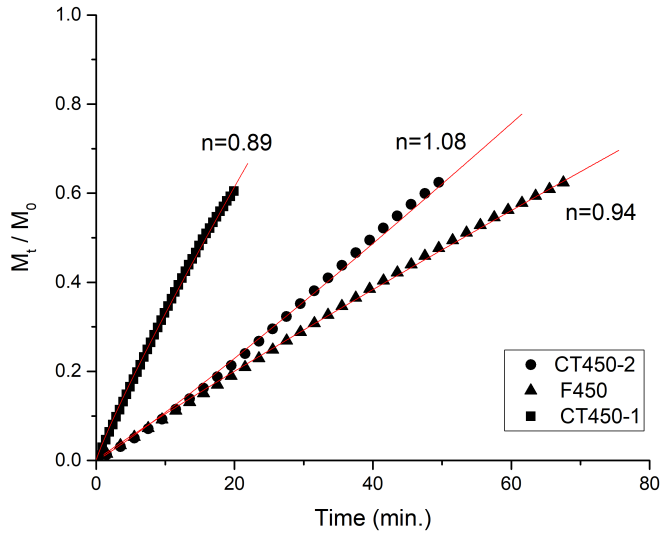

Figure V.14 – Dissolved silica mass normalized on initial silica mass (M_t/M_0) during dissolution in PBS at 37 °C. Data are reported for the first 60% of dissolution process ($M_t/M_0 \leq 0.6$) and have been fitted with equation V.9 (red lines) finding n values of 0.78 for CT130 (not reported), 0.89 for CT450-1, 1.09 for CT450-2 and 0.94 for F450.

V.3.3 Mesoporous Silica Nanoparticles film

All the informations gathered on mesoporous silica thin film dissolution are meant to provide knowledge about this process in order to gain control upon mesoporous nanoparticles use in biomedical applications. Thus, we wanted to check if the results obtained on mesoporous films could be applied in case of equivalent mesoporous nanoparticles.
To do so, we deposed mesoporous silica nanoparticles on a silicium wafer and analyzed their dissolution in PBS at 37 ° by *in situ* ellipsometry, employing the same experimental setup used for thin films.
The nanoparticles were synthesized adding 3 mL of a solution 0.88 M of TEOS in EtOH to a solution of CTAB (0.29 g) in water (125mL) and ammonia 0.512 M (25mL). The water/ammonia solution is kept at 50 °C under stirring (750 rpm) during the addition of TEOS solution. The nucleation happens in the first 3 minutes at 50 °C and the solution is then kept under stirring at r.t. for 2 hours.
Nanoparticles have diameters around 40 nm, 2D-hexagonal mesostructure and their morphology is shown in SEM pictures V.15.

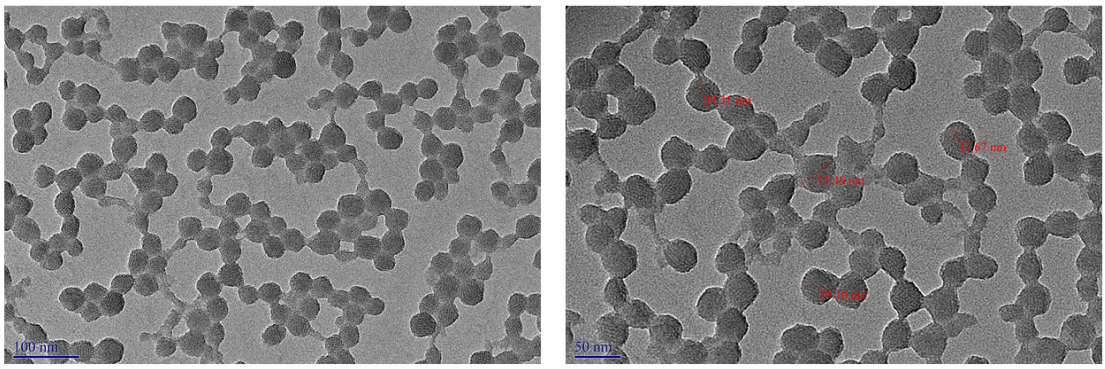

Figure V.15 – SEM images on mesoporous silica nanoparticles, synthesized using CTAB as templating agent.

The sol containing the silica particles has been dip-coated on a silicium substrate at 0.01 $mm \cdot s^{-1}$ and 50°C to obtain a layer of nanoparticles. The high temperature and slow withdrawal speed are necessary when dip-coating from aqueous solution, to avoid dewetting phenomena. The film has then been heated at 130 °C for 1 night and washed in EtOH to remove CTAB. The film refractive index at 632 nm was 1.102 meaning that the layer had a very high porosity, as expected for packed mesoporous nanoparticles. SEM images on the colloid layer (figure V.16) showed a dense packing of the nanoparticles.
We performed environmental ellipsometric porosimetry (EEP) on the nanoparticles film,

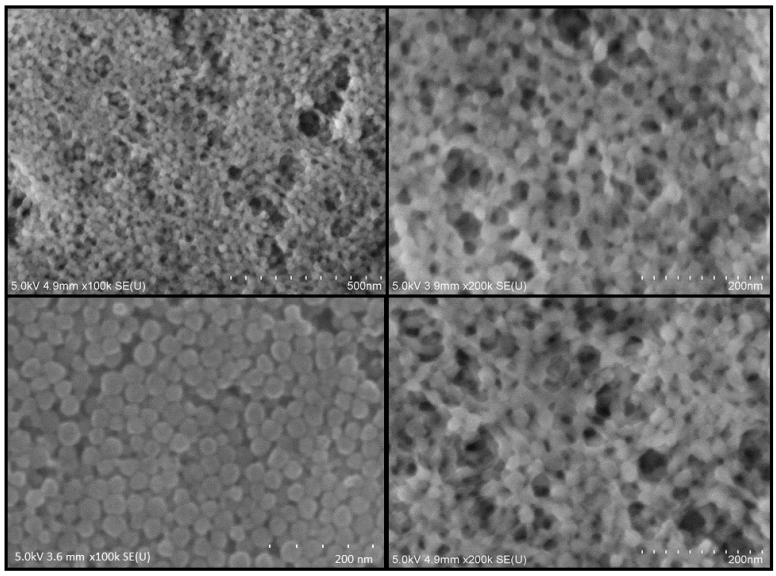

Figure V.16 – SEM images on mesoporous silica nanoparticles film, dip-coated at 0.01 $mm \cdot s^{-1}$ and 50°C. The bottom left picture has a higher resolution.

observing two adsorptions which corresponds to the capillary condensation in the mesopores (lower P/P_0) and to the filling of inter-particles pores (higherP/P_0). The water adsorption curve is reported in figure V.17. Anyway, it was not possible to calculate the specific surface area with the t-plot method, because of the huge incertitude on external surface. In fact, on a flat film, the external surface can be easily evaluated knowing the film volume, while in this case the layer has a huge surface roughness ($\approx$ 45 nm from ellipsometric measurements) and a complicated, irregular surface morphology, as can be seen from SEM images (figure V.16). These nanoparticles have usually surface area ranging from 900 to 1200 m^2/cm^3 but when packed in a multilayer film they will most probably lose some accessible surface due to the compact spatial arrangement.

Fitting the dissolution data with Noyes equation, considering a saturation limit of 145 μg/mL, we found a K value of $3 \cdot 10^{-3}$ s^{-1} for the first part of the release curve, very similar to the value found for silica mesoporous films with surface values of 800-850 m^2/cm^3 ($K = 2.5 - 2.55 \cdot 10^{-3}$ s^{-1}). The silica release is slightly slower than for mesoporous films after the 50% of dissolution, this is most probably due to a different surface evolution between a layer of nanoparticles and an homogeneous silica layer. Anyway, the 80% of silica is dissolved within 50 minutes, and the very similar dissolution rate observed is encouraging: it confirms the relevance of data obtained on mesoporous films for predicting nanoparticles behavior.

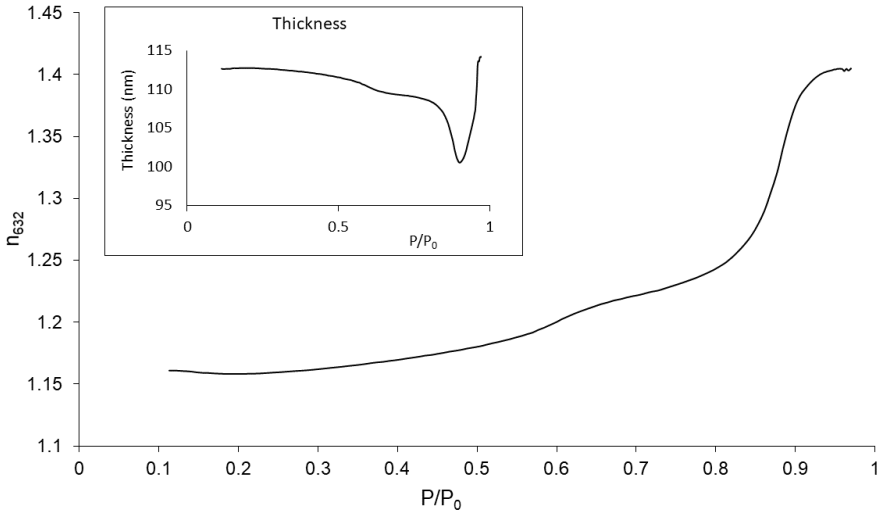

Figure V.17 – Evolution of refractive index vs P/P_0 of a layer of mesoporous silica nanoparticles (40 nm of diameter, pore size = 2.5-3 nm) during water adsorption. We can notice the capillary condensation in the mesopores at $P/P_0 = 0.60$ and the adsorption of water in the pores between nanoparticles at a P/P_0 value of 0.87. In the box is reported the evolution of film thickness vs P/P_0.

Since the starting rate of dissolution fit perfectly with the one of silica mesoporous films having a surface of 800-850 m^2/cm^3 we can assume a similar value of available surface for this nanoparticles film.

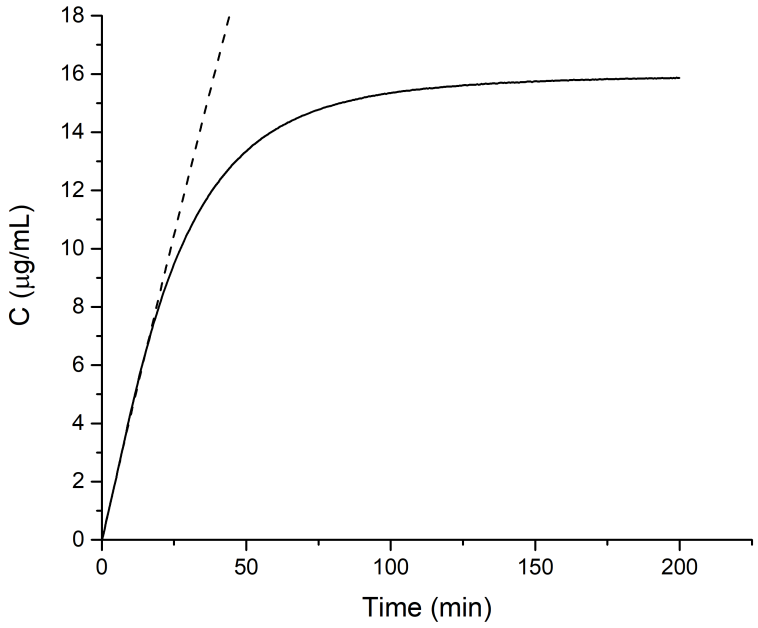

Figure V.18 – Silica concentration during dissolution in PBS at 37 °C of a film of mesoporous silica nanoparticles. Theoretical trend according to Noyes equation V.4 is reported with a dashed line and has a $K = 3 \cdot 10^{-3}$ s^{-1}.

V.4 Role of surface adsorbed biomolecules

It is nowadays established that a layer of proteins (corona) forms on the surface of nanoparticles when they are in contact with biological fluids. The protein corona mediates the interactions of nanomaterials with cells and it determines nanoparticles biocompatibility and biodistribution.

We want to investigate the influence of protein corona on silica dissolution rate, to be able to predict silica nanoparticles behavior in a more realistic environment. To do so, we started performing dissolution experiments in a bovine serum albumin (BSA) solution in PBS, to pass later to more complex biological fluids such as serum and blood.

BSA is widely used as a model protein because it has similar properties and molecular weight to its human variant, human serum albumin, while being easily available and less expensive. Albumin is found in all bodily fluids, being very often a major component of the corona. BSA has a molecular weight of approximately 66 kDa, an isoelectric point of 4.7 and it exists in multiple forms depending on the pH of its environment. The common forms of BSA are the normal form (N form, pH 9.0–4.5), the fast form (F form, pH 4.0–3.5), and the extended form (E form, pH below 3.5). The sizes of N, F, and E forms

of BSA are: 8.0 x 8.0 x 3.0 nm, 4.0 x 4.0 x 12.9 nm, and 2.1 x 2.1 x 25.0 nm, respectively. It has been proved that BSA can undergo conformational changes upon adsorption onto a surface. In particular, onto silica particles it showed a loss of α-helix structures because of strong interactions with hydroxyl groups on the surface, causing the protein secondary structure modification [210]. In fact, even if BSA and silica are both negatively charged (for example at pH = 7.4) strong hydrogen bonding interactions exist between the amino acid chain and the silica hydroxyl groups. Moreover, $NH_3{}^+$ groups present on the protein can participate in electrostatic interactions with deprotonated silanols.

In literature are reported values around $4.5 - 5 \cdot 10^{11}$molecules $\cdot$ cm^{-2} for BSA adsorption onto SiO_2 surface at neutral pH [210] and concentrations of 3-10 g/L, which describes a multi layer surface coverage (a monolayer should be around $2 - 4 \cdot 10^5$molecules $\cdot$ cm^{-2} depending on the adsorption conformation).

We perform dissolution experiments of mesoporous silica layers in a solution of BSA in PBS (37 g/L, pH = 7.4). The chosen concentration is in the range of albumin concentration in human blood. In these conditions, BSA will be in its N form and will bring a negative surface charge. At such concentration, we assume an uniform adsorbed layer on the silica surface which reaches its equilibrium before the start of dissolution experiments. Depending on its mobility, the protein surface layer should hinder diffusion (and so, dissolution) more or less, thus, we expect dissolution to happen at a slower rate compared to PBS.

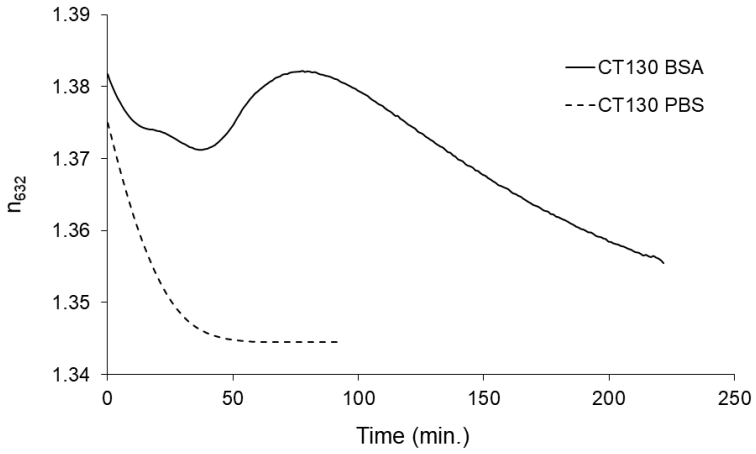

Figure V.19 – Refractive index of mesoporous silica film CT130 (CTAB templated, stabilized at 130 °C) during dissolution in BSA solution (37 g/L) at 37 °C in static conditions.

In such protein rich environment, the refractive index of the silica layer showed a very

different evolution compared to the dissolution in phosphate buffer, as reported in figure V.19. The decrease of refractive index n is much slower and it is interrupted after 40 minutes of dissolution. At this point, the refractive index value starts to increase sensibly, until it reaches the value of the beginning in about 40 min, then it decreases constantly. This peculiar behavior could be interpreted as a change in protein adsorption. In fact, adsorbed BSA may change its conformation when the silica surface evolves and proteins may pack differently on the surface, restoring a more compact surface coverage (which causes the rise of n).

However, this behavior was not observed on calcined silica samples CT450, of any porosity and structure. The evolution of their refractive index is an almost linear decrease, with no sign of modified adsorption on the surface, as showed in figure V.20. The only difference between CT130 and CT450 films (being equal surface and porous volume) is the method of removal of the surfactant. In CT450 the surfactant is decomposed by thermal treatment at 450 °C, while in CT130 it is extracted through ethanol washing. We started to think that the behavior observed for CT130 in a BSA solution could be due to the presence of some residual CTAB molecules.

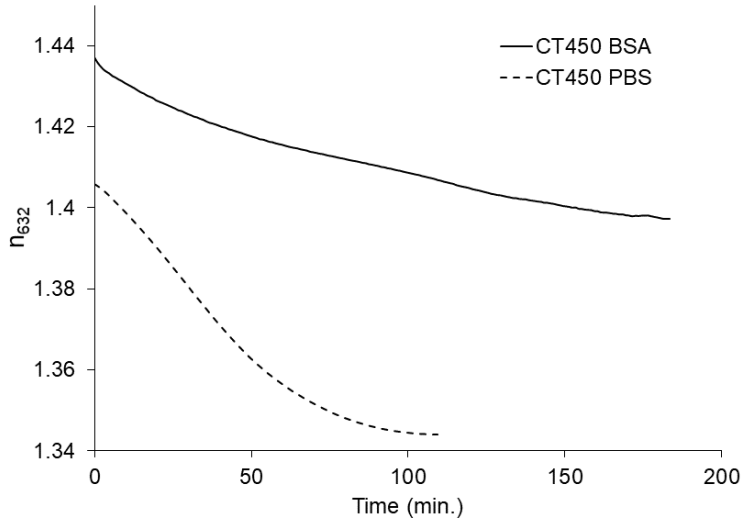

Figure V.20 – Refractive index of mesoporous silica film CT450 (CTAB templated, calcined at 450 °C) during dissolution in BSA solution (37 g/L) at 37 °C in static conditions.

An investigation of the literature on this subject showed that CTAB forms a protein-surfactant complex with BSA, not soluble in water, unfolding the protein and inducing its aggregation with other BSA molecules [211,212]. The positively charged head group of

CTAB interacts electrostatically with carboxylic groups of aspartic acid and glutammic acid on BSA, which are deprotonated at pH = 7.4. This process reduces the ζ-potential of BSA, triggering aggregation after an initial lag phase which was found to last around 20 minutes [211]. The presence of this CTAB-BSA complex and/or the BSA aggregates on the surface of mesoporous silica films could explain the optical response of the CT130 layers.

The refractive index of the mesoporous silica layers after the washing step is 1.2-1.23 at 632 nm, equal to the values measured for CT450, meaning that the residual amount of CTAB after ethanol extraction has to be very weak, because it is not influencing the optical properties of the layer (a porous layer before the washing step has a refractive index equal to 1.38-1.4) and could not be detected by ellipsometry.

We performed XPS experiments on ethanol-extracted samples, looking for bromine peaks (binding energy of 70 eV), without detecting any residual bromine presence (figure V.21).

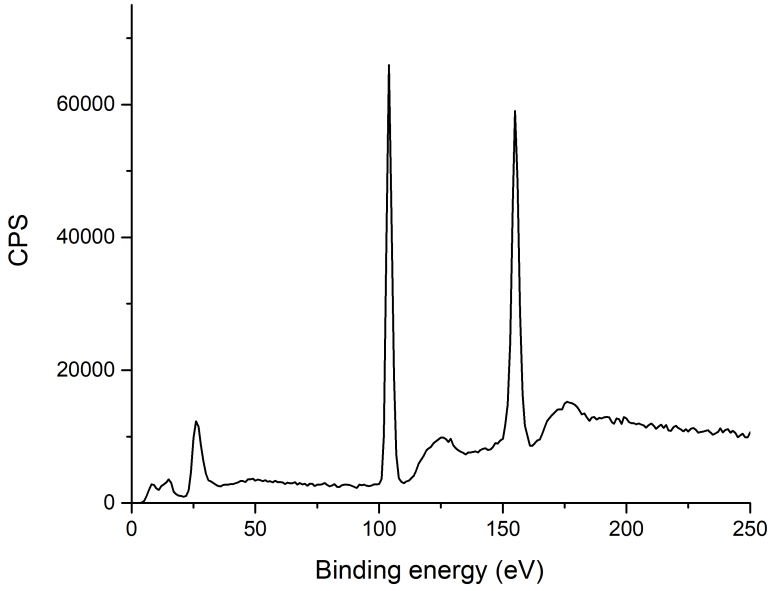

Figure V.21 – XPS survey spectra of CT130 sample after ethanol extraction of CTAB. No peak is detected in the typical bromine area, around 70 eV of binding energy. Data above 250 eV are not showed.

Yet, even if XPS analysis could not detect any residual bromine in the extracted samples, this doesn't mean that there aren't CTAB molecules inside the porous film. In fact, if it is true that the detection limit of XPS is very low ($\leq$ 0.5 atomic percent) it has to be considered that XPS is a surface technique and does not analyze the sample bulk. It is reasonable to imagine that if there are some few molecules of CTAB still embedded

in the silica layer, they will be placed deeper in the sample, because solvent extraction rely on diffusion. Even if there are only few CTAB molecules left, it is enough to form some CTAB-BSA complex and adsorb it on the surface of the film. The amount of these aggregates is probably very low and doesn't seem to influence the overall dissolution kinetics (considering the residual silica after 3h, measured ex-situ) but it is enough to be detected by *in situ* ellipsometry because it modifies sensibly the optical response of the sample.

When a weak flow (5 mL/min) was applied we noticed the shift of the perturbation to earliest times but the behavior is similar. In order to confirm the role of the surfactant in this process, we reloaded a calcined film CT450 with CTAB and analyzed it. So, in the silica film after calcination there is no surfactant left and it doesn't show any visible change in surface adsorbed layer (figure V.20). When CTAB is reintroduced in this layer (by soaking it in a CTAB-ethanol solution) we can see the same variation of refractive index as the one reported for CT130.

Thus, we can infer that this peculiar behavior is due to the residual presence of CTAB molecules in the mesopores. Even if their quantity is very low they influence the interactions with BSA and reshape the interface. The formed CTAB-BSA complex unfolds the protein and triggers its association in big aggregates which adsorb on the silica surface. A liquid flow isn't useful to remove them.

The observation of this phenomenon points out how important it is the washing step in the synthesis protocol of nanoparticles made for drug delivery. In fact, if the conformation of adsorbed protein may be not a main issue for dissolution experiments, it is indeed very important in a biological environment. CTAB promotes aggregation of BSA molecules which compromises their biological function. Actually, protein aggregation is linked with several disease such as Alzheimer's disease, Parkinson's disease, Down's syndrome and Cataract and Sickle cell diseases [213]. The origin of aggregation is often unclear but most of the times it involves partially unfolded native proteins. The formation of complexes protein-ligand provokes the unfolding of the native structure of proteins and can be a starting point for aggregation. It has been demonstrated in the case of CTAB, in which the reduced ζ-potential of the complex CTAB-BSA promotes aggregation [211]. Complexes with BSA have also been observed for other surfactants such as anionic sodium dodecyl sulfate (SDS) and nonionic polyoxyethylene 8 lauryl ether [212] so, it is evident to which extent washing protocols of nanoparticles need to be optimized to assure the complete removal of the templating surfactant. In fact, usually solvent extraction is the chosen method to eliminate the surfactants from nanocarriers, because nanoparticles of-

ten aggregate during thermal treatments and if they contain some organic ligand they can't be heated to high temperatures or all the organics will decompose.
In the case of nanocarriers, the protein corona mediates every interaction between cells and nanoparticles and if the proteins structure is altered their function will also be affected, impacting the biological activity of NPs. For example, it has been reported that the conformation of BSA induced by the CTAB-BSA complex has higher affinity for hematine hydrochloride than the N form of BSA [211].
Because of the interference of residual surfactant in the measurements, we decided to evaluate the influence of surface adsorbed proteins on silica dissolution on CT450 samples, in which the CTAB is completely removed by thermal treatment. These samples are dip-coated (speed $2\text{mm} \cdot \text{s}^{-1}, 26°\text{C}, \text{RH} = 30\%$) from a solution of TEOS/EtOH/CTAB/H_2O with molar ratio 1:40:0.14:5. The solution is acidified by adding HCl 37% (0.09 molar ratio with TEOS) and stirred at r.t. for 72h before use. Samples are then stabilized at 130 °C for one night and heated at 450 °C for 15 minutes.
From their dissolution experiments, we see that the presence of proteins slowed down silica dissolution by a 5x factor, as reported in figure V.22. Fitting data with equation V.4 we found a value for $\text{K} = 3.4 \cdot 10^{-6}$ s^{-1} when dissolution is performed in BSA solution and $\text{K} = 1.58 \cdot 10^{-3} \text{s}^{-1}$ for dissolution in PBS of samples with equivalent porous volume (0.42-0.43) and surface (650 m^2/cm^3). We removed samples after 3 hours of soaking at 37°C and after a quick rinsing in water we measured them by ellipsometry, finding almost no silica residual layer (1-5 nm) for samples soaked in PBS, while samples soaked in BSA solution still presented a thick layer of silica (about 70% of the starting thickness), as showed in figure V.23.
The observed slowdown in silica dissolution rate is due to the proteins adsorbed on the surface, which act as a barrier to diffusion and is consistent with the retarded drug release observed by Shahabi [70] for porous silica nanoparticles in the presence of proteins. The effect of protein surface layer on the dissolution rate has been observed for every sample analyzed, independently from its porosity, structure, composition and thermal treatment. The experiments have been repeated at least two times for each kind of samples, showing very good reproducibility, with a difference in calculated dissolution rates K always $\leq 6\%$ for samples of the same series.

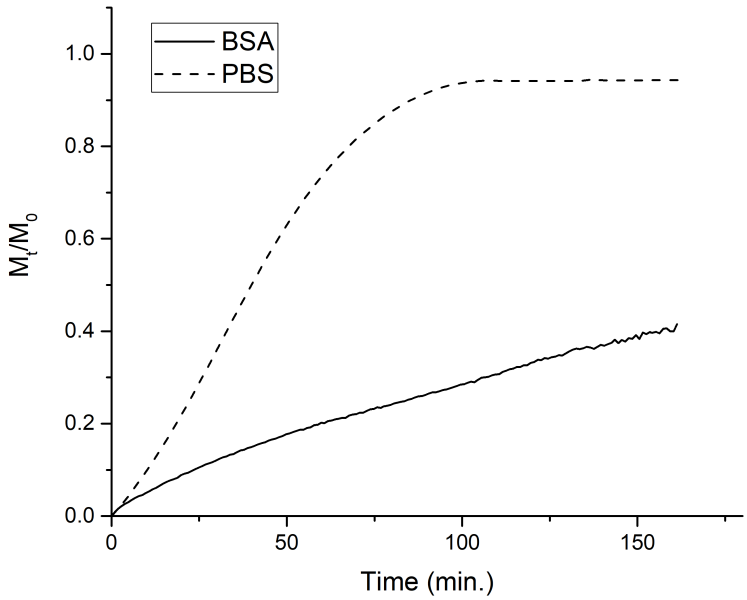

Figure V.22 – Dissolved silica mass normalized on initial silica mass (M_t/M_0) during dissolution at 37 °C in PBS (dashed line) and BSA solution in PBS (solid line), for CT450 samples with porosity values V_p = 0.42-0.43. BSA concentration in solution is 37 g/L.

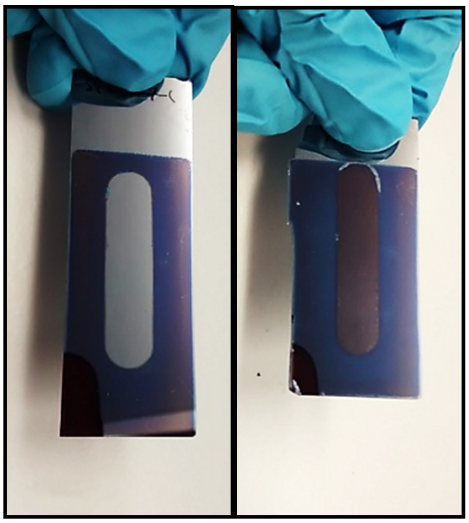

Figure V.23 – Mesoporous silica layers after 3 hours of dissolution at 37 °C in PBS (left) and BSA solution in PBS (right), for CT450 samples with porosity values V_p = 0.42-0.43. BSA concentration in solution is 37 g/L.

V.5 Hybrid silica films

In practical applications silica is often employed as hybrid silica, containing functions such as methyl or amine in a given percentage. Particularly, silica carrying amine moieties is usually employed because of its easy functionalization chemistry which allows to bind proteins, dyes or antibodies to the surface. Thus, we decided to investigate the dissolution kinetics of hybrid aminated silica in physiological conditions.

V.5.1 Synthesis and characterization

We perform the experiment as described above, dip-coating from a sol of similar composition to CT SiO_2 using TEOS and (3-Aminopropyl)triethoxysilane (APTES) as precursors in a molar ratio of 0.85:0.15 and CTAB as templating agent. Hybrid silica is formed through a co-condensation process, thus the organic moieties are anchored to the silica matrix. The obtained films have a so-called wormlike disordered mesostructure with interconnected pores, as revealed by GI-SAXS experiments (figure V.24). Hybrid films have been treated at 130 °C for one night, then washed in ethanol to remove CTAB. This kind of layers can't be heated at higher temperatures or their organic groups will decompose.

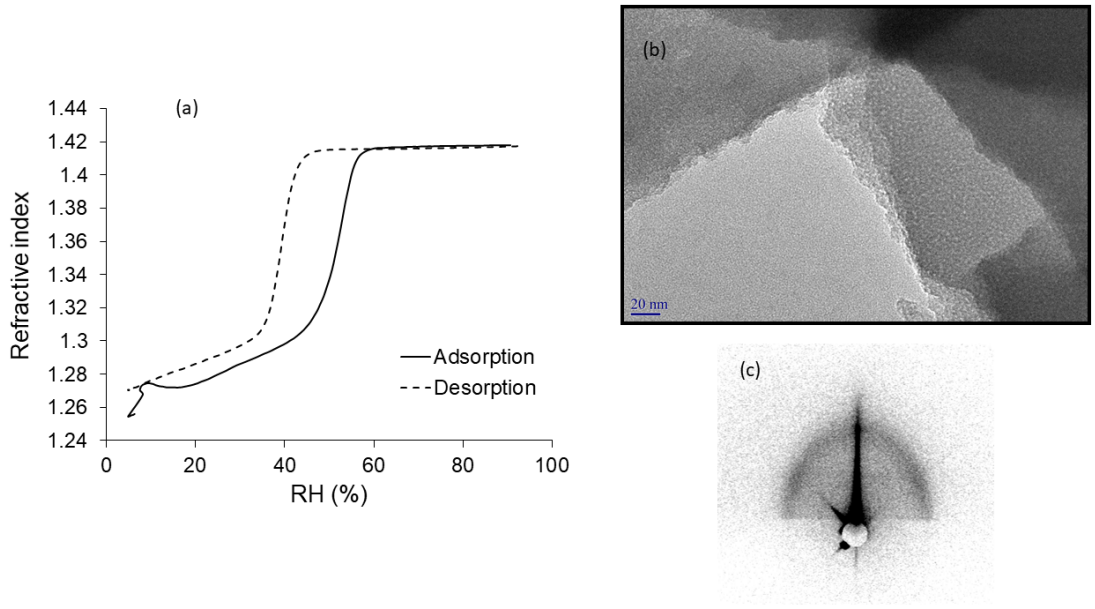

Figure V.24 – (a) ellipso porosimetry (b) TEM image and (c) GI-SAXS pattern of an hybrid mesoporous silica layer obtained through co-condensation of TEOS and APTES (0.85:0.15 molar ratio)

V.5.2 Dissolution in PBS

Following the dissolution of hybrid mesoporous films in PBS at 37°C, we noticed a much slower dissolution rate than pure silica layers. Actually, comparing silica and hybrid silica with similar porosity (0.42-0.45) and surface area (600 m^2/cm^3) we saw a very similar dissolution rate in the first 25 minutes, then hybrid silica slowed down sensibly and after 60 minutes of dissolution ($\approx 0.5\%$ of total mass released) changed its rate to a much slower one. Setting the experiment time to 16 hours we observed no acceleration: after the first hour, silica dissolution followed a slow linear rate. Fitting the concentration data with Noyes equation we found a starting rate of dissolution K=1.6·10^{-3} s^{-1}, very similar to the one of the equivalent pure silica films having the same V_p and surface (K=1.58·10^{-3} s^{-1}).

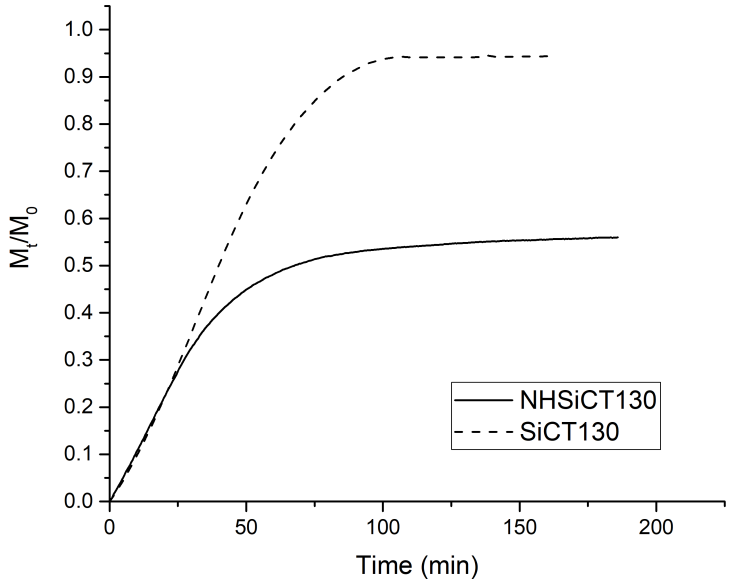

Figure V.25 – Dissolved silica mass normalized on initial silica mass (M_t/M_0) during dissolution at 37 °C in PBS for mesoporous silica (dashed line) and hybrid silica carrying amine moieties (solid line). Both samples have porosity values V_p = 0.42-0.45.

We performed XPS analysis on samples before and after dissolution, finding an increase in N/Si ratio which passes from 0.13 to 0.38. Observing the nitrogen peak we noticed a decrease in the peak of protonated/hydrogen-bonded amine, which is usually attributed to amines interacting through hydrogen bonding with silanols on the silica surface (figure

V.26). This peak diminished after dissolution, probably because there are less close silanols onto the silica surface for amines to interact with . In fact, given these data, we propose a dissolution mechanism for which at the beginning the hydrolysis concerns those Si-O bonds which are far enough from the amine moieties to be not influenced from the functional group. This is supported by the fact that the starting dissolution rate is coherent with the one of pure silica layers having the same characteristics.

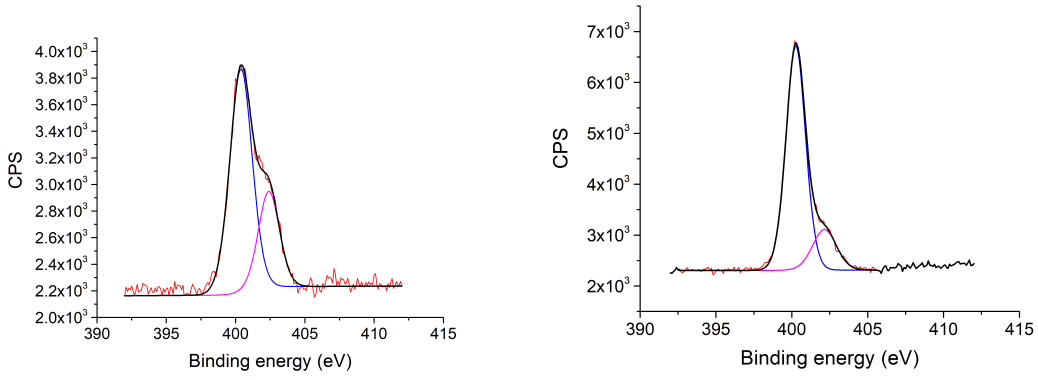

(a) (b)

Figure V.26 – Nitrogen peak of XPS spectra of hybrid aminated silica (a) before dissolution, (b) after dissolution in PBS at 37 °C for 3 hours. The atomic ratio N/Si calculated from the survey spectra (not showed) passes from 0.13 before dissolution to 0.38 after 3h in PBS.

The propyl-amine group deactivates by inductive effect the near Si atoms towards nucleophilic attack by water molecules, causing the material to be much more stable towards hydrolysis. Thus, the starting dissolution rate is due to the hydrolysis of Si-O bonds which aren't affected by the presence of the organic group, once they have all reacted the dissolution changes rate, slowing down. This means that playing on the composition of the initial solution it is possible to tune the dissolution easily, even if an excess in amine functions may produce a more fragile silica network, making the overall material less stable towards hydrolysis than a composition with a smaller organic percent, as already observed by Fontecave [98].

This is also interesting considering drug delivery applications because the amine group can interact with drugs loaded in the mesopores, retaining them and releasing them slowly. At the same time, any interaction with other molecules (electrostatic or hydrogen bonding) could modify the inductive effect on Si atoms. Indeed, the behavior of drug-loaded hybrid nanoparticles will strongly depend on the matrix/drug interaction and solubility of the

drug [214]. Thus, experiments with encapsulated or grafted drugs should be carried out, employing different ratio of silica functionalization and different drugs (cationic, anionic. hydrophobic, hydrophilic).

V.5.3 Role of surface adsorbed proteins

We performed the dissolution experiments on hybrid silica in presence of proteins, as previously described for pure silica films. We used the same experimental apparatus and the same protein solution (BSA in PBS 37 g/L, 37°C).

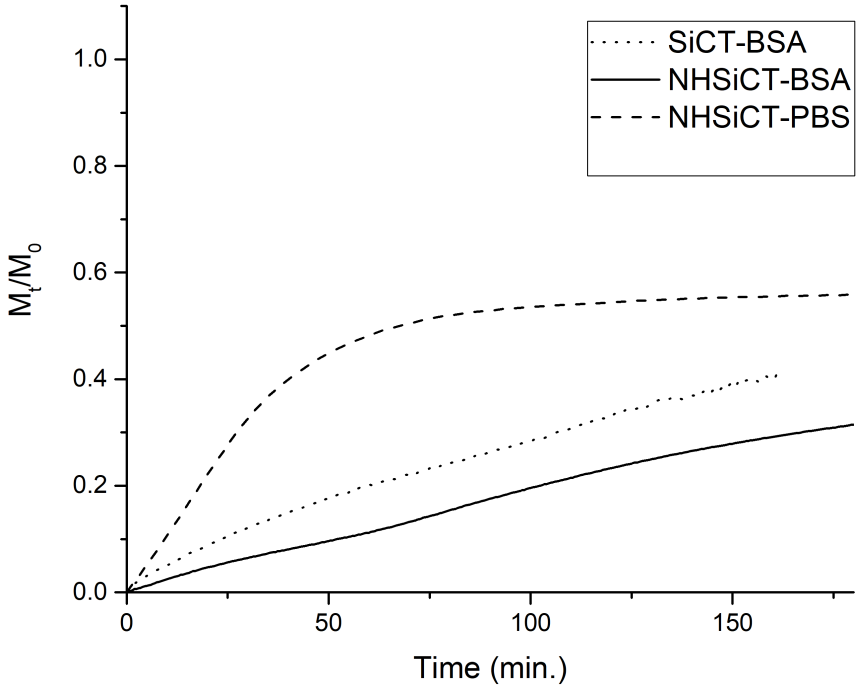

Figure V.27 – Dissolved silica mass normalized on initial silica mass (M_t/M_0) during dissolution at 37 °C for mesoporous silica (dotted line) and hybrid silica carrying amine moieties (solid line). Both samples have porosity values V_p = 0.42-0.45. For comparison, it is reported also the release of a similar hybrid mesoporous silica film in PBS at 37 °C (dashed line).

As can be seen in figure V.27 the presence of surface adsorbed proteins slows down the dissolution kinetics, in a similar way than observed on pure silica films. The diffusion barrier constituted by BSA molecules hinders the release of dissolved species, keeping the overall dissolution rate low. We didn't observe the formation of CTAB-BSA complexes onto the surface of hybrid films, although they have been washed in ethanol to remove the surfactant with the same protocol used for pure silica films. The washing proved itself

more efficient in the case of hybrid silica, probably because of the electrostatic repulsions between the cationic head of CTAB and the protonated amines on the silica surface. The values of dissolution rate K calculated from Noyes-Whitney equation V.4 for silica and hybrid silica dissolution in PBS and in BSA concentrated solution are reported in table V.3. We can notice that dissolution rate in protein solution is smaller for both materials but the protein effect on dissolution is more pronounced for pure silica than for hybrid silica.

Table V.3 – Dissolution rate K of silica and hybrid silica films with equivalent porous volume and surface area (V_p= 0.42-0.45 and S= 600 m^2/cm^3).

	SiO_2 PBS	SiO_2 BSA	NH-SiO_2 PBS	NH-SiO_2 BSA
K (s^{-1})	$1.58 \cdot 10^{-3}$	$3.4 \cdot 10^{-6}$	$1.6 \cdot 10^{-3}$	$2.4 \cdot 10^{-4}$

V.5.4 Surface chemistry

Before their use as drug delivery devices, mesoporous silica nanoparticles are usually functionalized with a surface layer of PEG, to minimize protein adsorption and recognition by the immune system. Thus, the material exposed to biological environment is an hybrid material formed by a silica (or, most often, hybrid silica carrying organic functions) core and a polymer outer shell.

We wanted to reproduce this structure and test its dissolution kinetics in physiological conditions. To do so, we prepared PEGylated hybrid silica films as described in Chapter II, section II.4. Unfortunately, we were not able to obtain the desired core-shell structure preserving the free access to the porous network. We successfully grafted pegylated polymer brushes on silica surface but from porosimetry data seems that the pores are blocked by polymer brushes and are not accessible to water vapors. This would make comparisons very difficult because, as we previously demonstrated, silica dissolution rates depend on surface area and pores tortuosity, two factors deeply modified from brushes growth inside pores.

We performed anyway dissolution experiments on these PEG-grafted films in PBS and in BSA solution in PBS (37 g/L) at 37°C. The ellipsometric modeling of the layers as a mesoporous silica layer and a surface polymer layer was not possible. The refractive index found for the silica layer was way too high (1.47 at $\lambda = 632$ nm), indicating that the material is an hybrid containing polymer brushes in the pores throughout its thickness.

Thus, without knowing the optical properties of this silica/polymer layer we couldn't calculate either the porous volume or the silica content.
For this reason, we will only comment the evolutions of layer refractive index and thickness.

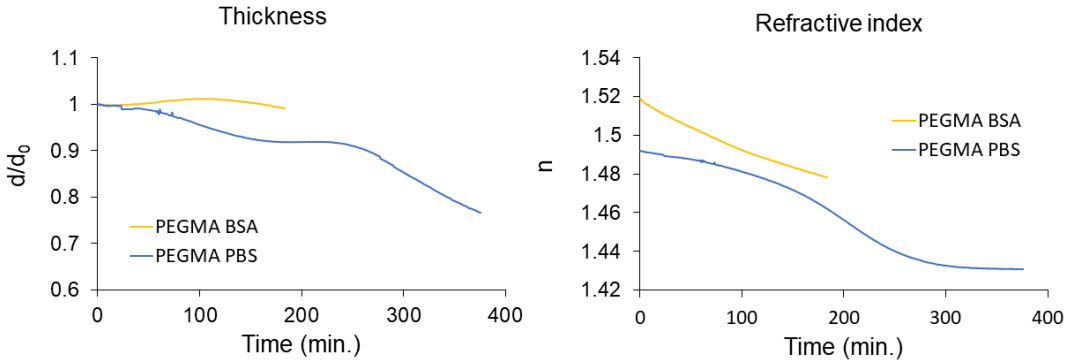

Figure V.28 – Thickness and refractive index evolutions of an hybrid silica layer functionalized with PEGMA (500) brushes. Results are reported for dissolution in PBS and in concentrated BSA solution (37 g/L in PBS) at 37 °.

Observing the refractive index in PBS we can see a slow decrease for the first 150 minutes, which then accelerates, to stabilize itself reaching a plateau around 300 minutes. Thickness decreased slowly in the beginning, then reached a plateau around 160 minutes to start diminishing again after 250 minutes, faster than at the beginning. What is evident, is that the dissolution kinetics of this polymer-hybrid silica are much slower than the one of the substrate silica before polymer grafting. These PEGMA-grafted samples were obtained from hybrid silica layers carrying amine moieties, after an ATRP reaction which grafted polymer brushes on amine groups, as reported in chapter II, section II.4.
Hybrid silica carrying amines dissolved the first 50% of the total mass within 75 minutes, then started a slower dissolution process concerning silica directly linked with the organic moieties. After the polymer grafting, the latter process seemed to happen after 300 minutes, meaning that the first step of dissolution is 4 times slower. This is likely to be due to a very hindered diffusion process caused by the presence of the brushes in the pores. Because the brushes are grafted on the amine moieties, it is reasonable to imagine that when the first step of dissolution process is finished the material will contain more PEGMA in percentage, as it happens with amine moieties. The acceleration in refractive index decrease is most probably due to an opening of the porous structure after a certain time and to a less hindered diffusion, which also allowed the polymer brushes located

in the pores to swell. This swelling would explain the simultaneous decrease of n and increase of thickness (thickness stopped to diminish).

In protein solution, we saw an increase in refractive index of 0.02 compared to the material in PBS, which is in the same range as the one observed for hybrid silica without brushes. The thickness also increased slightly. These behaviors indicates a surface adsorption of the proteins, which is not completely avoided by the PEGylated polymers. Nevertheless, it is not possible to quantify the amount of protein adsorbed and if it is smaller than onto silica without PEG. In fact, through ellipsometry in liquid medium in static conditions, the ellipsometer "sees" not only the irreversibly adsorbed layer but also the proteins weakly bonded to the surface layer.

Thus, to conclude, *in situ* ellipsometry is not the better analysis technique to study this kind of hybrid films and we would need parallel measurements with other methods such as neutron reflection, which could provide valuable informations on material density. In this way we could be able to study the evolutions of both silica and organic part of the material.

The grafting of poly(oligo(ethylene glycol) methacrylate brushes (p(OEGMA)) could be a powerful tool to obtain PEGylated silica surfaces in a controlled way but it is necessary to optimize the protocol for porous substrates, avoiding the reaction to take place also inside the pores and limiting the grafting to the surface moieties. This could be done performing the initiator grafting with pores occupied by surfactant or drug molecules, in solvents and pH conditions which avoid cargo diffusion outside the pores and which allow grafting reaction in the same time.

V.6 Monitoring Gold clusters embedded in mesoporous silica

Gold nanoparticles smaller than 2 nm (often also called gold clusters or gold quantum dots) have peculiar optical and magnetic behaviors, different from the ones exhibited by bigger particles, and are very promising for many applications including catalysis and health care [215–217]. As the size of gold nanoparticles decreases below 2 nm, their plasmonic properties are lost and their conduction band shows discrete energy levels, originating a molecule-like behavior. The gold clusters are interesting for biomedical application because they absorb light in the near-infrared (NIR) biological window (650–900 nm) and convert it into photons and heat, having great potential for imaging purposes and photothermal therapies. Some of them also showed magnetic properties. However,

they suffer a lack of stability in aqueous solvents and tend to aggregate quickly to form bigger nanoparticles, losing their peculiar properties.

Recently, they have been successfully integrated in a mesoporous silica shell to form an hybrid platform which preserves the properties of gold quantum dots in biological environments and which has demonstrated good efficacy in photothermal treatment against tumors *in vivo* [218]. The authors synthesized structures named "quantum rattles" which are hollow spherical particles ($\approx$ 150 nm total diameter) with mesoporous silica shells ($\approx$ 25 nm thickness), hosting both gold clusters (<2 nm diameter) and AuNPs (average diameter 7.3 nm). The NPs are hosted in the cavity while the gold quantum dots (AuQDs) are embedded in the mesoporous silica shell, as showed in figure V.29.

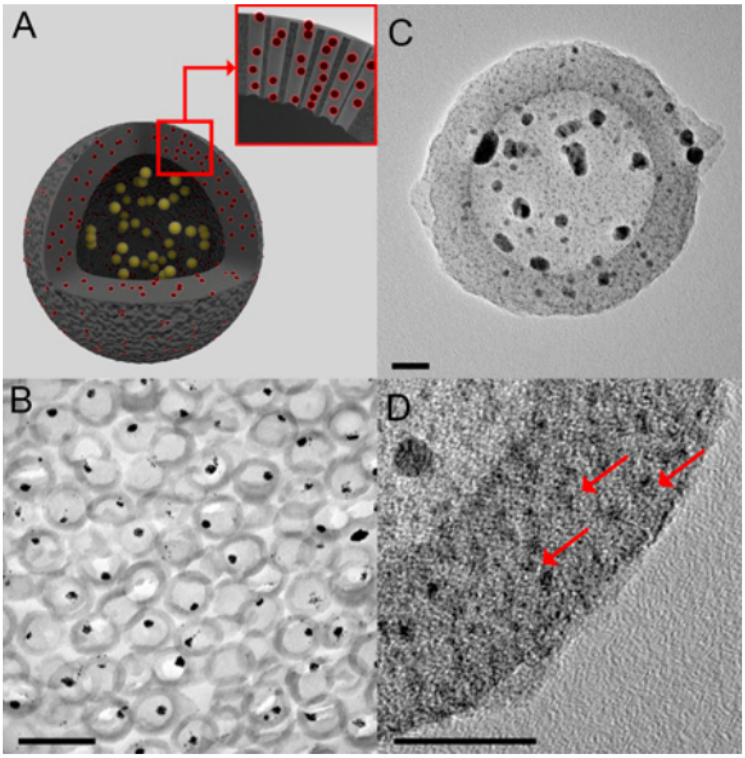

Figure V.29 – (A) Schematic structure of a silica quantum rattle. QRs hosts AuQDs (red) inside their mesopores and gold nanoparticles AuNPs (yellow) inside their macrocavity. (B) Bright field TEM image of an ultrathin section of resin-embedded QRs, showing AuNPs within the mesoporous silica shells. (Scale bar, 0.2 μm.) (C) Bright field TEM image of a QR showing AuNPs within the cavity of the mesoporous silica shell. (Scale bar, 20 nm.) (D) Higher-magnification bright field TEM image of the silica shell showing the AuQDs (red arrows). (Scale bar, 20 nm.) Adapted from [218]

The QRs displayed a NIR extinction peak at 672 nm, typical of AuQDs, which excited a

fluorescent emission mode at 827 nm and also exhibited T1 contrasting agent properties. They have been tested *in vitro* without showing cytotoxicity over several days, they were internalized by cells and accumulated in the perinuclear area within vesicles, as observed through fluorescent images. They have been proved excellent multimodal imaging agents, to be exploited in fluorescence, magnetic and photoacustic imaging. They have also proved themselves effective in tumor burden reduction through photothermal treatment. The QR-injected areas reached temperatures above 51 °C after less than 1 min irradiation with a 671 nm laser, causing necrosis of cancer cells. Moreover, the QRs prolonged the release of the drug payload when compared with hollow silica spheres filled with the same drug (Doxorubicine, DOX). In fact, the presence of gold clusters in the mesopores hindered the release of DOX forming a more tortuous pore structure and enhanced the affinity for DOX. Consequently, the release of DOX was extended to 12 h from 4 h observed for the silica particles free from AuQDs.

Similar structures, made of mesoporous silica nanoparticles with embedded gold quantum dots, have been monitored *in vivo* through fast micro-X-ray fluorescence and micro-X-ray absorption spectroscopy [219]. The theranostic vectors have been detected in the spleen, in the liver and in the kidneys, and their presence seems not inducing any inflammatory processes. The study reported no oxidation for the gold centers during their metabolism but could not establish whether the AuQDs are still confined in the silica particles or not.

For their great potential as theranostic vectors, we decided to reproduce the structure of quantum rattles and follow their evolution during dissolution of the silica shell. We synthesized gold clusters and confined them inside a mesoporous hybrid silica layer, then we monitored the optical properties of this hybrid layer in PBS through *in situ* ellipsometry. We employed the setup previously described for mesoporous silica thin films dissolution in PBS (figure V.1).

V.6.1 Gold QDs synthesis and characterization

Small gold clusters are not stable in their bare configurations and need ligand protection to avoid aggregation. We prepared gold clusters stabilized by 4-aminothiophenol (4ATP) which present 25 gold atoms and 17/18 ligands.

The $Au_{25}(4ATP)_{18}$ gold clusters were synthesized according to Demessence's methodology [220], employing gold (III) chloride trihydrate ($HAuCl_4 \cdot 3H_2O$) as metal precursor and lithium borohydride ($LiBH_4$) as reducing agent in tetrahydrofuran (THF). Three solutions need to be prepared as follows:

-**Solution A**: Dissolve 60 mg of $LiBH_4$ in 25 mL of THF and let under stirring for 1h.

Pay attention to the complete dissolution of the lithium borohydride, heat with a water bath if needed.

-**Solution B**: In a 100 mL flask, dissolve 128 mg of ATP in 20 mL of THF. Put the flask in an ice bath and let it under stirring at 500 rpm.

-**Solution C**: Dissolve 260 mg of $HAuCl_4 \cdot 3H_2O$ in 25 mL of THF.

Employing syringe pumps, add 20 mL of both solutions A (precursor) and C (reducing agent) to the solution B (ligand), at a rate of 1 mL/min. Solution B is kept under stirring at a temperature $\leq$ 25 °C for 5 hours. The reaction mixture have a brown/black color.

For the purification, eliminate the THF under reduced pressure at 40 °C and 300 mbar, then centrifugate the obtained black solid 3 times washing with ethanol (8000 rpm, 15 minutes). Dry the solid.

Transmission electron microscopy (TEM) characterisation was carried out, TEM samples were prepared by dispersing the gold clusters in tetrahydrofuran (THF), and then placing a drop of the suspension on a carbon coated Cu grid. After solvent evaporation the samples were ready. Figure V.30 shows the TEM micrograph of the $Au_{25}(4ATP)_{18}$ clusters synthesized. We can see the formation of large aggregates but also many well dispersed clusters. Particle diameter ranges from 0.53 to 3.5 nm, with an average diameter of 1.78 $\pm$ 0.62 nm.

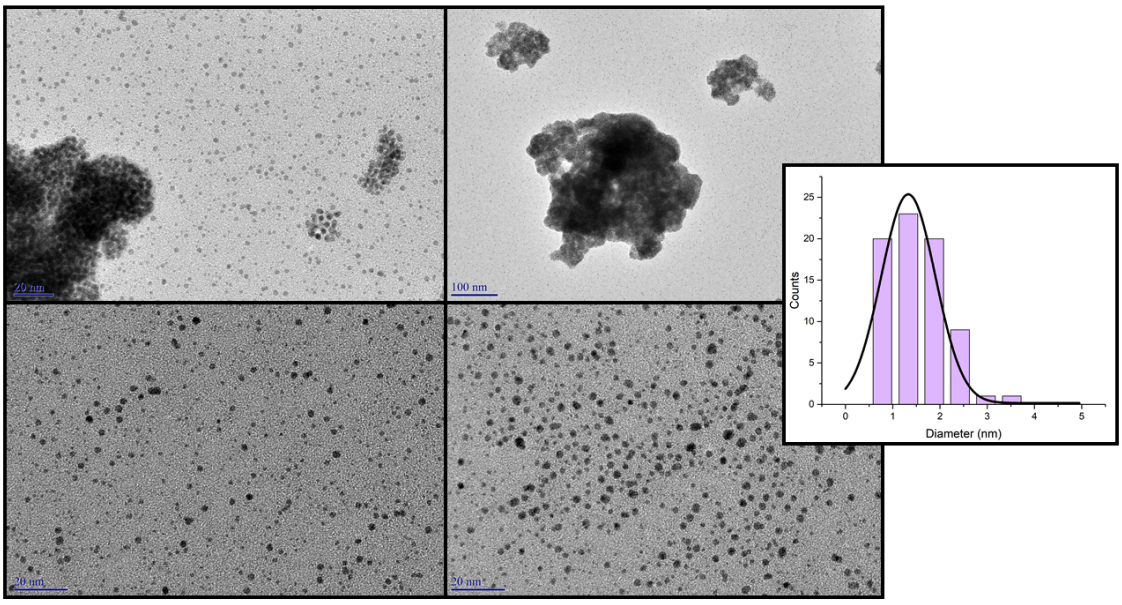

Figure V.30 – Transmission electron microscopy image of gold clusters. The cluster size distribution is shown on the right. The average diameter is 1.78 $\pm$ 0.62 nm.

Optical properties of gold clusters are different from the ones of gold nanoparticles, in fact, they don't show a surface plasmon resonance band but discrete energy levels. This is a consequence of the restricted size of the gold core and accounts for a molecular behavior of the clusters. Thus, their UV-visible spectra have absorption bands corresponding to specific electronic transitions.

The optical spectrum in THF was measured, it is shown in figure V.31 and has band absorptions at 382, 520 and 672 nm. If peaks at 382 and 672 are typical of gold clusters, the large peak at 520 indicates the presence of bigger NPs in solution, which have a plasmon resonance usually around 520 nm. These results are coherent with some previously reported [220].

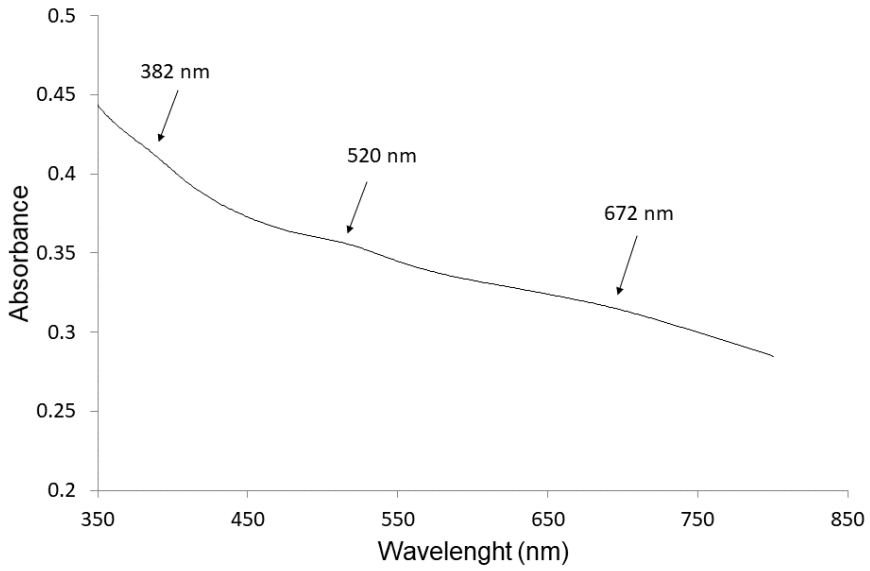

Figure V.31 – UV-visible spectrum of $Au_{25}(4ATP)_{18}$ clusters in THF.

Photoluminescent emission spectrum of AuQDs in solution was measured, showing an excitation peak centered at 763 nm and an emission peak centered at 823 nm.

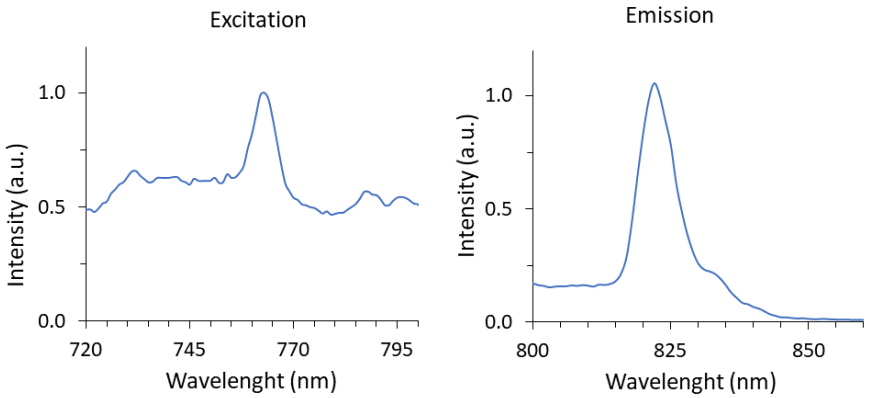

Figure V.32 – Fluorescence spectrum of $Au_{25}(4ATP)_{18}$ clusters in THF.

V.6.2 Gold QDs confined in mesoporous silica

We prepared thin mesoporous films of hybrid silica through co-condensation of TEOS and APTES, as already described in section V.24. These layers were immersed in a solution of AuQDs in ethanol for 1 and 10 minutes and then analyzed by ellipsometry and ellipsometric porosimetry. The two samples showed very similar results, indicating that the loading of QDs in the mesopores is very fast and reaches saturation level after one minute. To avoid misinterpretation due to little variations between samples we registered data before AuQDs loading and after it for every film, comparing only data taken on the same sample. From porosimetry results we observed a decrease in porous volume of 4-7% after the loading of gold clusters compared to the layers with empty mesopores. We also registered an increase in refractive index values around 0.03 unities, as evident from isotherms displayed in figure V.33.

These data suggested the presence of AuQDs in the pores, TEM micrographs confirmed the loading of mesopores with gold clusters, as showed in figure V.37. We measured the optical properties of thin films before and after dissolution through ellipsometry but we were not able to register an increment of extinction coefficient k. In fact, employing models for absorbing layers (which can account for absorption) the values of k obtained were always close to the sensitivity limit of the technique ($k = 0.002$). Most probably, the amount of gold embedded in the silica is too low to detect its absorption with this method. For this reason, we didn't discuss the k variations and we only evaluated the evolution of refractive index n.

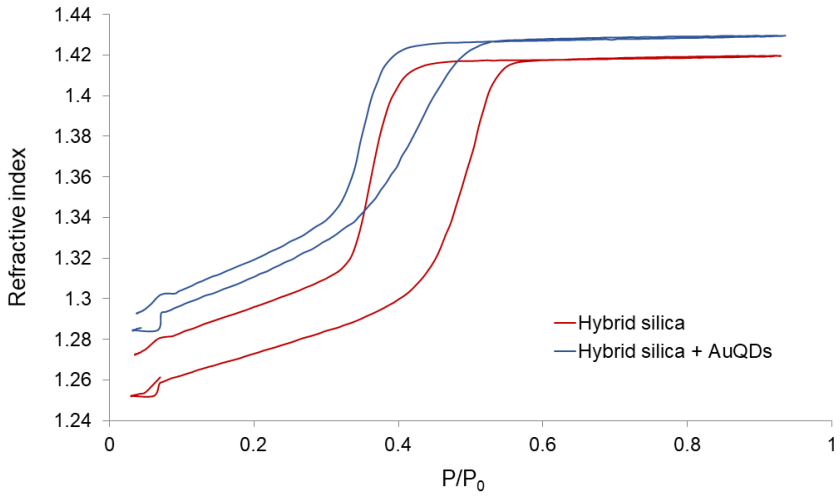

Figure V.33 – Refractive index n vs P/P_0 for mesoporous silica hybrid layers before (red line) and after (blue line) soaking in a solution containing AuQDs. The refractive index of the layer increased sensibly, indicating the loading of AuQDs inside the pores.

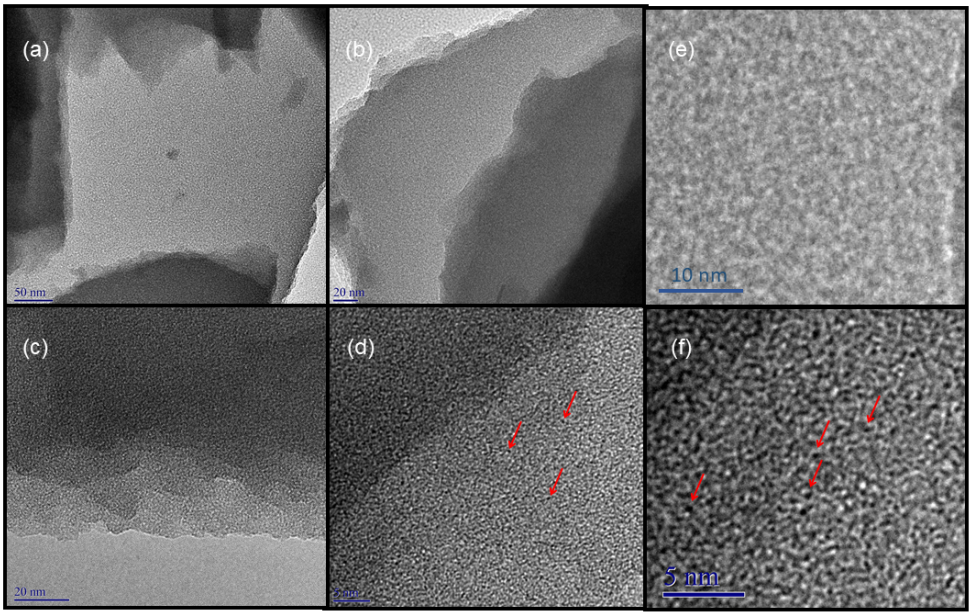

Figure V.34 – TEM images of (a-b) mesoporous hybrid silica and (c-d) quantum rattle structure, with gold QDs embedded in a mesoporous hybrid silica layer. (e) Blow-up of a mesoporous hybrid silica film, scale bar = 10 nm. (d) Blow-up of a mesoporous silica film loaded with AuQDs. Gold clusters are indicated with red arrows.

V.6.3 Dissolution of a quantum rattle structure in PBS

We dissolved the mesoporous hybrid silica films containing AuQDs in PBS at 37 °C. We observed a slowing down of dissolution compared to the empty layer, which is not surprising considering the decrease of porous volume due to the presence of gold clusters. For sure, AuQDs reduced the reactive surface available and could also increase the hydrophobicity of the pores because of the phenolic ligands, leading to a decreased rate of dissolution. The shape of the release curve drew a sigmoid, with a dissolution rate which increased after the first 20-25 minutes, stays constant for half an hour and then started to decrease to reach a linear slower rate corresponding to an higher amount of amine moieties in the material (see section V.24). We previously proposed an explanation to sigmoid release curves relying on a diffusion limitation in the beginning of the dissolution process, either due to non accessible pore surface or to a porous network with high tortuosity. Hosting gold clusters in the pores could cause both, decreasing the available pore surface and increasing the tortuosity of the diffusional path. When dissolution proceeds the tortuosity decreases and some clusters are released in the medium, making more surface available. At this point, when diffusion is not hindered anymore, the dissolution rate increases.

The observed behavior confirmed our hypothesis on hindered diffusion and dissolution due to a reduced surface and porous volume. In fact, when the rate increases after a slower starting period, its value is comparable to the one obtained for hybrid silica and mesoporous silica with equivalent surface area. In fact, fitting the silica concentration growth with Noyes equation (V.4) we found a K value of $7.1 \cdot 10^{-4}$ s^{-1} for the first 15 minutes, which then switched towards a value of $1.53 \cdot 10^{-3}$ s^{-1} (17-60 min), consistent with the rates previously observed for silica having the same V_p and surface ($K = 1.58 - 1.6 \cdot 10^{-3}$ s^{-1}).

Comparing the amount of silica released normalized on starting amount M_t/M_0 of hybrid silica and hybrid silica with embedded AuQDs we noticed an increase in the latter case. Before reaching the slower kinetic regime due to a concentration of organic groups in the matrix, the amount of dissolved silica is higher than for the empty matrix ($\approx 70\%$ vs $\approx 50\%$). We proposed a dissolution mechanism in which in a first step is dissolved the silica which is not affected by the inductive effect of the organic moieties and in a second time the hybrid matrix, now with increased percentage of organics, which has much slower dissolution rate. This hypothesis is supported by the fact that the first dissolution rate is almost identical to the one of mesoporous silica with equivalent surface area and that XPS analysis showed a concentration in N content (the organic functionality carries an

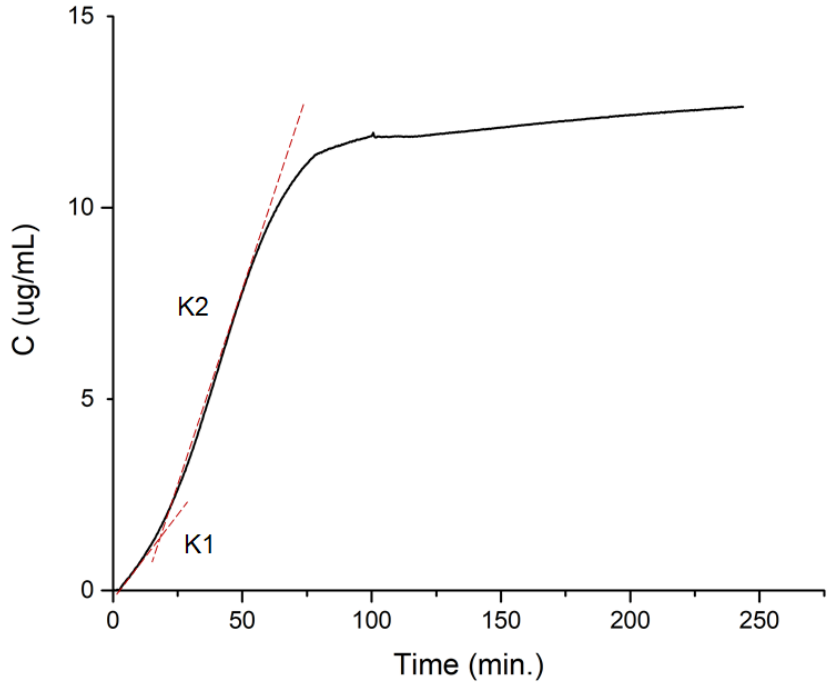

Figure V.35 – Concentration of dissolved silica in solution vs time for a dissolution experiment at 37 °C of a mesoporous hybrid silica layer containing AuQDs. The silica release curve has a sigmoid shape with a lower rate $k1$ at the beginning an a higher rate $k2$ after 15 minutes.

amine group) after the first step.

In the case of the quantum rattle structure, there is no reason for the gold clusters to modify the inductive effect of the organic moieties on the silica, making more Si centers "free" from the influence of the alkyl chain. The most probable hypothesis is that the observed increase in the amount of silica dissolved derived from an important decrease in refractive index. In fact, since the amount of silica is calculated from optical properties of the mesoporous layer, a huge drop in the refractive index results in a pronounced increase in dissolved silica amount. Dissolving the silica porous matrix some AuQDs are released and the refractive index variation associated with this process is larger than the one associated with substitution of silica with PBS. Thus, the behavior of the matrix doesn't change overall and the observed increase in dissolved material amount is due to an artifact due to the experimental method.

The measured kinetics suggests that the gold clusters stay confined in the silica matrix until its dissolution and don't diffuse outside in short times. If this was the case, we should see no influence of the presence of AuQDs throughout the dissolution. To verify

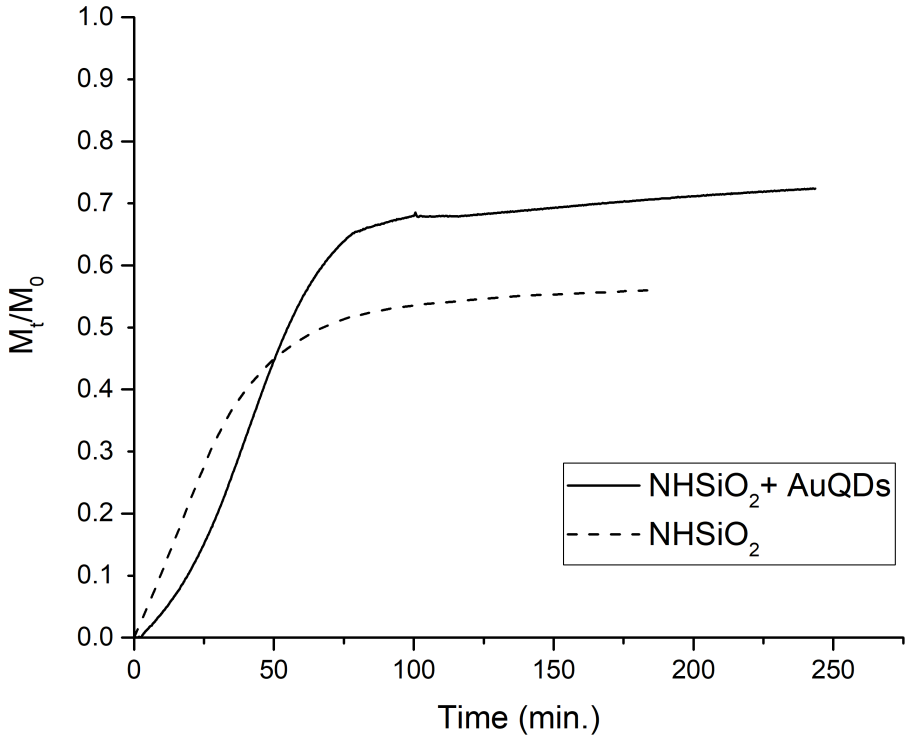

Figure V.36 – Dissolved silica mass normalized on initial silica mass (M_t/M_0) during dissolution at 37 °C in PBS for mesoporous hybrid silica carrying amine moieties (dashed line) and mesoporous hybrid silica with embedded AuQDs (solid line) . The porosity values of the two samples are similar before the loading of AuQDs (V_p = 0.40-0.43.), after the adsorption of the clusters into the pores V_p = 0.33 for the sample $NHSiO_2$ + AuQDs.

whether or not the gold clusters remained in the porous matrix during the dissolution process, we performed TEM on the films after 75 minutes of soaking in PBS at 37 °C and we noticed the presence of numerous gold clusters still embedded in the matrix (image V.37). This is not surprising because the amine group on the 4ATP ligands of the AuQDs is deprotonated at pH=7.4 and interacts strongly with silica surface silanols, anchoring the clusters to the pore walls. Some of the clusters aggregate when the matrix dissolves but they kept size smaller than 6 nm, which will assure their clearance through kidneys when employed as theranostic devices. The majority of them still had a diameter $\leq$ 2 nm after dissolution, which allows the preservation of clusters peculiar optical and magnetic characteristics (figure V.38).

Through *in situ* ellipsometry it wasn't possible to follow the evolution of extinction co-

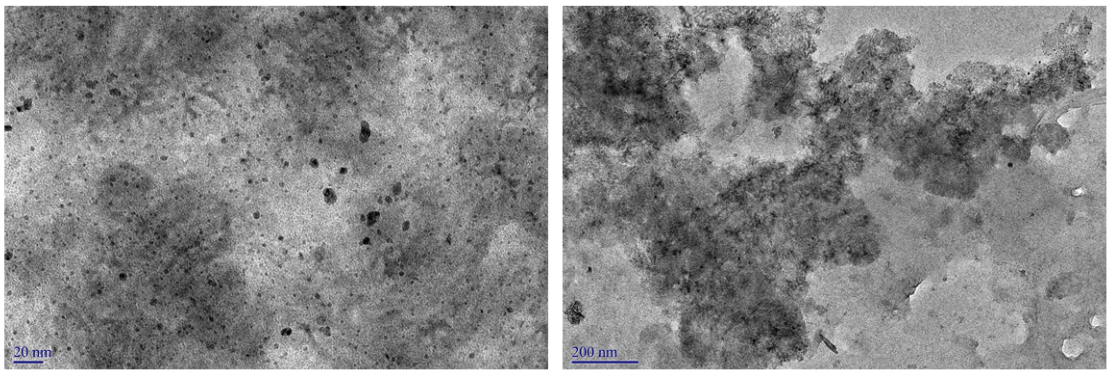

Figure V.37 – TEM images of mesoporous hybrid silica layers with embedded AuQDs after 75 minutes of dissolution in PBS at 37 °C. The gold clusters remained confined in the matrix and some of them aggregate but they kept dimensions $\leq$ 10 nm overall.

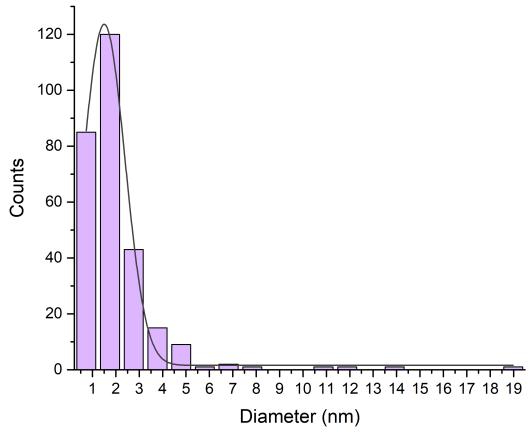

Figure V.38 – Size distribution of gold clusters observed in the silica matrix after dissolution. The sizes have been measured with ImageJ software on TEM micrographs, considering 280 clusters.

efficient k because of the very low amount of gold in the films, which furnished k values in the range of instrument sensitivity. To monitor the absorption and the appearance or not of a surface plasmon (meaning clusters aggregation inside the pores to form NPs) we should load more gold in the mesoporous layer, employing a film with higher porosity or using a thicker layer.

Otherwise, the absorption could be monitored through fluorescence experiments in liquid.

We were able to load AuQDs in a mesoporous hybrid silica layer carrying amine moieties and we verified that the clusters stay confined in the silica matrix during the dissolution process in PBS at 37 °C, being released when the wall dissolved themselves. We observed

some aggregation between the clusters while the porous network became more interconnected, nevertheless the average diameter of AuQDs stays lower than 2 nm, retaining the peculiar properties of gold clusters and being in the size range of NPs renal clearance.

V.7 Considerations about in vivo conditions: shear stress and particle flow dynamics

The purpose of targeted drug delivery devices is to reach the target site, anchor to it and release the encapsulated drug spontaneously or upon an external stimulus. Various vector administration methods exist depending on the localization of the target. For non-organ-specific administration of antitumoral drugs, the usual method is injection. The injected nanoparticles travel in the bloodstream, experiencing a fluid flow which depends on the environment (big arteries or small capillaries). In a second time, nanoparticles will be immobilized, either adsorbed at the surface of a target cell, removed by macrophages, or, if they are small enough, cleared out by the kidney. For any situation in which the nanoparticles anchor to some fixed surface, they are immobilized and must thus experience a different shear stress due to the blood flow. The knowledge about degradation of nanoparticles under a fluid flow is essential if we want to design efficient targeted nanocarriers which ideally would not dissolve and release their cargo before reaching their target site.

There are some applications for which controlling the dependence of particles degradation on flow is of major importance. For example to target kidney diseases, nanoparticles arrive quickly in the kidneys and there, they are exposed to a very important flow rate during the blood filtration. In this context, a drug carrier which accelerates its dissolution and drug release with the flow would be very efficient. We wanted to place our silica dissolution results in a more realistic context, performing some experiments under physiologically relevant flow conditions. To do so, we built a special setup coupling a microfluidic channel with total internal reflection ellipsometry, and to compare flow conditions between the experimental apparatus and the bloodstream we considered shear stress values experienced by the surface.

In the body, the wall of blood vessels is constantly exposed to hemodynamic shear stress because of blood circulation. The shear stress value can be calculated by Poiseuille's law which defines it as proportional to blood viscosity η and inversely proportional to the third power of the vessel's radius R (eq.V.10), considering vessels as uniform tubes with laminar and steady flow Q. The velocity profile in these conditions is parabolic, with

maximum speed u_{max} on the tube axis, u=0 at the walls surface (no slip condition) and average velocity V = $u_{max}/2$.

$$\tau_s = \frac{4\mu Q}{\pi R^3} \tag{V.10}$$

$$u_{max} = \frac{2Q}{\pi R^2} \tag{V.11}$$

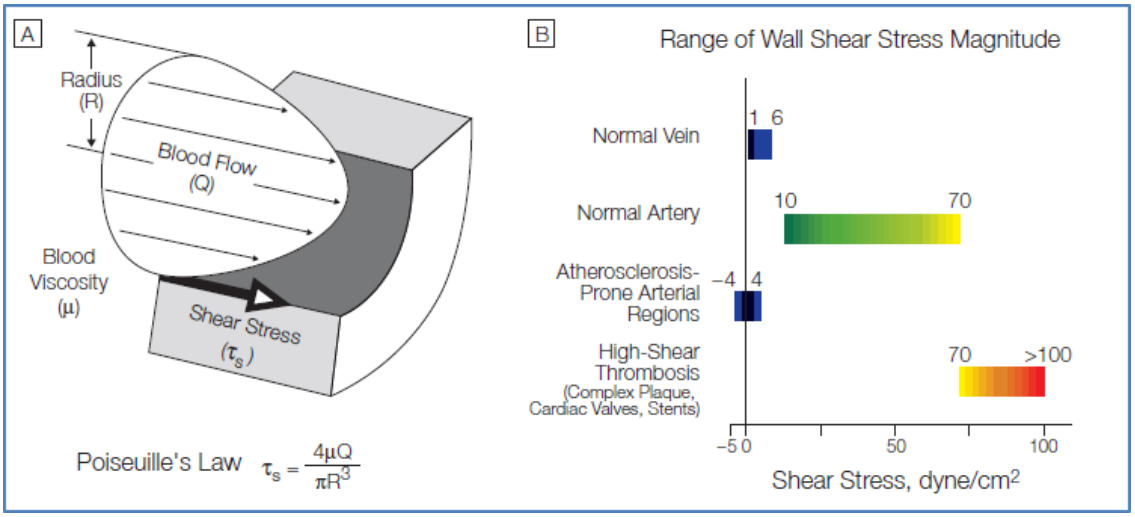

Figure V.39 – A) Scheme illustrating hemodynamic shear stress, dependent on the flow Q, on the walls of a blood vessel. B) Diagram showing the range of shear stress magnitudes in the vasculature and in cases of low-shear and high-shear pathologies. Reproduced from [221]

These equations can give a good approximation of the shear stress on the vessels walls, even if the blood is not properly a newtonian fluid (it contains cells which tend to concentrate at the center of the vessels leaving a depletion zone close to the walls) and its flow is not steady but pulsatile. Anyway, the Pouiseuille's law is an easier model which gives good estimations of the fluidodynamic of human circulatory system. This equation is valid only if the flow is laminar, that is if the Reynolds number R_e is < 2300. The R_e represents the balance between inertial forces and viscous forces within a moving fluid and it is used to predict flow patterns (laminar or turbulent flow). In most of blood vessels R_e value is much lower than 1, assuring laminar flow, with the exception of aorta and vena cava in which the high R_e (3000-4000) indicates a turbulent flow.

$$R_e = \frac{2R\rho V}{\mu} \tag{V.12}$$

V.7. Considerations about in vivo conditions: shear stress and particle flow dynamics

The Reynolds number can be calculated from equation V.12 where ρ is the fluid density, V is the average speed of the fluid, μ is the viscosity and R is the vessel radius.

Physiological shear stress values range from 1-6 Dyne/cm^{-2} in veins and aorta to 10-50 Dyne/cm^{-2} for arteries. Capillaries walls are usually exposed to shear stress values around 35-40 Dyne/cm^{-2}. There are some pathologic vascular conditions in which the shear stress can reach 70 Dyne/cm^{-2} and beyond or, on the contrary, drop to values close to zero [221]. The shear rate at the vessel axis, r = 0, is zero, so the blood cells and every circulating nanoparticle encounter a range of shear stresses and shear rates over the vessel's cross-section.

The mentioned values are shear stress values at the vessels walls, thus a nanoparticle traveling in bloodstream will experience such stress on its surface when it adheres to the cells forming the wall. Nevertheless, while it is moving in the blood flow, the shear stress on its surface will be much lower. In fact, for a sphere with radius r moving in a creeping flow (R_eł1)the surface shear stress is given by the following expression V.13 [222]:

$$\tau = \frac{3\mu V \sin\theta}{2r} \tag{V.13}$$

where θ is the angle between the point considered on the sphere surface and the flow direction (see figure V.40). The surface shear stress is zero for points lying in the flow direction and is maximum for points on the perpendicular direction. For this reason the sphere rolls while it is dragged by the fluid.

Calculating surface shear stress for a nanoparticle with radius r= 50 nm and considering blood viscosity as 3.5 mPa $\cdot$ s, we obtained values ranging from $5 \cdot 10^{-12}$ to $1.1 \cdot 10^{-9}$ Dyne/cm^2 (depending on blood velocity, which changes from arteries to capillaries). Thus, while traveling in the bloodstream, before adhesion to their target cells, nanoparticles undergo a very low surface shear stress, which allows to consider static measurements in undersaturated conditions as a good approximation for NPs behavior while injected in the circulatory system. On the other hand, as soon as a nanoparticle adsorbs onto a fixed surface, it will undergoes a shear stress several orders of magnitude higher.

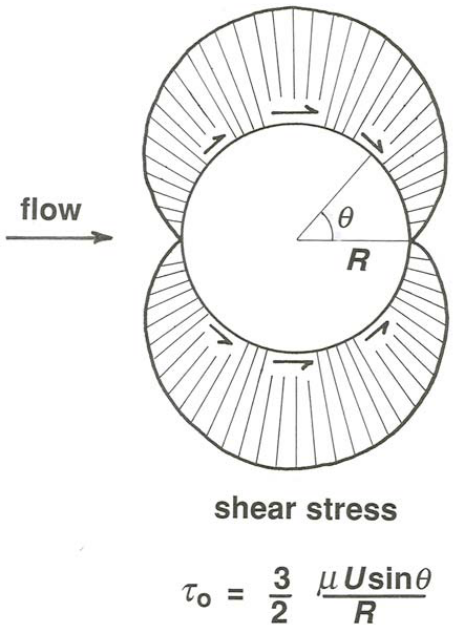

Figure V.40 – Distribution of shear stress on the surface of a sphere in a creeping flow.

V.8 Flow influence on dissolution rate

Nanoparticles employed as drug delivery carriers encounter several environments in the human body which differ for pH, biomolecules compositions and fluid dynamic conditions. The latter could play an important role on degradation process of NPs strongly influencing diffusion dynamics.

For these reasons we developed a special setup in which we coupled total internal reflection ellipsometry and microfluidics to study the dissolution of mesoporous silica under different flow conditions (V.41).

In this ellipsometric technique the shift of a plasmonic resonance peak is followed, and the value of refractive index of the material in contact with the fluid flow is extracted using a Cauchy dispersion as optical model for the mesoporous silica layer. As previously explained, the volume fraction of silica is calculated through a Bruggermann EMA model and the mass of dissolved silica M_t is obtained. The plasmon peak shifts towards shorter wavelengths during the dissolution process, due to a decrease in the refractive index of the layer probed by the evanescent wave.

To compare flow conditions applied with those of bloodstream we chose flow values to have physiological relevant shear stress values on the silica surface (1-35 Dyne/cm^2). To calculate the shear stress we used the following equation, derived from Stokes law in the

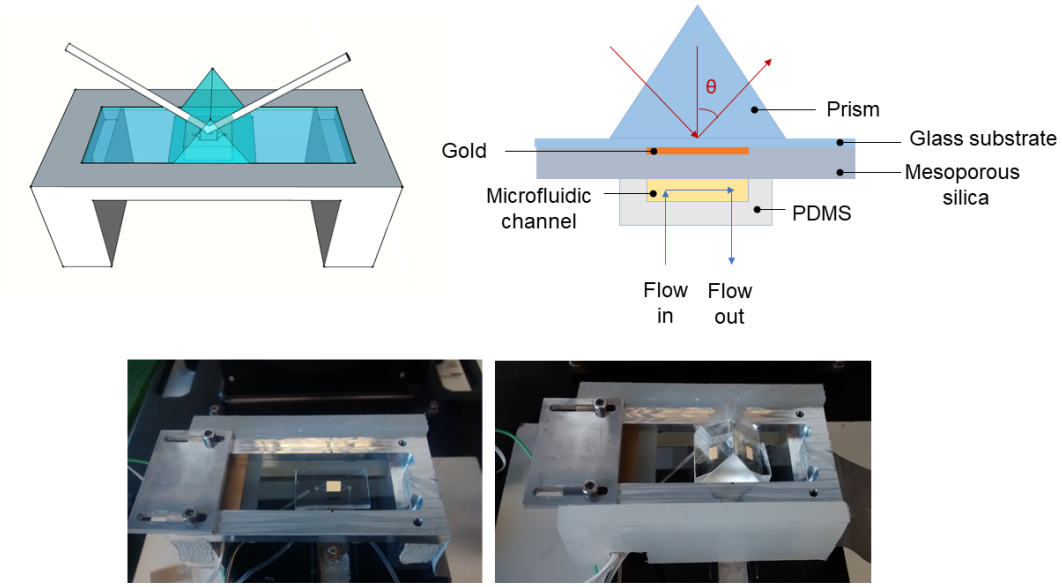

Figure V.41 – Setup to perform total internal reflection ellipsometry under flow conditions. The mesoporous silica film is deposited onto a glass substrate previously covered with a gold layer, the liquid is flowed through the microfluidic cell.

case of a laminar flow between two parallel plates:

$$\tau = \frac{6\mu Q}{h^2 w} \tag{V.14}$$

where h is the height of the microfluidic channel (30 μm) and w is the width (4.8 mm). However, we faced many problems of fabrication in the realization and optimization of the setup, as reported in Chapter 4.

Finally we found a robust protocol for sample preparation, but some difficulties persisted because the setup is pretty complicated and would need a calibrated stage and liquid cell to eliminate all the incertitudes due to the position and alignment of the different components.

The measurements in TIRE mode need a correction of ellipsometric function Δ and Ψ because of the prism presence. In fact, their value will be slightly shifted. Thus, it is important to set these offset for every experiment, otherwise the fitting of the data will not be possible. Moreover, the angle has also an offset, due to refraction inside the prism. These are fitting parameters to add to the layer parameters we want to find (refractive index, thickness), making the fitting process delicate. An offset has to be fixed at the beginning of the experiments and then only layer parameters should be fitted.

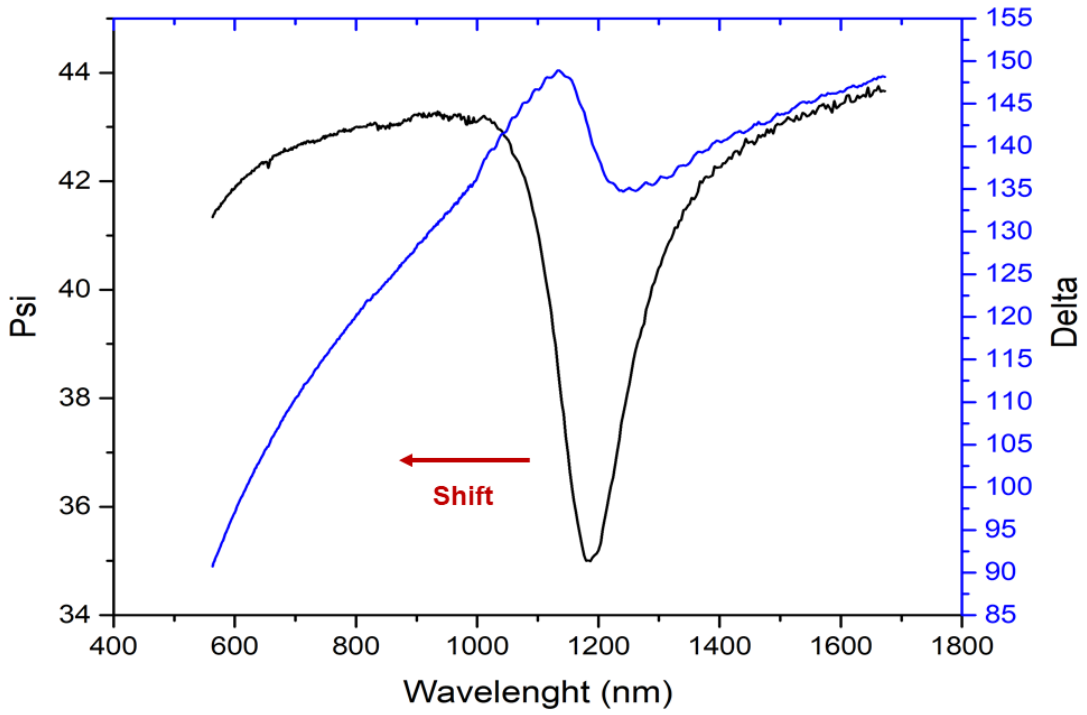

Figure V.42 – $\Psi(\lambda)$ and $\Delta(\lambda)$ spectra acquired in total internal reflection ellipsometry (TIRE). At the plasmon resonance wavelength the reflected intensity Ψ reaches its minimum value and the phase Δ shows a marked drop.

However, sometimes it is necessary to move the setup during experiments (because of a liquid leak for example) and than the offset won't be correct anymore.
Another important issue is air bubbles. If air bubbles enter in the microfluidic channel and stick to the surface the plasmon peak loses its intensity and sharpness until bubbles are removed. This happened very often and sometimes it took some minutes to remove the bubbles. For this reason following a dynamic experiment, fitting refractive index and thickness vs time, was sometimes complicated.
For all these reasons, we will comment only raw data from TIRE (Δ shift vs time) without extrapolating optical properties nor silica dissolved amount.
In TIRE $\Psi(\lambda)$ spectra resembles typical SPR curve, with the reflected intensity reaching the minimum at the plasmon resonance conditions, while the $\Delta(\lambda)$ spectra showed a drop in the phase near the resonance. The wavelenght of the minimum Ψ value will shift during the dissolution and so will do the Δ drop. This gives a possibility of kinetics study by following the spectral shifts of Ψ and Δ during the dissolution process. Usually the shift in Δ is higher that in Ψ, for this reason it is often the one selected to monitor the kinetics.

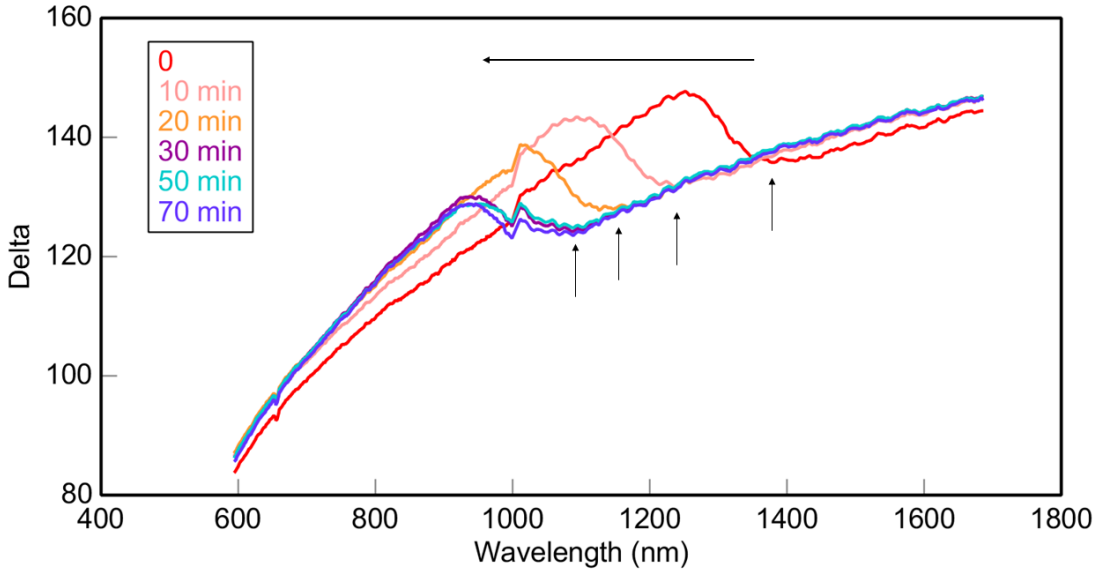

Figure V.43 – Series of TIRE $\Delta(\lambda)$ spectra corresponding to the dissolution of mesoporous silica in horse serum, with a flow rate of 600 μL/min and a surface shear stress of 17 Dyne/cm^2.

Plotting the λ value of the minimum in Δ function versus time we could evaluate the dissolution kinetics looking at the time needed to reach a plateau. In fact, when *Delta* doesn't shift anymore it means that there are no more changes in the layer probed by the evanescent wave, thus the dissolution is complete.

Comparing the Δ shift of mesoporous silica samples, exposed to a PBS flow producing shear stress equivalent to 9.5 and 18 Dyne/cm^2, we didn't observe a difference in the kinetics, at least for the first 100 minutes (figure V.44). Nevertheless, paying attention to the curve concerning the higher value of shear stress, we noticed that the plateau started after 180 minutes, which is 3 times slower than equivalent experiments in static condition. There is only one possible explanation for this behavior and it concerns a temperature bias between TIRE experiments and static dissolution experiments. Indeed, we verified that our system was not well thermostatted, also because of the particularly low temperature (12°C) experienced in the laboratory at the moment of the experiments. Moreover, the temperature in the microfluidic channel changed with the flow rate, making difficult to compare different experiments.

We finally found a method to keep the temperature at the desired value, passing the microfluidic tubes inside a thermostatted metallic tube before entering the microfluidic device. Unfortunately, we didn't have enough time to repeat experiments in PBS and we

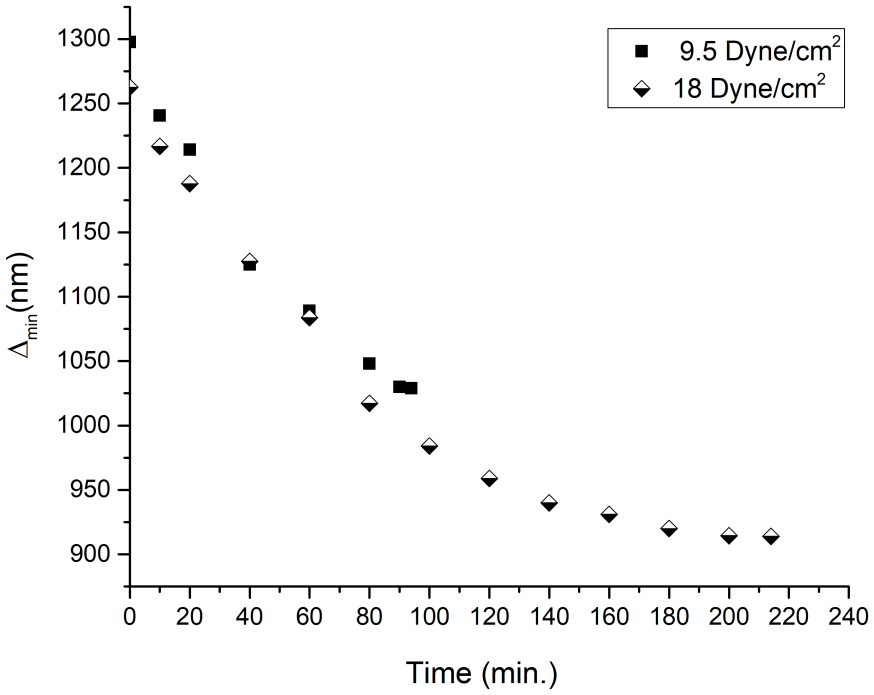

Figure V.44 – Wavelength of the minimum value of Δ vs time for mesoporous silica films exposed to a PBS flow, causing a surface shear stress of 9.5 and 18 Dyne/cm^2.

directly passed to experiments in real biological fluids such as serum and blood.

V.9 Dissolution in real biological fluids

We developed a special setup for TIRE because we wanted to perform dissolution experiments in real biological fluids, which usually are not transparent and can't be employed in standard reflection ellipsometry.

V.9.1 Serum

Thus, we tested mesoporous silica degradation when in contact to horse blood serum at three different shear stress values: 4, 17 and 35 Dyne/cm^2, corresponding to the shear stress on the wall of veins, arteries and capillaries, respectively.
Serum is blood plasma from which clotting proteins have been removed, it contains all the other blood proteins plus electrolytes, antibodies, antigens, and hormones. It doesn't contain cells.
Plotting the Δ shift versus time we can see an important influence of the flow rate, as reported in figure V.45. In fact, for the lower shear stress value, the plateau was reached after 60 min, for a shear stress of 17 Dyne/cm^2 after 30 minutes and for the higher value of shear stress (35 Dyne/cm^2) the Δ minimum is stable after only 20 minutes.
The collected data showed a strong influence of the flow rate on the dissolution rate of mesoporous silica. Indeed, considering the model of Noyes-Whitney (section V.3.1), increasing the flow means decreasing the thickness of diffusion layer h which is inversely proportional to k (see figure V.46). It is reasonable to think that when h has reached its minimum value, further flow increase will bring no acceleration to the dissolution rate. In the performed experiments, the increase of shear stress between 4 and 17 Dyne/cm^2 caused a bigger decrease in dissolution rate than the change between 17 and 35 Dyne/cm^2. These results suggested that an high surface shear stress can increase the dissolution rate of mesoporous silica of more than 10 times (compared to a static case where shear stress is zero or close to zero), even in presence of surface adsorbed biomolecules.
Fixing the layer thickness at 150 nm, we fitted the variation of refractive index δn during dissolution. The absolute value of refractive index doesn't represent the effective n of the mesoporous silica layer, because in the TIRE configuration the surface plasmon resonance responds to the total variation within its sensibility range, being not able to distinguish the silica layer from the adsorbed proteins. Anyway the variation in refractive index between the starting point and the end of dissolution reflects the kinetics of the process, even if it is not possible to extrapolate a dissolved silica amount.
Plotting the refractive index variation $\delta n/\delta t$ versus the average flow speed V, we found

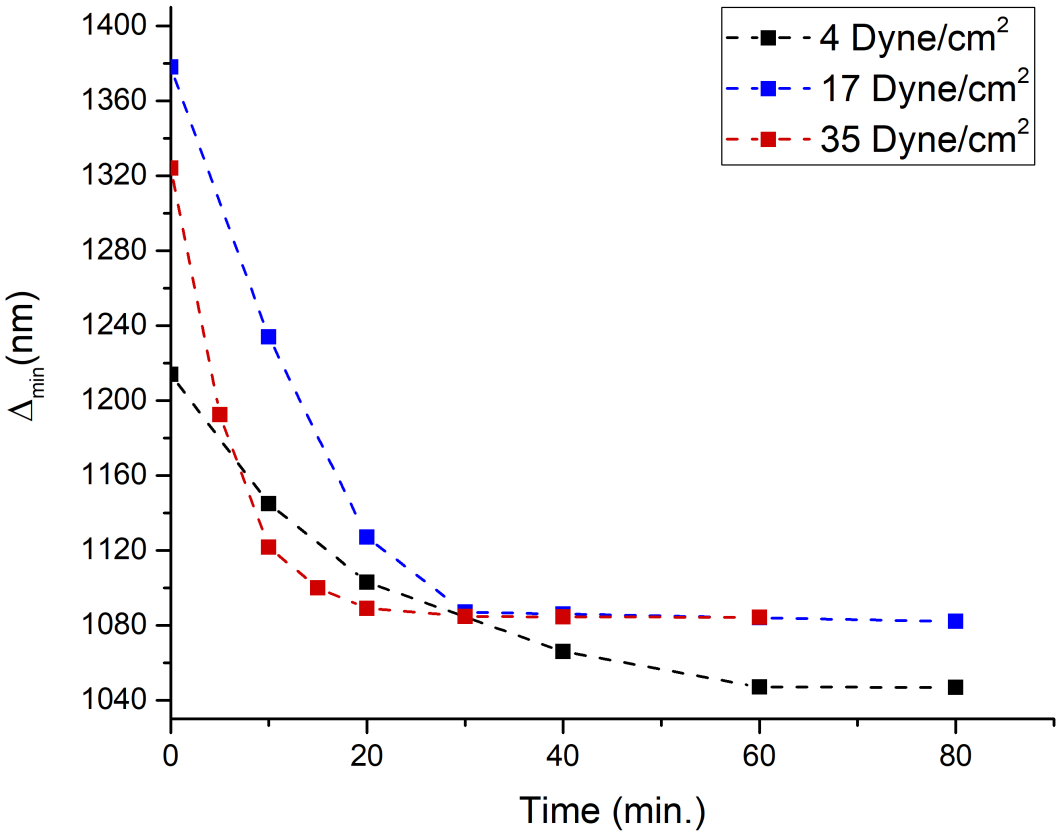

Figure V.45 – Wavelength of the minimum value of Δ vs time for mesoporous silica films exposed to horse serum, with a surface shear stress of 4, 17 and 35 Dyne/cm^2. Dashed lines are reported as guide for the eyes.

a square root dependence (figure V.47). This agrees with the model developed by Levich [204], which found a dissolution rate proportional to the square root of average fluid velocity, in the case of a planar surface dissolution with a liquid flow parallel to the surface.

Extrapolating the $\delta n/\delta t$ in static condition ($V = 0$) for mesoporous silica dissolution in serum (red dot in figure V.47, we found a value of $1.72 \cdot 10^{-4}$ min^{-1}. The static measurement in standard reflection ellipsometry employing the liquid cell (not TIRE mode) is not possible using serum as medium, because the light absorption from the liquid is high and the intensity of the reflected beam is too low when it comes to the detector. Nevertheless, the $\delta n/\delta t$ of the silica static dissolution in the presence of BSA protein is $2 \cdot 10^{-4}$ min^{-1}, a value very close to the one extrapolated for serum employing

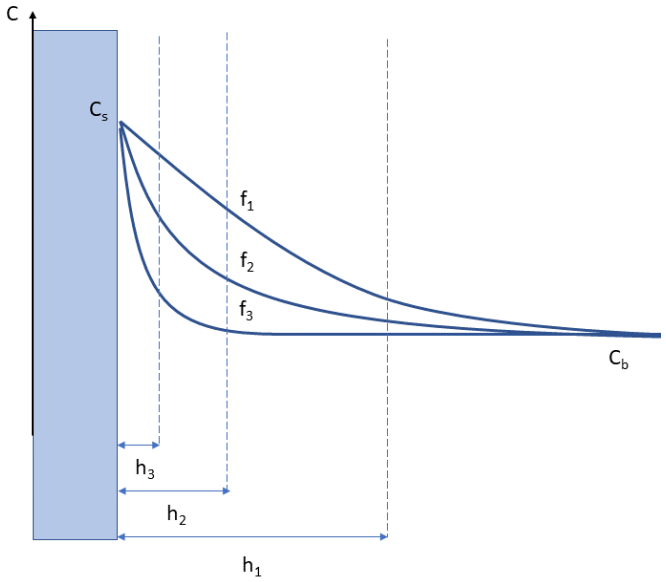

Figure V.46 – Concentration profiles vs distance of a dissolving solid substance exposed to different liquid flow rates, with $f_1 < f_2 < f_3$, representing the model of Noyes-Whitney in which an unstirred liquid boundary layer of thickness h is in contact with the solid surface. Through this boundary layer concentration decreases linearly from saturation value C_s to the bulk value C_b. If the bulk fluid is stirred by a flow, the thickness of the boundary layer diminishes.

the fitting equation. If we assume that serum and concentrated BSA solution will behave in a similar way respect to silica dissolution, with proteins acting as a diffusional barrier, the good agreement with BSA data from static measurements means that the obtained results may have some errors, due to setup differences, but the overall trend is correct.

This result has important consequences for drug delivery vectors, in fact, when the nanoparticles are traveling in the bloodstream they undergo a very low surface shear stress (equation V.13) and we can consider their dissolution rate almost equal to the one measured in static conditions. When they adhere to the membrane of target cells they are part of the vessel wall and they will experience the wall shear stress ($\approx$ 10 order of magnitude higher), dissolving much faster. This is ideal in drug delivery applications, because it means that any vector for which the drug release is related to matrix dissolution will have enough time to reach its target without degrading itself and when it arrives in the diseased area it will release its cargo quickly.

The registered kinetics for dissolution in serum were 6-12 times faster than the one measured in BSA solution and static condition. These experiments suggested that mesoporous silica dissolution *in vivo* could be much faster than usually reported in literature. The

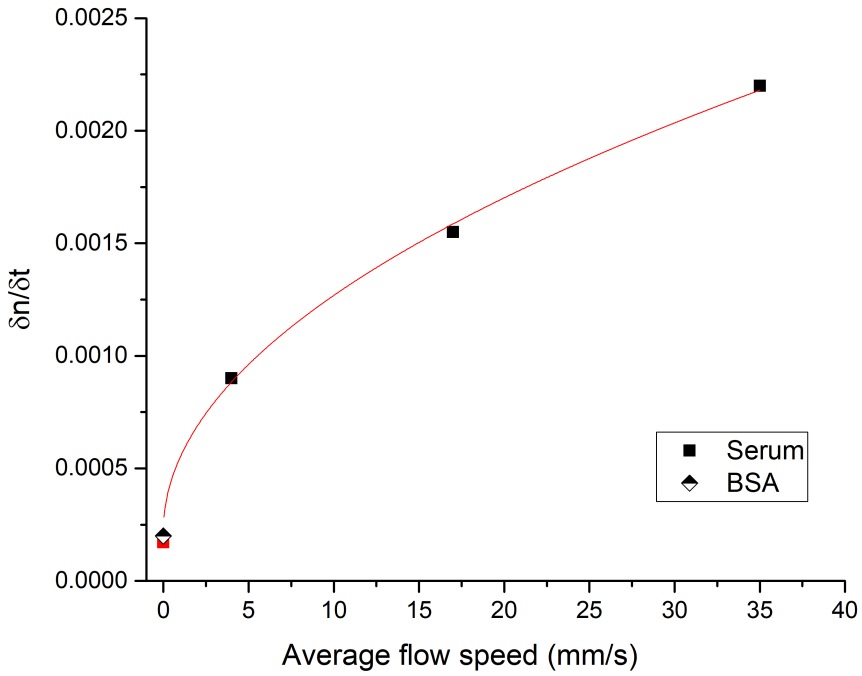

Figure V.47 – Refractive index variation $\delta n/\delta t$ versus the average flow speed V for mesoporous silica dissolution in horse serum. Experimental points (black dots) have been fitted with a power law $y = a+bx^c$ with c=0.5. From the fitting equation has been extrapolated the $\delta n/\delta t$ for $V = 0$ (red dot). The black and white diamond dot is the value of $\delta n/\delta t$ for mesoporous silica dissolution in a concentrated solution of BSA (37 g/L in PBS), reported for comparison.

relation between surface shear stress and dissolution rate could be used to predict the delivery kinetics accurately for each application, depending on the nanoparticle path in the body.

V.9.2 Blood

The interesting results obtained with serum pushed us to try a dissolution experiment in blood. We could obtain some pig blood stabilized with citrate-glucose anticoagulant from Dr. Serge Pin (LIONS, IRAMIS, DRF, CEA, CNRS, Université Paris-Saclay, France). The blood needed to be centrifuged (2000 rpm, 5min, 15 °C) to remove the leukocytes. In fact, these cells have diameters of 10-30 μm and block the microfluidic channel (which height is 30 μm), causing a huge increase of pressure which eventually detaches the cell from the sample. Centrifugation separates plasma (on the top) and erythrocytes (on the bottom). Between these two phases there is a thin white layer called "buffy coat" which

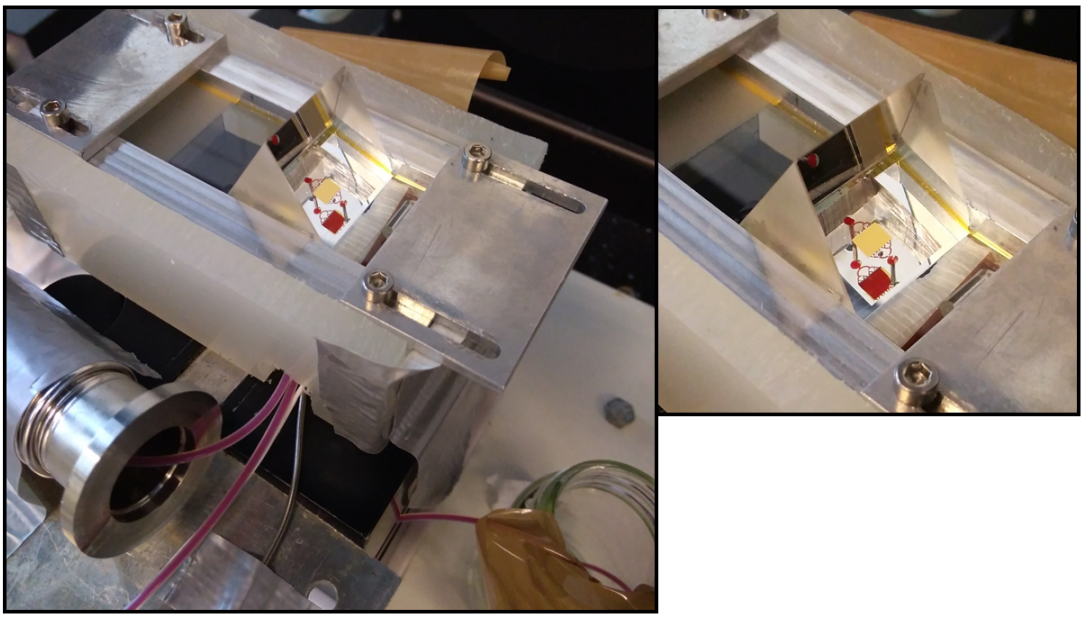

Figure V.48 – Photos of the TIRE setup to analyze silica samples in pig blood.

contains platelets and leukocytes. After removal of buffy coat the blood could be injected in the microfluidic channel and flowed at different speed for some hours without causing any blockage.

However, the TIRE spectra showed a plasmon resonance shifting towards longer wavelengths during dissolution and diminishing its intensity (figure V.49). This is due to the adsorption of red cells on the silica surface which balances the effect of dissolution on the refractive index of the probed layer. In fact, bulk dissolution of the mesoporous film decreases the refractive index of the layer in contact with the gold but molecules and cell adsorption increase n. If the contribution of proteins didn't mask the evolution due to the dissolution process, this seemed to happen for blood cells adsorption. Blood red cells are disc-shaped with a diameter of 6-8 μm and thickness of 2-2.5 μm and, in the real situation it will be most probably the nanoparticles to adsorb on their surface, given their relative dimensions. On the contrary, on our samples (flat thin films of some mm^2) the red cells saw a kind of infinite surface to adhere. The dimensions of the erythrocytes along with their high refractive index (1.4) shifted the plasmon resonance from 1148 to 1319 nm, masking all the successive evolutions due to silica dissolution. Throughout the experiment the plasmon resonance peak shifted back and forward, as reported in figure V.50, responding to adsorption and desorption (due to an high liquid flow rate) of red

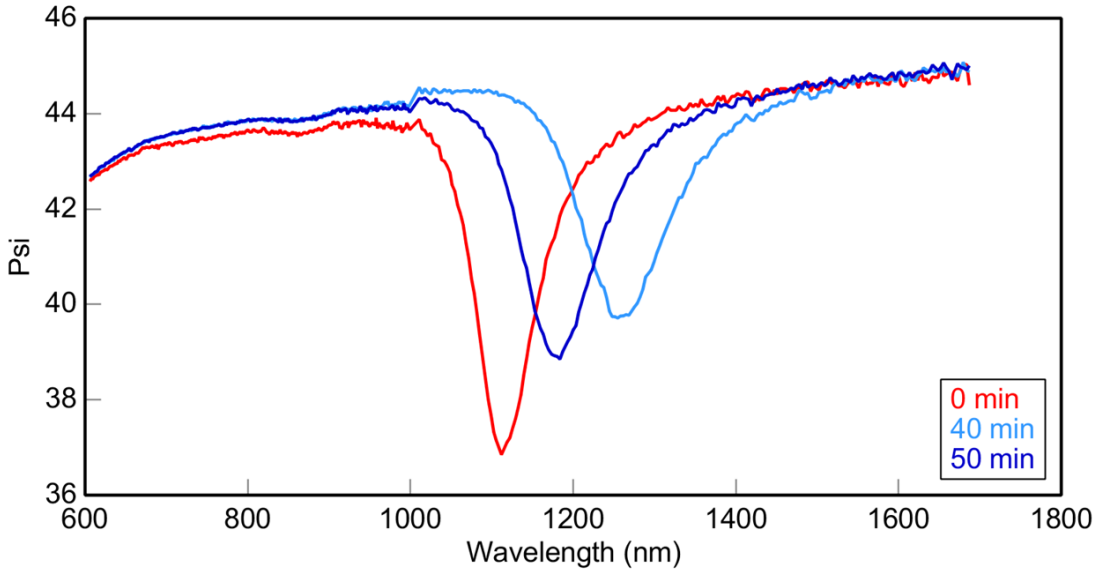

Figure V.49 – Series of TIRE $\Psi(\lambda)$ spectra of mesoporous silica dissolution in pig blood at 0, 40 and 50 minutes with a flow rate of 500 μL/min and a surface shear stress of 40 Dyne/cm^2. The minimum value of Ψ corresponding to the plasmon resonance shifted towards longer wavelength during dissolution, to return towards shorter wavelength later. Only three spectra are presented here for clarity but monitoring the plasmon shift during 120 minutes we observed several oscillations in both directions.

blood cells on the silica surface. After rinsing the surface with water flow, we still noticed red cells adsorbed on the surface, visible because of the red color of hemoglobin (figure V.51).

The experiments in blood displayed one limit of TIRE technique: when two effects influences the plasmon resonance shift in opposites direction it's not possible to separate them and thus, it is not possible to rely on this kind of analysis to follow the refractive index evolutions and reaction kinetics.

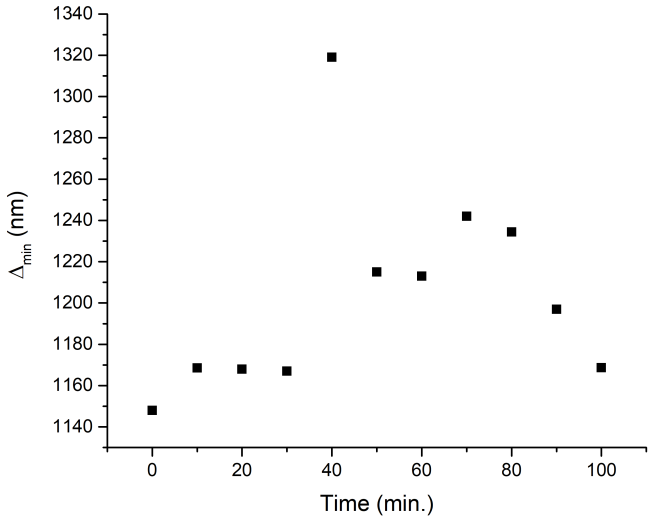

Figure V.50 – Wavelength of the minimum value of Δ vs time for mesoporous silica films exposed to pig blood, with a surface shear stress of 40 Dyne/cm^2. Any defined trend is visible.

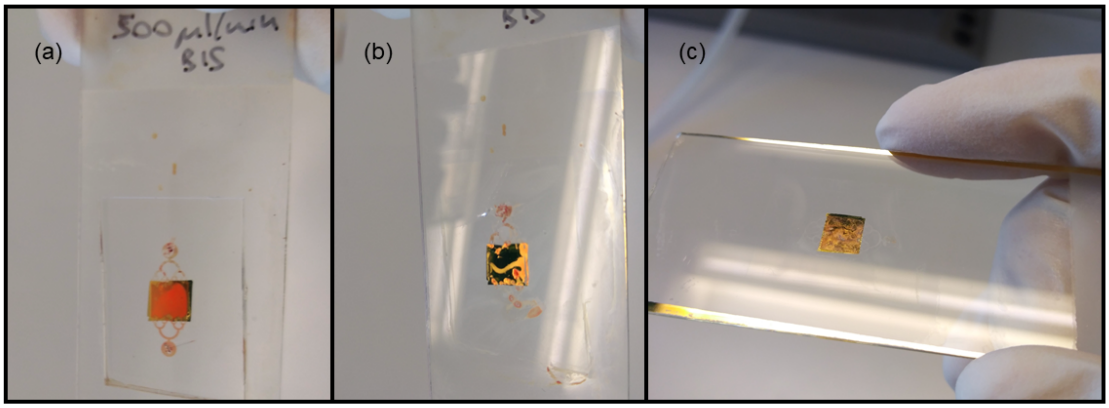

Figure V.51 – Photos of the silica sample analyzed with a blood flow of 500 μL/min and shear stress 40 Dyne/cm^2. (a) before microfluidic cell removal (b) after the cell removal (c) after rinsing with water

V.10 Conclusions

We monitored mesoporous silica thin films dissolution kinetics in physiologically relevant conditions through *in situ* ellipsometry employing two different setup. We used a liquid cell in standard reflection ellipsometry to soak the samples in transparent liquids such as PBS and a concentrated protein solution (BSA 37 g/L in PBS). We also designed and realized a setup to perform total internal reflection ellipsometry (TIRE) to analyze silica thin films in non-transparent biological fluids such as serum and blood. We employed a microfluidic cell to investigate different flow conditions and their influence on dissolution. The commercial liquid cell setup, employed with simpler media, allowed us to address deeply the factors playing on porous silica dissolution.

In undersaturated conditions, the dissolution process showed a very fast kinetics, in which more than 85 % of the starting material is degraded within 2 hours. The dissolution rate was found to be linearly dependent on surface, but the porous structure can cause a diffusion lag time if it exists some pore blocking.

The mesoporous structure seems not to influence dramatically the kinetics, when surface areas are equivalent, even if there are some little differences. In particular, a structure with high tortuosity can dissolve slower because the dissolution obeys the Noyes-Whitney law, which relies on diffusion, and if diffusion is hindered dissolution will be slower. At the same time this could be a factor which inserts a lag time in the matrix dissolution (and in the embedded drug release, consequently). Playing on the mesoporous structure and porous volume one could obtain a phase of slow degradation until the porous network becomes interconnected enough to allow free diffusion.

When designing porous particles as nanocarriers it has to be remembered that a high porous volume allows for elevated drug charge but it also implies faster degradation kinetics in liquids, as presented results confirmed. To thermally treat silica porous materials is not a very efficient way to improve their stability and, in the case of nanoparticles, it can be a tricky step which favors aggregation. On the other hand, to play on their accessible surface and volume allows to tune their dissolution kinetics.

We verified that the observed kinetics are respected even in the case of films made of nanoparticles and so the surface curvature should not be critical when evaluating degradation kinetics.

Analyzing hybrid silica carrying aminopropyl groups we found two different regimes of dissolution. In the first one, the dissolution rate is equivalent to the pure silica one, while after the 50% of silica mass is dissolved the rate slowed down and XPS analysis found an enrichment in N content. Thus, we inferred that in a first phase was dissolved the part

of silica which is not affected by the inductive effect of the organic groups and later the remained material which has a much slower dissolution kinetics.

In order to study a mesoporous silica matrix hosting a cargo, we choose to reproduce a quantum rattle structure in which a mesoporous silica layer hosted gold clusters of size < 2 nm, a system successfully employed as a theranostic platform for cancer. We had interesting results that denied a fast release of the clusters, which stayed embedded in the matrix during dissolution. We observed some aggregation phenomena during the dissolution process but most gold particles maintained sizes ≤ 5 nm, which should allow their excretion by renal clearance.

Performing experiments in protein solution we noticed a very efficient diffusional barrier constituted by surface adsorbed protein which slowed down the silica dissolution by a 5x factor. This behavior was confirmed also for hybrid silica carrying aminopropyl groups. The silica layers where templating surfactant was removed by solvent extraction displayed protein aggregates on their surface. This behavior was due to the strong interaction between CTAB and BSA, which leads to protein unfolding and aggregation even if the CTAB is present in small amount. It pointed out the extreme importance of employing a washing protocol able to completely remove the surfactant from mesoporous silica NPs employed as drug carriers, to avoid damage to biomolecules. Hybrid silica films didn't show this behavior, demonstrating a more efficient CTAB extraction due to the repulsive electrostatic interactions between CTAB and protonated amine groups on silica.

With the TIRE setup, even if we encountered many experimental problems, we could observe an important effect of the flow rate in dissolution kinetics in real biological media. This could be of major importance when designing a carrier to predict its release and degradation time considering its path inside the body, where it is exposed to many different flow conditions.

The experiment conducted in blood showed a limit of the TIRE technique employed, because red blood cell adsorption on the silica surface masked the plasmon shift used to monitor dissolution. Total internal reflection ellipsometry is thus a powerful tool to study kinetics in all biological media which don't contain cells, but it can't be employed with blood as liquid medium.

V.11 Future perspectives

The conducted work allowed to obtain many interesting informations on mesoporous silica dissolution in biological relevant media. The investigation should be continued to address

deeply some aspects.

For example, it would be interesting to synthesize some pegylated silica surface and look at the influence of surface chemistry on dissolution. Unfortunately, we were not able to functionalized the mesoporous silica only on the surface and what we obtained was an hybrid material containing polymer brushes on the surface and in the pores. For future perspective, some efforts to optimize the grafting process to obtain the desired material are necessary.

The TIRE technique showed great potential to perform kinetics studies in real biological media and under controlled flow conditions. Nevertheless, a calibrated setup is necessary to assure reproducibility and limit errors in the fit process. Temperature control is mandatory, unfortunately, once found the method to guarantee a stable temperature we didn't have enough time to perform large series of experiments with different surface chemistry and different biological media. This will be done in the future, to extrapolate general trends able to predict porous nanoparticles *in vivo* degradation.

General Conclusions

The main objective of this thesis was to investigate the dissolution processes of mesoporous silica in biological environment, since the employ of silica mesoporous nanoparticles as theranostic platforms is very promising and attracts many attentions in drug-delivery research.

In particular, we wanted to determine the influence of protein surface adsorption on the silica degradation, because often the data reported in literature on NPs dissolution are taken in buffered solutions which don't contain biomolecules. Thus, the behavior of silica nanoparticles *in vivo* can diverge sensibly from kinetics registered in buffer solutions, because the interface interactions are very different. Another goal of this project was to reproduce flow conditions which mimic the bloodstream and evaluate the impact of the flow on protein adsorption and on the overall material dissolution rate.

To investigated the silica-bio interfacial structure and its dynamics was chosen to work on thin films, which can be analyzed and modeled through in situ ellipsometry, to obtain detailed information on their structural evolution in time.

We carried out a detailed study on dip-coating deposition technique to obtain perfectly reproducible sol-gel silica mesoporous films. This study brought additional knowledge on this widely employed deposition method and allowed mastering an important fabrication step.

Since the drug delivery vectors constituted by nanoparticles have often a PEG-surface layer on the surface to minimize protein adsorption, we tried to obtain the same core-shell structure on films, grafting PEGylated polymer brushes on hybrid silica surface. Nevertheless, we couldn't obtain the desired outer polymer shell but we got an hybrid material in which polymers grew in the pores. This kind of material was difficult to analyzed through ellipsometry and, as a future perspective, efforts should be made to elaborate a better grafting protocol and to identify complementary analysis techniques, such as neutron reflectivity or quartz microbalance.

We performed dissolution experiments in PBS at 37° through a liquid cell, finding that

mesoporous silica dissolution follows the theory elaborated by Noyes and Whitney and expanded by Nernst and Brunner, in which dissolution is limited by saturation and its rate is proportional to the specific surface of the material. Diffusion processes have a central role in this dissolution mechanism and we verified that the porous structure can influence the dissolution rate by hindering diffusion.
We observed a huge decrease in silica dissolution rate in presence of proteins, which form a barrier to diffusion on the silica surface.
In order to mimic more closely *in vivo* environments, we wanted to perform dissolution experiments in complex, real biological fluids. This introduced a challenge because that sort of liquids (serum,blood) absorb and scatter light and ellipsometry can't be performed through them. Thus, we designed and developed a setup to employ ellipsometry in total internal reflection mode which allows working with opaque liquids. We proposed an innovative coupling of TIRE technique with microfluidics, which revealed itself very complicated in terms of fabrication. We spent a huge amount of time to optimize the sample preparation and the measurements, but finally we could perform dissolution experiments in real biological fluids under flow conditions. Even if we didn't have time to deeply exploit this kind of setup we obtained valuable informations on mesoporous silica behavior in flow, which can be employed to predict *in vivo* fate of nanoparticles and their cargo. In fact, we displayed that dissolution rate increases with the root-square of flow average velocity, as theorized by Levich. Nanoparticles undergo a relatively weak shear stress due to the flow when they are traveling in the bloodstream but once they adhere to their target they experience a flow shear stress from 5 to 40 times higher. Being able to predict their dissolution rate with different surface shear stress conditions will allow the design of more efficient nanocarriers once known their biodistribution.
This kind of setup, to the best of our knowledge, was never employed before and proved itself very powerful. To fully exploit it and make it a routine tool, it is still necessary to perform some experimental optimization on fabrication and calibration processes. However, employing this alternative and innovative system we could unify in a single model theory the dissolution behavior of mesoporous silica, in saturated or undersaturated media, in absence or presence of biomolecules and liquid flow and we could work in conditions as close as possible to real biological environment.
We believe that this approach can provide extensive informations on nanomaterials behavior in *in vivo*-like conditions, coupling the sensitivity of total internal reflection ellipsometry for interfaces to the flow conditions control of microfluidics.

Bibliography

[1] Richard P. Feynman . There's Plenty of Room at the Bottom. *Engineering and Science*, 23 (5):22–36, 1960. 1

[2] Bong Geun Chung, Lifeng Kang, and Ali Khademhosseini. Micro- and nanoscale technologies for tissue engineering and drug discovery applications. *Expert Opinion on Drug Discovery*, 2(12):1653–1668, December 2007. 2

[3] C. Y. Xu, R. Inai, M. Kotaki, and S. Ramakrishna. Aligned biodegradable nanofibrous structure: a potential scaffold for blood vessel engineering. *Biomaterials*, 25(5):877–886, February 2004. 2

[4] K. Tuzlakoglu, N. Bolgen, A. J. Salgado, M. E. Gomes, E. Piskin, and R. L. Reis. Nano- and micro-fiber combined scaffolds: A new architecture for bone tissue engineering. *Journal of Materials Science: Materials in Medicine*, 16(12):1099–1104, December 2005. 2

[5] X Zong, H Bien, C Chung, L Yin, D Fang, B Hsiao, B Chu, and E Entcheva. Electrospun fine-textured scaffolds for heart tissue constructs. *Biomaterials*, 26(26):5330–5338, September 2005. 2

[6] Melvin Schindler, Ijaz Ahmed, Jabeen Kamal, Alam Nur-E-Kamal, Timothy H. Grafe, H. Young Chung, and Sally Meiners. A synthetic nanofibrillar matrix promotes in vivo-like organization and morphogenesis for cells in culture. *Biomaterials*, 26(28):5624–5631, October 2005. 2

[7] Nasim Annabi, Ali Tamayol, Su Ryon Shin, Amir M. Ghaemmaghami, Nicholas A. Peppas, and Ali Khademhosseini. Surgical materials: Current challenges and nano-enabled solutions. *Nano Today*, 9(5):574–589, October 2014. 2

[8] Séverine Rose, Alexandre Prevoteau, Paul Elzière, Dominique Hourdet, Alba Marcellan, and Ludwik Leibler. Nanoparticle solutions as adhesives for gels and biological tissues. *Nature*, 505(7483):382–385, December 2013. 2

[9] Anne Meddahi-Pellé, Aurélie Legrand, Alba Marcellan, Liliane Louedec, Didier Letourneur, and Ludwik Leibler. Organ Repair, Hemostasis, and In Vivo Bonding of Medical Devices by Aqueous Solutions of Nanoparticles. *Angewandte Chemie International Edition*, 53(25):6369–6373, June 2014. 2

[10] Huilin Shao, Tae-Jong Yoon, Monty Liong, Ralph Weissleder, and Hakho Lee. Magnetic nanoparticles for biomedical NMR-based diagnostics. *Beilstein Journal of Nanotechnology*, 1:142–154, December 2010. 3

[11] Miriam Colombo, Susana Carregal-Romero, Maria F. Casula, Lucía Gutiérrez, María P. Morales, Ingrid B. Böhm, Johannes T. Heverhagen, Davide Prosperi, and Wolfgang. J. Parak. Biological applications of magnetic nanoparticles. *Chemical Society Reviews*, 41(11):4306, 2012. 3

[12] Tae-Jong Yoon, Hakho Lee, Huilin Shao, and Ralph Weissleder. Highly magnetic core-shell nanoparticles with a unique magnetization mechanism. *Angewandte Chemie (International Ed. in English)*, 50(20):4663–4666, May 2011. 3

[13] Ajay Kumar Gupta and Mona Gupta. Synthesis and surface engineering of iron oxide nanoparticles for biomedical applications. *Biomaterials*, 26(18):3995–4021, June 2005. 3

[14] Carlee E. Ashley, Eric C. Carnes, Genevieve K. Phillips, David Padilla, Paul N. Durfee, Page A. Brown, Tracey N. Hanna, Juewen Liu, Brandy Phillips, Mark B. Carter, Nick J. Carroll, Xingmao Jiang, Darren R. Dunphy, Cheryl L. Willman, Dimiter N. Petsev, Deborah G. Evans, Atul N. Parikh, Bryce Chackerian, Walker Wharton, David S. Peabody, and C. Jeffrey Brinker. The targeted delivery of multicomponent cargos to cancer cells by nanoporous particle-supported lipid bilayers. *Nature Materials*, 10(5):389–397, May 2011. 3, 17, 22

[15] N. Jaulin, M. Appel, C. Passirani, G. Barratt, and D. Labarre. Reduction of the uptake by a macrophagic cell line of nanoparticles bearing heparin or dextran covalently bound to poly(methyl methacrylate). *Journal of Drug Targeting*, 8(3):165–172, 2000. 3

[16] C. J. Coester, K. Langer, H. van Briesen, and J. Kreuter. Gelatin nanoparticles by two step desolvation–a new preparation method, surface modifications and cell uptake. *Journal of Microencapsulation*, 17(2):187–193, April 2000. 3

[17] Jason E. Fuller, Gregory T. Zugates, Lino S. Ferreira, Hooisweng S. Ow, Nicholas N. Nguyen, Ulrich B. Wiesner, and Robert S. Langer. Intracellular delivery of core-shell fluorescent silica nanoparticles. *Biomaterials*, 29(10):1526–1532, April 2008. 3

[18] Liman Cong, Motohiro Takeda, Yohei Hamanaka, Kohsuke Gonda, Mika Watanabe, Masutaka Kumasaka, Yoshio Kobayashi, Masaki Kobayashi, and Noriaki Ohuchi. Uniform Silica Coated Fluorescent Nanoparticles: Synthetic Method, Improved Light Stability and Application to Visualize Lymph Network Tracer. *PLOS ONE*, 5(10):e13167, October 2010. 3

[19] Torjus Skajaa, Yiming Zhao, Dave J. van den Heuvel, Hans C. Gerritsen, David P. Cormode, Rolf Koole, Matti M. van Schooneveld, Jan Andries Post, Edward A. Fisher, Zahi A. Fayad, Celso de Mello Donega, Andries Meijerink, and Willem J. M. Mulder. Quantum Dot and Cy5.5 Labeled Nanoparticles to Investigate Lipoprotein Biointeractions via Förster Resonance Energy Transfer. *Nano letters*, 10(12):5131–5138, December 2010. 3

[20] Zoran Popović, Wenhao Liu, Vikash P. Chauhan, Jungmin Lee, Cliff Wong, Andrew B. Greytak, Numpon Insin, Daniel G. Nocera, Dai Fukumura, Rakesh K. Jain, and Moungi G. Bawendi. A nanoparticle size series for in vivo fluorescence imaging. *Angewandte Chemie (International ed. in English)*, 49(46):8649–8652, November 2010. 3

[21] Mark Stroh, John P Zimmer, Dan G Duda, Tatyana S Levchenko, Kenneth S Cohen, Edward B Brown, David T Scadden, Vladimir P Torchilin, Moungi G Bawendi, Dai Fukumura, and Rakesh K Jain. Quantum dots spectrally distinguish multiple species within the tumor milieu in vivo. *Nature medicine*, 11(6):678–682, June 2005. 3

[22] Sungjee Kim, Yong Taik Lim, Edward G. Soltesz, Alec M. De Grand, Jaihyoung Lee, Akira Nakayama, J. Anthony Parker, Tomislav Mihaljevic, Rita G. Laurence, Delphine M. Dor, Lawrence H. Cohn, Moungi G. Bawendi, and John V. Frangioni. Near-infrared fluorescent type II quantum dots for sentinel lymph node mapping. *Nature Biotechnology*, 22(1):93–97, January 2004. 3

[23] Leo Y. T. Chou, Kevin Ming, and Warren C. W. Chan. Strategies for the intracellular delivery of nanoparticles. *Chem. Soc. Rev.*, 40(1):233–245, 2011. 4

[24] Nishit Doshi and Samir Mitragotri. Designer Biomaterials for Nanomedicine. *Advanced Functional Materials*, 19(24):3843–3854, December 2009. 4

[25] William B. Liechty, David R. Kryscio, Brandon V. Slaughter, and Nicholas A. Peppas. Polymers for Drug Delivery Systems. *Annual Review of Chemical and Biomolecular Engineering*, 1(1):149–173, June 2010. 4

[26] Xiaohua Huang, Ivan H. El-Sayed, Wei Qian, and Mostafa A. El-Sayed. Cancer Cell Imaging and Photothermal Therapy in the Near-Infrared Region by Using Gold Nanorods. *Journal of the American Chemical Society*, 128(6):2115–2120, February 2006. 5

[27] I. I. Slowing, B. G. Trewyn, S. Giri, and V. S.-Y. Lin. Mesoporous Silica Nanoparticles for Drug Delivery and Biosensing Applications. *Advanced Functional Materials*, 17(8):1225–1236, May 2007. 5

[28] Daniel Bobo, Kye J. Robinson, Jiaul Islam, Kristofer J. Thurecht, and Simon R. Corrie. Nanoparticle-Based Medicines: A Review of FDA-Approved Materials and Clinical Trials to Date. *Pharmaceutical Research*, 33(10):2373–2387, October 2016. 5

[29] C. Lee Ventola. Progress in Nanomedicine: Approved and Investigational Nanodrugs. *P & T: A Peer-Reviewed Journal for Formulary Management*, 42(12):742–755, December 2017. 6, 8, 13

[30] Joseph M. Caster, Artish N. Patel, Tian Zhang, and Andrew Wang. Investigational nanomedicines in 2016: a review of nanotherapeutics currently undergoing clinical trials: Investigational nanomedicines in 2016. *Wiley Interdisciplinary Reviews: Nanomedicine and Nanobiotechnology*, 9(1):e1416, January 2017. 6

[31] Nanotechnology Characterization Laboratory: National Cancer Institute US National Institues of Health. Available from: http://ncl.cancer.gov/., 2016. 7

[32] ClinicalTrials.gov. Available at: https://clinicaltrials.gov., 2017. 8, 11

[33] Gang Bao, Samir Mitragotri, and Sheng Tong. Multifunctional Nanoparticles for Drug Delivery and Molecular Imaging. *Annual Review of Biomedical Engineering*, 15(1):253–282, July 2013. 9, 10

[34] Prashant K. Jain, Xiaohua Huang, Ivan H. El-Sayed, and Mostafa A. El-Sayed. Noble Metals on the Nanoscale: Optical and Photothermal Properties and Some Applications in Imaging, Sensing, Biology, and Medicine. *Accounts of Chemical Research*, 41(12):1578–1586, December 2008. 9

[35] Christopher J Gannon, Chitta Patra, Resham Bhattacharya, Priyabrata Mukherjee, and Steven A Curley. Intracellular gold nanoparticles enhance non-invasive radiofrequency thermal destruction of human gastrointestinal cancer cells. *Journal of Nanobiotechnology*, 6(1):2, 2008. 9

[36] Naomi Halas. Playing with Plasmons: Tuning the Optical Resonant Properties of Metallic Nanoshells. *MRS Bulletin*, 30(05):362–367, May 2005. 10

[37] L. R. Hirsch, R. J. Stafford, J. A. Bankson, S. R. Sershen, B. Rivera, R. E. Price, J. D. Hazle, N. J. Halas, and J. L. West. Nanoshell-mediated near-infrared thermal therapy of tumors under magnetic resonance guidance. *Proceedings of the National Academy of Sciences*, 100(23):13549–13554, November 2003. 10

[38] E. Phillips, O. Penate-Medina, P. B. Zanzonico, R. D. Carvajal, P. Mohan, Y. Ye, J. Humm, M. Gonen, H. Kalaigian, H. Schoder, H. W. Strauss, S. M. Larson, U. Wiesner, and M. S. Bradbury. Clinical translation of an ultrasmall inorganic optical-PET imaging nanoparticle probe. *Science Translational Medicine*, 6(260):260ra149–260ra149, October 2014. 12

[39] Kai Ma, Hiroaki Sai, and Ulrich Wiesner. Ultrasmall Sub-10 nm Near-Infrared Fluorescent Mesoporous Silica Nanoparticles. *Journal of the American Chemical Society*, 134(32):13180–13183, August 2012. 12

[40] Andrew Burns, Hooisweng Ow, and Ulrich Wiesner. Fluorescent core–shell silica nanoparticles: towards "Lab on a Particle" architectures for nanobiotechnology. *Chem. Soc. Rev.*, 35(11):1028–1042, 2006. 12

[41] Theresa M. Allen and Pieter R. Cullis. Liposomal drug delivery systems: From concept to clinical applications. *Advanced Drug Delivery Reviews*, 65(1):36–48, January 2013. 12

[42] Lisa Sercombe, Tejaswi Veerati, Fatemeh Moheimani, Sherry Y. Wu, Anil K. Sood, and Susan Hua. Advances and Challenges of Liposome Assisted Drug Delivery. *Frontiers in Pharmacology*, 6, December 2015. 12

[43] K. S. Soppimath, T. M. Aminabhavi, A. R. Kulkarni, and W. E. Rudzinski. Biodegradable polymeric nanoparticles as drug delivery devices. *Journal of Controlled Release: Official Journal of the Controlled Release Society*, 70(1-2):1–20, January 2001. 12

[44] Sarah R MacEwan, Daniel J Callahan, and Ashutosh Chilkoti. Stimulus-responsive macromolecules and nanoparticles for cancer drug delivery. *Nanomedicine*, 5(5):793–806, July 2010. 12

[45] J Cheng, B Teply, I Sherifi, J Sung, G Luther, F Gu, E Levynissenbaum, A Radovic-moreno, R Langer, and O Farokhzad. Formulation of functionalized PLGA–PEG nanoparticles for in vivo targeted drug delivery. *Biomaterials*, 28(5):869–876, February 2007. 12

[46] Pilar Calvo, Bruno Gouritin, Irène Brigger, Corinne Lasmezas, Jean-Philippe Deslys, Alun Williams, Jean P Andreux, Dominique Dormont, and Patrick Couvreur. PEGylated polycyanoacrylate nanoparticles as vector for drug delivery in prion diseases. *Journal of Neuroscience Methods*, 111(2):151–155, September 2001. 12

[47] P. Calvo, B. Gouritin, H. Chacun, D. Desmaële, J. D'Angelo, J. P. Noel, D. Georgin, E. Fattal, J. P. Andreux, and P. Couvreur. Long-circulating PEGylated polycyanoacrylate nanoparticles as new drug carrier for brain delivery. *Pharmaceutical Research*, 18(8):1157–1166, August 2001. 12

[48] Li-Sheng Wang, Li-Chen Wu, Shin-Yi Lu, Li-Ling Chang, I-Ting Teng, Chia-Min Yang, and Ja-an Annie Ho. Biofunctionalized Phospholipid-Capped Mesoporous Silica Nanoshuttles for Targeted Drug Delivery: Improved Water Suspensibility and Decreased Nonspecific Protein Binding. *ACS Nano*, 4(8):4371–4379, August 2010. 17

[49] Susan J. Sofia, V. Premnath, and Edward W. Merrill. Poly(ethylene oxide) Grafted to Silicon Surfaces: Grafting Density and Protein Adsorption. *Macromolecules*, 31(15):5059–5070, July 1998. 17

[50] Roger Michel, Stephanie Pasche, Marcus Textor, and David G. Castner. Influence of PEG Architecture on Protein Adsorption and Conformation. *Langmuir*, 21(26):12327–12332, December 2005. 17

[51] Yu-Shen Lin, Katie R. Hurley, and Christy L. Haynes. Critical Considerations in the Biomedical Use of Mesoporous Silica Nanoparticles. *The Journal of Physical Chemistry Letters*, pages 364–374, January 2012. 17, 32

[52] Matthias Bartneck, Heidrun A. Keul, Smriti Singh, Katharina Czaja, Jörg Bornemann, Michael Bockstaller, Martin Moeller, Gabriele Zwadlo-Klarwasser, and Jürgen Groll. Rapid Uptake of Gold Nanorods by Primary Human Blood Phagocytes and Immunomodulatory Effects of Surface Chemistry. *ACS Nano*, 4(6):3073–3086, June 2010. 17, 30

[53] C. Allen, N. Dos Santos, R. Gallagher, G. N. C. Chiu, Y. Shu, W. M. Li, S. A. Johnstone, A. S. Janoff, L. D. Mayer, M. S. Webb, and M. B. Bally. Controlling the physical behavior and biological performance of liposome formulations through use of surface grafted poly(ethylene glycol). *Bioscience Reports*, 22(2):225–250, April 2002. 18

[54] Qianjun He, Jiamin Zhang, Jianlin Shi, Ziyan Zhu, Linxia Zhang, Wenbo Bu, Limin Guo, and Yu Chen. The effect of PEGylation of mesoporous silica nanoparticles on nonspecific binding of serum proteins and cellular responses. *Biomaterials*, 31(6):1085–1092, February 2010. 18

[55] A.-L. Lainé, J. Gravier, M. Henry, L. Sancey, J. Béjaud, E. Pancani, M. Wiber, I. Texier, J.-L. Coll, J.-P. Benoit, and C. Passirani. Conventional versus stealth lipid nanoparticles: Formulation and in vivo fate prediction through FRET monitoring. *Journal of Controlled Release*, 188:1–8, August 2014. 18

[56] Huan Meng, Min Xue, Tian Xia, Zhaoxia Ji, Derrick Y. Tarn, Jeffrey I. Zink, and Andre E. Nel. Use of Size and a Copolymer Design Feature To Improve the Biodistribution and the Enhanced Permeability and Retention Effect of Doxorubicin-Loaded Mesoporous Silica Nanoparticles in a Murine Xenograft Tumor Model. *ACS Nano*, 5(5):4131–4144, May 2011. 18, 21

[57] Dan Peer, Jeffrey M. Karp, Seungpyo Hong, Omid C. Farokhzad, Rimona Margalit, and Robert Langer. Nanocarriers as an emerging platform for cancer therapy. *Nature Nanotechnology*, 2(12):751–760, December 2007. 19

[58] Hak Soo Choi, Wenhao Liu, Preeti Misra, Eiichi Tanaka, John P Zimmer, Binil Itty Ipe, Moungi G Bawendi, and John V Frangioni. Renal clearance of quantum dots. *Nature Biotechnology*, 25(10):1165–1170, October 2007. 20

[59] Michelle Longmire, Peter L Choyke, and Hisataka Kobayashi. Clearance properties of nano-sized particles and molecules as imaging agents: considerations and caveats. *Nanomedicine*, 3(5):703–717, October 2008. 20

[60] H. Cabral, Y. Matsumoto, K. Mizuno, Q. Chen, M. Murakami, M. Kimura, Y. Terada, M. R. Kano, K. Miyazono, M. Uesaka, N. Nishiyama, and K. Kataoka. Accumulation of sub-100 nm polymeric micelles in poorly permeable tumours depends on size. *Nature Nanotechnology*, 6(12):815–823, October 2011. 20

[61] Vikash P. Chauhan, Zoran Popović, Ou Chen, Jian Cui, Dai Fukumura, Moungi G. Bawendi, and Rakesh K. Jain. Fluorescent Nanorods and Nanospheres for Real-Time In Vivo Probing of Nanoparticle Shape-Dependent Tumor Penetration. *Angewandte Chemie International Edition*, 50(48):11417–11420, November 2011. 20

[62] S. E. A. Gratton, P. A. Ropp, P. D. Pohlhaus, J. C. Luft, V. J. Madden, M. E. Napier, and J. M. DeSimone. The effect of particle design on cellular internalization pathways. *Proceedings of the National Academy of Sciences*, 105(33):11613–11618, August 2008. 21

[63] Kai Xiao, Yuanpei Li, Juntao Luo, Joyce S. Lee, Wenwu Xiao, Abby M. Gonik, Rinki G. Agarwal, and Kit S. Lam. The effect of surface charge on in vivo biodistribution of PEG-oligocholic acid based micellar nanoparticles. *Biomaterials*, 32(13):3435–3446, May 2011. 21

[64] Osamu Ishida, Kazuo Maruyama, Hiroyuki Tanahashi, Motoharu Iwatsuru, Katsunori Sasaki, Masazumi Eriguchi, and Hironobu Yanagie. Liposomes Bearing Polyethyleneglycol-Coupled Transferrin with Intracellular Targeting Property to the Solid Tumors In Vivo. *Pharmaceutical Research*, 18(7):1042–1048, July 2001. 22

[65] Jing Li, Edward A. Sausville, Patrick J. Klein, David Morgenstern, Christopher P. Leamon, Richard A. Messmann, and Patricia LoRusso. Clinical Pharmacokinetics and Exposure-Toxicity Relationship of a Folate- *Vinca* Alkaloid Conjugate EC145 in Cancer Patients. *The Journal of Clinical Pharmacology*, 49(12):1467–1476, December 2009. 22

[66] Virginia J. Yao, Sara D'Angelo, Kimberly S. Butler, Christophe Theron, Tracey L. Smith, Serena Marchiò, Juri G. Gelovani, Richard L. Sidman, Andrey S. Dobroff, C. Jeffrey Brinker, Andrew R.M. Bradbury, Wadih Arap, and Renata Pasqualini. Ligand-targeted theranostic nanomedicines against cancer. *Journal of Controlled Release*, 240:267–286, October 2016. 23

[67] Z. Cheng, A. Al Zaki, J. Z. Hui, V. R. Muzykantov, and A. Tsourkas. Multifunctional Nanoparticles: Cost Versus Benefit of Adding Targeting and Imaging Capabilities. *Science*, 338(6109):903–910, November 2012. 23

[68] Candace C. Fleischer and Christine K. Payne. Nanoparticle–Cell Interactions: Molecular Structure of the Protein Corona and Cellular Outcomes. *Accounts of Chemical Research*, 47(8):2651–2659, August 2014. 26

[69] Carl D. Walkey, Jonathan B. Olsen, Hongbo Guo, Andrew Emili, and Warren C. W. Chan. Nanoparticle Size and Surface Chemistry Determine Serum Protein Adsorption and Macrophage Uptake. *Journal of the American Chemical Society*, 134(4):2139–2147, February 2012. 26

[70] Shakiba Shahabi, Svea Döscher, Tobias Bollhorst, Laura Treccani, Michael Maas, Ralf Dringen, and Kurosch Rezwan. Enhancing Cellular Uptake and Doxorubicin Delivery of Mesoporous Silica Nanoparticles via Surface Functionalization: Effects of Serum. *ACS Applied Materials & Interfaces*, 7(48):26880–26891, December 2015. 26, 27, 144

[71] Martin Lundqvist, Cecilia Augustsson, Malin Lilja, Kristoffer Lundkvist, Björn Dahlbäck, Sara Linse, and Tommy Cedervall. The nanoparticle protein corona formed in human blood or human blood fractions. *PLOS ONE*, 12(4):e0175871, April 2017. 26

[72] Yang Qiu, Ying Liu, Liming Wang, Ligeng Xu, Ru Bai, Yinglu Ji, Xiaochun Wu, Yuliang Zhao, Yufeng Li, and Chunying Chen. Surface chemistry and aspect ratio mediated cellular uptake of Au nanorods. *Biomaterials*, 31(30):7606–7619, October 2010. 27, 29

[73] Maria Kokkinopoulou, Johanna Simon, Katharina Landfester, Volker Mailänder, and Ingo Lieberwirth. Visualization of the protein corona: towards a biomolecular understanding of nanoparticle-cell-interactions. *Nanoscale*, 9(25):8858–8870, 2017. 27

[74] Neus Feliu, Dominic Docter, Markus Heine, Pablo del Pino, Sumaira Ashraf, Jelena Kolosnjaj-Tabi, Paolo Macchiarini, Peter Nielsen, Damien Alloyeau, Florence Gazeau, Roland H. Stauber, and Wolfgang J. Parak. *In vivo* degeneration and the fate of inorganic nanoparticles. *Chem. Soc. Rev.*, 45(9):2440–2457, 2016. 27

[75] Martin Schäffler, Manuela Semmler-Behnke, Hakan Sarioglu, Shinji Takenaka, Alexander Wenk, Carsten Schleh, Stefanie M Hauck, Blair D Johnston, and Wolfgang G Kreyling. Serum protein identification and quantification of the corona of 5, 15 and 80 nm gold nanoparticles. *Nanotechnology*, 24(26):265103, July 2013. 27

[76] Anna Salvati, Andrzej S. Pitek, Marco P. Monopoli, Kanlaya Prapainop, Francesca Baldelli Bombelli, Delyan R. Hristov, Philip M. Kelly, Christoffer Åberg, Eugene Mahon, and Kenneth A. Dawson. Transferrin-functionalized nanoparticles lose their targeting capabilities when a biomolecule corona adsorbs on the surface. *Nature Nanotechnology*, 8(2):137–143, January 2013. 27

[77] Daniele Dell'Orco, Martin Lundqvist, Tommy Cedervall, and Sara Linse. Delivery success rate of engineered nanoparticles in the presence of the protein corona: a systems-level screening. *Nanomedicine: Nanotechnology, Biology and Medicine*, 8(8):1271–1281, November 2012. 27

[78] Alexey A. Vertegel, Richard W. Siegel, and Jonathan S. Dordick. Silica Nanoparticle Size Influences the Structure and Enzymatic Activity of Adsorbed Lysozyme. *Langmuir*, 20(16):6800–6807, August 2004. 27

[79] Chester E. Rodriguez, Jon M. Fukuto, Keiko Taguchi, John Froines, and Arthur K. Cho. The interactions of 9,10-phenanthrenequinone with glyceraldehyde-3-phosphate dehydrogenase (GAPDH), a potential site for toxic actions. *Chemico-Biological Interactions*, 155(1-2):97–110, June 2005. 27

[80] Andre E. Nel, Lutz Mädler, Darrell Velegol, Tian Xia, Eric M. V. Hoek, Ponisseril Somasundaran, Fred Klaessig, Vince Castranova, and Mike Thompson. Understanding biophysicochemical interactions at the nano–bio interface. *Nature Materials*, 8(7):543–557, July 2009. 29

[81] B. Devika Chithrani and Warren C. W. Chan. Elucidating the Mechanism of Cellular Uptake and Removal of Protein-Coated Gold Nanoparticles of Different Sizes and Shapes. *Nano Letters*, 7(6):1542–1550, June 2007. 29

[82] B. Devika Chithrani, Arezou A. Ghazani, and Warren C. W. Chan. Determining the Size and Shape Dependence of Gold Nanoparticle Uptake into Mammalian Cells. *Nano Letters*, 6(4):662–668, April 2006. 29

[83] H. Gao, W. Shi, and L. B. Freund. Mechanics of receptor-mediated endocytosis. *Proceedings of the National Academy of Sciences*, 102(27):9469–9474, July 2005. 29

[84] Wen Jiang, Betty Y. S. Kim, James T. Rutka, and Warren C. W. Chan. Nanoparticle-mediated cellular response is size-dependent. *Nature Nanotechnology*, 3(3):145–150, March 2008. 29

[85] Haiyuan Zhang, Zhaoxia Ji, Tian Xia, Huan Meng, Cecile Low-Kam, Rong Liu, Suman Pokhrel, Sijie Lin, Xiang Wang, Yu-Pei Liao, Meiying Wang, Linjiang Li, Robert Rallo, Robert Damoiseaux, Donatello Telesca, Lutz Mädler, Yoram Cohen, Jeffrey I. Zink, and Andre E. Nel. Use of Metal Oxide Nanoparticle Band Gap To Develop a Predictive Paradigm for Oxidative Stress and Acute Pulmonary Inflammation. *ACS Nano*, 6(5):4349–4368, May 2012. 31

[86] M. Vallet-Regi, A. Rámila, R. P. del Real, and J. Pérez-Pariente. A New Property of MCM-41: Drug Delivery System. *Chemistry of Materials*, 13(2):308–311, February 2001. 32

[87] Christian Argyo, Veronika Weiss, Christoph Bräuchle, and Angelini Bein, Thomas E. Multifunctional Mesoporous Silica Nanoparticles as a Universal Platform for Drug Delivery. *Chemistry of Materials*, 26(1):435–451, January 2014. 32, 35

[88] Si-Han Wu, Yann Hung, and Chung-Yuan Mou. Mesoporous silica nanoparticles as nanocarriers. *Chemical Communications*, 47(36):9972, 2011. 33

[89] Tsuneo Yanagisawa, Toshio Shimizu, Kazuyuki Kuroda, and Chuzo Kato. The Preparation of Alkyltrimethylammonium–Kanemite Complexes and Their Conversion to Microporous Materials. *Bulletin of the Chemical Society of Japan*, 63(4):988–992, April 1990. 33

[90] J. S. Beck, J. C. Vartuli, W. J. Roth, M. E. Leonowicz, C. T. Kresge, K. D. Schmitt, C. T. W. Chu, D. H. Olson, E. W. Sheppard, S. B. McCullen, J. B. Higgins, and J. L. Schlenker. A new family of mesoporous molecular sieves prepared with liquid crystal templates. *Journal of the American Chemical Society*, 114(27):10834–10843, December 1992. 33

[91] C. T. Kresge, M. E. Leonowicz, W. J. Roth, J. C. Vartuli, and J. S. Beck. Ordered mesoporous molecular sieves synthesized by a liquid-crystal template mechanism. *Nature*, 359(6397):710–712, October 1992. 33

[92] P. T. Tanev and T. J. Pinnavaia. A Neutral Templating Route to Mesoporous Molecular Sieves. *Science*, 267(5199):865–867, February 1995. 33, 50

[93] S. A. Bagshaw, E. Prouzet, and T. J. Pinnavaia. Templating of Mesoporous Molecular Sieves by Nonionic Polyethylene Oxide Surfactants. *Science*, 269(5228):1242–1244, September 1995. 33, 50

[94] Éric Prouzet and Cédric Boissière. A review on the synthesis, structure and applications in separation processes of mesoporous MSU-X silica obtained with the two-step process. *Comptes Rendus Chimie*, 8(3-4):579–596, March 2005. 33

[95] null Zhao, null Feng, null Huo, null Melosh, null Fredrickson, null Chmelka, and null Stucky. Triblock copolymer syntheses of mesoporous silica with periodic 50 to 300 angstrom pores. *Science (New York, N.Y.)*, 279(5350):548–552, January 1998. 34

[96] Dongyuan Zhao, Qisheng Huo, Jianglin Feng, Bradley F. Chmelka, and Galen D. Stucky. Nonionic Triblock and Star Diblock Copolymer and Oligomeric Surfactant Syntheses of Highly Ordered, Hydrothermally Stable, Mesoporous Silica Structures. *Journal of the American Chemical Society*, 120(24):6024–6036, June 1998. 34

[97] Charles T. Kresge and Wieslaw J. Roth. The discovery of mesoporous molecular sieves from the twenty year perspective. *Chemical Society Reviews*, 42(9):3663, 2013. 34

[98] Thomas Fontecave, Clément Sanchez, Thierry Azaïs, and Cédric Boissière. Chemical Modification As a Versatile Tool for Tuning Stability of Silica Based Mesoporous Carriers in Biologically Relevant Conditions. *Chemistry of Materials*, 24(22):4326–4336, November 2012. 35, 118, 119, 123, 148

[99] Xiaoxing Sun, Yannan Zhao, Victor S.-Y. Lin, Igor I. Slowing, and Brian G. Trewyn. Luciferase and Luciferin Co-immobilized Mesoporous Silica Nanoparticle Materials for Intracellular Biocatalysis. *Journal of the American Chemical Society*, 133(46):18554–18557, November 2011. 35

[100] Helen Vallhov, Natalia Kupferschmidt, Susanne Gabrielsson, Staffan Paulie, Maria Strømme, Alfonso E. Garcia-Bennett, and Annika Scheynius. Adjuvant Properties of Mesoporous Silica Particles Tune the Development of Effector T Cells. *Small*, 8(13):2116–2124, July 2012. 35

[101] Werner Stöber, Arthur Fink, and Ernst Bohn. Controlled growth of monodisperse silica spheres in the micron size range. *Journal of colloid and interface science*, 26(1):62–69, 1968. 35

[102] C. Jeffrey Brinker and George W. Scherer. *Sol-gel science: the physics and chemistry of sol-gel processing*. Academic Press, Boston, 1990. 35, 48

[103] C. E. Fowler, D. Khushalani, B. Lebeau, and S. Mann. Nanoscale Materials with Mesostructured Interiors. *Advanced Materials*, 13(9):649–652, May 2001. 36, 37

[104] Robert I. Nooney, Dhanasekaran Thirunavukkarasu, Yimei Chen, Robert Josephs, and Agnes E. Ostafin. Synthesis of Nanoscale Mesoporous Silica Spheres with Controlled Particle Size. *Chemistry of Materials*, 14(11):4721–4728, November 2002. 37

[105] Keisei Suzuki, Kenichi Ikari, and Hiroaki Imai. Synthesis of Silica Nanoparticles Having a Well-Ordered Mesostructure Using a Double Surfactant System. *Journal of the American Chemical Society*, 126(2):462–463, January 2004. 37

[106] Kazuhisa Yano and Yoshiaki Fukushima. Synthesis of mono-dispersed mesoporous silica spheres with highly ordered hexagonal regularity using conventional alkyltrimethylammonium halide as a surfactantElectronic supplementary information (ESI) available: time courses of particle size and scattering intensity of samples obtained with TEOS and C16tmacl. See http://www.rsc.org/suppdata/jm/b3/b313712k/. *Journal of Materials Chemistry*, 14(10):1579, 2004. 37

[107] Yu Han and Jackie Y. Ying. Generalized Fluorocarbon-Surfactant-Mediated Synthesis of Nanoparticles with Various Mesoporous Structures. *Angewandte Chemie International Edition*, 44(2):288–292, January 2005. 37

[108] K. Möller, J. Kobler, and T. Bein. Colloidal Suspensions of Nanometer-Sized Mesoporous Silica. *Advanced Functional Materials*, 17(4):605–612, March 2007. 37

[109] Andreas Berggren and Anders E. C. Palmqvist. Particle Size Control of Colloidal Suspensions of Mesostructured Silica. *The Journal of Physical Chemistry C*, 112(3):732–737, January 2008. 37

[110] Fang Lu, Si-Han Wu, Yann Hung, and Chung-Yuan Mou. Size Effect on Cell Uptake in Well-Suspended, Uniform Mesoporous Silica Nanoparticles. *Small*, 5(12):1408–1413, June 2009. 37

[111] Qianjun He, Xiangzhi Cui, Fangming Cui, Limin Guo, and Jianlin Shi. Size-controlled synthesis of monodispersed mesoporous silica nano-spheres under a neu-

tral condition. *Microporous and Mesoporous Materials*, 117(3):609–616, January 2009. 37

[112] Chihiro Urata, Yuko Aoyama, Akihisa Tonegawa, Yusuke Yamauchi, and Kazuyuki Kuroda. Dialysis process for the removal of surfactants to form colloidal mesoporous silica nanoparticles. *Chemical Communications*, (34):5094, 2009. 36, 37

[113] Teeraporn Suteewong, Hiroaki Sai, Roy Cohen, Suntao Wang, Michelle Bradbury, Barbara Baird, Sol M. Gruner, and Ulrich Wiesner. Highly Aminated Mesoporous Silica Nanoparticles with Cubic Pore Structure. *Journal of the American Chemical Society*, 133(2):172–175, January 2011. 37

[114] Valentina Cauda, Christian Argyo, Davin G. Piercey, and Thomas Bein. "Liquid-Phase Calcination" of Colloidal Mesoporous Silica Nanoparticles in High-Boiling Solvents. *Journal of the American Chemical Society*, 133(17):6484–6486, May 2011. 36

[115] Yu-Shen Lin and Christy L. Haynes. Impacts of Mesoporous Silica Nanoparticle Size, Pore Ordering, and Pore Integrity on Hemolytic Activity. *Journal of the American Chemical Society*, 132(13):4834–4842, April 2010. 36

[116] Yu-Shen Lin, Nardine Abadeer, and Christy L. Haynes. Stability of small mesoporous silicananoparticles in biological media. *Chem. Commun.*, 47(1):532–534, 2011. 36

[117] Qianjun He, Jianlin Shi, Min Zhu, Yu Chen, and Feng Chen. The three-stage in vitro degradation behavior of mesoporous silica in simulated body fluid. *Microporous and Mesoporous Materials*, 131(1-3):314–320, June 2010. 36, 118, 119

[118] Valentina Cauda, Axel Schlossbauer, and Thomas Bein. Bio-degradation study of colloidal mesoporous silica nanoparticles: Effect of surface functionalization with organo-silanes and poly(ethylene glycol). *Microporous and Mesoporous Materials*, 132(1-2):60–71, July 2010. 36

[119] Valentina Cauda, Christian Argyo, and Thomas Bein. Impact of different PEGylation patterns on the long-term bio-stability of colloidal mesoporous silica nanoparticles. *Journal of Materials Chemistry*, 20(39):8693–8699, September 2010. 36, 118

[120] Chihiro Urata, Hironori Yamada, Ryutaro Wakabayashi, Yuko Aoyama, Shota Hirosawa, Satoshi Arai, Shinji Takeoka, Yusuke Yamauchi, and Kazuyuki Kuroda. Aqueous Colloidal Mesoporous Nanoparticles with Ethenylene-Bridged Silsesquioxane Frameworks. *Journal of the American Chemical Society*, 133(21):8102–8105, June 2011. 36

[121] Binaya Rimal, Alissa K. Greenberg, and William N. Rom. Basic pathogenetic mechanisms in silicosis: current understanding. *Current Opinion in Pulmonary Medicine*, 11(2):169–173, March 2005. 38

[122] Mara Ghiazza, Manuela Polimeni, Ivana Fenoglio, Elena Gazzano, Dario Ghigo, and Bice Fubini. Does Vitreous Silica Contradict the Toxicity of the Crystalline Silica Paradigm? *Chemical Research in Toxicology*, 23(3):620–629, March 2010. 38

[123] Haiyuan Zhang, Darren R. Dunphy, Xingmao Jiang, Huan Meng, Bingbing Sun, Derrick Tarn, Min Xue, Xiang Wang, Sijie Lin, Zhaoxia Ji, Ruibin Li, Fred L. Garcia, Jing Yang, Martin L. Kirk, Tian Xia, Jeffrey I. Zink, Andre Nel, and C. Jeffrey Brinker. Processing Pathway Dependence of Amorphous Silica Nanoparticle Toxicity: Colloidal vs Pyrolytic. *Journal of the American Chemical Society*, 134(38):15790–15804, September 2012. 38, 118

[124] Sandrine Quignard, Gervaise Mosser, Michel Boissière, and Thibaud Coradin. Long-term fate of silica nanoparticles interacting with human dermal fibroblasts. *Biomaterials*, 33(17):4431–4442, June 2012. 39

[125] Tian Yu, Alexander Malugin, and Hamidreza Ghandehari. Impact of Silica Nanoparticle Design on Cellular Toxicity and Hemolytic Activity. *ACS Nano*, 5(7):5717–5728, July 2011. 39

[126] Frank Hoffmann, Maximilian Cornelius, Jürgen Morell, and Michael Fröba. Silica-Based Mesoporous Organic–Inorganic Hybrid Materials. *Angewandte Chemie International Edition*, 45(20):3216–3251, May 2006. 39, 40, 42

[127] Alexander Liberman, Natalie Mendez, William C. Trogler, and Andrew C. Kummel. Synthesis and surface functionalization of silica nanoparticles for nanomedicine. *Surface science reports*, 69(2-3):132–158, 2014. 39

[128] Reiner Anwander, Iris Nagl, Markus Widenmeyer, Günter Engelhardt, Olaf Groeger, Clemens Palm, and Thomas Röser. Surface Characterization and Func-

tionalization of MCM-41 Silicas via Silazane Silylation. *The Journal of Physical Chemistry B*, 104(15):3532–3544, April 2000. 40

[129] Louis Mercier and Thomas J. Pinnavaia. Heavy Metal Ion Adsorbents Formed by the Grafting of a Thiol Functionality to Mesoporous Silica Molecular Sieves: Factors Affecting Hg(II) Uptake. *Environmental Science & Technology*, 32(18):2749–2754, September 1998. 40

[130] A. M. Liu, K. Hidajat, S. Kawi, and D. Y. Zhao. A new class of hybrid mesoporous materials with functionalized organic monolayers for selective adsorption of heavy metal ions. *Chemical Communications*, (13):1145–1146, 2000. 40

[131] Nawal Kishor Mal, Masahiro Fujiwara, and Yuko Tanaka. Photocontrolled reversible release of guest molecules from coumarin-modified mesoporous silica. *Nature*, 421(6921):350–353, January 2003. 41

[132] Q. Fu, G.V.R. Rao, L.K. Ista, Y. Wu, B.P. Andrzejewski, L.A. Sklar, T.L. Ward, and G.P. López. Control of Molecular Transport Through Stimuli-Responsive Ordered Mesoporous Materials. *Advanced Materials*, 15(15):1262–1266, August 2003. 41

[133] Ye-Zi You, Kennedy K. Kalebaila, Stephanie L. Brock, and David Oupický. Temperature-Controlled Uptake and Release in PNIPAM-Modified Porous Silica Nanoparticles. *Chemistry of Materials*, 20(10):3354–3359, May 2008. 41

[134] Chuanbo Gao, Haoquan Zheng, Lei Xing, Mouhai Shu, and Shunai Che. Designable Coordination Bonding in Mesopores as a pH-Responsive Release System. *Chemistry of Materials*, 22(19):5437–5444, October 2010. 41

[135] Rui Liu, Xiang Zhao, Tao Wu, and Pingyun Feng. Tunable Redox-Responsive Hybrid Nanogated Ensembles. *Journal of the American Chemical Society*, 130(44):14418–14419, November 2008. 41

[136] Supratim Giri, Brian G. Trewyn, Michael P. Stellmaker, and Victor S.-Y. Lin. Stimuli-Responsive Controlled-Release Delivery System Based on Mesoporous Silica Nanorods Capped with Magnetic Nanoparticles. *Angewandte Chemie International Edition*, 44(32):5038–5044, August 2005. 41

[137] Valentina Cauda, Axel Schlossbauer, Johann Kecht, Andreas Zürner, and Thomas Bein. Multiple Core Shell Functionalized Colloidal Mesoporous Silica Nanoparticles. *Journal of the American Chemical Society*, 131(32):11361–11370, August 2009. 41

[138] Sandra L. Burkett, Stephen D. Sims, and Stephen Mann. Synthesis of hybrid inorganic–organic mesoporous silica by co-condensation of siloxane and organosiloxane precursors. *Chem. Commun.*, (11):1367–1368, 1996. 41

[139] Duncan J. Macquarrie. Direct preparation of organically modified MCM-type materials. Preparation and characterisation of aminopropyl–MCM and 2-cyanoethyl–MCM. *Chem. Commun.*, (16):1961–1962, 1996. 41

[140] Louis Mercier and Thomas J. Pinnavaia. Direct Synthesis of Hybrid Organic Inorganic Nanoporous Silica by a Neutral Amine Assembly Route: Structure Function Control by Stoichiometric Incorporation of Organosiloxane Molecules. *Chemistry of Materials*, 12(1):188–196, January 2000. 41

[141] Christabel E. Fowler, Sandra L. Burkett, and Stephen Mann. Synthesis and characterization of ordered organo–silica–surfactant mesophases with functionalized MCM-41-type architecture. *Chemical Communications*, (18):1769–1770, 1997. 41

[142] Pascal Van Der Voort, Dolores Esquivel, Els De Canck, Frederik Goethals, Isabel Van Driessche, and Francisco J. Romero-Salguero. Periodic Mesoporous Organosilicas: from simple to complex bridges; a comprehensive overview of functions, morphologies and applications. *Chem. Soc. Rev.*, 42(9):3913–3955, 2013. 42

[143] C. Jeffrey Brinker, Yunfeng Lu, Alan Sellinger, and Hongyou Fan. Evaporation-Induced Self-Assembly: Nanostructures Made Easy. *Advanced Materials*, 11(7):579–585, May 1999. 49, 51

[144] Galo J. de A. A. Soler-Illia, Clément Sanchez, Bénédicte Lebeau, and Joël Patarin. Chemical Strategies To Design Textured Materials: from Microporous and Mesoporous Oxides to Nanonetworks and Hierarchical Structures. *Chemical Reviews*, 102(11):4093–4138, November 2002. 49, 50

[145] Thiam-Leng Chew, Abdul L. Ahmad, and Subhash Bhatia. Ordered mesoporous silica (OMS) as an adsorbent and membrane for separation of carbon dioxide (CO2). *Advances in Colloid and Interface Science*, 153(1-2):43–57, January 2010. 50

[146] Makoto Ogawa. Preparation of Layered Silica Dialkyldimethylammonium Bromide Nanocomposites. *Langmuir*, 13(6):1853–1855, March 1997. 50

[147] D. Grosso, F. Cagnol, G. J. de A. A. Soler-Illia, E. L. Crepaldi, H. Amenitsch, A. Brunet-Bruneau, A. Bourgeois, and C. Sanchez. Fundamentals of Mesostructuring Through Evaporation-Induced Self-Assembly. *Advanced Functional Materials*, 14(4):309–322, April 2004. 50, 51, 52, 73

[148] T. Martin, A. Galarneau, F. Di Renzo, F. Fajula, and D. Plee. Morphological control of MCM-41 by pseudomorphic synthesis. *Angewandte Chemie (International Ed. in English)*, 41(14):2590–2592, July 2002. 50

[149] Peter T. Tanev, Malama Chibwe, and Thomas J. Pinnavaia. Titanium-containing mesoporous molecular sieves for catalytic oxidation of aromatic compounds. *Nature*, 368(6469):321–323, March 1994. 50

[150] Plinio Innocenzi, Tongjit Kidchob, Johnny Mio Bertolo, Massimo Piccinini, Mariangela Cestelli Guidi, and Claudio Marcelli. Time-Resolved Infrared Spectroscopy as an In Situ Tool To Study the Kinetics During Self-Assembly of Mesostructured Films. *The Journal of Physical Chemistry B*, 110(22):10837–10841, June 2006. 50

[151] L. Landau and B. Levich. Dragging of a Liquid by a Moving Plate. *Acta Physicochim. URSS*, 17:42–54, 1942. 53, 76

[152] Jung Soo Suk, Qingguo Xu, Namho Kim, Justin Hanes, and Laura M. Ensign. PEGylation as a strategy for improving nanoparticle-based drug and gene delivery. *Advanced Drug Delivery Reviews*, 99:28–51, April 2016. 53

[153] Catherine Pale-Grosdemange, Ethan S. Simon, Kevin L. Prime, and George M. Whitesides. Formation of self-assembled monolayers by chemisorption of derivatives of oligo(ethylene glycol) of structure HS(CH2)11(OCH2ch2)mOH on gold. *Journal of the American Chemical Society*, 113(1):12–20, January 1991. 53, 63

[154] Emmanuel Delamarche, Christian Donzel, Fadhil S. Kamounah, Heiko Wolf, Matthias Geissler, Richard Stutz, Patrick Schmidt-Winkel, Bruno Michel, Hans Jörg Mathieu, and Kjeld Schaumburg. Microcontact Printing Using Poly(dimethylsiloxane) Stamps Hydrophilized by Poly(ethylene oxide) Silanes. *Langmuir*, 19(21):8749–8758, October 2003. 53

[155] Bryan Parrish, Rebecca B. Breitenkamp, and Todd Emrick. PEG- and Peptide-Grafted Aliphatic Polyesters by Click Chemistry. *Journal of the American Chemical Society*, 127(20):7404–7410, May 2005. 53

[156] Steve Edmondson and Wilhelm T. S. Huck. Controlled growth and subsequent chemical modification of poly(glycidyl methacrylate) brushes on silicon wafers. *Journal of Materials Chemistry*, 14(4):730, 2004. 54

[157] Darren M. Jones, Andrew A. Brown, and Wilhelm T. S. Huck. Surface-Initiated Polymerizations in Aqueous Media: Effect of Initiator Density. *Langmuir*, 18(4):1265–1269, February 2002. 54

[158] Krzysztof Matyjaszewski and Jianhui Xia. Atom Transfer Radical Polymerization. *Chemical Reviews*, 101(9):2921–2990, September 2001. 54, 56, 62

[159] H. Ma, J. Hyun, P. Stiller, and A. Chilkoti. "Non-Fouling" Oligo(ethylene glycol)-Functionalized Polymer Brushes Synthesized by Surface-Initiated Atom Transfer Radical Polymerization. *Advanced Materials*, 16(4):338–341, February 2004. 56

[160] Andrew A. Brown, Neelam S. Khan, Lorenz Steinbock, and Wilhelm T.S. Huck. Synthesis of oligo(ethylene glycol) methacrylate polymer brushes. *European Polymer Journal*, 41(8):1757–1765, August 2005. 56, 63

[161] Nora Graf, Eda Yegen, Thomas Gross, Andreas Lippitz, Wilfried Weigel, Simone Krakert, Andreas Terfort, and Wolfgang E.S. Unger. XPS and NEXAFS studies of aliphatic and aromatic amine species on functionalized surfaces. *Surface Science*, 603(18):2849–2860, September 2009. 58, 64

[162] Cédric Boissiere, David Grosso, Sophie Lepoutre, Lionel Nicole, Aline Brunet Bruneau, and Clément Sanchez. Porosity and Mechanical Properties of Mesoporous Thin Films Assessed by Environmental Ellipsometric Porosimetry. *Langmuir*, 21(26):12362–12371, December 2005. 68, 69, 70, 71

[163] Peer Löbmann. Characterization of sol–gel thin films by ellipsometric porosimetry. *Journal of Sol-Gel Science and Technology*, 84(1):2–15, October 2017. 68, 70

[164] Elisa Bindini, Guillaume Naudin, Marco Faustini, David Grosso, and Cédric Boissière. Critical Role of the Atmosphere in Dip-Coating Process. *The Journal of Physical Chemistry C*, 121(27):14572–14580, July 2017. 75

[165] M. Faustini, B. Louis, P. A. Albouy, M. Kuemmel, and D. Grosso. Preparation of Sol-Gel Films by Dip-Coating in Extreme Conditions. *J. Phys. Chem. C*, 114:7637–7645, 2010. 76, 83

[166] Marco Faustini. *Nanopatterning through bottom-up approach; an alternative way for data storage device.* PhD thesis, Université Pierre et Marie Curie, 2011. 77

[167] G. J. A. A. Soler-Illia, P. C. Angelome, M. C. Fuertes, D. Grosso, and C. Boissiere. Critical aspects in the production of periodically ordered mesoporous titania thin films. *Nanoscale*, 4:2549–2566, 2012. 79

[168] C. Sanchez, C. Boissiere, D. Grosso, C. Laberty, and L. Nicole. Design, Synthesis, and Properties of Inorganic and Hybrid Thin Films Having Periodically Organized Nanoporosity. *Chem.Mater.*, 20:682–737, 2008. 79

[169] Benjamin Louis, Natacha Krins, Marco Faustini, and David Grosso. Understanding Crystallization of Anatase into Binary SiO $_2$ /TiO $_2$ Sol Gel Optical Thin Films: An in Situ Thermal Ellipsometry Analysis. *The Journal of Physical Chemistry C*, 115(7):3115–3122, February 2011. 79, 92

[170] H. Hertz. On the evaporation of liquids, especially mercury. In Vacuo. *Ann. Phys. Chem.*, 17:177–198, 1882. 83

[171] M. Knudsen. *Ann. Phys.*, 47:697, 1915. 83

[172] Marco Faustini, Davide R. Ceratti, Benjamin Louis, Mickael Boudot, Pierre-Antoine Albouy, Cédric Boissière, and David Grosso. Engineering Functionality Gradients by Dip Coating Process in Acceleration Mode. *ACS Applied Materials & Interfaces*, 6(19):17102–17110, October 2014. 91

[173] Harland G. Tompkins and Eugene A. Irene, editors. *Handbook of ellipsometry.* William Andrew Pub. ; Springer, Norwich, NY : Heidelberg, Germany, 2005. 99

[174] Alexei Nabok and Anna Tsargorodskaya. The method of total internal reflection ellipsometry for thin film characterisation and sensing. *Thin Solid Films*, 516(24):8993–9001, October 2008. 100

[175] Hans Arwin, Michal Poksinski, and Knut Johansen. Total internal reflection ellipsometry: principles and applications. *Applied Optics*, 43(15):3028, May 2004. 100, 102

[176] M. Poksinski and H. Arwin. Protein monolayers monitored by internal reflection ellipsometry. *Thin Solid Films*, 455–456:716–721, May 2004. 100

[177] M.K. Mustafa, A. Nabok, D. Parkinson, I.E. Tothill, F. Salam, and A. Tsargorodskaya. Detection of \beta-amyloid peptide (1–16) and amyloid precursor protein (APP770) using spectroscopic ellipsometry and QCM techniques: A step forward towards Alzheimers disease diagnostics. *Biosensors and Bioelectronics*, 26(4):1332–1336, December 2010. 100

[178] Ieva Baleviciute, Zigmas Balevicius, Asta Makaraviciute, Almira Ramanaviciene, and Arunas Ramanavicius. Study of antibody/antigen binding kinetics by total internal reflection ellipsometry. *Biosensors and Bioelectronics*, 39(1):170–176, January 2013. 100

[179] Erwin Kretschmann. Die Bestimmung optischer Konstanten von Metallen durch Anregung von Oberflächenplasmaschwingungen. *Zeitschrift für Physik A Hadrons and nuclei*, 241(4):313–324, August 1971. 100

[180] Karsten Hinrichs and Klaus-Jochen Eichhorn, editors. *Ellipsometry of Functional Organic Surfaces and Films*. Springer Series in Surface Sciences. Springer-Verlag, Berlin Heidelberg, 2014. 102

[181] Jaeyoun Kim. Joining plasmonics with microfluidics: from convenience to inevitability. *Lab on a Chip*, 12(19):3611, 2012. 103

[182] Lifang Niu, Nan Zhang, Hong Liu, Xiaodong Zhou, and Wolfgang Knoll. Integrating plasmonic diagnostics and microfluidics. *Biomicrofluidics*, 9(5):052611, September 2015. 103

[183] Alexander van Reenen, Arthur M. de Jong, Jaap M. J. den Toonder, and Menno W. J. Prins. Integrated lab-on-chip biosensing systems based on magnetic particle actuation – a comprehensive review. *Lab Chip*, 14(12):1966–1986, 2014. 106

[184] Ángel Ríos, Mohammed Zougagh, and Mónica Avila. Miniaturization through lab-on-a-chip: Utopia or reality for routine laboratories? A review. *Analytica Chimica Acta*, 740:1–11, August 2012. 106

[185] P Abgrall and A-M Gué. Lab-on-chip technologies: making a microfluidic network and coupling it into a complete microsystem—a review. *Journal of Micromechanics and Microengineering*, 17(5):R15–R49, May 2007. 106

[186] Paul Yager, Thayne Edwards, Elain Fu, Kristen Helton, Kjell Nelson, Milton R. Tam, and Bernhard H. Weigl. Microfluidic diagnostic technologies for global public health. *Nature*, 442(7101):412–418, July 2006. 106

[187] Quinton Smith and Sharon Gerecht. Going with the flow: microfluidic platforms in vascular tissue engineering. *Current Opinion in Chemical Engineering*, 3:42–50, February 2014. 106

[188] A.C.C. Esteves, J. Brokken-Zijp, J. Laven, H.P. Huinink, N.J.W. Reuvers, M.P. Van, and G. de With. Influence of cross-linker concentration on the cross-linking of PDMS and the network structures formed. *Polymer*, 50(16):3955–3966, July 2009. 107

[189] Jessamine Ng Lee, Cheolmin Park, and George M. Whitesides. Solvent Compatibility of Poly(dimethylsiloxane)-Based Microfluidic Devices. *Analytical Chemistry*, 75(23):6544–6554, December 2003. 107

[190] Amy L. Paguirigan and David J. Beebe. From the cellular perspective: exploring differences in the cellular baseline in macroscale and microfluidic cultures. *Integrative Biology*, 1(2):182, 2009. 111

[191] S. Yunus, C. de Crombrugghe de Looringhe, C. Poleunis, and A. Delcorte. Diffusion of oligomers from polydimethylsiloxane stamps in microcontact printing: Surface analysis and possible application. *Surface and Interface Analysis*, 39(12-13):922–925, December 2007. 111

[192] Jenny Andersson, Jessica Rosenholm, Sami Areva, and Mika Lindén. Influences of Material Characteristics on Ibuprofen Drug Loading and Release Profiles from Ordered Micro- and Mesoporous Silica Matrices. *Chemistry of Materials*, 16(21):4160–4167, October 2004. 118

[193] I. Izquierdo-Barba, M. Colilla, M. Manzano, and M. Vallet-Regí. In vitro stability of SBA-15 under physiological conditions. *Microporous and Mesoporous Materials*, 132(3):442–452, August 2010. 118

[194] Katharina Braun, Alexander Pochert, Michaela Beck, Richard Fiedler, Jens Gruber, and Mika Lindén. Dissolution kinetics of mesoporous silica nanoparticles in different simulated body fluids. *Journal of Sol-Gel Science and Technology*, 79(2):319–327, August 2016. 118

[195] John D. Bass, David Grosso, Cédric Boissiere, Emmanuel Belamie, Thibaud Coradin, and Clément Sanchez. Stability of Mesoporous Oxide and Mixed Metal Oxide Materials under Biologically Relevant Conditions. *Chemistry of Materials*, 19(17):4349–4356, August 2007. 118, 119, 122, 123

[196] Jonathan P. Icenhower and Patricia M. Dove. The dissolution kinetics of amorphous silica into sodium chloride solutions: effects of temperature and ionic strength. *Geochimica et Cosmochimica Acta*, 64(24):4193–4203, 2000. 118

[197] P. M. Dove, N. Han, A. F. Wallace, and J. J. De Yoreo. Kinetics of amorphous silica dissolution and the paradox of the silica polymorphs. *Proceedings of the National Academy of Sciences*, 105(29):9903–9908, July 2008. 118

[198] Go B. Alexander, W. M. Heston, and R. K. Iler. The Solubility of Amorphous Silica in Water. *The Journal of Physical Chemistry*, 58(6):453–455, June 1954. 118

[199] Renato Mortera, Sonia Fiorilli, Edoardo Garrone, Enrica Verné, and Barbara Onida. Pores occlusion in MCM-41 spheres immersed in SBF and the effect on ibuprofen delivery kinetics: A quantitative model. *Chemical Engineering Journal*, 156(1):184–192, January 2010. 118

[200] Xinxin Li, Sutapa Barua, Kaushal Rege, and Bryan D. Vogt. Tuning Stability of Mesoporous Silica Films under Biologically Relevant Conditions through Processing with Supercritical CO $_2$. *Langmuir*, 24(20):11935–11941, October 2008. 119

[201] R. O. Fournier and J. J. Rowe. The solubility of amorphous silica in water at high temperatures and high pressures. *American Mineralogist*, 62:1052–1056, 1977. 119

[202] Diane Rebiscoul, Pierre Frugier, Stéphane Gin, and André Ayral. Protective properties and dissolution ability of the gel formed during nuclear glass alteration. *Journal of Nuclear Materials*, 342(1-3):26–34, June 2005. 124

[203] P. Frugier, S. Gin, Y. Minet, T. Chave, B. Bonin, N. Godon, J.-E. Lartigue, P. Jollivet, A. Ayral, L. De Windt, and G. Santarini. SON68 nuclear glass dissolution kinetics: Current state of knowledge and basis of the new GRAAL model. *Journal of Nuclear Materials*, 380(1-3):8–21, October 2008. 124

[204] Veniamin Grigorevich Levich. *Physicochemical hydrodynamics*. Prentice-Hall, 1962. Google-Books-ID: EtoIAQAAIAAJ. 126, 172

[205] T. Higuchi. Mechanism of sustained action medication. Theoretical analysis of rate of release of solid drugs dispersed in solid matrices. *Journal of Pharmaceutical Sciences*, 52(12):1145–1149, December 1963. 127, 133

[206] Philip L. Ritger and Nikolaos A. Peppas. A simple equation for description of solute release I. Fickian and non-fickian release from non-swellable devices in the form of

slabs, spheres, cylinders or discs. *Journal of Controlled Release*, 5(1):23–36, June 1987. 134

[207] Philip L. Ritger and Nikolaos A. Peppas. A simple equation for description of solute release II. Fickian and anomalous release from swellable devices. *Journal of controlled release*, 5(1):37–42, 1987. 134

[208] Jörn E. Möckel and Bernhard C. Lippold. Zero-Order Drug Release from Hydrocolloid Matrices. *Pharmaceutical Research*, 10(7):1066–1070, July 1993. 134

[209] J Siepmann. Mathematical modeling of bioerodible, polymeric drug delivery systems. *Advanced Drug Delivery Reviews*, 48(2-3):229–247, June 2001. 134

[210] Brittany E. Givens, Zhenzhu Xu, Jennifer Fiegel, and Vicki H. Grassian. Bovine serum albumin adsorption on SiO 2 and TiO 2 nanoparticle surfaces at circumneutral and acidic pH: A tale of two nano-bio surface interactions. *Journal of Colloid and Interface Science*, 493:334–341, May 2017. 140

[211] Anurag Sharma, Pratibha K. Agarwal, and Shashank Deep. Characterization of different conformations of bovine serum albumin and their propensity to aggregate in the presence of N-cetyl-N,N,N-trimethyl ammonium bromide. *Journal of Colloid and Interface Science*, 343(2):454–462, March 2010. 141, 142, 143, 144

[212] Ank Valstar, Mats Almgren, Wyn Brown, and Marilena Vasilescu. The Interaction of Bovine Serum Albumin with Surfactants Studied by Light Scattering. *Langmuir*, 16(3):922–927, February 2000. 141, 143

[213] Christopher Dobson. Protein Aggregation and Its Consequences for Human Disease. *Protein & Peptide Letters*, 13(3):219–227, March 2006. 143

[214] Thomas Fontecave, Cedric Boissiere, Niki Baccile, Francisco J. Plou, and Clement Sanchez. Using Evaporation-Induced Self-Assembly for the Direct Drug Templating of Therapeutic Vectors with High Loading Fractions, Tunable Drug Release, and Controlled Degradation. *Chemistry of Materials*, 25(23):4671–4678, December 2013. 149

[215] Enkeleda Dervishi, Shawn Bourdo, Joshua A. Driver, Fumiya Watanabe, Alexandru R. Biris, Anindya Ghosh, Brian Berry, Viney Saini, and Alexandru S. Biris. Catalytic Conversion of Graphene into Carbon Nanotubes *via* Gold Nanoclusters at Low Temperatures. *ACS Nano*, 6(1):501–511, January 2012. 152

[216] Cheng-An J. Lin, Ting-Ya Yang, Chih-Hsien Lee, Sherry H. Huang, Ralph A. Sperling, Marco Zanella, Jimmy K. Li, Ji-Lin Shen, Hsueh-Hsiao Wang, Hung-I Yeh, Wolfgang J. Parak, and Walter H. Chang. Synthesis, Characterization, and Bioconjugation of Fluorescent Gold Nanoclusters toward Biological Labeling Applications. *ACS Nano*, 3(2):395–401, February 2009. 152

[217] Kyuju Kwak, S. Senthil Kumar, Kyunglim Pyo, and Dongil Lee. Ionic Liquid of a Gold Nanocluster: A Versatile Matrix for Electrochemical Biosensors. *ACS Nano*, 8(1):671–679, January 2014. 152

[218] Mathew Hembury, Ciro Chiappini, Sergio Bertazzo, Tammy L. Kalber, Glenna L. Drisko, Olumide Ogunlade, Simon Walker-Samuel, Katla Sai Krishna, Coline Jumeaux, Paul Beard, Challa S. S. R. Kumar, Alexandra E. Porter, Mark F. Lythgoe, Cédric Boissière, Clément Sanchez, and Molly M. Stevens. Gold–silica quantum rattles for multimodal imaging and therapy. *Proceedings of the National Academy of Sciences*, 112(7):1959–1964, February 2015. 153

[219] Emmanuel Esteve, Solenn Reguer, Cédric Boissiere, Corinne Chanéac, Gustavo Lugo, Chantal Jouanneau, Cristian Mocuta, Dominique Thiaudière, Nicolas Leclercq, Bernard Leyh, Jean-François Greisch, Julien Berthault, Michel Daudon, Pierre Ronco, and Dominique Bazin. Flyscan opportunities in medicine: the case of quantum rattle based on gold quantum dots. *Journal of Synchrotron Radiation*, 24(5):991–999, September 2017. 154

[220] Christophe Lavenn, Florian Albrieux, Gérard Bergeret, Rodica Chiriac, Pierre Delichère, Alain Tuel, and Aude Demessence. Functionalized gold magic clusters: Au25(SPhNH2)17. *Nanoscale*, 4(23):7334, 2012. 154, 156

[221] A. M. Malek, S. L. Alper, and S. Izumo. Hemodynamic shear stress and its role in atherosclerosis. *JAMA*, 282(21):2035–2042, December 1999. 164, 165

[222] George Gabriel Stokes. *On the effect of the internal friction of fluids on the motion of pendulums*. Cambridge : Printed at the Pitt Press, by John W. Parker, 1851. 165